

Department of Chemistry
Adran Chemeg



The Catalytic Oxidation of Volatile Organic Compounds

**Thesis submitted to Cardiff University for the
degree of Doctor of Philosophy in Chemistry**

By

Edwin Ntainjua Ndifor

June 2007

UMI Number: U584974

All rights reserved

INFORMATION TO ALL USERS

The quality of this reproduction is dependent upon the quality of the copy submitted.

In the unlikely event that the author did not send a complete manuscript and there are missing pages, these will be noted. Also, if material had to be removed, a note will indicate the deletion.



UMI U584974

Published by ProQuest LLC 2013. Copyright in the Dissertation held by the Author.
Microform Edition © ProQuest LLC.

All rights reserved. This work is protected against
unauthorized copying under Title 17, United States Code.



ProQuest LLC
789 East Eisenhower Parkway
P.O. Box 1346
Ann Arbor, MI 48106-1346

For Florence Ntainjua B. and Jude Ntainjua B.

'A man's fortunes are the fruit of his character'. Ralph Waldo Emerson.

TABLE OF CONTENTS

Acknowledgement

List of abbreviations

Abstract

Chapter 1: Introduction.....	1
1.1 Volatile organic compounds (VOCs).....	1
1.1.1 Sources, health and environmental hazards of VOCs.....	2
1.1.1.1 Sources of VOCs	2
1.1.1.2 Health and environmental hazards of VOCs.....	4
1.1.2 Legislation against the emission of VOCs.....	5
1.2 Technologies for the control of VOCs.....	5
1.2.1 Absorption	6
1.2.2 Adsorption.....	6
1.2.3 Biodegradation.....	7
1.2.4 Thermal incineration.....	7
1.2.5 Non-thermal plasmas (NTP).....	7
1.2.6 Catalysis.....	10
1.3 Oxidation catalysis: Basic concepts and theoretical background.....	12
1.3.1 Definitions.....	12
1.3.2 Catalytic activity and selectivity of metal-supported catalysts.....	14
1.3.2.1 Active component.....	14
1.3.2.2 Support.....	14
1.3.2.3 Promoter (modifier).....	15
1.3.3 Chemical thermodynamics and kinetics of catalysis	15
1.3.3.1 Catalysis and chemical thermodynamics.....	16
1.3.3.2 Catalysis and chemical kinetics.....	17
1.3.4 Steps in a catalytic reaction.....	19
1.3.4.1 Adsorption and desorption.....	19
1.3.4.2 The Langmuir adsorption isotherm.....	21
1.4 Review of catalysts used to date for naphthalene oxidation	22
1.4.1 Oxidative decomposition of naphthalene by supported metal catalysts.....	23
1.4.1.1 BET results.....	24
1.4.1.2 XRD results.....	25
1.4.1.3 TPD results.....	26

1.4.2 Naphthalene oxidation over 1%Pt and 5%Co/ γ -Al ₂ O ₃ : reaction intermediates and possible pathways.....	28
1.4.3 Catalytic oxidation of organic compounds including polycyclic aromatic hydrocarbons (PAHs) from motor exhaust gases	33
1.4.4 Application of metal-exchanged zeolites in removal of emissions from combustion of biofuels.....	34
1.4.5 An Investigation of the activity of Pd and Pd-Zr modified Y-zeolite catalysts for the removal of PAH, CO, CH ₄ and NO _x emissions.....	35
1.4.6 Catalytic clean-up of emissions from small-scale combustion of biofuels.....	36
1.4.7 Catalytic abatement of emissions from small-scale combustion of wood: A comparison of catalytic effect in model and real flue gases.....	37
1.4.8 Recent advances in the catalytic oxidation of naphthalene.....	38
1.4.8.1 Catalytic oxidation of naphthalene using a Pt/Al ₂ O ₃ catalyst.....	38
1.4.8.2 Nano-crystalline ceria catalysts for the abatement of polycyclic aromatic hydrocarbons.....	39
1.4.8.3 Naphthalene total oxidation over metal oxide catalysts.....	40
1.4.8.4 Complete naphthalene oxidation over Pd/V and Pt/V-supported catalysts, Pt-supported catalysts, nano-crystalline CeO ₂ catalysts and metal-supported CeO ₂ catalysts.....	41
References.....	42
 Chapter 2: Experimental.....	47
2.1 Introduction.....	47
2.2 Catalyst preparation.....	47
2.2.1 Preparation of metal-supported catalysts for naphthalene oxidation.....	47
2.2.1.1 Preparation of Pd/ γ -Al ₂ O ₃ , Pt/ γ -Al ₂ O ₃ , Pd/V/ γ -Al ₂ O ₃ , and Pt/V/ γ -Al ₂ O ₃ ...	47
2.2.1.2 Preparation of Pt/SiO ₂ , Pt/SnO ₂ , Pt/TiO ₂ and Pt/CeO ₂	48
2.2.2 Precipitation methods for the preparation of crystalline ceria for naphthalene oxidation.....	50
2.2.2.1 Precipitation with urea: Urea Route (UR).....	50

2.2.2.2 Precipitation with sodium carbonate: Carbonate Route (CR).....	52
2.2.3 Preparation of Ceria using supercritical carbon dioxide: Supercritical carbon dioxide Route (Sc).....	52
2.2.4 Preparation of Pt/CeO ₂ by homogeneous precipitation with urea.....	54
2.3 Catalyst characterisation.....	55
2.3.1 Introduction.....	55
2.3.2 Theory of atomic absorption spectroscopy.....	55
2.3.3 Atomic absorption experimental procedure.....	58
2.3.4 Theory of Brunauer-Emmet-Teller method	59
2.3.5 BET experimental procedure.....	62
2.3.6 Theory of CO chemisorption.....	62
2.3.7 CO Chemisorption experimental procedure.....	64
2.3.8 Theory of powder x-ray diffraction (XRD).....	64
2.3.9 XRD experimental procedure.....	68
2.3.10 Theory of laser Raman spectroscopy.....	69
2.3.11 Raman spectroscopy experimental procedure.....	71
2.3.12 Temperature programmed reduction (TPR).....	72
2.3.13 TPR experimental procedure.....	72
2.3.14 Theory of thermal gravimetric analysis.....	73
2.3.15 TGA experimental procedure.....	73
2.3.16 Theory of Scanning electron microscopy (SEM).....	73
2.3.17 SEM experimental procedure.....	75
2.3.18 Theory of X-ray photoelectron spectroscopy.....	77
2.3.19 XPS Experimental procedure.....	79
2.4 Catalyst testing.....	80
2.4.1 Naphthalene oxidation process and equipment.....	80
2.4.2 Naphthalene oxidation experimental procedure.....	84
References.....	86

Chapter 3: Naphthalene oxidation over vanadium-modified Pd and Pt catalysts supported on γ -alumina.....88

3.1 Introduction.....	88
3.2 Atomic Absorption spectroscopy results for Pd/V/Al ₂ O ₃ Catalysts.....	90

3.3 BET and CO chemisorption results for vanadium-modified Pd and Pt-supported alumina catalysts.....	91
3.4 XRD results for vanadium-modified Pd and Pt-supported alumina catalysts.....	93
3.5 Raman Results for vanadium-modified Pd and Pt-supported alumina catalysts...	96
3.6 Temperature-programmed reduction results for vanadium-modified Pd and Pt-supported alumina catalysts.....	99
3.7 Naphthalene oxidation activity over vanadium-modified Pd-supported alumina catalysts.....	103
3.8 Naphthalene oxidation activity over vanadium-modified Pt-supported alumina catalysts.....	108
3.9 Conclusion.....	114
References.....	116

Chapter 4: Influence of support on the performance of platinum-supported catalysts for the total oxidation of naphthalene.....119

4.1 Introduction.....	119
4.2 Characterisation data for Pt catalysts supported on various metal oxides.....	120
4.3 Catalytic activity results for Pt catalysts supported on various metal oxides.....	130
4.4 conclusions.....	140
References.....	141

Chapter 5: Influence of preparation conditions of nano-crystalline ceria catalysts on the total oxidation of naphthalene.....143

5.1 Introduction.....	143
5.2 Effect of calcination temperature on properties and activity of CeO ₂ (UR).....	145
5.2.1 Effect of calcination temperature on surface area of CeO ₂ (UR).....	145
5.2.2 Effect of calcination temperature on XRD results of CeO ₂ (UR).....	147
5.2.3 Effect of calcination temperature on Raman results of CeO ₂ (UR).....	148
5.2.4 Effect of calcination temperature on SEM results of CeO ₂ (UR).....	150
5.2.5 Effect of calcination temperature on TPR Results of CeO ₂ (UR).....	151
5.2.6 Effect of calcination temperature on activity of CeO ₂ (UR) for the total oxidation of naphthalene.....	154
5.3 Effect of calcination time on properties and activity of CeO ₂ (UR).....	157
5.3.1 Effect of calcination time on the surface area of CeO ₂ (UR)	158

5.3.2 Effect of calcination time on XRD results of CeO ₂ (UR)	158
5.3.3 Effect of calcination time on Raman results of CeO ₂ (UR)	160
5.3.4 Effect of calcination time on SEM results of CeO ₂ (UR)	163
5.3.5 Effect of calcination time on TPR results of CeO ₂ (UR)	165
5.3.6 Effect of calcination time on the activity of CeO ₂ (UR) for the total oxidation of naphthalene.....	166
5.4 Effect of aging time on properties and activity of CeO ₂ (UR).....	169
5.4.1 Effect of aging time on BET surface area of CeO ₂ (UR).....	169
5.4.2 Effect of aging time on XRD results of CeO ₂ (UR).....	170
5.4.3 Effect of aging time on Raman results of CeO ₂ (UR).....	171
5.4.4 Effect of aging Time on SEM results of CeO ₂ (UR).....	173
5.4.5 Effect of aging Time on TPR results of CeO ₂ (UR).....	174
5.4.6 Effect of aging time on the activity of CeO ₂ (UR) catalyst for the total oxidation of naphthalene.....	175
5.5 Effect of Ce salt/urea ratio on properties and activity of CeO ₂ (UR).....	178
5.5.1 Effect of Ce salt/urea ratio on BET surface area of CeO ₂ (UR).....	179
5.5.2 Effect of Ce salt/urea ratio on XRD results of CeO ₂ (UR).....	179
5.5.3 Effect of Ce salt/urea ratio on Raman results of CeO ₂ (UR).....	181
5.5.4 Effect of Ce salt/urea ratio on SEM results of CeO ₂ (UR).....	183
5.5.5 Effect of Ce salt/urea ratio on TPR results of CeO ₂ (UR).....	185
5.5.6 Effect of cerium salt to urea ratio on the activity of CeO ₂ (UR) catalyst for the total oxidation of naphthalene.....	187
5.6 Effect of GHSV on the activity of CeO ₂ (UR) catalysts for naphthalene oxidation.....	192
5.7 Summary of the activity of CeO ₂ (UR) catalysts for naphthalene oxidation.....	193
5.8 Conclusions.....	196
References.....	197

Chapter 6: Ceria and Pt-loaded ceria catalysts for the total oxidation of naphthalene.....	200
6.1 Introduction.....	200
6.2 Influence of preparation method of crystalline ceria catalysts for the total oxidation of naphthalene.....	201

6.2.1 Influence of preparation method on characteristics of crystalline ceria catalysts.....	201
6.2.2 Influence of preparation method on the naphthalene oxidation activity of ceria catalysts.....	212
6.3 Influence of Pt-doping of nano-crystalline ceria catalysts for the total oxidation of naphthalene.....	217
6.3.1 Surface and structural studies of CeO ₂ (UR) and Pt/ CeO ₂ (UR) catalysts....	218
6.3.2 Raman results for CeO ₂ (UR) and Pt/CeO ₂ (UR) catalysts.....	221
6.3.3 TPR results for CeO ₂ (UR) and Pt/CeO ₂ (UR) catalysts.....	223
6.3.4 Effect of Pt-doping on the activity of a nano-crystalline CeO ₂ (UR) catalyst for the complete oxidation of naphthalene.....	225
6.4 Conclusions.....	228
References.....	230
Chapter 7: Conclusions and recommendations.....	231
Publications.....	236

Acknowledgements

This work would not have been accomplished without the advice, help and support of a handful of people.

I would first like to thank God for all His wonderful blessings over the years.

Special thanks to my Supervisor, Dr. Stuart H. Taylor, for his excellent supervision throughout my PhD project.

Many thanks to Prof. Kingsley Carvell and Cardiff School of Chemistry for funding my PhD; Prof. Graham Hutchings and all the members of his research group for providing the equipment, technical support and serene working atmosphere which I very much enjoyed. I am particularly thankful to Dr. Tomas Garcia (former Research Fellow in the group), Dr. Thomas Davies, Graham Laing, Pete L., Umacaran S., Dr. Zi-rong Tang, Kieran Cole, Matt Davies, J. Ferguson, Dr. Phill Landong, Alun Davies, Dr. Jonathan Bartley and Dr. Nick Dummer for helping me with the initial stages of catalyst preparation and characterisation, equipment modification, catalyst testing and for their continuous assistance in the course of the project. Thanks also to Dr. Albert F. Carley for helping me with XPS analysis.

I am thankful to my MSc. Eng. mate George Saforo for letting me know about the PhD position at Cardiff School of Chemistry. I am very thankful to my MSc. Eng. Supervisor Ass. Prof. Terence E. Warner, of the University of Southern Denmark, and my friend Emmanuel Ngwengi for encouraging me to accept the PhD position at Cardiff University.

I would also like to thank my family for their love, understanding, support, and encouragement.

I had a very entertaining social life in Cardiff and the UK, thanks to the great friends I interacted with. Sincere gratitude to my friends (Enow A. Tabe, Valery F. Tangham, Edith Ofegbe, Evelyne Tangham, Michael Nkemka, DePaul, Ayukebang Eta, Conrad E. Ntoko, Nicol Nsobam, Collins Awambeng, Chiatoh Louis, Edmund Mbuh, Edmund Boakye, Wakuna Galega, Christine Langhoff, Silot Ambe, Marcial, Cyril, Pat, Julio, Richard Valery K., Martin, Smith, Chinje, Nina, Mario and Jean) for making my stay in Cardiff and the UK so enjoyable.

List of Abbreviations

VOCs - Volatile organic compounds

LOT – Light-off temperature

PACs - Polycyclic aromatic compounds

PAHs - Polycyclic aromatic hydrocarbons

NTP - Non-thermal plasmas

Np – Naphthalene

TWV – Two way valve

D - Dimension

Å – Angstrom

μ – micro

nm – Nano metre

KV – kilo volt

Mol – mole

° – Degree

°C – Degree celcius

wt – weight

ml – milli litre

min – Minute

g - Gram

s – Second

h – Hour

keV – Kilo electron volt

Ca. – approximately

o.d. – outer diameter

Δ - Change

< - less than

> - greater than

≥ - greater than or equal to

G – Gibb's free energy

H – Enthalpy or heat

S – Entropy

k- Rate constant

K - equilibrium constant
 A - Pre-exponential factor or frequency factor
 E_a - Activation energy
 R - Gas constant
 T - Temperature
 k_a - Rate constants for adsorption
 k_d - Rate constant for desorption
 NGVs - Natural gas driven vehicles
 BET - Brunauer-Emmet-Teller
 H_L - Heat of condensation
 ΔH - Enthalpy or heat change
 Θ - Fraction of surface coverage
 P - Equilibrium pressure
 P_o - Saturated vapour pressure of gas at temperature of experiment
 V - Amount of gas adsorbed or volume
 V_m - Monolayer coverage or volume of monolayer
 STP - Standard condition of temperature and pressure
 cc - Cubic centi-metre
 λ - Wavelength
 AAS - Atomic absorption spectroscopy
 XRD - powder X-ray diffraction
 TPR - temperature programmed reduction
 TPD - temperature programmed desorption
 GC - Gas chromatography
 XPS - X-ray photoelectron spectroscopy
 SEM - Scanning electron microscopy
 T100 - Temperature at which 100 % conversion is achieved
 UR - Urea route
 CR - Carbonate route
 Sc - Supercritical carbon dioxide
 HT - High temperature
 LT - Low temperature

All other abbreviations not included here are clearly specified in the text.

Abstract

Polycyclic aromatic hydrocarbons (PAHs) are an important class of volatile organic compounds (VOCs) which pose enormous health and environmental threats. This thesis investigates different catalyst formulations for the complete oxidation of naphthalene (Np), a model PAH.

Low loadings of vanadium added during the impregnation step of catalyst preparation were found to enhance the naphthalene oxidation activity of Pd-alumina and Pt-alumina catalysts while higher loadings were detrimental to the catalysts' performance. The promotional effect has been attributed to the presence of a low concentration of a particular type of vanadium species which fosters the redox behaviour of the binary system (Pd/V or Pt/V) coupled with the change in the active metal (Pd or Pt) particle size (Pd or Pt dispersion). The presence of high concentrations of crystalline V_2O_5 species has been suggested to account for the lower activity observed for Pd/V and Pt/V catalysts with vanadium loadings in the range of 6 – 12% and 1 - 12 % respectively. It is postulated that the mechanism of naphthalene oxidation over Pd/V differs from the mechanism of oxidation over Pt/V catalysts.

The nature of support material was established to be crucial for the activity of Pt-supported catalysts for naphthalene oxidation. The Pt dispersion, metal-support interaction (MSI) and oxidation state of Pt varied as a function of the nature of support and hence resulted in differences in the Np oxidation efficiency of five Pt-supported catalysts with equal Pt loading but different supports. Low Pt dispersion (high Pt particle size), weak MSI and metallic state of Pt favoured Np oxidation. SiO_2 proved to be the best amongst five Pt supports investigated for Np oxidation.

A variation in the preparation method and preparation conditions of ceria affected the surface area, crystallite size, oxygen defect concentration, morphology and surface reducibility of the ceria catalyst and hence the Np oxidation activity. High surface area, small crystallite size, and high oxygen defect concentration of CeO_2 favoured the activity of the catalyst for Np oxidation. The best preparation methods in this study were found to be homogeneous precipitation with urea (UR) and precipitation with the carbonate (CR). Optimum preparation conditions for ceria (UR) were established and a highly active nano-crystalline ceria catalyst for Np oxidation was

derived. The addition of low and high loadings of Pt during the precipitation of this ceria (UR) catalyst resulted in less active naphthalene oxidation catalysts. The drop in activity of ceria with Pt doping has been attributed to a strong metal support interaction between Pt and ceria which limits the ease at which lattice oxygen is consumed in the Mars-Van Krevelen redox cycle.

CHAPTER 1: INTRODUCTION

Volatile organic compounds (VOCs) make up major atmospheric pollutants. Due to the severe health and environmental hazards associated with the emission of VOCs in to the atmosphere, various research groups and laboratories [1-22] around the world have concentrated interest in the development of catalysts with potential for effectively converting VOCs in to more environmentally benign compounds like CO₂ and H₂O.

In this thesis, previous and most recent work on the catalytic abatement of an important group of VOCs, called polycyclic aromatic hydrocarbons (PAHs) are discussed. Catalysts used for the destruction of PAH and gas mixtures composed of PAH, CO and other VOCs are reviewed. Naphthalene is used as a model PAH to investigate the effect of different catalyst formulations on the total destruction of PAHs.

1.1 Volatile organic compounds (VOCs)

Volatile organic compounds (VOCs) are organic compounds that easily become vapours or gases and as such are commonly found in our indoor and outdoor environment. Examples of VOCs include methane, propane, perchloroethylene, formaldehyde, benzene, toluene, and xylene.

Polycyclic aromatic compounds (PACs) such as naphthalene, phenanthrene and pyrene make up a major class of VOCs. Two groups of PACs; polycyclic aromatic hydrocarbons

(PAHs) and nitro-polycyclic aromatic hydrocarbons (nitro-PAHs) are known. Naphthalene is the simplest, least toxic and most volatile PAH [24, 25] and as such has been used in several research laboratories [2, 3, 4, 5, 6, 26, 27] as a model PAH to develop catalysts with potential to effectively destroy PAHs. In this thesis, the catalytic oxidation of naphthalene is investigated in a bit to develop catalysts potentially useful in PAH abatement catalytic systems.

1.1.1 Sources, Health and Environmental Hazards of VOCs

Various sources of VOCs and their health and environmental hazards have been reported [24, 28-37].

1.1.1.1 Sources of VOCs

Sources of VOCs include:

- Fuel (gasoline, wood, coal, and natural gas) combustion
- Production, distribution and use of solvents, paints, upholstery, fabrics, adhesives, carpets and cleaning materials.
- Biomass burning
- Industrial Processes
- Gas leakage
- Offshore oil and gas
- Petrol distribution

- Forest
- Non-landfill waste treatment and disposal.

Figure 1.1 shows the estimated UK emission of VOCs by source category in 1998 [37]. The figure shows that, solvent use and road traffic represented the most important sources. PAHs and nitro-PAHs have been identified in diesel emissions [26] while motor vehicle emissions in general have been documented as one of the prime sources of VOCs and PACs in Hong Kong [38].

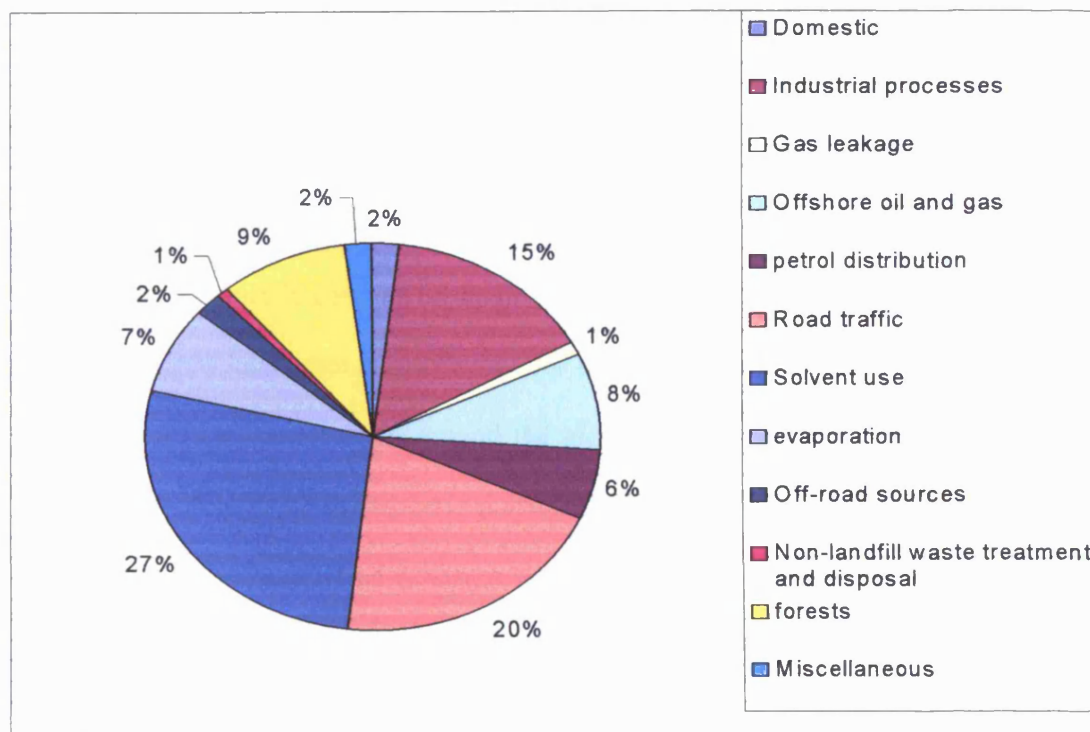


Fig. 1.1 Estimated UK emission of VOCs by source category for 1998: adapted from [37].

1.1.1.2 Health and Environmental Hazards of VOCs

While short term exposures to VOCs can cause eye and respiratory tract irritations, visual disorders, fatigue and allergic skin reactions, prolonged exposures might result to cancer and damage to the liver, kidney, and central nervous system.

VOCs react with NO_x to form ground level ozone which together with other greenhouse gases (e.g. CO₂) account for global warming (one of the greatest environmental challenges in this era).

1.1.2 Legislation against the Emission of VOCs

The health hazards associated with the emission of VOCs into the atmosphere have led to an increasing public concern for environmental protection and safety. Although there are no stringent international restrictions for the level of most of these emissions, most governments and organisations around the globe are setting up their own rules to cut down the level of these atmospheric pollutants. The Comité Européen de Normalisation has for instance suggested an emission standard of 2500, 100, and 150 mg/Nm³ for CO, total hydrocarbons, and particulate matters from boilers and wood stoves, for fuel supply of 50-150 kW⁵ [4, 39].

1.2 Technologies for the Control of VOCs

Increasing regional and international enforcement of environmental regulations has over the years led to the development of technologies to combat atmospheric pollution by destroying or removing VOCs. Methods such as biodegradation [40], high-energy electron beam [41], ozonization [42], adsorption [43], absorption [44], thermal incineration [45] and catalytic oxidation [2, 3, 4, 5, 6, 26, 27] have been employed to cut down the level of polycyclic aromatic hydrocarbons emitted in the atmosphere. In this section, a number of such technologies used for VOC abatement are discussed.

1.2.1 Absorption

It is a technique in which the VOC is recovered by absorption in a liquid. This generally prevents the VOC from getting in to the atmosphere but does not destroy it. There is therefore a storage or further treatment problem associated with the use of this technique.

1.2.2 Adsorption

In this technique, the VOC is removed or recovered by attachment (forms a gas film) on the surface of a solid material known as an adsorbent. Tenax for example is a good adsorbent for VOCs such as naphthalene.

Absorption and adsorption abatement techniques result in the generation of liquid and solid waste which require further treatment. Adsorbers which make use of desorption to recover the VOCs give rise to wastewater when the VOCs are condensed and separated from the emission stream. This leaves an aqueous stream which can contain residual VOCs. In a similar way, absorbers make use of a solvent to remove VOCs from a vapour stream. This leads to the generation of wastewater when the used solvent is discharged to a water treatment system. Solid or semi-solid sludge which commonly emanate from absorption and adsorption VOC abatement systems require proper disposition or recycling and as such make both methods to be uneconomical when compared to alternative methods like catalysis.

1.2.3 Biodegradation

Biodegradation has been widely used for the destruction of volatile organic compounds [40, 46-48]. This technique involves the decomposition of VOCs in to smaller compounds by microbial organisms. Biodegradation processes vary greatly, but in most cases, the end product of degradation is carbon dioxide or methane. The type of microbial organism required depends on the nature of VOC to be destroyed. The technique is a major process in the natural attenuation of contaminants at hazardous waste sites.

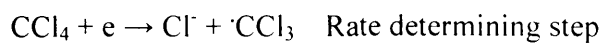
1.2.4 Thermal incineration

Thermal incineration is the oldest and one of the most common methods employed for the abatement of VOCs. It involves combustion of VOCs in air at temperatures as high as 1000 °C. The high temperature involved makes this method of abatement quite expensive when compared to other lower temperature methods. The method equally presents very little or no control over the nature of end products and as such can lead to the generation of more toxic species. For example, phosgene (COCl_2), chloroacetylene (C_2Cl_2) and radicals ($\cdot\text{CCl}_2\text{CH}$ and $\cdot\text{CCl}_3$) have been reported as highly toxic products emanating from some clean-up processes [49].

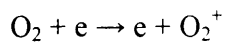
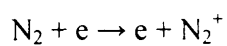
1.2.5 Non-thermal Plasmas (NTP)

NTP processing is quite an emerging technology for the abatement of VOCs [50].

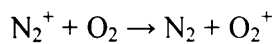
Although the method might be less costly than thermal incineration (due to low temperatures involved), there is still very limited control over the nature of products. The major challenge of NTP processes is therefore how to deal with energy consumption and control by-products. The basic principle of all NTP systems is the production of plasma in which most of the energy is consumed in the production of high-energy electrons, rather than gas heating. The bombardment of these free electrons with neighbouring gas molecules results to ionization and dissociation of the molecules to form highly reactive species like redox radicals which can spontaneously break down entrained pollutants in the atmosphere. Highly oxidative and reductive radicals produced by these plasmas are capable of attacking a great variety of pollutants, and in some cases can simultaneously decompose multiple species. Two types of dielectric-discharge-driven NTPs: dielectric barrier (silent) discharges and pulsed corona discharges have been reported for the abatement of VOCs [51]. Both types are easy to operate at or above atmospheric pressure and as such give rise to a high process throughput when compared to low-pressure NTPs. Pulsed corona and electron beam reactors have been used for the treatment of various VOCs [50]. This study revealed that electron beam processing is more energy efficient than pulse corona processing for most of the VOCs studied. For CCl_4 and other VOCs requiring massive quantities of electrons for their decomposition, electron beam processing significantly predominates. The decomposition of some VOCs depends on the rate of reaction with the plasma-produced radicals and/or by the occurrence of back reactions. In such cases, energy consumption can be kept at a minimum by making use of elevated but non-combusting temperatures. The pathway for the abatement of CCl_4 as reported by the above study [50] is summarized below.

1) Dissociative attachment of CCl₄ to plasma-generated energetic electrons

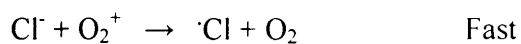
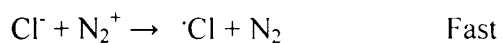
2) Generation of electron-ion pair during plasma reaction



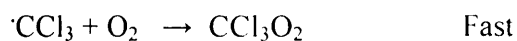
3) Charge exchange reaction of cations with background oxygen



4) Neutralization reactions



5) Scavenging reaction



In the absence of this reaction (5), energy input would have been wasted due to the regeneration of the original pollutant in the following recombination reaction.



6) CCl_3O_2 reacts with $\cdot\text{Cl}$ in a series of reactions to form phosgene (also a pollutant) as main organic product. Cl_2 formed in the termination step below is another major product of the decay process.



The energy consumed in step 2 above determines the energy consumed in the decay of CCl_4 by this process. Since step 1 is the rate determining step, the rate of CCl_4 decomposition can be written as:

$$-\text{d}[\text{CCl}_4]/\text{dt} = k[\text{CCl}_4][\text{e}]$$

1.2.6 Catalysis

Catalysis is a destructive VOC control technique in which the VOC is oxidized in the presence of a catalyst. Among the various methods proposed for controlling VOC emission in to the atmosphere, catalytic oxidation of VOCs to more environmentally

friendly CO₂ and H₂O appears to be one of the most cost-effective. Apart from being relatively less expensive (as use of catalyst ensures combustion at temperatures below 500-600 °C) than thermal incineration, it has a higher extend of selectivity to desired end products than most of the other abatement methods. Despite the low temperatures and higher level of selectivity, the use of a catalyst could as well result in the formation of other toxic or undesirable by-products. This usually accounts for the mismatch between the amount of compound combusted and the amount of carbon dioxide produced. Xiao-Wen and co-workers have for instance identified and classified the intermediates derived from naphthalene oxidation over 1%Pt/γ-Al₂O₃ in to three categories [1]. A good oxidation catalyst must therefore be one that guarantees a lower level of toxicity and excellent environmental protection. The design of a frugal and efficient oxidation catalyst will thus represent a giant step towards the eradication of the health and environmental problems associated with VOC emission. Such a catalyst should have a low light-off temperature (temperature at which conversion changes from a low to a high value), high thermal stability, large active surface area, long life- time (low deactivation tendency) and capable of operating over a wide range of space velocities.

Thermal stability of most metal catalysts is often achieved by supporting them on ceramic materials (mainly metal oxides). The mechanical properties of ceramics (as well as many other materials) depend on their microstructure (which consists of size, shape, and distribution of crystalline grains, bonding between grains and the segregation of any impurities to the surface or intergranular regions) [52]. The method of synthesis in turns governs the microstructure of a material. As such, variations in composition and general

synthetic procedure/method often trigger changes in microstructure of metal oxide and metal-supported catalysts and hence changes in catalyst properties and catalytic activity.

The main goal of this work as we shall see later is to investigate the effect of different catalyst formulations on the oxidation of naphthalene (most abundant PAC identified in diesel emissions [26]). This is done in a bid to develop efficient catalysts, potentially useful for the control of emissions from diesel exhaust, wood-fired heaters and end of pipe in industries. Although this thesis later concentrates on the catalytic combustion of naphthalene, it is essential to look at the basic concepts that apply to all catalytic reactions.

1.3 Oxidation Catalysis: Basic Concepts and theoretical Background

The concepts and theory of catalytic reactions have been covered in-depth in various publications [53-58]. This chapter gives a brief summary of these concepts and the theory governing catalysis.

1.3.1 Definitions

A catalyst is a substance which speeds up or retards the rate at which a chemical reaction approaches equilibrium without undergoing any permanent chemical change. However,

prolonged use of a catalyst can result to decrease in performance. The process involving catalyst at work is termed catalysis.

Two main types of catalysis are known: heterogeneous catalysis in which catalyst and reactants have different phases and homogeneous catalysis in which catalyst and reactants have the same phase. Since this thesis dwells mainly on the catalytic oxidation of gas-phase naphthalene or VOC over solid metal-supported or metal oxide catalysts, the concepts discussed herein are mostly applicable to heterogeneous catalysis. Note however that some of the concepts to be discussed might also apply for homogeneous catalysis.

A catalyst's activity refers to its ability to convert reactants to products while its selectivity is its ability to convert reactants to a particular product. The lifetime of a catalyst refers to how long it can maintain its activity while deactivation is a term use to express the drop in a catalyst's activity, selectivity or both over time. A catalyst's light-off temperature (LOT) is the temperature at which conversion or yield changes from a very low value to a high value. In automotive catalysis it is considered as the temperature at which conversion efficiency is 50 % (i.e. T₅₀). For a catalyst to be successful in its performance, it should be active, have optimum selectivity and an economic lifetime (low deactivation tendency). The lower the light-off temperature and temperature of maximum yield of product, the higher the selectivity of the catalyst.

1.3.2 Catalytic Activity and Selectivity of Metal-supported Catalysts

The majority of catalysts investigated in this thesis (chapters 3 - 6) are metal-supported catalysts (i.e made up of metal(s) supported on another material – mostly metal oxides). The activity and selectivity of such catalysts are often provided by three components; active component, support, and promoter (modifier).

1.3.2.1 Active Component

Active components are mostly metals, oxides/sulphides or aluminosilicates. In this thesis, Pd and Pt are used as active components for metal-supported catalysts for naphthalene oxidation. The main role of the active component is to speed up the rate at which a desired chemical reaction approaches equilibrium by providing an easier selective path for the reaction to follow.

1.3.2.2 Support

Ceramics (mainly metal oxides) are often used as supports for metal supported catalysts. In this thesis Al_2O_3 , TiO_2 , SiO_2 , SnO_2 , and CeO_2 have been employed as supports for a variety of metals (mostly Pt and Pd). The main functions of the support include:

- Mechanical: Provide particle size, shape, strength and thermal stability

- Textural: Provide high internal surface area, optimum pore shape and size and to disperse the active component.
- Chemical: Modify the active component, stabilize the dispersion of the active component and provide a bi functional activity.

1.3.2.3 Promoter (Modifier)

Modifiers modify the active component (e.g alloy formation) or the support. In chapter 3 of this thesis, vanadium has been used as a modifier for Pt/Al₂O₃ and Pd/Al₂O₃ catalysts for naphthalene oxidation. The promoter increases the rate at which the reaction proceeds by modifying the properties of the active component or support. Modifiers also help in providing alternative easier routes for the catalytic process.

1.3.3 Chemical Thermodynamics and Kinetics of Catalysis

Chemical thermodynamics and chemical kinetics make up the most essential considerations in the design of a chemical process. While thermodynamics deals with whether or not a reaction will proceed (and to what extent if it does), kinetics has to do with how fast the reaction will go. Both concepts are inseparable and must be put together in order to achieve the best possible outcome. The thermodynamics of a system is indicative of the maximum yield of product that can be attained under some specified conditions. Irrespective of how fast a reaction might proceed, if the yield is low (small equilibrium constant), the entire process is still not viable. On the other hand, it is

absolutely of no use to have a large equilibrium constant (high yield), provided the equilibrium is reached only extremely slowly. Process economics therefore requires both high yield and speed of production.

1.3.3.1 Catalysis and chemical thermodynamics

For a chemical reaction to be plausible, the Gibbs free energy, G of that reaction must be negative. While a positive value of G signifies a backward reaction, a zero value represents an equilibrium condition. The change in Gibbs free energy for any system is given by equation (1).

$$\Delta G = \Delta H - T\Delta S \quad (1)$$

Where ΔH = enthalpy change, ΔS = entropy change and T = temperature

ΔG , ΔH and ΔS are called state functions because they are independent of the path of a reaction and only depend on the initial and final state of the system. Thus, ΔG , ΔH and ΔS for the oxidation of naphthalene (and all other reactions) must be the same for both catalyzed and uncatalyzed reactions. Figure 1.2 illustrates that the enthalpy change is the same for catalytic and non-catalytic exothermic reactions such as the combustion of naphthalene.

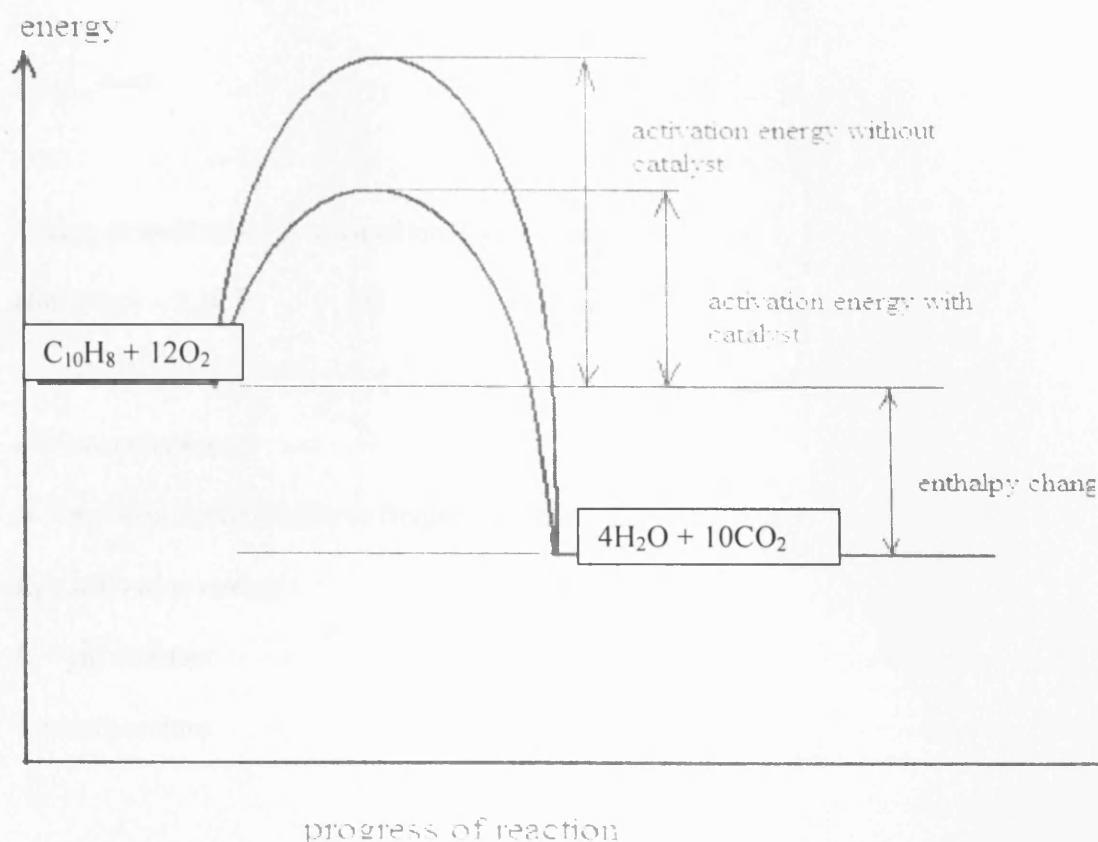


Fig. 1.2 Energy changes for catalyzed and non-catalyzed exothermic reaction (the combustion of naphthalene).

1.3.3.2 Catalysis and chemical kinetics

As mentioned earlier, a catalyst is defined as any substance that will alter the rate of a reaction without itself undergoing any change. Note however that prolonged usage and temperature treatment often leads to loss in activity and/or selectivity. The primary effect of most catalysts is to speed up the rate of a chemical reaction (increase the rate coefficient of the reaction). The rate coefficient for a reaction is related to the temperature

at which the reaction occurs as given by the Arrhenius equation, (2).

$$k = Ae^{-E_a/RT} \quad (2)$$

Taking \ln on both sides of equation 2 gives:

$$\ln k = \ln A - E_a/RT \quad (3)$$

k = rate constant

A = pre-exponential factor or frequency factor

E_a = activation energy

R = gas constant

T = temperature

E_a can be obtained from a plot of $\ln K$ against $1/T$. The gradient of the line increases with increase in the value of E_a , signifying a stronger temperature dependence of the rate constant. A zero value of E_a means that K is independent of T . The use of a catalyst provides an alternative path with lower activation energy and as such ensures that a reaction that will normally occur at very high temperatures can actually proceed at relatively lower temperatures. J-L Shie et al. [27] showed that the use of a $\text{Pt}/\gamma\text{-Al}_2\text{O}_3$ catalyst accelerated the rate of naphthalene decomposition and lowered the reaction temperature. While 95 % conversion was achieved at a temperature of 480 K ($\text{GHSV} < 35.000 \text{ h}^{-1}$) in the presence of the catalyst, non-catalytic thermal oxidation gave the same conversion at a temperature above 1000 K.

1.3.4 Steps in a catalytic reaction

Like all other catalytic reactions, the oxidation of naphthalene and other VOCs in the presence of a catalyst involves the following sequence of events:

- a) Transfer of reactants in the gas phase to the surface of the catalyst
- b) Adsorption of the reactants at the surface of the catalyst
- c) Chemical reactions between the reactants and the active sites of the catalyst
- d) Desorption of products from the active sites of the catalyst
- e) Transfer of products from the active sites into the gas phase

As indicated by the above sequence, adsorption and desorption are both very important steps in a catalytic process. It is very common for one or both processes to control the rate of a catalytic reaction. It is therefore important that we have a sound understanding of these processes since they also form the basis for the quantitative measure of the kinetics of catalyzed reactions.

1.3.4.1 Adsorption and desorption

Adsorption refers to the attachment of fluid at the surface of a solid. It can be physical (physisorption – involving weak Van der-Waal forces between adsorbate and surface) or chemical (chemisorption – in which bonds similar to covalent bonds are formed between the adsorbate and substrate i.e. the solid surface). Desorption refers to the detachment of the adsorbate from the surface into the surroundings. While it is usually difficult to make

a clear-cut distinction between physisorption and chemisorption, table 1.1 provides some parameters that are often used to differentiate between these two processes.

Table 1.1 Differences between physical and chemical adsorption

Physisorption	Chemisorption
Unselective	Selective
No activation energy needed	Small amount of activation energy needed
No breakage of molecular bonds and negligible changes in bond energies	Bonds in adsorbed molecules can be changed in strength (associative) or broken (dissociative chemisorption}
Occurs at low temperatures which depend on boiling point	Occurs at low temperatures which depend on E
Multi-layer adsorption possible	Only monolayer adsorption possible
Weak Van der-Waal forces involved	Covalent interactions involved

A schematic representation of the different ways in which CO can be adsorbed at the surface of a solid is shown in figure 1.3.

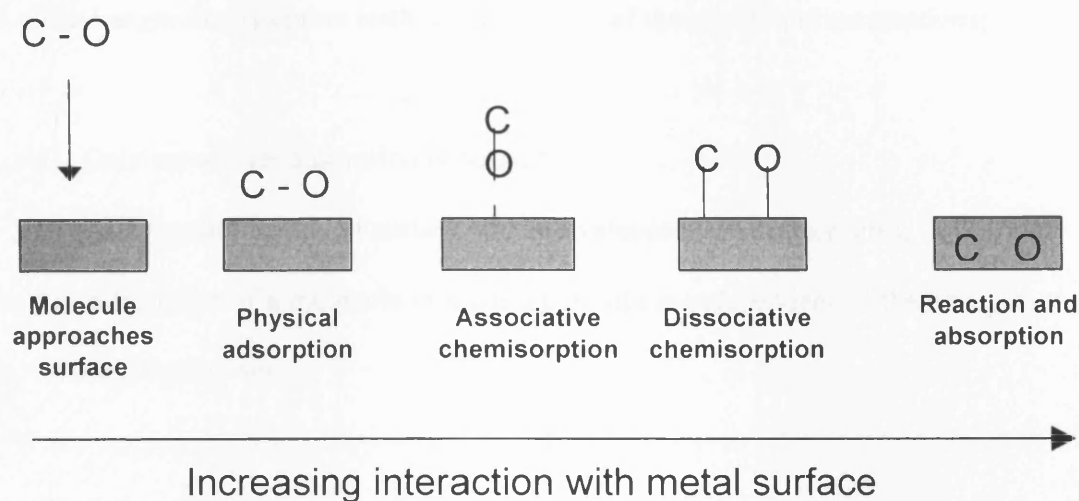


Fig.1.3 Possible ways of CO adsorption at solid surfaces. Adapted from [54]

1.3.4.2 The Langmuir adsorption isotherm

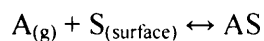
For quantitative analysis of the rate of catalyzed reactions, it is usually useful to develop a relationship between the amount of substance (reactant) adsorbed at the surface of the catalyst and the vapour pressure above the surface at a given temperature. The variation in surface coverage with pressure at a given temperature gives rise to an adsorption isotherm. Such isotherms are very essential as:

- 1) They provide a good basis for quantitative description of the degree and strength of adsorption of different molecules at the surface of a catalyst.
- 2) They form the basis for quantitative analysis of catalytic reaction rates.
- 3) They constitute the foundation for a useful method of measuring the surface areas of catalysts as we shall see later in chapter 2.

The Langmuir adsorption isotherm makes use of three principal assumptions;

- a) Only monolayer adsorption is possible,
- b) Assumes uniformity of surface and equivalence of all surface sites,
- c) Adsorption of a molecule to a particular site is independent of the occupation of neighboring sites.

Equilibrium exists between the free molecules and the adsorbed molecules as shown in the equation below:



For associative adsorption, the surface coverage, θ , is given by:

$$\theta = KP / (1 + KP)$$

For dissociative adsorption,

$$\theta = (KP)^{0.5} / (1 + KP)^{0.5}$$

The equilibrium constant $K = k_a/k_d$, where k_a and k_d are rate constants for adsorption and desorption respectively. P is the vapour pressure of $A_{(g)}$.

1.4 Review of catalysts used to date for naphthalene oxidation

Prior to the start of work reported in this thesis (October 2004) oxidation of naphthalene and gas mixtures containing naphthalene had been attempted using a number of metal oxide and metal-supported catalysts [1-5, 26, 39 and 59]. These studies revealed that

noble metal catalysts were more active and less easily deactivated than metal oxide catalysts [3]. They also showed that precious metal catalysts (Pd and Pt) were the most active metal-supported catalysts (with Pt activity being predominant) [3 and 26]. CuO-Pd/La-Al₂O₃ catalyst had also been reported to be effective in the oxidation of naphthalene [2]. Here, La was found to stabilize the γ -Al₂O₃ and as such helped in maintaining the amorphous nature of the latter. The following sections summarize most of the research patterning to the catalytic oxidation of naphthalene and naphthalene-containing mixtures prior to October 2004.

1.4.1 Oxidative decomposition of naphthalene by supported metal catalysts

In this work [26], the activity of six metal catalysts (1%Pt, 1%Pd, 1%Ru, 5%Co, 5%Mo and 5%W on γ -Al₂O₃) were examined for the decomposition of naphthalene in a fixed-bed reactor. The reaction rates were determined based on the amount of CO₂ produced and on the conversion of naphthalene. The results obtained indicated that the latter was a better measure for the activities of catalysts. The kinetic study of naphthalene oxidation over 1%Pt/ γ -Al₂O₃ in this study showed that the overall rate of the reaction was a function of the concentration of reactants (naphthalene and oxygen) and could be expressed using the Langmuir-Hinshelwood Kinetic Model. At temperatures over 140 °C the rate of this reaction was greatly dependent on the amount of naphthalene adsorbed. The reaction was found to be 1st order w.r.t P_{naphthalene} and w.r.t P_{O₂}, it was found to decrease with increasing reaction temperature.

The catalysts prepared in this study were characterised by BET, XRD, TPD and TPR. Some of the findings are summarised in this section.

1.4.1.1 BET results

Table 1.1 shows that catalysts synthesized in this work had surface areas close to but lower than that of the alumina support. M/alumina catalysts showed surface areas in the range 133-154 g/m² while the alumina support had a surface area of 178 g/m².

Table 1.1 BET results

Catalyst	Calcination temperature (°C)	Surface area (g\m ²)	Total pore volume
γ -Al ₂ O ₃	-	178	0.253
1%Pt on γ -Al ₂ O ₃	500	146	0.212
1%Pd on γ -Al ₂ O ₃	700	151	0.244
1%Ru on γ -Al ₂ O ₃	700	133	0.274
5%Co on γ -Al ₂ O ₃	700	154	0.265
5%Mo on γ -Al ₂ O ₃	700	140	0.242
5%W on γ -Al ₂ O ₃	700	148	0.219

1.4.1.2 XRD results

The XRD patterns recorded for catalysts in this study [26] are shown in figure 1.4. Broad peaks were observed at 2theta values of 35, 45 and 67° in the XRD pattern of γ -Al₂O₃. These peaks reflected the high surface area and small crystallites of this material. The primary peaks observed in the XRD patterns of the different catalysts were attributed to the presence of γ -Al₂O₃, thus suggesting that the metal oxides for 1%Pt/ γ -Al₂O₃, 5%Co/ γ -Al₂O₃, 5%Mo/ γ -Al₂O₃, and 5%W/ γ -Al₂O₃ were fairly well dispersed on the γ -Al₂O₃ support. XRD peaks corresponding to Pd, and Ru-oxides identified suggested that there were reasonably larger crystallites of PdO and RuO dispersed on the γ -Al₂O₃ support.

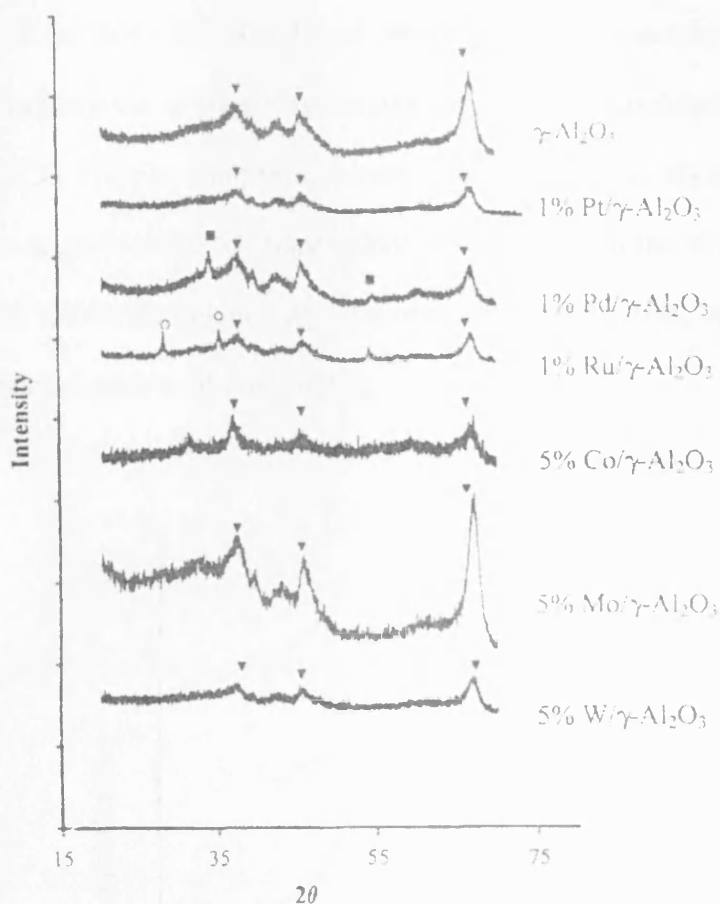


Fig. 1.4 XRD patterns of M/Al₂O₃ catalysts

1.4.1.3 TPD results

From the TPD curves of naphthalene from the six catalysts (figure 1.5), it was seen that naphthalene desorption from the Pt commenced at approximately 120 °C and attained a maximum at 190 °C, whereas for the Pd catalyst, desorption went on almost at a constant rate from 160-450 °C. This showed that naphthalene chemisorption was stronger on the Pd catalyst. Just like the Pd catalyst, the Ru catalyst showed strong naphthalene chemisorption as it retained some amount of naphthalene at higher temperatures (main

peak at 200 °C with broad band). The Co catalyst showed weak naphthalene chemisorption as there was complete desorption of naphthalene from this catalyst before 200 °C. The two non-precious metal catalysts (Mo and W) had desorption peaks covering the range 150-500 °C. Naphthalene desorption from the W catalyst only started at about 260 °C (the maximum start point observed) and therefore indicated stronger naphthalene chemisorption on the W catalyst.

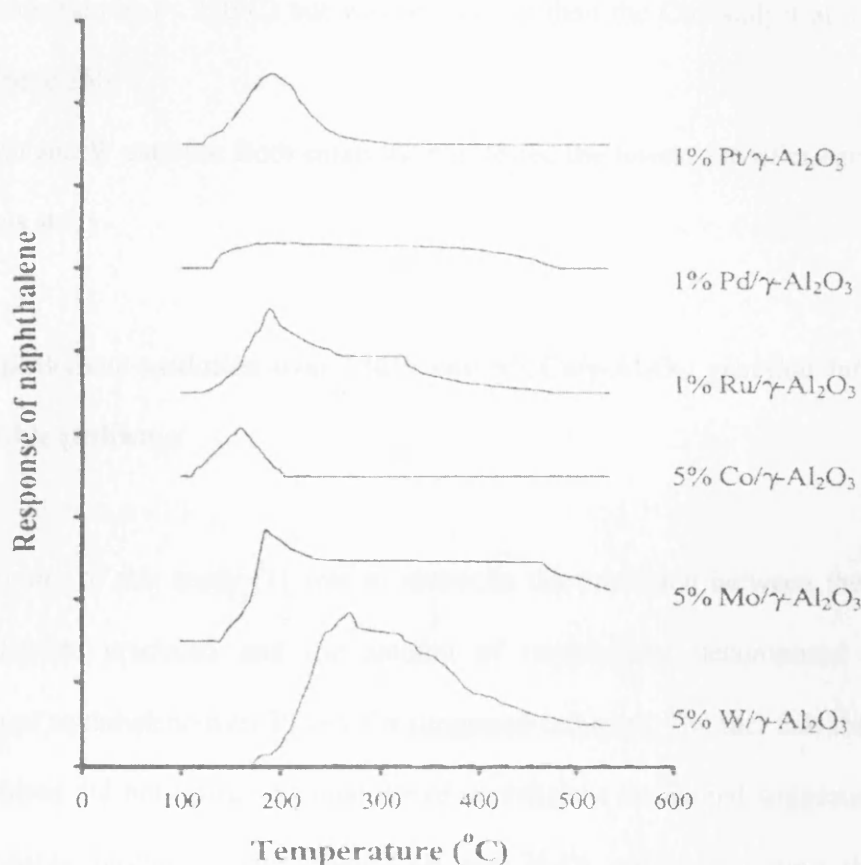


Fig. 1.5 TPD curves for naphthalene from M/ γ - Al_2O_3 catalysts

Based on the amount of CO₂ that was produced, the catalysts were grouped in to the following three categories:

- 1) Pt and Pd catalyst: These were the most active among the six catalysts tested. Pt activity was superior since it required the lowest temperature (300 °C) for complete combustion of naphthalene.
- 2) Ru and Co catalyst: Ru catalyst showed slightly higher activity at low temperatures (< 350°C) but was less active than the Co catalyst at temperatures above 350 °C.
- 3) Mo and W catalyst: Both catalysts manifested the lowest activities encountered in this study.

1.4.2 Naphthalene oxidation over 1%Pt and 5%Co/ γ -Al₂O₃: reaction intermediates and possible pathways

The main aim of this study [1] was to reconcile the mismatch between the amount of carbon dioxide produced and the amount of naphthalene decomposed during the oxidation of naphthalene over Pt and Co supported catalysts. The fact that the amount of CO₂ produced did not reflect the quantity of naphthalene consumed suggested that there were probably products (other than CO₂ and H₂O) produced during the catalytic combustion process. Gas phase intermediates and those adsorbed on the surface of the catalysts were identified and analysed so as to study the effect of different reaction conditions. The results presented in this work confirmed that stronger chemisorption of

naphthalene on the Pt catalyst led to the generation of more by-products whereas shorter residence time resulted in the formation of other types of heavy PACs on the surface of the catalyst. The identified intermediates were classified as:

- a) Naphthalene-decomposed by-products with major fragments resulting from naphthalene decomposition.
- b) Naphthalene derivatives, which comprised of alkyl and/or oxygenated substituents.
- c) Polymerised PACs, which included heavy PACs with and without oxygenated substituents.

According to this study, the total concentration of gas-phase intermediates was less than 100 ppb for 100 ppm supply of naphthalene. The fact that more intermediates resulted from the use of the Pt catalyst (rather than the Co catalyst) suggested that naphthalene oxidation over the Co catalyst involved relatively less complex pathways. The weak adsorption of naphthalene on the Co catalyst favoured the complete combustion of naphthalene.

Based on the findings of this study and a review of a number of reaction pathways, Xiao-Wen and co-workers concluded that the following three pathways could be the genesis of the three categories of intermediates mentioned above.

- 1) Naphthalene-decomposed intermediates originated mainly from the formation of phthalic anhydride, followed by esterification and other oxidation processes.

- 2) Methylation and dimerisation mechanisms were considered to be the prime contributors for the production of naphthalene derivatives.
- 3) An initial growth of naphthalene prior to its decomposition during the catalytic oxidation process, accounted for the formation of heavy PACs.

Figures 1.6, 1.7, 1.8 and 1.9 show reaction schemes, for the different pathways, through which intermediates could be produced.

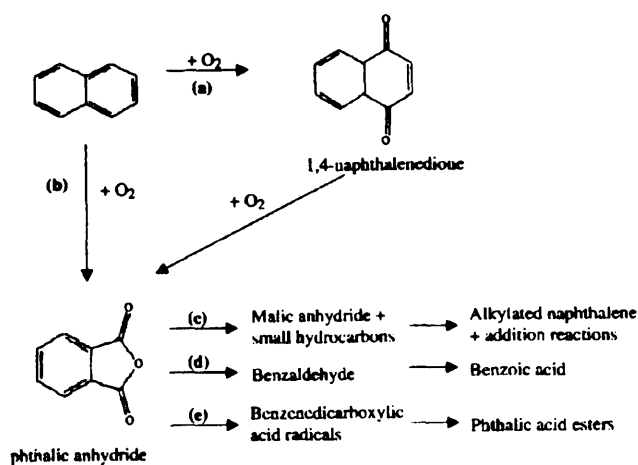


Fig. 1.6. Possible pathways of formation of various phthalates during naphthalene catalytic oxidation (according to Brückner and Baerns (1997), and Linstromberg and Baumgarten (1983)).

Taken from reference [1].

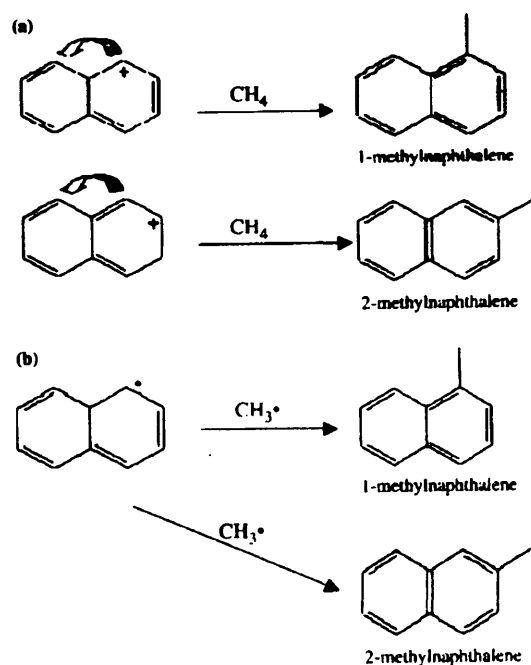


Fig. 1.7 Potential methylation pathways for methylnaphthalene (taken from reference [1]).

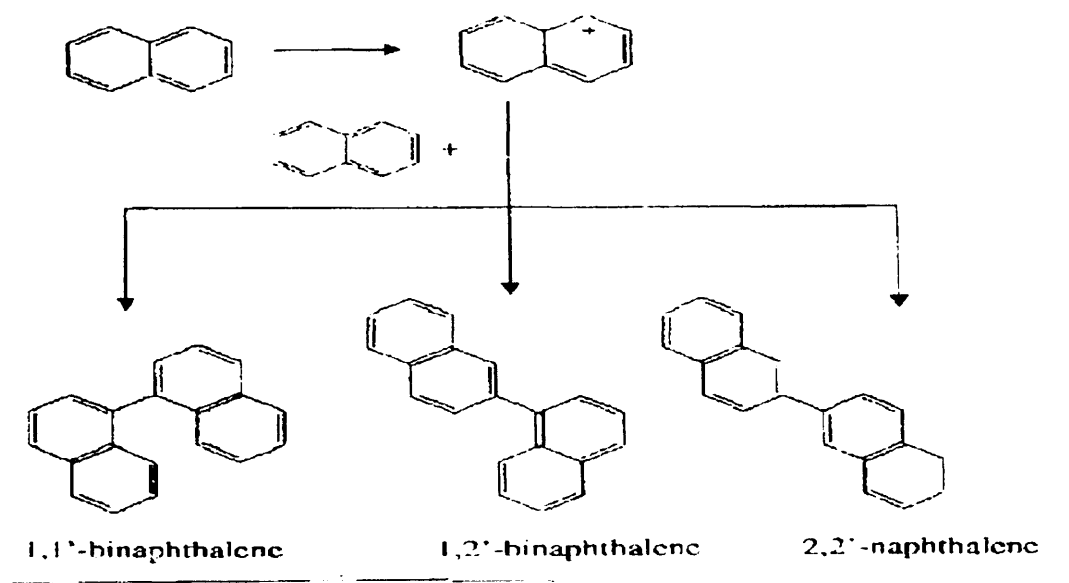


Fig. 1.8 Potential cationic intermediate pathway for dimerization of naphthalene (taken from reference [1]).

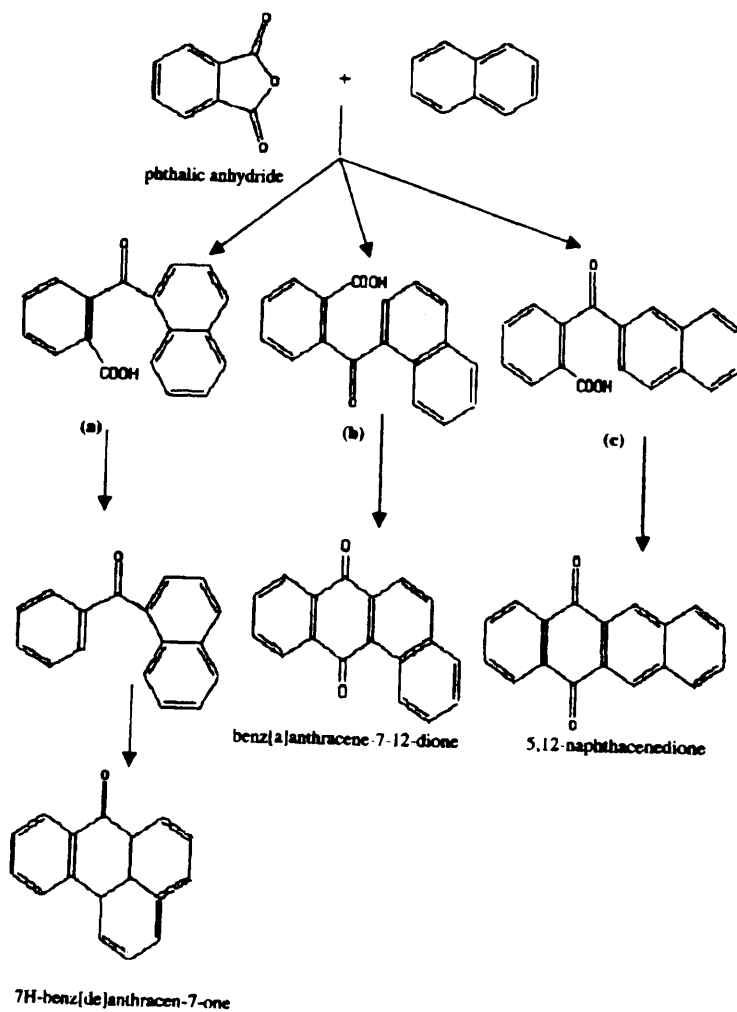


Fig. 1.9 Possible formation pathways of heavy by-products during catalytic oxidation of naphthalene (taken from reference [1]).

The identification of intermediates and the derivation of possible originating routes, therefore provide a useful basis for developing more efficient and safe catalytic systems for pollution control.

Apart from the two studies already reviewed (section 1.4.1 and 1.4.2), all other studies cited at the beginning of this section (1.4) do not specifically relate to naphthalene abatement, rather, they have to do with the abatement of naphthalene-containing mixtures (mostly comprised of CH₄, CO, naphthalene and other VOCs). A number of these studies are briefly reviewed in the following sections.

1.4.3 Catalytic oxidation of organic compounds including polycyclic aromatic hydrocarbons (PAHs) from motor exhaust gases

In this work [59], a monolithic noble metal catalyst (Pt, Pd, Rh) was manufactured and tested for the oxidation of VOCs and PAHs emitted with real exhaust gases from one-cylinder spark ignition engine. The catalytic oxidation of VOCs was found to depend on the engine load and air/fuel ratio. Under regulated engine work conditions, the catalysts showed high activities as the PAHs were almost completely oxidised; only trace amount of naphthalene was detected in the off-gases. Operating the motor without regulation (shortage of oxygen) led to the generation of soot, which partially blocked and deactivated the catalyst. Regeneration of the catalyst occurred as it regained its high initial activity upon reinstallation of efficient engine regulation.

The use of catalytic systems in motor vehicle exhaust must therefore be accompanied with excellent engine regulation in order to yield maximum performance of such systems.

1.4.4 Application of metal-exchanged zeolites in removal of emissions from combustion of biofuels

Pd, Pt, Pd-Pt/HZSM-5 and Pd/HZSM-35 catalysts were prepared and tested for the conversion of gas mixtures containing CH₄, C₂H₄, CO, naphthalene (model PAH), O₂, CO₂, H₂O, and N₂ at temperatures between 120-600 °C [4]. The catalysts showed high activities in the complete removal of model pollutants like CO and C₃H₈. An increase in the Pd content of the catalysts was found to affect the low temperature activity of the catalyst in methane oxidation. Sulphur poisoning was found to deactivate the catalysts while ageing of the catalysts in the reactant flow only affected the oxidation of methane. The addition of Zr and La helped in improving the low temperature activities of freshly prepared Pd, and Pd-Pt/HZSM-5 catalysts and stabilized the catalysts against deactivation.

The XPS and O₂-TPD results showed that Pd was present as Pd⁺ and Pd²⁺ on the freshly prepared catalysts. The ageing of the catalysts favoured the less active PdOx species as there was a decrease in the number of highly active Pd²⁺ sites.

1.4.5 An Investigation of the activity of Pd and Pd-Zr modified Y-zeolite catalysts for the removal of PAH, CO, CH₄ and NO_x emissions

Apart from metal oxide and metal-supported catalysts, zeolitic catalysts can also be useful for the control of VOC emissions from car exhaust and wood-fired stoves. In this study [5], Pd-Y- and Pd-Zr-Y-zeolite catalysts were prepared by ion-exchange of parent NH₃-Y-zeolite, thermally pre-treated Y-zeolite and hydrothermally pre-treated Y-zeolite. The activities of these catalysts were investigated in the conversion of gas mixtures simulating the flue gases from combustion of biofuels and natural gas driven vehicles (NGVs) at temperatures ranging from 120-800 °C. Freshly prepared Pd-exchange Y-zeolite exhibited high activities in removal of model pollutants simulating emissions from biofuel combustion and NGVs. The ageing of the catalyst (in the reactant flow and through hydrothermal treatment) led to strong catalyst deactivation in methane oxidation (evident by an increase in light-off temperature). The deactivation was less conspicuous for CO and naphthalene oxidation. The de-alumination of the catalyst was the main reason for deactivation as shown by changes in XRD patterns and strong decrease in the zeolite activity. Thermal and hydrothermal pre-treatment of the parent zeolite prior to the ion-exchange, yielded a less active catalyst. These catalysts suffered similar deactivation, both due to de-alumination and migration of Pd from the ion-exchange site to the external zeolite surface where they aggregated. Coating of the de-aluminated Y-zeolite with colloidal alumina enhanced the activity of the catalyst in methane oxidation. This however failed to stabilise the catalyst against deactivation. Both fresh and aged Pd-Zr-Y catalysts proved fairly good activities in the removal of emissions from NGVs.

1.4.6 Catalytic clean-up of emissions from small-scale combustion of biofuels

In this work [39], a prepared knitted silica-fibre was used as support material for a number of Pd-MeO (Me = Ni, Co, Cu, and Mn) catalysts. The activity of each of these catalysts was investigated for the combustion of a gas mixture containing methane, ethane, naphthalene, carbon monoxide, carbon dioxide, nitrogen and water vapour at temperatures between 150-800 °C. The prepared catalysts showed high activities (high combustion efficiencies) for CO, CH₄, C₂H₄, and C₁₀H₈. Combination of Pd and MeO (Me = Ni, Co, Cu), with the exception of Pd-Cu catalysts, gave improved low-temperature activities in methane combustion over freshly prepared catalysts. This activity was superior to that of the Pd/silica-fibre catalyst. Combination of Pt and MeO (Me = Ni, Co, and Mn), with the exception of the Pt-Ni catalyst, failed to improve the low temperature activity in methane oxidation. Catalyst prepared by impregnation showed higher activities than those prepared by consecutive impregnation.

Thermal treatment of the catalysts at 800 °C for 6 h led to deactivation, which was more easily observed in methane oxidation. In addition to support and metal sintering, changes in the nature of Pd-O species were considered a major cause of deactivation of the Pd-Ni-containing catalysts.

1.4.7 Catalytic abatement of emissions from small-scale combustion of wood: A comparison of catalytic effect in model and real flue gases

In this study [3], the activity of precious metal catalysts were tested for the oxidation of a mixture of CH₄, naphthalene, CO, CO₂ and water vapour in a laboratory flow reactor. The observed activities were compared with activities resulting from the oxidation of CH₄, C₂ hydrocarbons, benzene, and CO in real flue gases in a 15 KW wood-fired heater. The noble metal catalysts exhibited higher activities in naphthalene and CO oxidation than the metal oxide catalysts. In general, the Pt-based catalysts had a higher activity for total oxidation of unburnt compounds (both for simulated flue gas and real flue gases) from small-scale wood combustion than metal oxide-based catalysts. The metal oxide-based catalysts equally showed stronger deactivation tendencies. The laboratory results obtained in this study were found to correlate results from the use of real flue gases (from a wood-fired stove). The only significant difference noticed between the two systems was the formation of methane from higher hydrocarbons that occurred over the catalyst in the wood-fired heater. This was particularly dominant at temperatures below 550 °C.

The findings of this work is powerful evidence to show that research in heterogeneous catalysis aimed at decomposing toxic VOCs can go a long way to improve a wide variety of catalytic systems such as in wood-fired stoves and as such make our environment more conducive.

Notice that most of the naphthalene catalytic oxidation studies reviewed in this chapter (section 1.4) make use of $\gamma\text{-Al}_2\text{O}_3$ as support material for the metal catalysts used for the destruction of naphthalene and naphthalene-containing mixtures. $\gamma\text{-Al}_2\text{O}_3$ is probably chosen due to its high surface area and thermal stability. Zirconia and silica supports have also been reported. To the best of my knowledge, there is no work reporting the use of TiO_2 , SnO_2 and CeO_2 as metal catalyst- support for naphthalene oxidation. Part of the work reported in this thesis (chapter 4) investigates the influence of different supports (Al_2O_3 , SiO_2 , TiO_2 , SnO_2 and CeO_2) on the activity of supported-Pt catalysts.

1.4.8 Recent Advances in the Catalytic Oxidation of Naphthalene

In this section, the most recent studies (2005-2007) reported for naphthalene catalytic oxidation, are summarized.

1.4.8.1 Catalytic Oxidation of Naphthalene Using a Pt/ Al_2O_3 Catalyst

In this work [27], naphthalene is used as a model PAH to investigate the use of catalytic oxidation (over a Pt/ $\gamma\text{-Al}_2\text{O}_3$ catalyst) in decomposing PAHs. The relationships between conversion, operating parameters and relevant factors like treatment temperatures, catalyst sizes and space velocities are evaluated and a reaction kinetic expression is postulated so as to give a simplified expression of the relevant kinetic parameters.

The results obtained in this work revealed that the use of the Pt/ γ -Al₂O₃ catalyst increased the naphthalene decomposition reaction rate. It was possible to attain a high conversion (over 95 %) at a moderate reaction temperature (480 K) and a space velocity lower than 35,000 h⁻¹. In the absence of the catalyst, the same conversion was only attainable at a temperature over 1000 K. It was equally observed that the Rideal-Eley mechanism and Arrhenius equation can be sensibly applied to account for the data collected by using the pseudo-first-order reaction kinetic equation with activation energy of 149.97 kJ/mol and frequency factor of $3.26 \times 10^{17} \text{ s}^{-1}$.

1.4.8.2 Nano-crystalline Ceria Catalysts for the Abatement of Polycyclic Aromatic Hydrocarbons

Nano-crystalline ceria catalysts were prepared by different precipitation routes and evaluated for the catalytic oxidation of naphthalene (a PAH). The results of this study [60] revealed that ceria prepared by precipitation with urea was the most active catalyst for converting naphthalene to carbon dioxide. This catalyst demonstrated an activity of over 90 % naphthalene conversion to carbon dioxide at 175 °C (100 vppm naphthalene, GHSV = 25,000 h⁻¹) whereas ceria precipitated by a carbonate only showed a similar conversion at 275 °C.

When compared with some known high activity catalysts (e.g. Mn₂O₃ and Pt/ γ -Al₂O₃) for naphthalene decomposition, it was found that the urea precipitated CeO₂ was more efficient for naphthalene total oxidation.

It was also observed that at temperatures too low to yield any significant catalytic activity, the adsorption capacity of the urea precipitated catalyst was quite higher than all other catalysts studied. The Authors suggest that this high adsorption capacity of the material gives it an added advantage as it can be used both as a catalyst and an adsorbent for the removal of PAHs from waste streams.

1.4.8.3 Naphthalene Total Oxidation over Metal Oxide Catalysts

Metal oxide catalysts (CoOx, MnOx, CuO, ZnO, Fe₂O₃, CeO₂, TiO₂ and CuZnO) were prepared by a precipitation method and tested for the complete oxidation of naphthalene [61]. The results revealed that the CeO₂ catalyst prepared by homogeneous precipitation method with urea had the highest performance. This catalyst showed stable conversion with 100 % selectivity to CO₂ with time-onstream at very low temperatures (175 °C).

The total oxidation of propane was also investigated using the same range of catalysts but no correlation seemed to occur between naphthalene and alkane oxidation. It was observed that redox properties were the main factors accounting for propane total oxidation. On the other hand, the surface area and the strength of the bond between adsorbed molecules and catalyst surface were equally considered determining factors influencing naphthalene catalytic combustion.

1.4.8.4 Complete Naphthalene Oxidation over Pd/V and Pt/V-supported catalysts, Pt-supported catalysts, Nano-crystalline CeO₂ catalysts and Metal-supported CeO₂ Catalysts

The work reported in this section has been explicitly elaborated in chapters 3-6. It is shown that vanadium added during the impregnation step of catalyst preparation promoted the activity of Pd and Pt- supported alumina catalysts in naphthalene oxidation.

The influence of support material on the activity of Pt-supported catalysts in naphthalene oxidation was evaluated.

The influence of catalyst preparation conditions and preparation methods for Ceria catalysts was studied for total naphthalene decomposition.

Metal-doped ceria catalysts were also prepared and tested for total oxidation of naphthalene.

The results of the above studies are detailed in chapters 3-6.

References

1. X-W. Zhang, S-C. Shen, K. Hidajat, S. Kawi, L. E. Yu and K. Y. Simon, *Catal. Lett.* 96 (2004) 87.
2. M. Ferrandon and E. Bjornbom, *J. Catal.*, 200 (2001) 148.
3. Johanna Carno, Magnus Berg and Sven J., *Fuel*, 75 (1996) 959.
4. A. K. Neyestanaki, L.-E Lindfors, T. Ollonqvist, and J. Vayrynen, *Appl. Catal. A: Gen.* 196 (2000) 233.
5. F. Klingstedt, A. K. Neyestanaki, L.-E Lindfors, T. Salmi, T. Heikkila and E. Laine, *Appl. Catal. A: Gen.* 6210 (2002) 1.
6. E. Ntainjua N., T. Garcia, and S. H. Taylor, *Catal. Lett.* 110 (2006) 125.
7. H. Shaper, E. B. M. Doesburg, and L. L. Van Reijen, *Appl. Catal.*, 7 (1983) 211.
8. L. S. Escandon, S. Ordóñez, F. V. Diez, and H. Sastre, *Catal. Today*, 78 (2003) 191.
9. C. Neyertz, and M. Volpe, *Colloid Surf. A*, 136 (1998) 63.
10. G. Groppi, C. Cristiani, L. Lietti, C. Ramella, M. Valentini, and P. Forzatti, *Catal. Today*, 50 (1999) 399.
11. M. Machida, K. Eguchi, and H. Arai, *J. Catal.* 103 (1987) 385.
12. P. Euzen, J. H. LeGal, B. Rebours, and G. Martin, *Catal. Today*, 47 (1999) 19.
13. C. B. Wang, H. K. Lin, and C. M. Ho, *J. Mol. Catal. A: Chem* 180 (2002) 285.
14. G. J. Hutchings., M. Sideiqi, H. Rafiq , A. Burrows, C. Kiely, and R. Whyman, *J. Chem. Soc., Faraday Trans.* 93 (1) (1997) 187.

15. R. O. de Souza Tania, J. S. Mascarenhas Artur, and M. C. Andrade Heloysa, Catal. Lett. 87 (2006) 3.
16. W. Shurong, H. Jing, Z. Yingqiang, W. Shuping, W. Shihua, Z. Shouming, and H. Weiping, Mat. Lett. 60 (2006) 1706.
17. G.M. Schwab and G. Drikos, Z.Phys. Chem. 185 (1940) 405.
18. J. Jansson, A.E.C. Palmquist, E. Fridell, M. Skoghlundh, L. Osterlund, P. Thormahlen and V. Langer, J. Catal. 211 (2002) 387.
19. A. Bourane and D. J. Bianchi, J. Catal. 222 (2004) 499.
20. A. N. Akin, G. Kilaz, A. I. Isli and Z. I. Onsan, Chem. Eng. Sci., 56 (2001) 881; J. L. Margitfalvi, I. Borbath, K. Lazar, E. Tfirst, A. Szegedi, M. Hegedűs and S. Göbölös, J. Catal. 203 (2001) 94.
21. G. C. Bond and D. T. Thompson, Catal. Rev. – Sci. Eng. 41 (1999) 319.
22. Agnes Szegedi, M. Hegedűs, J. L. Margitfalvi and Imre Kiricsi, Chem. Comm., 2005, 1441.
23. C. W. Lee, S.-J. Park, K. Young-Sang and P. J. Chong, Bull. Korean Chem. Soc. 16 (1995) 296.
24. B. J. Finlayson-Pitts, and J. N. Pitts, Jr, Chemistry of the Upper and Lower Atmosphere, (Academic Press, First Edition, 1999) 436.
25. R. Preuss, J. Anggerer, and H. Drexler, Int. Arch. Occup. Environ. Health, 76 (2003) 556.
26. X. W. Zhang, S. C. Shen, L. E. Yu, S. Kawi, K. Hidajat, and K. Y. Simon Ng, Appl. Catal. A:Gen. 250 (2003) 341.

27. J.-L. Shie, C.-Y. Chang, J.-H. Chen, W.-T. Tsai, Y.-H. Chen, C.-S. Chiou and C.-F. Chang, *Appl. Catal. B: Environ.* 56 (2005) 289.
28. L. Tilley, Ten Pollutant Study in Jacksonville, Florida, US Regulatory and Environmental Services: Department of Air and Water Quality.
29. US Environmental Protection Agency (EPA) 402-R-94-007, 1994.
30. National Health Report, Department of Environment and Heritage, GPO Box 787 Canberra Act 201, Australia.
31. US Department of Labour: Occupational Safety and Health Administration, DC20210, 57FR22290, May 27, 1992.
32. Case Study in Environmental Medicine: Toxicology Profile for Benzene, Agency for Toxic Substances and Disease Registry (ATSDR), Atlanta, GA:US Department of Health and Human Services, Public Health Service
33. Australian Government Department of the environment and Heritage, CASR number 1330-20-7.
34. R. Lajis, Irritant Abuse, National Poison Centre, Universiti Sains Malaysia, Penang.
35. US EPA, Health and Environmental Effects Profile for naphthalene, EPA/600/x-86/241
36. US EPA, Toxicology Review of Naphthalene.
37. R. M. Harrison (Editor), *Pollution: Causes, Effects and Control*, Fourth Edition, Royal Society of Chemistry, p 184.
38. K. F. Ho, S. C. Lee, *Sci Total Environ.* 289 (2002) 145.
39. A. K. Neyestanaki and L.-E Lindfors, *Fuel*, 77 (1998) 1727.

40. G. Chen, K. A. Strevett, and B.A. Vanegas, *Biodegradation* 12 (2001) 433.
41. W. Cooper, M. G. Nickelsen, R. V. Green and S. P. Mezyk, *Radiat. Phys. Chem.* 65 (2002) 571.
42. B. Legube, S. Guyon, H. Sugimitsu and M. Dore, *Water Res.* 20 (1986) 197.
43. S. Y. Lee and S. J. Kim, *Appl. Clay Sci.* 22 (2002) 55.
44. H. L. Huang, and W. M. Lee, *J. Environ. Eng., ASCE* 128 (2002) 60.
45. U. S., E. P. A., *Air Pollution Control Technology Fact Sheet*, EPA-452/F-03-022.
46. *Natural Attenuation for Groundwater Remediation*, 2000, National Academic Press.
47. F. H. Chapelle, *Ground-Water Microbiology and Geochemistry*: New York, John Wiley and Sons, 2000, 468.
48. *Alternatives for Ground Water Cleanup*, 1994: National Academic Press.
49. R. H. Harris, Cardiff University, *The vapour Phase Destruction of Volatile Organic Compounds Using Uranium Oxide Catalysts*, PhD Thesis, 2002.
50. Burkhardt and J. R. Bayless, *Pure and Appl. Chem.*, 68 (1996) 1083.
51. L. A. Rosocha, and R. A. Korzekwa, *LOS ALAMOS NATIONAL LAB NB*, *Environmental Engineering*, Chapter 47, Report number A966975, 1999
52. A. R West, *Basic Solid State Chemistry*, 2nd Edition, John Wiley and Sons Ltd, pp126,.
53. Atkins and J. Paula, *Physical Chemistry*, seventh edition, 2002, pp 977.
54. G. C. Bond, *Heterogeneous catalysis: Principles and Applications*, second edition, Clarendon Press – Oxford, pp 1.

55. Paul Monk. *Physical Chemistry: Understanding Our Chemical World*, John Wiley and Sons Ltd., 2000.
56. R. K. Grasselli and A. W. Sleight (Editors) *Structure-Activity and Selectivity Relationships in Catalysis*, Royal Society of Chemistry and Contributors, 1982.
57. J. M. Thomas and W. J. Thomas, *Principles and Practice of Heterogeneous Catalysis*, VCH, Weinheim, 1997.
58. A. Clark, *The Theory of Adsorption and Catalysis*, Academic Press, New York (1970).
59. A. Musialik-Piotrowska, K. Syczewska and B. Mendyka, *Environmental Protection Engineering*, Vol 24, No. 1-2, (1998).
60. T. Garcia, B. Solsona, and S. H. Taylor, *Catal. Lett.* 105 (2005) 183.
61. T. Garcia, B. Solsona, and S. H. Taylor, *Appl. Catal. B:Environ.* 66 (2006) 92.

CHAPTER 2: EXPERIMENTAL

2.1 Introduction

In this chapter, the methods employed for catalyst preparation are detailed and theories governing the different methods of characterisation are discussed. Characterisation equipment specifications, characterisation methods and catalyst testing are also detailed.

2.2 Catalyst Preparation

Several catalysts were prepared and tested for the complete oxidation of naphthalene. This chapter covers detail preparation methods/procedures employed for the synthesis of the various catalysts tested for the complete destruction of naphthalene.

2.2.1 Preparation of Metal Supported Catalysts for Naphthalene Oxidation

2.2.1.1 Preparation of Pd/ γ -Al₂O₃, Pt/ γ -Al₂O₃, Pd/V/ γ -Al₂O₃, and Pt/V/ γ -Al₂O₃

Pd/V/Al₂O₃, and Pt/V/Al₂O₃ catalysts were prepared by dissolving a known amount of metal salt (PdCl₂ – Aldrich 99% or hydrogen hexachloroplatinate (IV) hydrate, Aldrich 99.9%) in 100 ml of deionised water. The solution was heated to 80 °C and stirred continuously. An appropriate amount of ammonium metavanadate (Aldrich 99+%) and oxalic acid (1.59g, Aldrich 99+%) were added to the solution of the salt. γ -Al₂O₃ (

Aldrich 99+ %) was then added to the heated solution and stirred at 80 °C to form a paste. This was then dried at 110 °C for 16 h. The catalysts had Pd loading of 0.5 wt%, Pt loading of 0.5 wt% and V in the range 0.5-12 wt%. A similar method was used to prepare Pd and Pt-supported alumina catalysts without vanadium. The catalysts were finally calcined in static air at 550 °C for 6 h. The method used is called impregnation (for catalysts containing a single metal species) and co-impregnation for vanadium-modified catalysts.

2.2.1.2 Preparation of Pt/SiO₂, Pt/SnO₂, Pt/TiO₂ and Pt/CeO₂

A method of impregnation similar to that used for the preparation of vanadium-free Pt-supported alumina catalyst was used to prepare Pt catalysts supported on different materials (SiO₂, SnO₂, TiO₂, and CeO₂). In each of these cases, alumina was replaced by the appropriate support material to prepare 0.5 %Pt/SiO₂, 0.5 %Pt/SnO₂, 0.5 %Pt/TiO₂ and 0.5 %Pt/CeO₂. The raw materials were composed of 0.0432 g of hydrogen hexachloroplatinate (IV) hydrate (Aldrich, 99.9 %), and 3 g of the appropriate support (SiO₂ – Matrex Silica 60- Fischer Scientific Ltd, 99+ %, Tin (iv) oxide – 325 mesh, 99.9 % - Aldrich, TiO₂ – P 25, Degussa, and cerium (iv) oxide, Aldrich, 99.9 %). All Pt-supported catalysts prepared had 0.5wt% of Pt.

Table 2.1 gives the complete range of metal-supported catalysts prepared and tested for naphthalene oxidation.

Table 2.1 Range of catalysts prepared by impregnation

Catalysts prepared
0.5 %Pd/Al ₂ O ₃
0.5 %Pd/0.5%V/Al ₂ O ₃
0.5 %Pd/1%V/Al ₂ O ₃
0.5 %Pd/3%V/Al ₂ O ₃
0.5 %Pd/6%V/Al ₂ O ₃
0.5 %Pd/12%V/Al ₂ O ₃
0.5 %Pt/Al ₂ O ₃
0.5 %Pt/0.5%V/Al ₂ O ₃
0.5 %Pt/1%V/Al ₂ O ₃
0.5 %Pt/3%V/Al ₂ O ₃
0.5 %Pt/6%V/Al ₂ O ₃
0.5 %Pt/12%V/Al ₂ O ₃
0.5 %Pt/SiO ₂
0.5 %Pt/SnO ₂
0.5 %Pt/TiO ₂
0.5%Pt/CeO ₂

2.2.2 Precipitation Methods for the Preparation of Crystalline Ceria for Naphthalene Oxidation

2.2.2.1 Precipitation with urea: Urea Route (UR)

A homogeneous precipitation method involving the use of a cerium salt $[(\text{NH}_4)_2\text{Ce}(\text{NO}_3)_6]$ and urea ($\text{H}_2\text{N}-\text{CO}-\text{NH}_2$) as precipitating agent was used to prepare ceria (CeO_2) catalysts. A 1:3 ratio of $(\text{NH}_4)_2\text{Ce}(\text{NO}_3)_6$ and $\text{H}_2\text{N}-\text{CO}-\text{NH}_2$ were dissolved in 100 ml of deionised water. The resulting solution was stirred continuously and heated to 100°C to form a brownish gel-like solution, which was boiled and aged at 100°C for 24 h. The final precipitate was obtained by filtering and complete evaporation at 120°C . The resulting yellowish solid was then calcined in static air at 400°C for 10 h.

The above method had been reported [1] to be effective in obtaining an efficient nano-crystalline ceria catalyst for naphthalene oxidation. In this study, the calcination temperature, calcination time, aging time, and cerium salt:urea ratio were varied to optimise the activity of the catalyst in naphthalene oxidation. The complete range of ceria catalysts prepared by precipitation with urea is detailed in table 2.2.

Table 2.2 Range of nana-crystalline ceria catalysts prepared by precipitation with urea

Catalyst	Cerium salt:urea ratio	Aging Time / hours	Calcination Temperature / °C	Calcination Time / hours
CeO ₂	1:3	24	300	10
CeO ₂	1:3	24	400	10
CeO ₂	1:3	24	500	10
CeO ₂	1:3	24	600	10
CeO ₂	1:3	24	500	6
CeO ₂	1:3	24	500	3
CeO ₂	1:3	12	500	6
CeO ₂	1:3	3	500	6
CeO ₂	2:1	24	500	6
CeO ₂	1:1	24	500	6
CeO ₂	1:2	24	500	6
CeO ₂	1:4	24	500	6
CeO ₂	1:4	12	500	6

In later sections in this thesis CeO₂ catalysts prepared by UR shall be named as CeO₂ followed by Ce salt:urea ratio, aging time, and calcination temperature/calcination time. E.g. CeO₂, 1:3, 24 h, 400 °C /10 h.

2.2.2.2 Precipitation with sodium carbonate: Carbonate Route (CR)

Ceria was also prepared using a precipitation method reported by T. Garcia et al. [1]. This precipitation method involved using cerium nitrate and sodium carbonate. Here 20 g of Ce-nitrate salt was dissolved and heated to 80 °C while stirring. 0.25M solution of aqueous sodium carbonate was then added drop wise until a pH of 8.2 -9.0 was reached. The solution obtained was stirred and aged at 80 °C for 1 h to obtain a paste, which was then filtered and washed several times with cold and hot water to remove any nitrates and sodium cations. The resulting solid was dried in an oven maintained at 120 °C followed by calcination at 500 °C for 10 h in static air. The calcination temperature/time employed in this synthesis (500 °C and 10 h) was different from the 400 °C and 3 h employed in the literature [1].

2.2.3 Preparation of Ceria using Supercritical carbon dioxide: Supercritical carbon dioxide Route (sc)

A CeO₂ catalyst prepared by Zi-rong Tang (PhD Student in Prof. Graham Hutchings Research Group) using supercritical CO₂ was also tested for the complete abatement of naphthalene. Here, the synthesis of the precursor scCeO₂ was performed using the apparatus shown in figure 2.1. Supercritical (sc) CO₂ was pumped to the reaction vessel at pressures of up to 150 bar with the flow rate of 7 ml min⁻¹. The whole system was held at 40 °C. Initially pure methanol was pumped through a fine capillary into the precipitation vessel at a flow rate around 0.1 ml min⁻¹ for 25 min in co-current mode with

supercritical CO_2 in order to obtain steady-state conditions in the vessel. After the initial period, the flow of liquid solvent was stopped and the solution of $\text{Ce}(\text{acac})_3$ in methanol (13.33mg/ml) was delivered at 0.1 ml min^{-1} flow rate. The system pressure and temperature were maintained constant during the course of feeding the solution and CO_2 . As the solution exited the capillary, the droplet and scCO_2 rapidly diffused into each other, causing expansion, simultaneously reducing the solvent power. The solute was precipitated rapidly. When all the solution had been processed, scCO_2 was pumped for a further hour to wash the vessel in case the residual methanol condensed during the depressurization and partly solubilized the precipitated powder modifying its morphology. When the washing process was completed, the CO_2 flow rate was stopped and the vessel was depressurized to atmospheric pressure and the light green precipitate was collected. Experiments were conducted for 20 h, which resulted in the synthesis of approximately 0.7 ~0.8g of solid. The precursor was calcined at 400°C for 2 h with the ramp of 10°C .

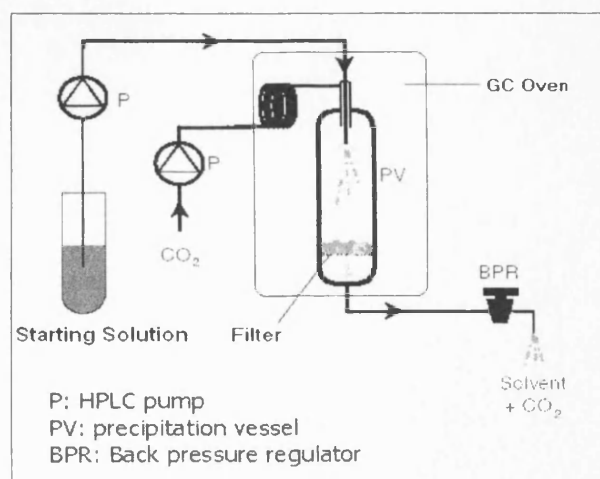


Fig. 2.1 Experimental setup for preparation of CeO_2 by Sc

2.2.4 Preparation of Pt/CeO₂ by Homogeneous Precipitation with urea

Pt/CeO₂ catalysts were prepared using a homogeneous precipitation method, with urea as precipitating agent. Here a 1:4 mixture of cerium salt [(NH₄)₂Ce(NO₃)₆] and urea (H₂N–CO–NH₂) (20 g cerium salt + 80 g of urea, both Aldrich and purity of 99+ %) were dissolved in 200 ml of dionised water and stirred continuously at 100 °C. After aging this mixture at 100 °C for 4 h, 0.2 g of hydrogen hexachloroplatinate (IV) hydrate (Aldrich, 99.9%) was dissolved in 2 ml of deionised water and added to the resulting brownish reaction mixture. The mixture was then further aged for 8 h to obtain a yellow solid which was filtered and dried at 120 °C followed by calcination in static air at 500 °C for 6 h (heating rate of 10 °C /min was used and final catalyst was allowed to cool in air). The Pt/CeO₂ prepared as described herein was thus prepared from a raw material mass ratio of 0.2: 20:80 Pt salt, cerium salt and urea respectively. In a separate experiment, the Pt content in the final catalyst was increased by starting with same raw materials in ratio of 1:20:80.

2.3 Catalyst characterisation

2.3.1 Introduction

There is a vast variety of methods in industry and research laboratories used to characterise heterogeneous catalysts. In this section, only the methods used for characterisation of catalysts prepared in this work are discussed. These include atomic absorption spectroscopy (AAS), BET, CO chemisorption, XRD, laser Raman spectroscopy, temperature-programmed reduction (TPR), thermal gravimetric analysis (TGA), scanning electron microscopy (SEM) and XPS.

2.3.2 Theory of Atomic Absorption Spectroscopy

AA spectroscopy is a quantitative method of analysis which uses the absorption of light by free atoms to measure the concentration of atoms in the gas-phase [2, 3, 4] and as such is based on the Beer-Lambert Law;

$$A = abc \dots\dots\dots(2.1)$$

Where,

A = Absorbance

a = wavelength-dependent absorptivity

b = path length

c = analyte concentration.

For experimental measurements transmittance (T) is often made use of.

$$T = I/I_0 \dots\dots\dots (2.2)$$

Where,

I_0 = intensity of incident light

I = intensity of light after passing through the sample

The relationship between transmittance and absorbance is given by the equation (2.3).

$$A = -\log T = -\log I/I_0 \dots\dots\dots (2.3)$$

Equation (2.1) shows that the amount of light absorbed is proportional to the analyte's concentration.

A schematic representation of an AA experiment is shown in figure 2.2.

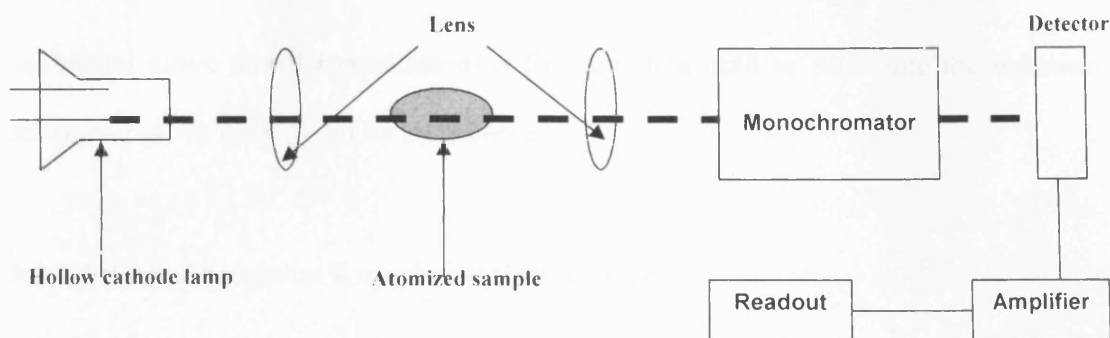


Fig 2.2 Schematic representation of an atomic-absorption apparatus

Atoms or ions of the analyte in the sample are vaporized using a high-temperature source such as a flame or a graphite furnace. While the flame can only atomise solutions, the graphite furnace can atomise solutions in addition to slurries and solid samples. Light from a source (usually the hollow cathode lamp of the element to be analyzed or laser) passes through the sample to the detector. The absorption of light by the atoms of the analyte results to their transition to higher energy levels. Since light absorption is proportional to the concentration of the analyte, it can therefore be used to determine the concentration of the analyte. The main function of the monochromator is to separate the absorption line from any background light resulting from interference. As the light passing through the sample and monochromator strikes the detector, a signal is transferred from the detector to the computer which indicates the absorbance. The variation in the atomization efficiency from the sample matrix and non-uniformity of concentration and path length of analyte atoms make it difficult to apply Beer-Lambert law directly to AA spectroscopy. Concentration measurements are therefore usually made by first calibrating the instrument with a number of standards of known concentration. A

calibration curve and the equation of a line are then used to determine the unknown concentration on the basis of its absorbance.

2.3.3 Atomic Absorption Experimental Procedure

In this work, standard solutions of V and Pd (5 ppm, 10 ppm, 20 ppm, 30 ppm, and 40 ppm) were prepared by diluting appropriate quantities of V and Pd AA standard solutions (Aldrich) with water to make 100 ml solutions of each in a 100 ml volumetric flask. Appropriate quantities of some Pd/V/ Al_2O_3 catalysts were then dissolved in aqua regia ($3\text{HCl} : 1\text{HNO}_3$) and made up to 100 ml with deionised water in 100 ml volumetric flasks to yield expected amounts of metal species. For each AA run, a sample was taken by an aspirator tube in to the flame where it was vaporized before it absorbed light. After calibrating the instrument with the prepared standard solutions for each metal under investigation, the concentration of that metal in the solution of each catalyst was determined by carrying out AA spectroscopy. The cathode hollow lamp of each element (V and Pd) was used as excitation source for its investigation and vaporization was done in air-acetylene flame. The detected signal was registered on the monitor and from the calibration curve drawn for the standards; the computer automatically computed the concentration of each metal in the solution of the catalyst. It is worth noting that only one metal could be analyzed at a time.

2.3.4 Theory of Brunauer-Emmet-Teller method

The Brunauer-Emmet-Teller (BET) method is widely used in research and industry for the determination of surface areas of solid state materials. The theory of this characterization technique has been well elaborated by several authors [5-8]. The Langmuir isotherm discussed in chapter 1 is limited to the adsorption of a monolayer of adsorbate. If the latent heat of vaporization of a system is significantly high compared to the heat of adsorption, adsorption will occur at temperatures higher than the boiling point of the adsorbate and the formation of multilayers becomes very unlikely. However, if the heat of adsorption and the latent heat of vaporization are similar, a low temperature is then required to bring about considerable adsorption in the first layer and under these conditions, the probability of multiple layer formation becomes significant. The BET isotherm takes in to account the formation of multilayers. It is actually an extension of the Langmuir model, which takes in to consideration the physisorbed multilayers. This isotherm relies on the following assumptions:

- 1) Each layer of adsorbate is considered to be a Langmuir monolayer and must be completed before the next layer starts to form.
- 2) The heat of adsorption for the first layer, ΔH_{ads1} is characteristic of the adsorbate/adsorbent system.
- 3) Heat of adsorption for subsequent layers equals the heat of condensation, H_L .

This implies that, $\Delta H_1 = \Delta H_2 = \Delta H_3 = \Delta H_4 = \Delta H_5 = \Delta H_6 = \dots\dots\dots$

The BET isotherm is generally represented by the equation 2.4.

$$\Theta = C (P/P_o) / (1 - P/P_o) [1 + (C - 1)P/P_o] \quad (2.4)$$

Where,

Θ = Fraction of surface coverage

P = Equilibrium pressure over the solid

P_o = Saturated vapour pressure of gas at temperature of experiment

$$C = \exp[(\Delta H_1 - \Delta H_n)/RT] \quad (2.5)$$

Where H_n = heat of adsorption in subsequent layers.

If $\Delta H_1 \gg \Delta H_n$, the BET isotherm reduces in to the Langmuir isotherm.

Considering $\Theta = V/V_m$,

Where V = amount of gas adsorbed and V_m = monolayer coverage

Equation 2.4 can be written as:

$$V = V_m CP / (P_o - P) [1 + (C - 1) (P/P_o)] \quad (2.6)$$

A plot of V against the relative pressure P/P_o is called a BET isotherm.

Equation 2.6 can be rearranged to give the linear BET equation, 2.4.

$$P / V(P_0 - P) = 1 / V_m C + (C - 1)P / V_m C P_0 \quad (2.7)$$

Equation 2.7 is similar to $Y = MX + C$

Where $Y = P / V(P_0 - P)$ and $X = P/P_0$

The plot of Y versus X gives a straight line with gradient, $M = (C - 1) / V_m C$ and intercept, $C = 1 / V_m C$

The useful region of the plot is only from 0.05 to 0.35 on the X -axis

The determination of the surface area is based on the following principle: A gas close to its boiling point will concentrate (physisorb) at the surface of the solid at a pressure, P , lower than its saturated pressure P_0 . From the monolayer coverage and the known cross section of an adsorbing molecule, it is possible to determine the total surface area as shown below:

If liquid N_2 is used for analysis, it implies that at its temperature, each N_2 molecule covers about 16.2 \AA^2 . From the value of molecules in a statistical monolayer,

Surface area,

$$m^2/g = (1m^2/10^{20} \text{ \AA}^2)(16.2 \text{ \AA}^2/N_2)(6.023 \times 10^{23} N_2/22400 \text{ cc-STP})(V_m, \text{ cc-STP}/W_{\text{cat}}, g)$$

The BET technique involves the use of volumetric or mass devices to determine the amount of gas adsorbed (V in cc-STP) as a function of relative pressure (P/P_0) in the range 0.05 - 0.35. The data is plotted according to the linear BET equation to obtain V_m and C , from which the surface area can be calculated.

2.3.5 BET Experimental procedure

Catalyst surface areas were measured using multi point N_2 adsorption at 77K in accordance with the BET method described above. For this, a micromeritics Gemini instrument controlled by a computer was used. Samples were degassed at 120 °C before dosing nitrogen gas in to the sample tube at 196 °C. For all experiments 110 mg of powdered sample was used and an adsorption isotherm was measured.

2.3.6 Theory of CO Chemisorption

This technique is generally used to measure the metal dispersion on the support. It is based on the fact that some molecules (e.g. CO) will only selectively adsorb on some metal surfaces. The amount of CO absorbed is therefore proportional to the number of metal atom present. The monolayer uptake, N_m ($\mu\text{mol g}^{-1}$), is given by:

$N_m = 44.6V_m$, where V_m is the volume of monolayer.

CO chemisorption analysis gives very useful parameters [active metal surface area (ASA), metal dispersion (D) and the average particle size (d)] crucial for catalytic activity.

$$ASA = N_m S A_m / 166$$

Where, N_m = number of adsorbed gas molecules, S = adsorption stoichiometry (M/CO) and A_m = cross-sectional area occupied by each active surface atom.

The metal dispersion (D) is defined as the fraction of metal atoms found on the surface of metal particles. Atoms found inside the metal particles do not take part in surface reactions and are thus wasted in relation to catalytic activity. D is expressed as a percentage of metal atoms present in the sample.

$D = N_m S M / 100 L$, where, M and L represent the molecular weight and percentage loading of the supported metal respectively.

If ASA is known, a spherical particle shape can be assumed to estimate an equivalent particle diameter, d .

$d = 100 L f / ASA \times Z$, where, L = mass of supported metal, Z = density of supported metal and f = particle shape correction factor (= 6 for spherical particles).

2.3.7 CO Chemisorption Experimental Procedure

CO chemisorption was performed using Autosorb-1 Quantachrome equipment. For each analysis involving a Pt-supported catalyst, the sample was first treated with He and H₂ prior to CO uptake. The sample was degassed by flowing He through the sample while heating to 120 °C (ramp = 20 °C min⁻¹). At 120 °C He was flown for further 30 mins. The sample was then reduced with H₂ while heating to 400 °C. At 400 °C, the sample was treated with H₂ for further 2 h before evacuating for 3 h to remove any adsorbed H₂. This was followed by CO chemisorption at 40 °C.

For analysis involving a Pd-supported catalyst, the sample was also treated with He and H₂ prior to CO uptake. The sample was degassed by flowing He through while heating to 140 °C (ramp = 20 °C min⁻¹). At 140 °C, He was flown for further 30 mins before cooling to 100 °C (ramp = 20 °C min⁻¹). This was followed by reduction with H₂ at 100 °C for 2 h before evacuating at 140 °C for 3 h. CO chemisorption then followed at 40 °C. 0.23 g of sample was used for each CO chemisorption analysis. An adsorption stoichiometry of M/CO = 1 was assumed [9] to enable calculation of the metal dispersion.

2.3.8 Theory of Powder X-ray diffraction (XRD)

The identification of inorganic materials that are non-molecular and crystalline is usually done by powder X-ray diffraction (XRD) [10, 11] supplemented, where necessary, by

chemical analysis. In addition to the identification of a material, the XRD technique also gives information about the arrangement of atoms in a material [10-13]. The technique is a rapid and non-destructive method widely used in Chemistry and Biochemistry to determine the structure of a large variety of molecules, including inorganic compounds, DNA, and proteins. Each crystalline solid has a unique XRD pattern, which can be used as a 'fingerprint' for its identification. The powder patterns and crystallographic data for most known inorganic solids are included in an updated version of the powder diffraction file provided by the International Centre for Diffraction data. The use of appropriate search methods can therefore lead to quick and unambiguous identification of unknowns in a sample.

X-rays are produced from the collision of high-energy charged particles (e.g. electrons accelerated at 30,000 V) with matter. The resulting X-ray spectra usually compose of a broad spectrum of wavelength known as white radiation and a number of fixed or monochromatic wavelengths. White radiation formation occurs when electrons are slowed down or stopped by the collision and some of the lost energy changes in to electromagnetic radiation.

Most diffraction experiments make use of monochromatic X-rays produced from a process different from the one described above. Here, a beam of electrons accelerated through about 30,000 V is directed to a metal target, often Cu. Upon collision with the target, the high-energy electron beam triggers the ionization of some of the Cu 1S (K shell) electrons. An electron then drops from the outer orbital (2p or 3p) to occupy the

vacancy created. This electronic transition is accompanied by the release of energy, which appears as X-rays. Since the transition energies have fixed values, a spectrum of characteristic X-rays is formed. The transition from the 2p – 1s orbital of Cu with a wavelength of 1.5418 Å is called $K\alpha$ while the 3p – 1s transition is termed $K\beta$ and has a wavelength of 1.3922 Å. The $K\alpha$ transition is more intense and occurs more frequently than the $K\beta$. This transition occurs as a doublet ($K\alpha_1 = 1.54051$ Å and $K\alpha_2 = 1.54433$ Å) because it has slightly different energies for the two possible spin states of the 2p electron, constituting the transition, relative to the spin of the 1s orbital. In some X-ray experiments such as powder diffractometry at low angle, diffraction by $K\alpha_1$ and $K\alpha_2$ is not resolved. In such cases, a single line or spot is observed rather than a doublet. Other experiments may show separate diffraction peaks. The removal of the weaker $K\alpha_2$ from the incident beam can be used to obtain a single signal.

Once produced the monochromatic Cu $K\alpha$ radiation (X-ray beam) is incident on to a sample which diffracts (scatters or reflects) it. A detector picks up the diffracted X-rays and the diffraction pattern consists of spots for single crystals and concentric circles for powdered samples. These correspond to regions of constructive interference. For constructive interference of the diffracted X-rays to be observed, the Bragg equation 2.8 must be satisfied.

$$2d\sin\theta = n\lambda \quad (2.8)$$

Fig 2.3 shows the schematic representation of the diffraction of an X-ray beam by a crystal.

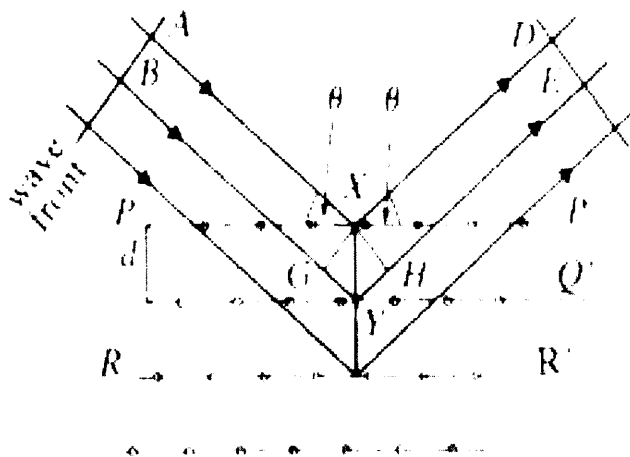


Fig 2.3 Schematic representation of diffraction by a crystal

A computer connected to the XRD equipment automatically records the signal which appears in the form of peaks of given intensities at given 2θ values. Fig 2.4 shows the XRD patterns recorded for two titania samples.

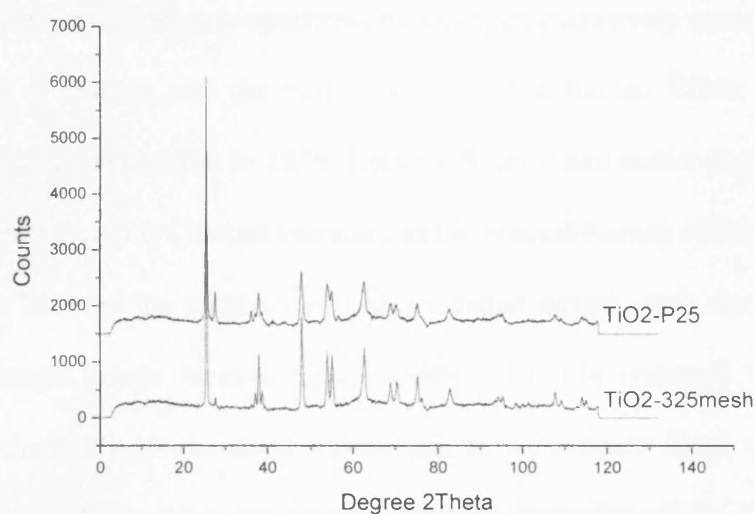


Fig 2.4 Powder diffraction patterns for two TiO_2 samples

2.3.9 XRD Experimental Procedure

Powder X-ray diffraction was used to identify the crystalline phases present in the catalysts synthesised in this work. For this, an Enraf Nonius PSD120 diffractometer with monochromatic $\text{Cu K}\alpha$ source operated at 1.2KW (40KeV and 30mA) was used. Powdered Samples were placed in the sample holder and rotated as X-rays struck the sample. The experimental patterns were calibrated against silicon standard and by

matching experimental patterns to the JCPDS powder diffraction file; the phases present in the catalysts were identified. Traces software was used to determine the particle size for some catalysts.

2.3.10 Theory of Laser Raman spectroscopy

The theory governing Raman spectroscopy has been extensively covered in the literature [14-17]. C V Raman was the first to describe the Raman Effect after a successful experimental demonstration in 1928. Because Smekal had earlier theoretically predicted it, it is often referred in German literature as the Smekal-Raman effect. It results from the interaction between the molecules of an irradiated sample with the incident radiation. This interaction causes the exciting or incident light to be scattered. Most of the light is scattered elastically (at the same wavelength as the incident light) while some of it is scattered inelastically (at a wavelength different from that of the exciting light). The elastic scattering is termed Rayleigh scattering while the inelastic scattering is called Raman scattering. The difference in energy between the incident and the Raman scattered light corresponds to the energy involved in changing the vibrational motion of the molecule and is called Raman shift. When an excited molecule returns to a vibrational level higher than its initial state, the spectral line has a shorter wavelength (and higher frequency) than the incident radiation and is called Stokes lines. On the other hand, if a molecule in an excited state (say $v = 1$) is moved to a higher unstable state by interacting with the incident photon, the spectral line resulting from its decay to the ground state is called an anti-Stokes line. Since most molecules reside in the ground state and not the

excited state at room temperature, the Stokes lines are usually of higher intensity than the anti-Stokes lines. Fig 2.5 illustrates the three scattering phenomena described above. The Raman spectrum is a plot of the detected number of photons (intensity) against Raman shift from the incident laser energy. Each Raman shifted signal observed in a spectrum corresponds to a vibrational or rotational mode of a molecule in the sample.

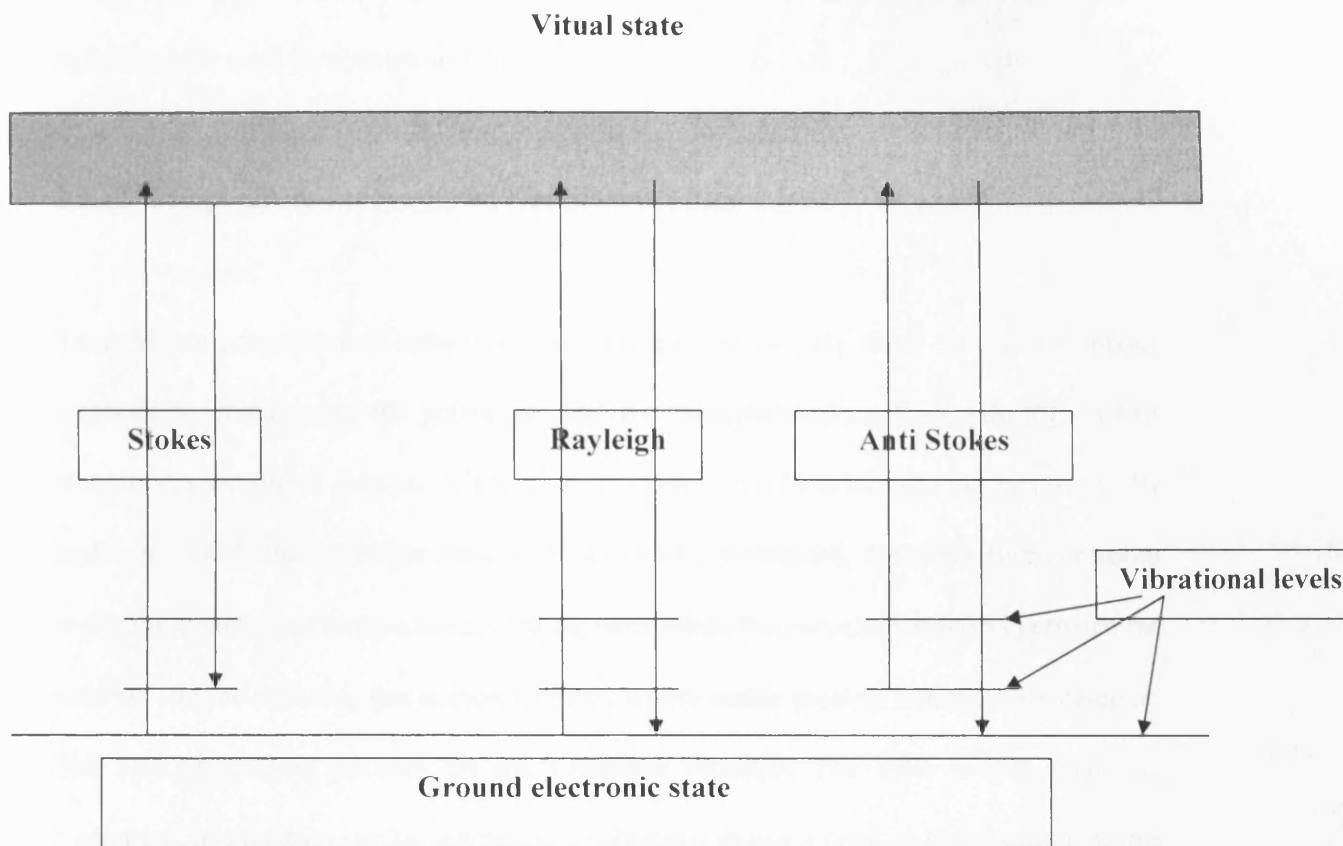


Fig 2.5 Schematic representation of Rayleigh and Raman scattering (Stokes and anti-Stokes)

2.3.11 Raman Spectroscopy Experimental Procedure

In this work, a Renishaw system - 1000 dispersive laser Raman microscope was used for recording Raman spectra of catalysts synthesised. The excitation source used was an Ar ion laser (514.5 nm) operated at a power of 20 mW. The laser was focused on powdered samples placed on the microscope slide to produce a spot size of ca. 3 μm in diameter. A

backscattering geometry with an angle of 180° between illuminating and collected radiation was used for spectra collection.

2.3.12 Temperature Programmed Reduction (TPR)

Temperature-programmed reduction experiments are widely used in heterogeneous catalysis to characterise the activation and the reactivity of catalysts [18-20]. In this technique a sample of catalyst is heated continuously in a flow of reducing gas (typically hydrogen) while the hydrogen consumption is being monitored. A temperature controller is used to control and ensure linear heating rates while the reduction reaction between the catalyst and the reducing gas is monitored by a very stable thermal conductivity detector. The resulting signal appears on the computer monitor. The TPR profile (showing hydrogen consumption versus temperature) obtained shows a peak or peaks unique to the sample and thus acting as a 'fingerprint' for its identification.

2.3.13 TPR Experimental Procedure

In this work, temperature-programmed reduction was carried out using either a Micrometrics Autochem 2910 equipment (for M/V/alumina catalysts) or a TPDRO 1100 Series Thermo Electron Corporation instrument (for ceria-based catalysts) both equipped with a TCD detector. Prior to treatment of each catalyst with the reducing gas (hydrogen), the sample was pretreated by flowing Ar (20 ml min^{-1}) through it while heating from $30-110^\circ\text{C}$ (ramp rate of $20^\circ \text{ min}^{-1}$). The sample was then maintained at 110°C for 45 mins

before cooling to 30 °C. For reduction, the reducing gas employed was 10 % H₂ in Ar (20 or 50 ml min⁻¹). The temperature ranged from room temperature to 650 °C and a heating rate of 10 °C min⁻¹ was maintained for all catalysts under investigation. Catalysts masses ranged between 50-110 mg depending on sample under investigation.

2.3.14 Theory of Thermal Gravimetric Analysis

Thermal gravimetric analysis involves the measurement of changes in weight of sample (resulting from chemical reactions, decomposition, solvent and water evolution, or oxidation) as a function of temperature. Samples tested are usually samples of catalysts which have not yet been calcined. Samples are treated thermally in a gaseous atmosphere (air, H₂ in Ar or nitrogen) depending on the calcination atmosphere.

2.3.15 TGA Experimental Procedure

Thermal gravimetric analysis (TGA) was performed using SETARAM 10013707 equipment. Approximately 20 mg of powdered sample was investigated in air using a temperature range from ambient temperature to 800 °C and a ramp rate of 10 °C min⁻¹.

2.3.16 Theory of Scanning Electron Microscopy (SEM)

SEM is a technique used as a complement for optical microscopy to study the texture, topography and surface features of powders or solid pieces [10]. Pictures resulting from

SEM instruments have a definite 3D quality due to the depth of focus of these instruments. Unlike optical microscopy a scanning electron microscope uses electrons rather than light to produce an image. The larger depth of the SEM field enables large amounts of samples to be focused at one time. The images produced have a high resolution (between lower resolution limit of optical microscopy (approximately 1 μm) and the upper practical working limits of transmission electron microscopy (approximately 0.1 μm) or higher (approximately 10^{-2} to approximately 10^2 μm). The high resolution of the SEM allows for closer spaced features to be examined at high magnification. The main advantages of SEM therefore include:

- Higher resolution
- Greater magnification
- Larger depth of focus
- Easy sample preparation and observation

These advantages have made SEM a widely applicable microscopic technique in various heterogeneous catalysis research and other research laboratories worldwide.

In the scanning electron microscope, a beam of electrons produced from an electron gun travels vertically through the column of the microscope and as it goes past electro magnetic lenses, it is focused to a small spot (50-100Å in diameter) on the sample surface. The electron beam scans the sample, rather like the spot on the television screen. The interaction of the electron beam with the sample results to the emission of both X-rays and secondary electrons. Secondary electrons are used to produce an image of the

sample surface which is displayed on a screen while X-rays are used for chemical analysis. Some SEM instruments are furnished with a valuable additional feature which allows for important elemental analysis of sample composition.

2.3.17 SEM Experimental Procedure

The particle size and morphology of powdered CeO_2 (UR) and Pt-supported catalysts synthesized in this work were evaluated by scanning electron microscopy (SEM) using EVO 40 Oxford instrument composed of an electron gun (with tungsten filament and anode), two condenser or magnetic lenses, and a detector which analyses the secondary electrons and X-rays emitted from the interaction of the electron beam and the sample. Prior to turning on the electron gun, the SEM system was evacuated to 10^{-5} - 10^{-6} mBar. Pictures of samples were taken at high and low magnification to observe both the nature of particle and closer view of the surface. Figure 2.6 shows pictures of the EVO 40 SEM equipment used.



Fig. 2.6 (a) SEM Equipment

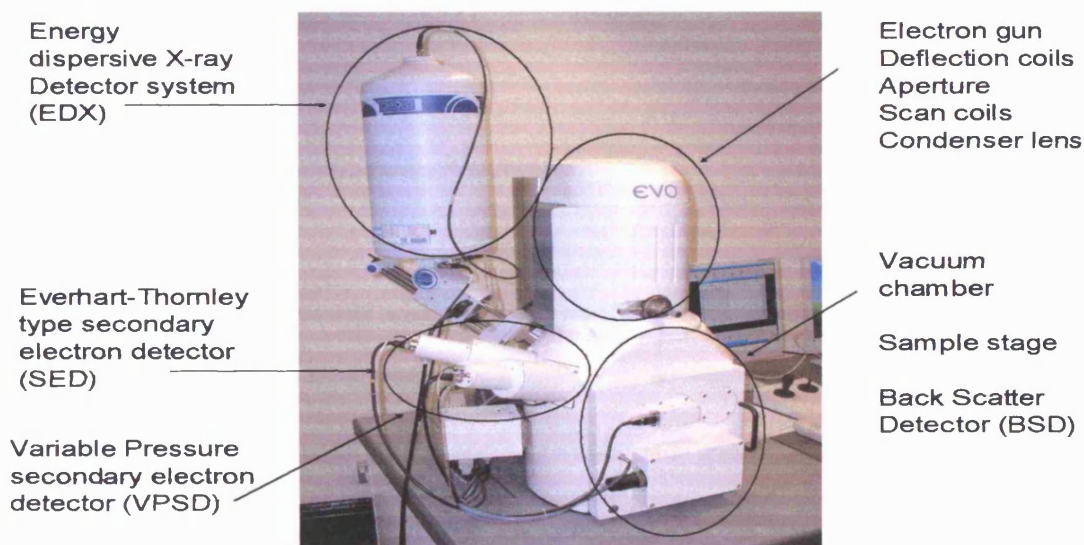
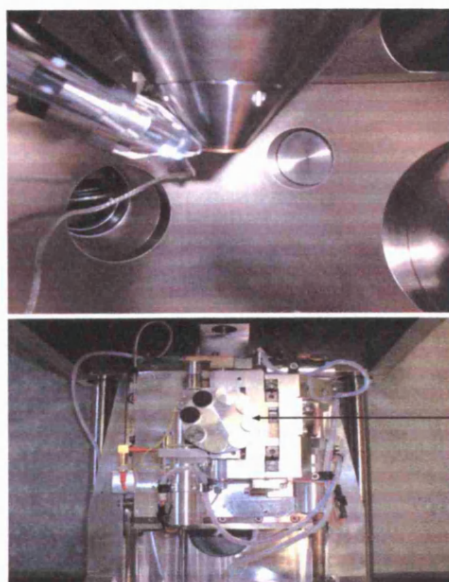


Fig. 2.6 (b) Picture showing parts of the SEM equipment



Retractable Back scattered electron detector located directly above sample consisting of four individual diodes

8 bed sample holder

Fig. 2.6 (c) Internal view of the SEM equipment showing sample stage and back scattered electron detector.

2.3.18 Theory of X-ray Photoelectron Spectroscopy

X-ray photoelectron spectroscopy (XPS) is an electron spectroscopy technique which measures the kinetic energy of electrons emitted when matter is bombarded with high-energy X-rays [10]. The technique is used to determine energy levels in atoms and molecules and is particularly useful for surface studies since electrons produced are not very energetic (energy $\ll 1\text{KeV}$) and are easily absorbed by the solid matter. Hence, the electrons can not escape from the solid unless ejected within $20 - 50 \text{ \AA}$ of the surface.

In XPS, X-rays (usually Mg K α , 1254eV or Al K α , 1487eV monochromatic radiation) interact with matter, leading to the emission of primary electrons which are detected. The kinetic energy, E , of the emitted electrons correspond to the difference in the energy of the incident photon ($h\nu$) and the binding energy, E_b of the electron.

$$E = h\nu - E_b$$

The kinetic energy and binding energy of each emitted electron is characteristic of the atom or element from which it is emitted. Each atom can give rise to several characteristic E_b corresponding to the emission of electrons from different energy levels in the atom.

Auger electron spectroscopy is a related technique in which secondary electrons are detected. The emission of primary electrons from an atom A, results to the creation of vacancies and the ionized atom is said to be in the excited state, A^{+*} . The decay of the excited atom is accompanied by the drop of an electron to a lower energy level and energy is evolved in this process. The energy evolved can be in the form of X-rays or can be transferred to another electron in the same atom which is then ejected. Such secondary ionized electrons are called Auger electrons. The XPS and AES process are summarized in the equations below.





The AES spectra are usually observed together with XPS spectra, showing the intensity of ionized electrons against the energy of electrons.

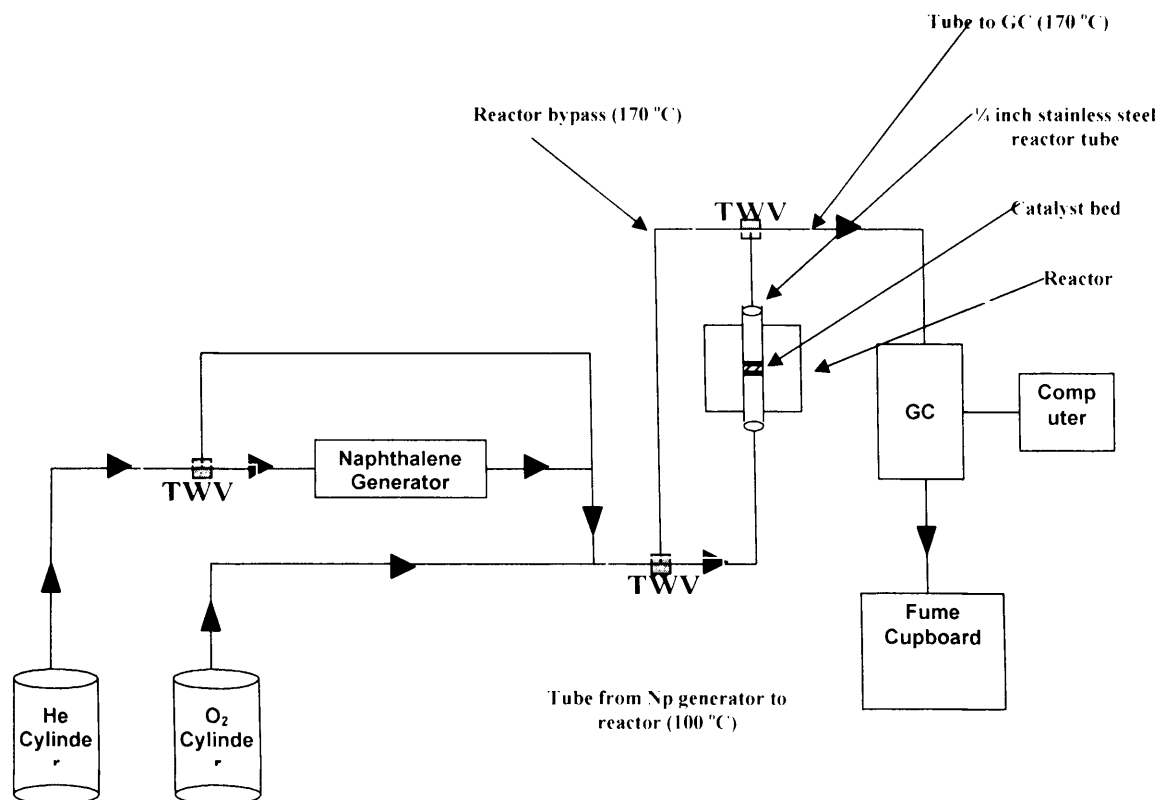
2.3.19 XPS Experimental Procedure

XPS measurements were made using a Kratos Axis Ultra DLD spectrometer at Kratos Analytical, Manchester UK, using monochromatic AlK α radiation, and analyser pass energies of 160 eV (survey scans) or 40 eV (detailed scans). Binding energies were referenced to the C(1s) peak from adventitious carbonaceous contamination, assumed to have a binding energy of 284.7 eV.

2.4 Catalyst Testing

2.4.1 Naphthalene Oxidation Process and Equipment

The flow diagram for the naphthalene oxidation catalytic system used for the work reported in this thesis (chapters 3-7) is shown in figure 2.7. Figures 2.8 (a) and (b) show a photograph of the actual equipment used for PAH oxidation. Naphthalene from the naphthalene generator maintained at 30 °C flows with the aid of helium and mixes with oxygen in the tube from the naphthalene generator. Depending on the positions of the two-way valves, the reaction mixture can either flow through the bypass (for control experiment) to the GC or through the reactor to the GC. Naphthalene oxidation occurs in the reactor. The reactor is composed of a ¼ inch o.d. stainless steel tube insulated with a steel cover lined in the inside by quartz wool and furnished with a heating coil for heating. The micro reactor tube is connected with a thermocouple to the reactor temperature controller used to vary the reaction temperature. Products from the reactor flow to the gas chromatograph (GC) where injection occurs and the products are separated in two columns in the GC and detected by a thermal conductivity detector (TCD) and a flame ionisation detector (FID). A computer connected to the GC records signals detected by both detectors. The TCD shows peaks corresponding to air, CO and CO₂ while the FID detects mainly the presence of naphthalene and possibly other hydrocarbons (if present as by-products or intermediates).



Np – Naphthalene
TWV – Two-way valve

Fig. 2.7 Flow diagram for naphthalene total catalytic oxidation process

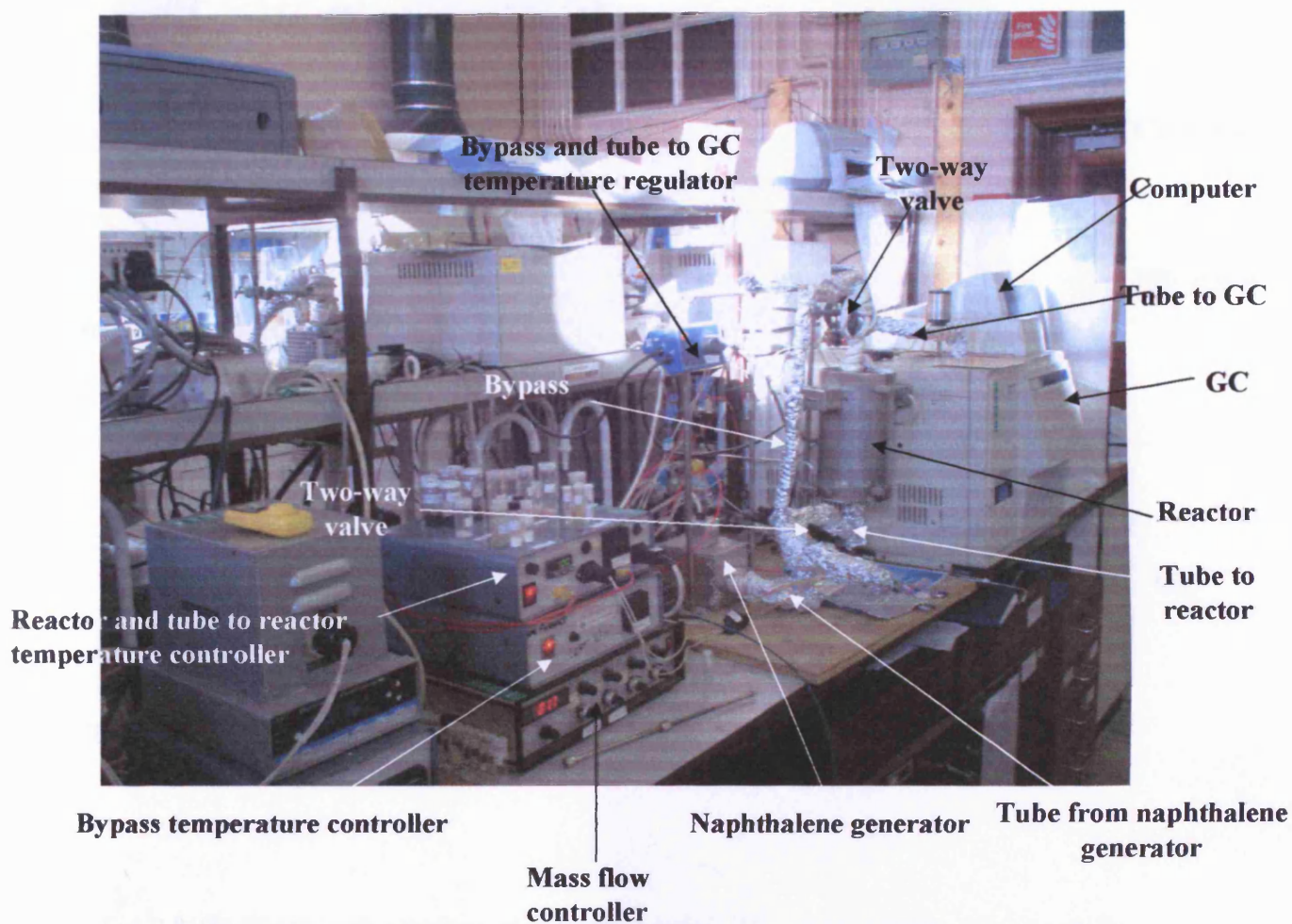


Fig. 2.8 (a) Photograph of equipment used for total catalytic oxidation of naphthalene

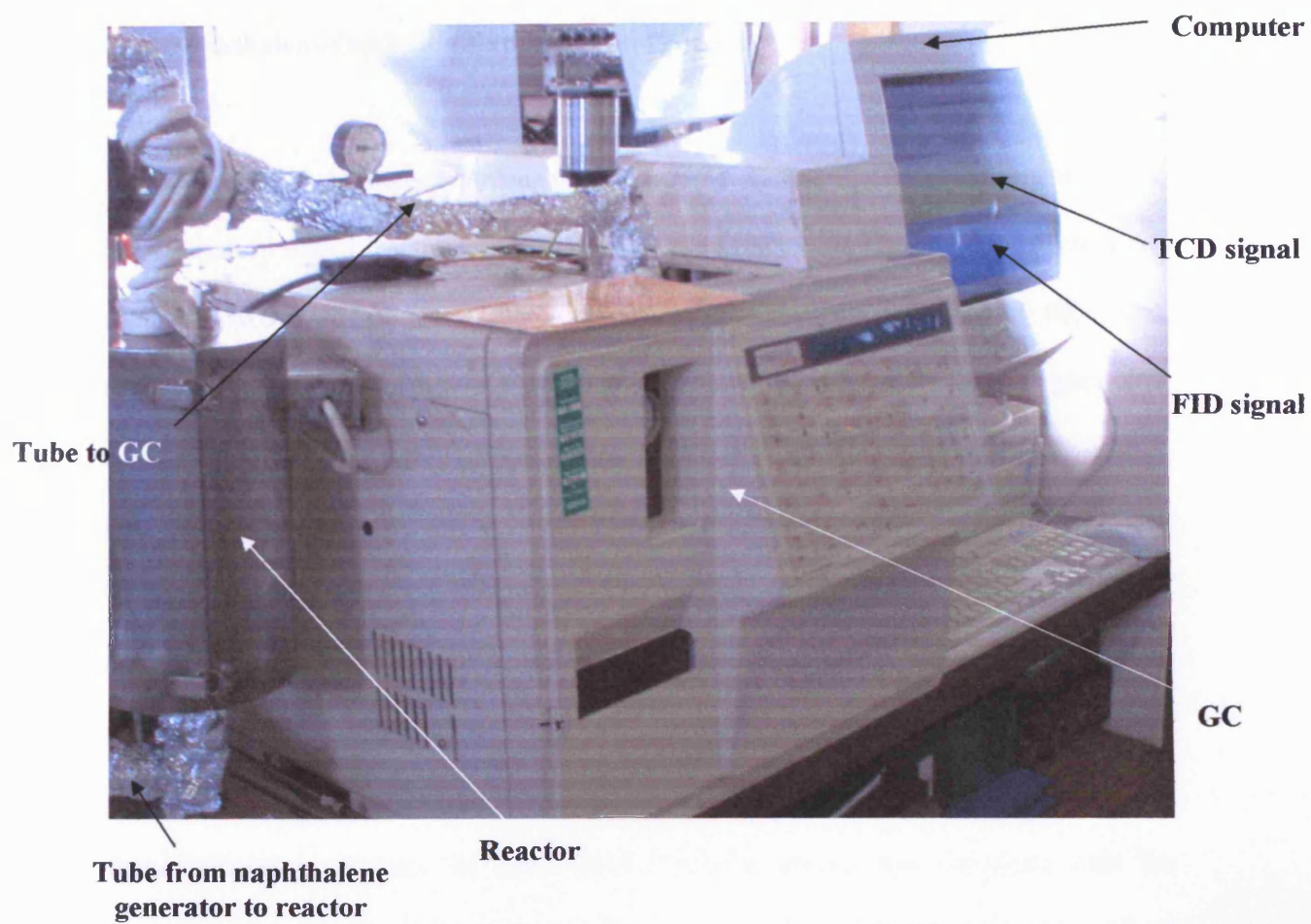


Fig 2.8 (b) Photograph showing clearly the reactor, GC and computer setup used for naphthalene catalytic oxidation.

2.4.2 Naphthalene Oxidation Experimental Procedure

The activity of each catalyst for naphthalene oxidation was determined using the fixed bed laboratory micro reactor described earlier. Catalysts were tested in powdered form using a $\frac{1}{4}$ o.d. stainless steel reactor tube. The reaction feed consisted of 100 vppm naphthalene in air. A total flow rate of 50 ml min^{-1} was used and catalysts were packed to a constant volume to give a gas hourly space velocity of $45\,000 \text{ h}^{-1}$ for all studies (except otherwise stated). To do this, a bubble meter was used to measure the flow of gases through the system and a calibration curve was derived relating the flow of individual gases to numerical values on their mass flow controllers.

Analysis was performed by an on-line gas chromatograph with thermal conductivity and flame ionisation detectors. In most cases, catalytic activity was measured over the temperature range $100\text{-}300\text{ }^{\circ}\text{C}$ in incremental steps, and temperatures were measured by a thermocouple placed in the catalyst bed. Data were obtained at each temperature after a stabilization time. Three analyses were made at each temperature to ensure that steady state data were collected. The reaction temperature was increased and the same procedure followed to determine each data point. An average of the three readings recorded at each temperature was taken to determine the conversion and yield to CO_2 . There was an error margin of within 0.1 - 2 % conversion (or CO_2 yield) between the three readings at each temperature. The activity of each catalyst tested was calculated based on:

- a) The fraction of naphthalene decomposed (naphthalene conversion) over these catalysts as a function of temperature. This fraction represents the fraction of naphthalene decomposed relative to the maximum amount of naphthalene from the naphthalene generator prior to combustion. This maximum amount of naphthalene was detected by doing a blank analysis through the bypass at a temperature low enough to prevent naphthalene combustion.
- b) The fraction of carbon dioxide generated (conversion to CO_2) over these catalysts as a function of temperature. This fraction of CO_2 represents the amount of CO_2 produced during the catalytic oxidation relative to the maximum amount of CO_2 resulting from the complete oxidation of naphthalene. To obtain the counts for the maximum amount of CO_2 , some reported excellent naphthalene oxidation catalysts ($\text{Pt}/\text{Al}_2\text{O}_3$) were tested in the reactor at temperatures higher (300 – 600 °C) than temperatures (200 - 300 °C) at which 100 % CO_2 yield and complete naphthalene combustion are known to be achieved over such catalysts. An approximately constant value of CO_2 count was obtained for these catalysts between 300-600 °C. This value was considered as the CO_2 count corresponding to 100 % conversion to CO_2 .

Since it had been shown (see chapter 1) that conversion to CO_2 was a better measure of activity than naphthalene conversion, most of the naphthalene oxidation catalytic data reported in later sections of this thesis (chapters 3-6) make use of CO_2 yield and not naphthalene decomposition. A comparison made between activity data based on CO_2 yield and naphthalene conversion confirmed findings of the work reported in chapter 1 (1.4.1).

References

1. T. Garcia, B. Solsona, and S. H. Taylor, *Catal. Lett.*, 105, (2005) 183.
2. J. A. Dean, and T. C. Rains, *Flame Emission and Atomic Absorption Spectrometry*, New York: Marcel Deker, 1975.
3. B. Welz, *Atomic Absorption Spectrometry*, Weinheim:VCH, 1985.
4. B. Kreuz, *Atomic Absorption Spectroscopy*, University of Michigan – Dearborn, 2000, produced by Ruth Dusenbery.
5. S. Brauner, P. H. Emmett, and E. Teller, *J. Am. Chem. Soc.*, 60 (1938) 309.
6. E. M. McCash, *Surface Chemistry*, Oxford University Press, 2001, 77.
7. G. C. Bond, *Heterogeneous catalysis: Principles and Applications*, second edition, Clarendon Press – Oxford.
8. James T. Richardson, Department of Chemical Engineering, University of Houston, *Bibliography in Catalysis*, Section F, 1-2.
9. J. R. Anderson, *Structure of Metallic Catalysts*, Academic Press, London, 1975.
10. A. R. West, *Basic Solid State Chemistry*, 2nd Edition, John Wiley and Sons, 1999 pp125.
11. J. P. Glusker, M. Lewis, and M. Rossi, *Chrystal Structure Analysis for Chemist and Biologists*, VCH Publishers, NY: 1994. ISBN 0471185434.
12. J. Drenth, *Principles of Protein X-Ray Crystallography*, Springer P. Verlag Inc. NY: 1999, ISBN 0387985875.
13. G. Rhodes, *Crystallography Made Crystal Clear*, Academic Press, CA: 2000, ISBN 0125870728.

14. N. B. Colthup, S. E. Wiberley and L. H. Daly, Introduction to Infrared and Raman Spectroscopy, Academic Press, New York and London, 1964.
15. P. W. Atkins, The Elements of Physical Chemistry, 2000.
16. J. M. Brown, Molecular Spectroscopy, Oxford Chemistry Primer, 1998.
17. G. Herzberg, Infrared and Raman Spectra of Polyatomic Molecules, Vanoststrand Reinhold, NY, 1945.
18. S. Besselmann, C. Freitag, O. Hinrichsen, and M. Muhler, Phy. Chem. Phys., 2001, 4633.
19. J. L. Falconer and J. A. Schwarz, Catal. Rev. – Sci. Eng., 25 (1983) 141.
20. S. Behatia, J. Beltramini, and D. D. Do, Catal. Today, 7 (1990) 309.

CHAPTER 3: NAPHTHALENE OXIDATION OVER VANADIUM MODIFIED Pd AND Pt-ALUMINA CATALYSTS

3.1 Introduction

Pd/Al₂O₃ and Pt/Al₂O₃ catalysts have been extensively used for the oxidation of volatile organic compounds (VOCs) and chlorinated VOCs [1-8] in a vast number of research laboratories around the world. As mentioned earlier in chapter 1, Pd and Pt-supported alumina catalysts feature among the best catalysts reported for the complete oxidation of naphthalene. It is well known that the addition of modifiers to metal-supported catalysts can have significant effects on the textural, crystallographic and catalytic properties of these catalysts. A number of studies [9-15] have shown that the activity of supported-metal catalysts such as Pd/Al₂O₃ in the oxidation of short chain hydrocarbons can be promoted by a variety of modifiers (V, TiO₂, V₂O₅, La₂O₃, CeO₂, ZrO₂ and BaO). M. Ferrandon and E. Bjornbom [16] have equally investigated Pd-alumina catalyst modified by CuO/La for naphthalene oxidation. To date, there is not much in the literature on the use of other modifiers to promote the activity of Pd and Pt-supported alumina catalysts for naphthalene oxidation.

It has been demonstrated that the catalytic efficiency of a number of systems in alkane and mono-aromatic compound oxidation can not be directly extrapolated to the complete abatement of PAHs [17]. Hence, the influence of vanadium modifier on the activity of Pd

and Pt-supported alumina catalysts can not be drawn from similar studies patterning to alkane, benzene or toluene oxidation. The main purpose of the work reported in this chapter was to investigate the catalytic effect of the addition of varying loadings of vanadium to 0.5%Pd/Al₂O₃ and 0.5%Pt/Al₂O₃ catalysts for complete naphthalene oxidation. Previous studies [8, 10, 11, 18] relating to the modification of Pd-alumina catalysts by vanadium hold different schools of thought to account for the promotion in alkane and mono-aromatic compound oxidation activity. Escando et al. [11] relate this promotion to the interactions between Pd and V or a modification of the support properties while Neyertz and Volpe [10] suggest a change in the Pd reducibility and particle size. Contrary to both schools of thought, Vassileva et al. [18] proposed a redox effect in which the activation of oxygen on the metal particles fosters the reverse oxidation of V⁴⁺ and thus establishes a redox equilibrium in the redox process. Feirrer R. S. G. et al. [8] attributed this promotion, for benzene oxidation, to the presence of high amounts of V⁴⁺ and more importantly to the decrease in Pd dispersion as the vanadium oxide content increased. In this chapter, characterization and naphthalene oxidation activity data for V-modified Pd and Pt-Al₂O₃ catalysts are reported.

Pd and Pt-supported alumina catalysts modified by vanadium were prepared by impregnation, characterised (atomic absorption spectroscopy, BET, CO chemisorption, XRD, Raman spectroscopy, and temperature-programmed reduction) and tested for the complete oxidation of naphthalene (a model PAH). Detail descriptions of preparation method, characterisation techniques and catalyst testing have already been discussed in chapter 2.

3.2 Atomic Absorption Spectroscopy Results for Pd/V/Al₂O₃ Catalysts

Atomic absorption spectroscopy results are shown in table 3.1. It can be observed from the results that experimental values for V concentration closely matched their expected concentrations and the concentration increased with increase in vanadium loading. The experimental Pd concentrations recorded were too low and did not match the expected concentration. This might have been as a result of the presence of alumina in the catalyst as the AA signal for Pd is suppressed in the presence of Al in an air-acetylene flame [19]. AAS results thus show that the method of synthesis employed in this work was appropriate for the preparation of catalysts with varied V loading as specified in table 3.2. Although the presence of Al made it difficult to quantify Pd by AAS, the fact that V loadings were close to the expected amount indicates that true Pd loadings should be close to the theoretical quantities. Hence, the preparation of metal-supported catalysts by impregnation gives rise to catalysts with metal concentrations that reflect desired metal loadings.

Table 3.1 Table showing theoretical and actual concentrations (AAS experimental values) of Pd and V in Pd/V/Al₂O₃ catalysts

Catalyst	Expected		Experimental	
	Concentrations / ppm		Concentrations / ppm	
	Pd	V	Pd	V
0.5%Pd/0.5%V/ γ -Al ₂ O ₃	2.5	2.5	0.1	2
0.5%Pd/1%V/ γ -Al ₂ O ₃	2.8	5	0.2	4
0.5%Pd/3%V/ γ -Al ₂ O ₃	2.5	15	0.1	11
0.5%Pd/6%V/ γ -Al ₂ O ₃	2.5	30	0.1	22
0.5%Pd/12%V/ γ -Al ₂ O ₃	2.5	60	0.1	53

3.3 BET and CO Chemisorption Results for Vanadium-modified Pd and Pt-supported Alumina Catalysts

Table 3.2 shows the BET surface areas and metal dispersions for catalysts synthesised in this work. The BET results show that all catalysts had surface areas slightly lower than the alumina support. There was a general decrease in surface area of the catalysts with increase in metal loading. This could be attributed to the filling of micro-pores in the support by particles of the metal species.

Table 3.2 Chemical composition, BET surface area and metal (Pd or Pt) dispersion of Pd/Al₂O₃, Pd/V/Al₂O₃, Pt/Al₂O₃ and Pt/V/Al₂O₃ catalysts

Catalysts	BET surface area / m ² g ⁻¹	M (Pd or Pt) dispersion / %
Al ₂ O ₃	194	-
0.5%Pd/Al ₂ O ₃	166	9
0.5%Pd/0.5%V/Al ₂ O ₃	180	32
0.5%Pd/1%V/Al ₂ O ₃	175	14
0.5%Pd/3%V/Al ₂ O ₃	160	13
0.5%Pd/6%V/Al ₂ O ₃	151	11
0.5%Pd/12%V/Al ₂ O ₃	140	9
0.5%Pt/Al ₂ O ₃	169	52
0.5%Pt/0.5%V/Al ₂ O ₃	180	78
0.5%Pt/1%V/Al ₂ O ₃	185	62
0.5%Pt/3%V/Al ₂ O ₃	169	59
0.5%Pt/6%V/Al ₂ O ₃	164	57
0.5%Pt/12%V/Al ₂ O ₃	149	54

The M (Pd or Pt)/V/Al₂O₃ catalysts showed a decrease in surface area with increasing V loading. The difference in porosity is the major factor accounting for the difference in surface areas observed between the catalysts and their support.

Table 3.2 also shows the change in Pd and Pt dispersion with the addition of varying loadings of V to the Pd and Pt-alumina catalysts. The Pd and Pt dispersion for catalysts with 0.5 - 12 %V loading decreased with increasing V loading. This is analogous to the decrease in Pd dispersion with increase vanadium oxide content reported in the literature [8]. The table shows that the addition of vanadium to the Pd/Al₂O₃ and Pt/Al₂O₃ catalyst enhanced the Pd and Pt dispersion and the dispersion decreased as the vanadium content increased. Catalysts with 0.5 %V yielded the maximum Pd and Pt dispersions whilst the catalyst without vanadium and with 12 %V had the lowest Pd and Pt dispersions. Pt catalysts had higher metal dispersion than Pd catalysts with the same vanadium loading. BET and CO chemisorption results therefore suggest that the addition of vanadium modified both the textural properties of the alumina support and the distribution of the active metal (palladium or platinum).

3.4 XRD Results for Vanadium-modified Pd and Pt-supported Alumina Catalysts

The results of XRD analysis are summarised in table 3.3 and figures 3.1 (a) and (b). These results revealed that except for catalysts with 12 %V loading, diffraction peaks seen in patterns of all the other catalysts were representative of γ -Al₂O₃.

The additional peaks observed in the patterns of catalysts with 12 %V loading were from V_2O_5 , which probably resulted from the dispersion of large crystallites of V_2O_5 on the surface of the Al_2O_3 support. The absence of diffraction from Pd or Pt in all catalysts and from V in catalysts with lower V loadings can be attributed to a low concentration or the presence of phases that are not detectable due to their high dispersion.

Table 3.3 Phases identified in XRD patterns of Pd/ Al_2O_3 , Pd/V/ Al_2O_3 , Pt/ Al_2O_3 and Pt/V/ Al_2O_3 catalysts

Catalysts	Phases identified
0.5%Pd/ Al_2O_3	γ - Al_2O_3
0.5%Pd/0.5%V/ Al_2O_3	γ - Al_2O_3
0.5%Pd/1%V/ Al_2O_3	γ - Al_2O_3
0.5%Pd/3%V/ Al_2O_3	γ - Al_2O_3
0.5%Pd/6%V/ Al_2O_3	γ - Al_2O_3
0.5%Pd/12%V/ Al_2O_3	γ - Al_2O_3 , V_2O_5 (Scherbinaite, syn)
0.5%Pt/ Al_2O_3	γ - Al_2O_3
0.5%Pt/0.5%V/ Al_2O_3	γ - Al_2O_3
0.5%Pt/1%V/ Al_2O_3	γ - Al_2O_3
0.5%Pt/3%V/ Al_2O_3	γ - Al_2O_3
0.5%Pt/6%V/ Al_2O_3	γ - Al_2O_3
0.5%Pt/12%V/ Al_2O_3	V_2O_5 (Scherbinaite, syn)

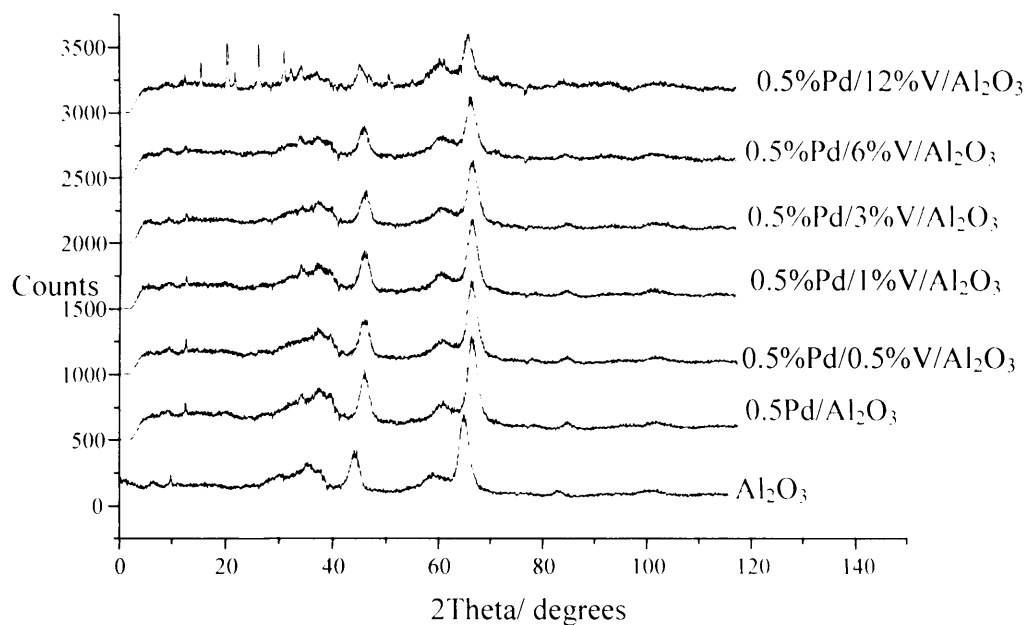


Fig. 3.1 (a) XRD patterns of Al₂O₃, Pd/Al₂O₃ and Pd/V/Al₂O₃ catalysts

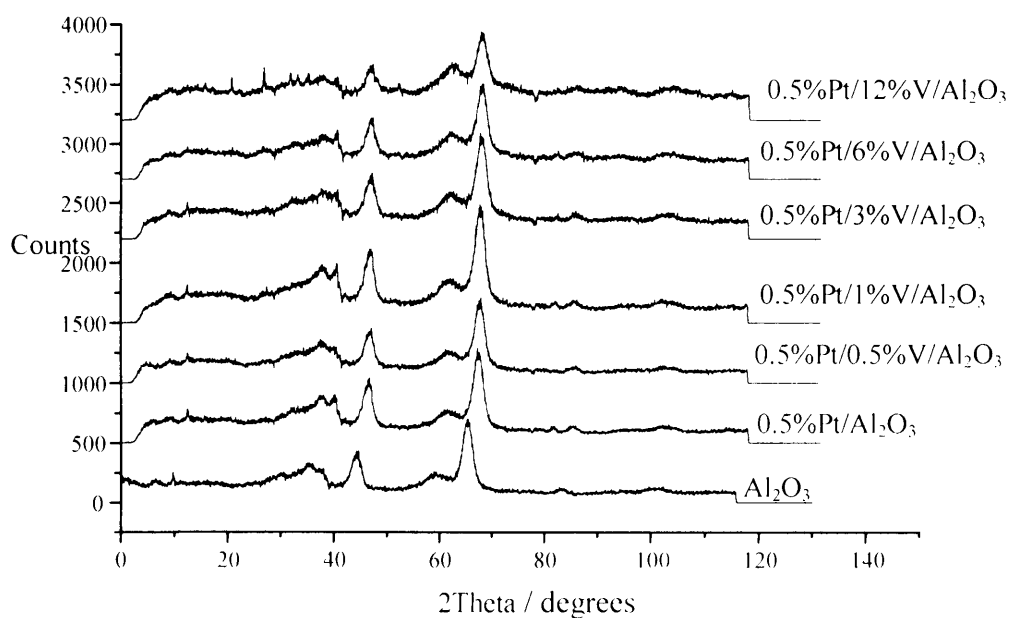


Fig. 3.1 (b) XRD patterns of Al₂O₃, Pt/Al₂O₃ and Pt/V/Al₂O₃ catalysts

3.5 Raman Results for Vanadium-modified Pd and Pt-supported Alumina Catalysts

Raman spectra recorded for Pd and Pt catalysts are shown in figures 3.2 (a), (b) and (c). From figures (a) and (c) it can be observed that all the catalysts showed major bands corresponding to Al_2O_3 . These bands occurred in the range $2000 - 4000 \text{ cm}^{-1}$. The intensities of these bands decreased with increasing vanadium loading. The reflective laser Raman technique is relatively surface sensitive and the decrease of the intensity of the alumina peaks is consistent with increase in coverage of another phase over the support.

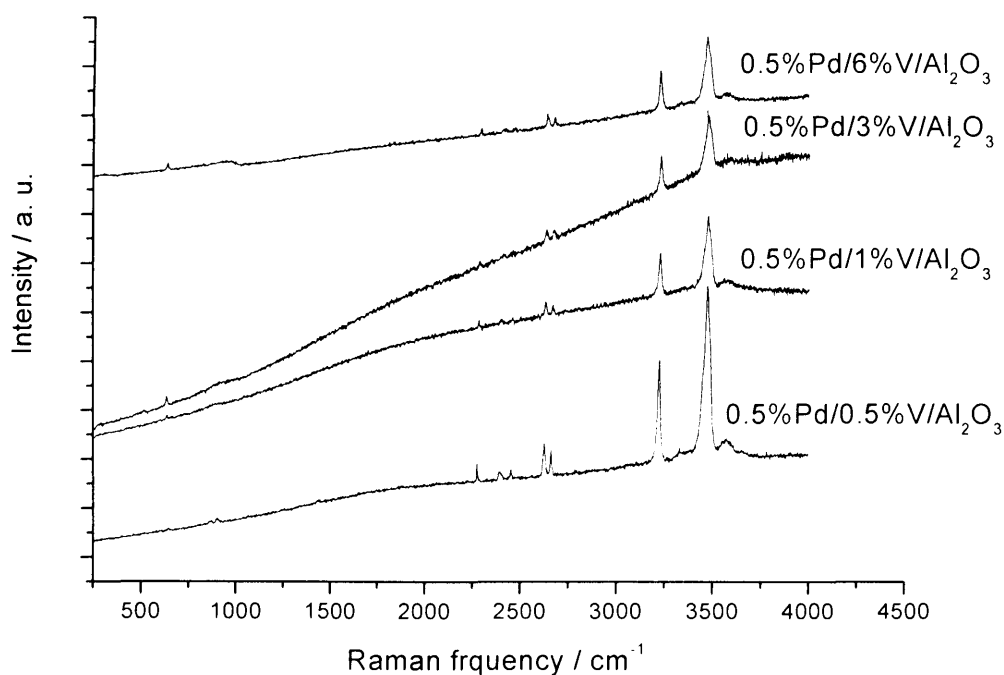


Fig 3.2 (a) Figure showing Raman spectra recorded for Pd/V/ Al_2O_3

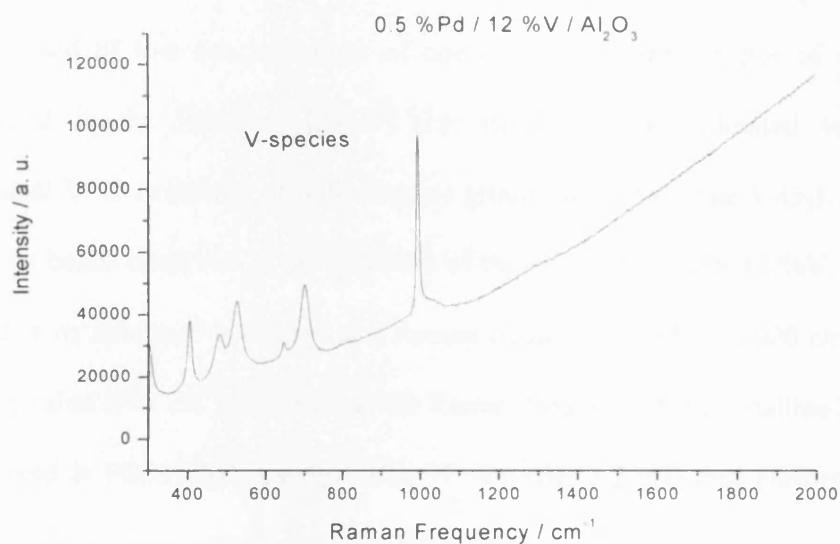


Fig 3.2 (b) Figure showing Raman spectrum of 0.5 %Pd/12 %V/ Al_2O_3

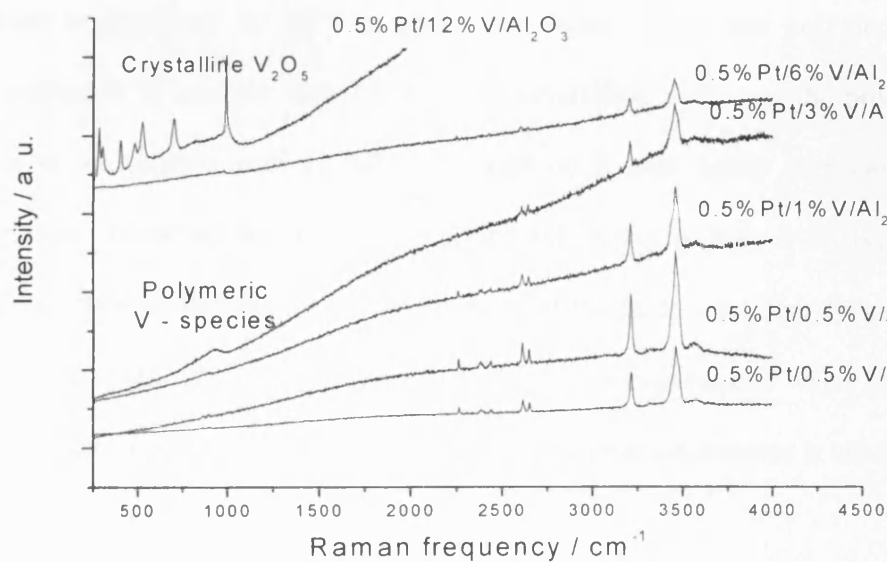


Fig 3.2 (c) Figure showing Raman spectra recorded for Pt/V/ Al_2O_3 catalysts

Fig 3.2 (a) shows that Raman spectra of Pd/V/Al₂O₃ catalysts with 0.5 – 6 %V did not indicate the presence of any vanadium species. However, it is likely that these catalysts comprised of low concentrations of one or more of three types of vanadium species reported in the literature [24-29] (i.e. isolated tetracoordinated vanadium species, terminal V=O stretching of polyvanadate groups and crystalline V₂O₅). Fig 3.2 (b) shows Raman bands observed in the spectrum of the Pd catalyst with 12 %V. The most intense band in its spectrum is centred at a Raman frequency of 980 – 1000 cm⁻¹, which is close to the value (997 cm⁻¹) reported as the Raman frequency for crystalline V₂O₅ [25]. Bands observed in Pd/V/Al₂O₃ catalyst with 12 %V (fig. 3.2 (b)) thus confirm the presence of crystalline V₂O₅ in accordance with XRD results.

Bands labelled in the Raman spectra of Pt/V catalysts (Fig 3.2 c) are based on a similar argument as explained for Pd/V catalysts. The figure shows that polymeric V-species were present in Pt catalyst with 3 %V whilst crystalline V₂O₅ was the predominant V-species in the catalyst with 12 %V. Although no Raman bands corresponding to V-species were observed for most Pt catalysts with 0.5 - 6 %V, it is likely that they contained lower concentrations of one or more of the three vanadium species discussed for Pd/V catalysts. There is a degree of fluorescence experienced when using alumina with an Ar ion laser, and hence identification of weak Raman features is hindered.

3.6 Temperature-programmed Reduction Results for Vanadium-modified Pd and Pt-supported Alumina Catalysts

Temperature-programmed reduction profiles for Pd/V/Al₂O₃ catalysts are shown in figure 3.3 (a). 0.5 %Pd/6 %V/Al₂O₃ gave 2 well defined TPR peaks (at approximately 150 °C and 210 °C). Both peaks closely matched 2 of the 3 reduction peaks for 0.5 % Pd/12 %V/Al₂O₃ (centred at 125, 150 and 200 °C). 0.5 %Pd/3 %V/Al₂O₃ only showed a single well defined peak centred at 150 °C whereas catalyst with 0.5 %V did not show any TPR peaks. The catalyst containing 1 %V showed a small unique peak at very low temperature (centred at 60 °C). The three reduction peaks observed in catalysts with 3 – 12 %V are most likely related to the reduction of three different vanadium species [21, 28-31]. The TPR peak centred at 150 and about 200 °C increased with the vanadium loading and probably represent the reduction of polymeric VO_x species and V₂O₅ crystallites, respectively. The peak at 125 °C can be attributed to isolated low-coordinated vanadium species. Small peaks observed at temperatures below 100 °C (at about 80 °C) in Pd/V/Al₂O₃ catalysts have been accounted for by the release of hydrogen in the decomposition of palladium hydride species [26]. The single peak (centred at 60 °C) unique to the catalyst with 1% V therefore relates to the release of hydrogen in the decomposition of palladium hydride. Palladium reduction peaks, reported to occur at temperatures below ambient [27] were not observed as 25-650 °C was used for analysis.

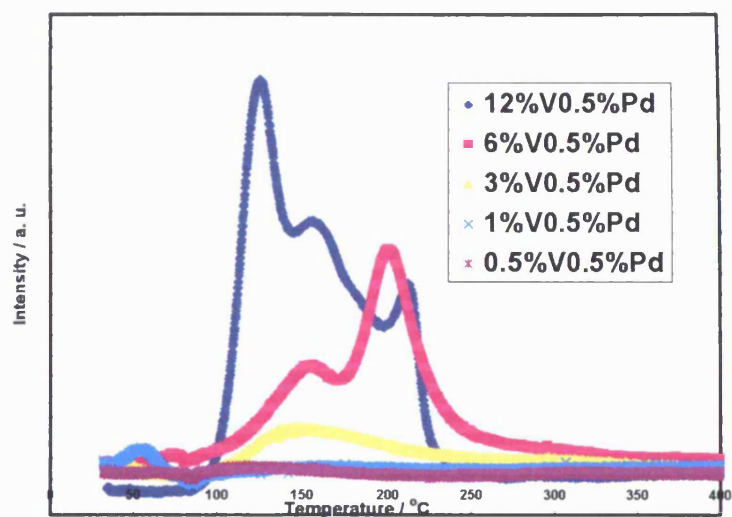


Fig. 3.3 (a) Hydrogen TPR profiles for Pd/V/ Al₂O₃ catalysts, 110 mg of sample, 20 mL min⁻¹ H₂, 5 °C min⁻¹.

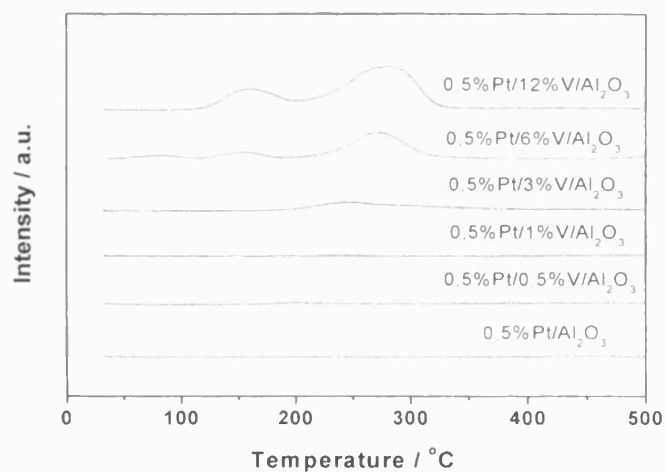


Figure 3.3 (b) Hydrogen temperature programmed reduction profiles for Pt/Al₂O₃ and Pt/V/Al₂O₃ catalysts, 110 mg of sample, 20 mL min⁻¹ H₂, 5 °C min⁻¹.

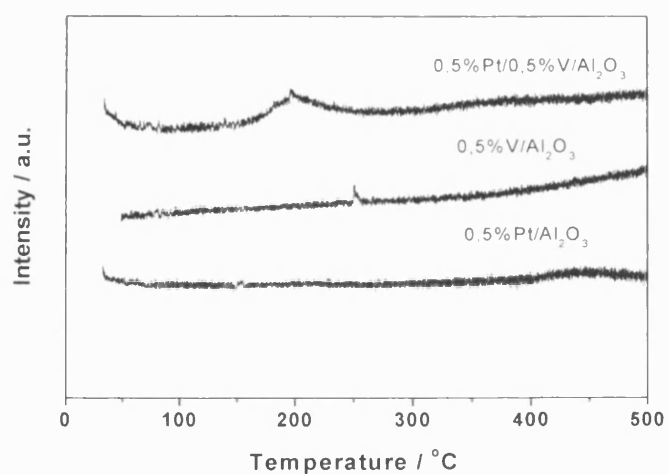


Figure 3.3 (c) Hydrogen temperature programmed reduction profiles for 0.5 %Pt/Al₂O₃, 0.5 % V/Al₂O₃, and 0.5 % Pt/0.5 %V/Al₂O₃, 110 mg of sample, 20 mL min⁻¹ H₂, 5 °C min⁻¹.

Figures 3.3 (b) and (c) show the evolution of TPR assays for Pt/V/Al₂O₃ catalysts as the vanadium content increased. TPR profiles for Pt/V/ γ -Al₂O₃ catalysts (figure 3.3b) show an increase in the intensity of reduction peaks with increasing vanadium loading. This suggests an increase in the concentration of reducible V-species as the V loading was increased. The absence of major reduction peaks common to both catalysts with and without vanadium suggests that all reduction peaks observed for V-containing catalysts correspond to the reduction of vanadium species. Catalysts with 6 and 12 %V both showed two well defined peaks at 150 and 250 °C (fig 3.3b) whereas the 3 %V catalyst only showed a single smaller peak (at 225 °C) which closely matched the most intense peaks for catalysts with 6 and 12 %V. The fact that XRD and Raman results for the catalyst with 12 %V mainly showed the presence of crystalline V₂O₅ suggests that V₂O₅ was the predominant vanadium species in this catalyst. As such, the TPR peak (between 200 - 300 °C) common to catalysts with 3 – 12 %V can be attributed to the reduction of V₂O₅. The assignment of the reduction peak at 150 °C is not clear. However, it probably corresponds to highly dispersed vanadium species [21, 28 – 31]. Close examination of the low loading 0.5 %V catalyst (fig 3.3c) showed the presence of a reduction peak at 175 °C which probably corresponds to either (isolated tetra coordinated vanadium species or polymeric vanadium species). From the size of this reduction peak, it is clear that the corresponding vanadium species was only present in low concentration.

3.7 Naphthalene oxidation activity over Vanadium-modified Pd-supported Alumina Catalysts

Figures 3.4 show the naphthalene conversion (a) and yield to CO₂ (b) obtained over Pd/V/Al₂O₃ catalysts.

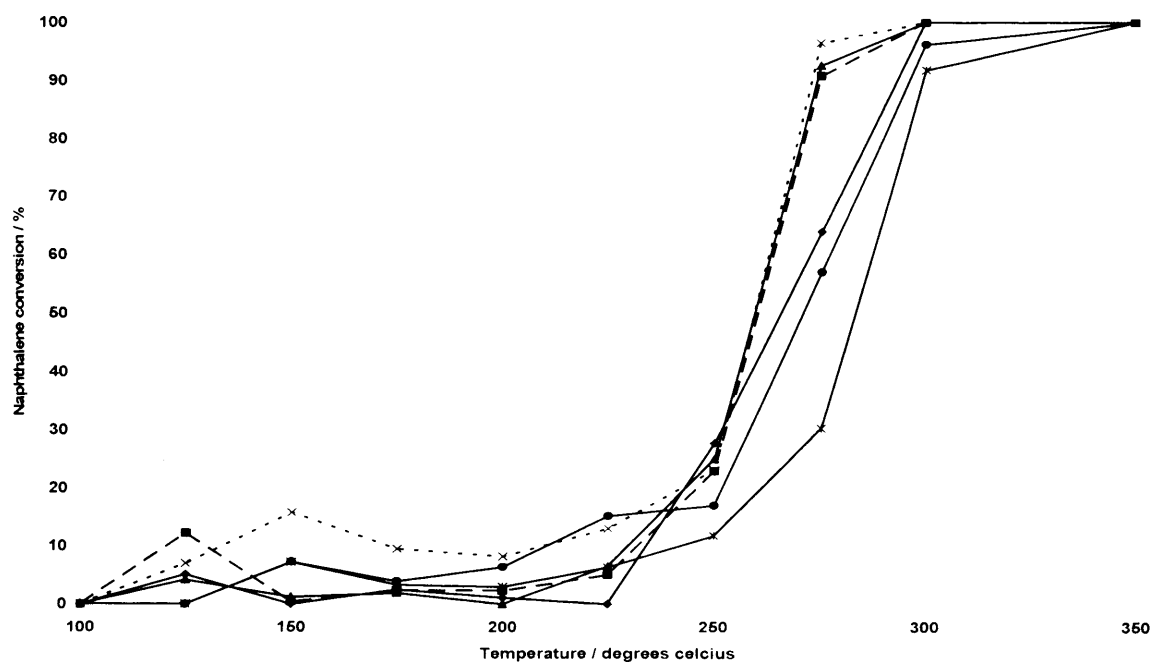


Fig. 3.4 (a) Activity of Pd/Al₂O₃ and Pd/V/Al₂O₃ catalysts in naphthalene oxidation.

—◆— 0.5 %Pd/Al₂O₃ —■— 0.5 %Pd/0.5 %V/Al₂O₃ —▲— 0.5 %Pd/1 %V/Al₂O₃
 - - x - - 0.5 %Pd/3 %V/Al₂O₃ —*— 0.5 %Pd/6 %V/Al₂O₃ —●— 0.5 %Pd/12 %V/Al₂O₃

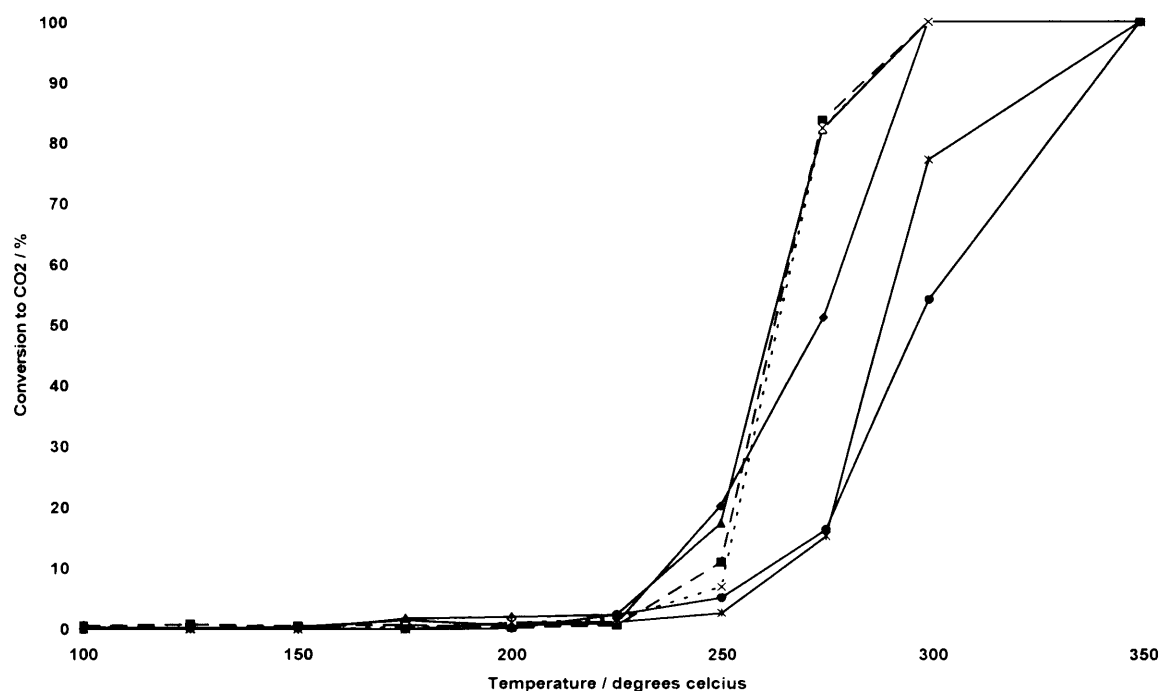


Fig. 3.4 (b) Selectivity of Pd/Al₂O₃ and Pd/V/Al₂O₃ catalysts in naphthalene oxidation

—◆— 0.5 %Pd/Al₂O₃ -■- 0.5 %Pd/0.5 %V/Al₂O₃ —▲— 0.5 %Pd/1 %V/Al₂O₃
 --x-- 0.5 %Pd/3 %V/Al₂O₃ —*— 0.5 %Pd/6 %V/Al₂O₃ —●— 0.5 %Pd/12 %V/Al₂O₃

The difference between the trends presented in figures 3.4 (a) and (b) is evidence for the mismatch between the quantity of naphthalene combusted and the amount of carbon dioxide produced over Pd/V catalysts. Notice that naphthalene conversion did not match the conversion to CO₂ at temperatures below 250 °C. This either suggests the production of naphthalene intermediates (or partial oxidation products) similar to those reported in the literature [32] or the non-equilibrium adsorption of naphthalene [33] at low temperatures (see chapter 1). Thus conversion to CO₂ and not naphthalene conversion should be used to measure naphthalene and PAH catalytic activity. For this reason,

naphthalene oxidation catalytic activity data is only reported in terms of conversion to carbon dioxide in later sections of this thesis.

Figure 3.4 (a) shows that addition of V to the Pd/Al₂O₃ catalyst enhanced the activity of the catalyst at low temperatures (< 225 °C). At higher temperatures, the Pd/Al₂O₃ catalyst proved more active than the Pd/V/Al₂O₃ catalysts with 6 % and 12 %V loading but was less active than those with V loading between 0.5 - 3 %. The high temperature (>250 °C) activity of the catalysts with V loading ranging between 0.5 - 3 % was very similar. 0.5 %Pd/3 %V/Al₂O₃ was most active while 0.5 %Pd/6 %V/Al₂O₃ had the lowest activity.

Figure 3.4 (b) shows that all the catalysts had very low yield to CO₂ at temperatures less than 225 °C. Between 225 - 250 °C, the yield to CO₂ decreased in the order: 0.5 %Pd/Al₂O₃ > 0.5 %Pd/1 %V/Al₂O₃ > 0.5 %Pd/0.5 %V/Al₂O₃ > 0.5 %Pd/3 %V/Al₂O₃ > 0.5 %Pd/6 %V/Al₂O₃ > 0.5 %Pd/12 %V/Al₂O₃. At temperatures above 250 °C, the Pd/Al₂O₃ catalyst had a higher yield to CO₂ than catalysts with 6% and 12%V loading but yielded less CO₂ than catalysts with V loading in the range 0.5 - 3 %.

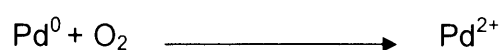
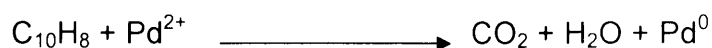
Catalysts with V loading between 0.5 - 3 % also had comparable yield to CO₂ over the temperature range investigated. The similarity in activity and selectivity of these catalysts could be due to their similarity in microstructure and nature of surface species as suggested by XRD, Raman and TPR results. While the similarity in the XRD patterns of these catalysts suggests that they had similar microstructures, the similarity observed

between their Raman and TPR spectra suggests that they had similar vanadium species in small concentrations. Hence the presence of a small concentration of a particular type of vanadium species might have been responsible for the enhanced activity of these catalysts. CO chemisorption suggested a decrease in Pd dispersion as the vanadium loading increased while XRD, Raman and TPR results showed that the addition of 6 – 12 %V to the Pd/Al₂O₃ catalysts was accompanied by the formation of crystalline V₂O₅ on the surface of the support. The redox chemistry of high concentrations of these vanadium species coupled with the drop in Pd dispersion might have been responsible for the lower activity demonstrated by these catalysts. Although it might be argued that catalyst pretreatment prior to CO chemisorption might have change the active metal surface area and size of catalyst tested for PAH oxidation (as catalyst did not undergo similar treatment prior to testing), CO chemisorption results were used as qualitative evidence for the variation of active metal dispersion with addition of varying V loading. The effect of decrease in Pd dispersion with increase in vanadium loading on naphthalene oxidation activity is not very consistent with the effect reported for benzene oxidation [8], in which the decrease in Pd dispersion with increase in vanadium oxide content resulted to an increase in catalytic performance. In this study, no significant difference in Np oxidation activity was observed as the V loading increased (Pd dispersion decreased) from 0.5 – 3%. Higher V loadings (6 and 12%) yielded catalysts with lower Pd dispersion and lower Np oxidation activity. The fact that the change in Pd dispersion with increase in V content in this study does not correlate with results obtained for benzene oxidation [8] therefore confirms previous research findings suggesting that catalytic activity in alkane and mono-aromatic compound oxidation cannot directly be extrapolated to PAH

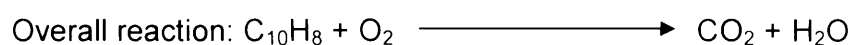
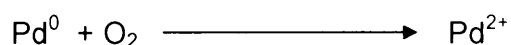
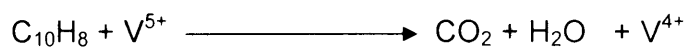
oxidation [17]. Although the change in Pd dispersion upon addition of V is likely to affect the Np oxidation efficiency, the enhanced catalytic performance in this study relies more on the presence of small concentrations of some kind of vanadium species (V^{4+} or V^{5+}).

From the trend in activity observed upon addition of vanadium, it is probable that the oxidation of naphthalene over Pd/V catalysts proceeded analogous to the Mars Van Krevelen scheme reported for benzene oxidation over Pd- V_2O_5/Al_2O_3 catalysts [34]. In the absence of vanadium, naphthalene is oxidised in the redox cycle involving transitions between Pd^{2+} and Pd^0 . The promotional effect observed for catalysts with low vanadium loadings (0.5 – 3%) may have been because such vanadium loadings facilitate the oxidation as it proceeds through a double cycle involving both transitions between V^{5+} and V^{4+} and the Pd species transitions (between Pd^{2+} and Pd^0). At higher V loadings (6 and 12 %) surface Pd^{2+} sites probably become covered by vanadium (evident in the drop in Pd dispersion with increasing V loading) and the oxidation is performed to a greater extent through a single cycle involving less active vanadium species (i.e. V^{5+} and V^{4+}). This explains the lower activity observed for catalysts with 6 and 12 %V relative to catalysts with 0.5 – 3 %V and the catalyst without vanadium. The Mars-Van Krevelen scheme for naphthalene oxidation is summarised in the following reactions:

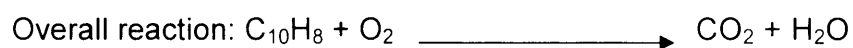
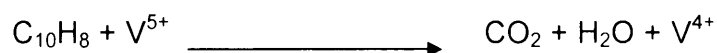
a) Catalyst without vanadium.



b) Low loadings of V



C) High loadings of V



3.8 Naphthalene oxidation activity over Vanadium-modified Pt-supported Alumina Catalysts

The addition of 0.5 %V to the Pt/ γ - Al_2O_3 catalyst promoted the activity for naphthalene total oxidation, whilst, the addition of 1 - 12 %V had a negative effect, suppressing activity (Figure 3.5).

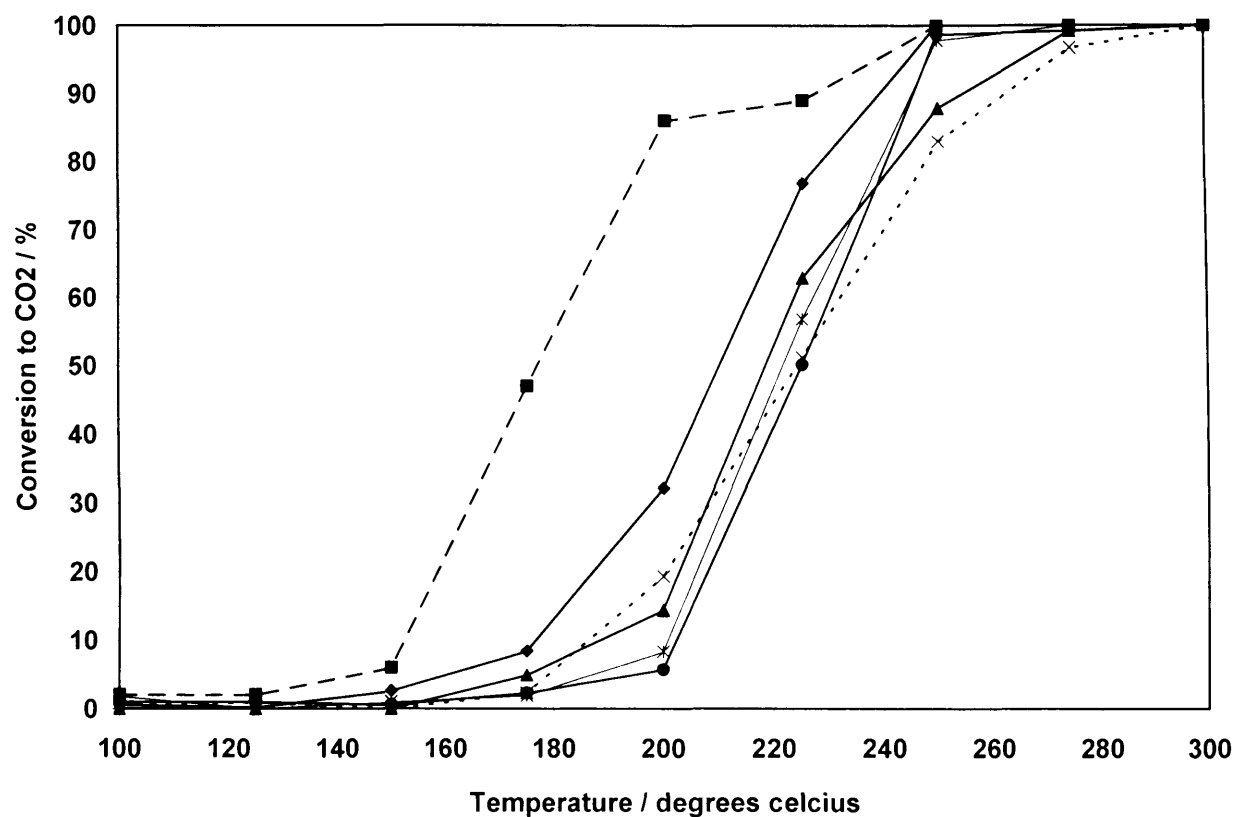


Fig. 3.5 Activity of Pt/Al₂O₃ and Pt/V/Al₂O₃ catalysts for naphthalene oxidation:

—●— 0.5 %Pt/Al₂O₃ -■- 0.5 %Pt/0.5 %V/Al₂O₃ —▲— 0.5 %Pt/1 %V/Al₂O₃ --x-- 0.5 %Pt/3 %V/Al₂O₃ —*— 0.5 %Pt/6 %V/Al₂O₃ —●— 0.5 %Pt/12 %V/Al₂O₃

Catalysts containing 1 - 12 % V showed light-off temperature (LOT) of 200 °C and temperature of complete Np combustion (T100) of 250 – 275 °C, whereas, the 0.5 %V catalyst showed a relatively lower LOT (175 °C) and T100 (225 °C). It is postulated that the enhanced activity of 0.5%Pt/0.5%V/ γ -Al₂O₃ compared to the Pt/ γ -Al₂O₃ and other Pt/V/ γ -Al₂O₃ catalysts resulted from two factors. Firstly, the most active catalyst showed a unique vanadium species that was identified by TPR. Secondly, the Pt dispersion

appeared to have a crucial influence on the catalyst activity. The most active 0.5%Pt/0.5%V/ γ -Al₂O₃ catalyst had the highest Pt dispersion amongst all catalysts under investigation. The relationship between the number of Pt surface sites exposed and naphthalene oxidation rate is not a simple one. Although the 1-6 % V catalysts had higher Pt dispersion than the catalyst without V they clearly were less active than the Pt/ γ -Al₂O₃ catalyst. It is evident that the nature of the vanadium species that was present with the Pt particles exerts a major influence over the catalytic activity. Consequently the increased oxidation rate of naphthalene over the catalyst with 0.5 % V was due to a combination of the dispersed Pt with the relatively facile reducible vanadium species unique to the catalyst. This combination may promote activity by aiding the activation of oxygen and/or the adsorption of naphthalene. Furthermore, it appears that the presence of relatively large V₂O₅ crystallites was detrimental to naphthalene oxidation: therefore, in order to promote activity the form of the vanadium is critical.

Figure 3.6 and table 3.4 show that Pt/V catalysts were generally more active than Pd/V catalysts. Although XRD, Raman and TPR results suggest that both Pd/V and Pt/V catalysts had similar vanadium species, the activity results show a mark disparity in the effect of vanadium loading on the activity of Pd/V catalysts compared to Pt/V catalysts. While 0.5 – 3 %V promoted the activity of the Pd catalyst, only 0.5 %V enhanced the activity of the Pt catalysts. Higher V loadings (1 - 12 %) did not yield a similar influence on the activity of both sets of catalysts. It is likely therefore that the mechanism of oxidation over Pt/V catalysts is different from the Mars-Van Krevelen scheme suggested for oxidation over Pd/V catalysts. There is evidence in the literature [35, 36] that the

oxidation of naphthalene over Pt catalysts occurs either via the Langmuir-Hinshelwood scheme [35] or follows the Eley-Rideal mechanism [36]. It is therefore likely that naphthalene oxidation over Pt/V catalysts occurred via one of these mechanisms or a combination of both.

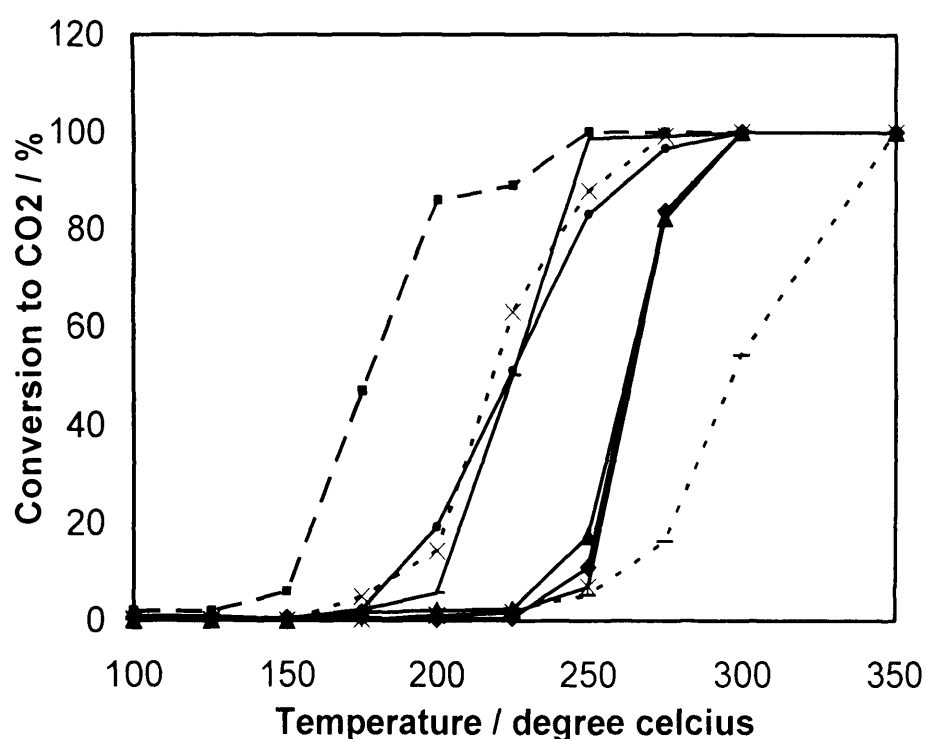


Fig. 3.6 Activity of Pd/V catalysts compared with activity of Pt/V catalysts with same metal loading —◆— 0.5 %Pd/0.5%V/Al₂O₃ —■— 0.5 %Pt/0.5 %V/Al₂O₃ —▲— 0.5 %Pd/1 %V/Al₂O₃ —×— 0.5 %Pt/1 %V/Al₂O₃ —*— 0.5 %Pd/3 %V/Al₂O₃ —●— 0.5 %Pt/3 %V/Al₂O₃ —|— 0.5 %Pd/12 %V/Al₂O₃ ——— 0.5 %Pt/12 %V/Al₂O₃

Chapter 3 Naphthalene oxidation over vanadium modified Pd and Pt-alumina catalysts

Table 3.4 Light off temperature and complete naphthalene combustion temperature for each catalyst investigated

Catalysts	Light-off temperature / °C (LOT)	Temperature of complete C ₁₀ H ₈ combustion (T100) / °C
0.5%Pd/Al ₂ O ₃	250	300
0.5%Pd/0.5%V/Al ₂ O ₃	250	300
0.5%Pd/1%V/Al ₂ O ₃	250	300
0.5%Pd/3%V/Al ₂ O ₃	250	300
0.5%Pd/6%V/Al ₂ O ₃	275	350
0.5%Pd/12%V/Al ₂ O ₃	275	350
0.5%Pt/Al ₂ O ₃	200	250
0.5%Pt/0.5%V/Al ₂ O ₃	175	225
0.5%Pt/1%V/Al ₂ O ₃	200	250
0.5%Pt/3%V/Al ₂ O ₃	200	275
0.5%Pt/6%V/Al ₂ O ₃	200	250
0.5%Pt/12%V/Al ₂ O ₃	200	250

Figure 3.6 and table 3.4 show that 0.5%Pt/0.5%V/Al₂O₃ was the best catalyst investigated in this study. The activity of this catalyst is compared with some of the best catalysts reported for naphthalene oxidation (table 3.5).

Table 3.5 Activity data for catalysts reported for naphthalene oxidation

Catalyst	T10 / °C	T50 / °C	T90 / °C	GHSV / h ⁻¹	Reference
0.5%Pt/0.5%V/Al ₂ O ₃	160	178	225	45,000	This work
CeO ₂ (urea) ^a	110	160	190	25,000	[41]
Pt/Al ₂ O ₃ ^a	135	170	210	25,000	[41]
Pt/Al ₂ O ₃ ^b	169	185	202	25,000	[36]
Pt/Al ₂ O ₃ ^c	194	-	203	20,000	[35]
Pd/Al ₂ O ₃ ^c	197	-	206	20,000	[35]
Pt/Al ₂ O ₃ ^d	194	204	310	20,000	[37]
Cu/Mn/V/Al ₂ O ₃ ^d	180	207	-	20,000	[37]
2.0%Pd/HZSM-5 ^e	-	156	-	20,000	[38]
0.3%Pt/Silica fibre ^e	186	209	233	20,000	[39]
1.2%Pd-Zr-Yzeolite ^e	-	135	-	20,000	[40]
CuO-Pd/La-Al ₂ O ₃ ^f	-	270	-	23,000	[16]

^a100 vppm naphthalene, conversion based on CO₂ yield.

^b600 ppmv naphthalene, 20.95 vol. % O₂, conversion based on CO₂ yield.

^c100 ppmv naphthalene, 10 vol. % O₂, conversion based on CO₂ yield.

^d50 ppmv naphthalene, 200 ppmv CH₄, 2550 ppmv CO, 12 vol. % CO₂, 10 vol. % O₂, 0-20 vol. % H₂O, conversion in terms of naphthalene decomposition.

^e50 ppmv naphthalene, 200 ppmv CH₄, 2500 ppmv CO, 12 vol. % CO₂, 10 vol. % O₂, 12 vol. % H₂O, conversion in terms of naphthalene decomposition.

^f50 ppmv naphthalene, 200 ppmv CH₄, 2550 ppmv CO, 12 vol. % CO₂, 10 vol. % O₂, 13.5 vol. % H₂O, conversion in terms of naphthalene decomposition.

T10 – Temperature at which 10 % conversion or CO₂ yield is observed.

T50 – Temperature at which 50 % conversion or CO₂ yield is observed.

T90 – Temperature at which 90 % conversion or CO₂ yield is observed.

Taking in to consideration the fact that activity usually drops with increase in GHSV, coupled with the fact that conversion to carbon dioxide is a better measure for activity than Np conversion, table 3.5 suggests that the 0.5 %V-modified Pt-alumina catalyst in this study is one of the best catalysts researched for naphthalene oxidation. Only the recently reported ceria catalyst [41] appears to be more active than or as active as the latter.

3.9 Conclusions

It has been shown that the activity and selectivity of alumina-supported palladium and platinum catalysts in naphthalene oxidation are promoted by vanadium added during the impregnation step of catalyst preparation. The addition of vanadium modified the Pd and Pt dispersion on the support while the nature of vanadium species was altered as the vanadium loading increased. 0.5 – 3 %V loading enhanced the activity of the Pd/Al₂O₃ catalyst whereas 6 – 12 %V loading reduced its activity. Unlike the Pd-based catalysts, only 0.5 %V was required to optimise the activity of the Pt-alumina catalyst. All other vanadium loadings did not yield any significant positive effect. The promotional effect has been attributed to the presence of a low concentration of a particular type of vanadium species (for Pd-based catalysts) which fosters oxidation in a redox cycle and to the presence of more easily reducible vanadium species coupled with the enhanced number of platinum sites (for the Pt catalyst with 0.5 %V). On the other hand, the redox

Chapter 3 Naphthalene oxidation over vanadium modified Pd and Pt-alumina catalysts

chemistry of high concentrations of crystalline V_2O_5 has been suggested to account for the lower activity observed for Pd/V and Pt/V catalysts with vanadium loadings in the range 1 - 12 % for Pt/V catalysts and 6-12% for Pd/V catalysts. While the Mars-Van Krevelen redox mechanism is suggested for oxidation over Pd/V catalysts, oxidation over Pt/V catalysts is more complex and thought to proceed either via the Langmuir-Hinshelwood mechanism, Eley-Rideal mechanism or a combination of both. Pt/V catalysts were generally more active than Pd/V catalysts and 0.5 %Pt/0.5 %V/ Al_2O_3 demonstrated the best Naphthalene oxidation activity amongst all catalysts investigated.

References

1. A. Asier, L. Ruben, G.-Velasco, J. Ramon, G.-Ortiz, J. Ignacio, M. Angel, G.-Marcos, and J. Antonio, Abstracts of Papers, 222nd ACS National Meeting, San Diego, C. A., U. S. A., April 1-5, (2001), CATI-027.
2. M. Paulis, L. M. Gandia, A. Gil, J. Sambeth, J. A. Odriozola, and M. Montes, Appl. Catal., B: Environ. 26 (2000) 37.
3. E. M. Cordi, and J. L. Falconer, J. Catal. 162 (1996) 104.
4. O. Duclaux, T. Chafik, H. Hicham, J. L. Gass, and D. Bianchi, React. Kin. and Catal. Lett. 76 (2002) 19.
5. I. Mazzarino, and A. A. Barresi, Catal. Today 17 (1993) 335.
6. G. Bosko, T.-B. Ana, A. Zorana, and R. Nenad, Hemijska Industrija, 49 (1995) 322.
7. Z. Mingqian, Z. Bing, and C. Karl T., Appl. Catal. B: Environ. 13 (1997) 123.
8. R. S. G. Ferreira, P. G. P. de Oliveira, and F. B. Noronha, Appl. Catal. B: Environ. 50 (2004) 243.
9. H. Shaper, E. B. M. Doesburg, and L. L. Van Reijen, Appl. Catal., 7 (1983) 211.
10. C. Neyertz, and M. Volpe, Colloid Surf. A, 136 (1998) 63.
11. L. S. Escandon, S. Ordóñez, F. V. Diez, and H. Sastre, Catal. Today, 78 (2003) 191.
12. G. Groppi, C. Cristiani, L. Lietti, C. Ramella, M. Valentini, and P. Forzatti, Catal. Today, 50, (1999) 399.
13. M. Machida, K. Eguchi, and H. Arai, J. Catal., 103 (1987) 385.
14. P. Euzen, J. H. LeGal, B. Rebours, and G. Martin, Catal. Today, 47 (1999) 19.
15. C. B. Wang, H. K. Lin, and C. M. Ho, J. Mol. Catal. A: Chem., 180 (2002) 285.

Chapter 3 Naphthalene oxidation over vanadium modified Pd and Pt-alumina catalysts

16. M. Ferrandon and E. Bjornbom, *J. Catal.*, 200 (2001) 148.
17. T. Garcia, B. Solsona, D. Carzola-Amoros, A. Linares-Solano and S. H. Taylor, *Appl. Catal. B: Environ.*, 62 (2006) 66.
18. M. Vassileva, A. Andreev, S. Dancheva, and N. Kotsev, *Appl. Catal.*, 449 (1989) 125.
19. Varian Australia Pty Ltd., Flame Atomic Absorption Spectrometry, Analytical Methods, Publication No. 85-100009-00, Revised March 1989.
20. G. Busca, L. Marchetti, G. Centi, and F. Trifiro, *Langmuir*, 2 (1986) 568.
21. D. A. Bulushev, L. Kiwi-Minsker, F. Rainone, and A. Renken, *J. Catal.*, 115 (2002) 205.
22. C. B. Rodella, R. W. A. Franco, C. J. Magon, J. P. Donoso, L. A. O. Nunes, M. J. Saeki, M. A. Aegerter, V. Sargentelli, and A. O. Florentino, *J. Sol Gel. Sci. Technol.*, 83 (2002) 25.
23. I.E. Wachs, and B. M. Weckhuysen, *Appl. Catal.*, A, 157 (1997).
24. I. E. Wachs, *J. Catal.*, 124 (1990) 570.
25. T. Garcia, B. Solsona, D. M. Murphy, K. L. Antcliff, and S. H. Taylor, *J. Catal.*, 299 (2005) 1.
26. G. Chen, W. T. Chou, and C. T Yeh, *Appl. Catal.*, 8 (1983) 389.
27. G. Chen-Bin, L. Hung-Kuan, and H. Chi-Man, *J. Mol. Catal. A: Chem.* 180 (2002) 285.
28. H. Berndt, A. Martin, A. Bruckner, E. Schreier, D. Muller, H. Kosslick, G. V. Wolf, and B. Lucke, *J. Catal.*, 191 (2000) 284.

Chapter 3 Naphthalene oxidation over vanadium modified Pd and Pt-alumina catalysts

29. B. Solsona, T. Blasco, J. M. Lopez Nieto, M. L. Pena, F. Rey, A. and Vidal-Moya, J. Catal., 203 (2001) 443.
30. J. Santamaria-Gonzalez, J. Luque-Zambrana, J. Merida-Robles, P. Maireles-Torres, E. Rodriguez-Castellon, and A. Jimenez-Lopez, Catal Lett., 68 (2000) 67.
31. M. Baltes, K. Cassiers, P. Van der Voort, B. M. Weckhuysen, R. A. Schoonheydt, and E. F. Vansant, J. Catal., 197 (2001) 160.
32. X-W. Zhang, S-C. Shen, K. Hidajat, S. Kawi, L. E. Yu, and K. Y. Simon, Catal. Lett., 96 (2004) 87.
33. A. M. Mastral, T. Garcia, M. S. Callen, M. V. Navarro, and J. Galban, Environ. Sci. Technol., 35 (2001) 2395.
34. D. L. Ilieva, N. Kotsev and A. Andreev, Collection of Czechoslovak Chem. Comm., 59 (1994) 1922.
35. X-W. Zhang, S-C. Shen, L. E. Yu, S. Kawi, K. Hidajat, and K. Y. Simon, Appl. Catal. A: Gen. 250 (2003) 341.
36. Je-L. Shie, C-Y. Chang, J-H. Chen, W-T. Tsai, Y-H Chen, C-S. Chiou and C-F. Chang, Appl. Catal., B: Environ., 56 (2005) 289.
37. J. Carno, M. Berg and S. Jaras., Fuel, 75 (1996) 959.
38. A. K. Neyestanaki, L.-E. Lindfors, T. Ollonqvist, and J. Vayrynen, Appl. Catal. A: Gen., 196 (2000) 233.
39. A. K. Neyestanaki and L.-E. Lindfors, Fuel 77 (1998) 1727.
40. F. Klingstedt, A. K. Neyestanaki, L.-E. Lindfors, T. Salmi, T. Heikkila and E. Laine, Appl. Catal. A: Gen. 239 (2003) 229.
41. T. Garcia, B. Solsona, and S. H. Taylor, Catal. Lett., 105 (2005) 183.

CHAPTER 4: INFLUENCE OF SUPPORT ON THE PERFORMANCE OF PLATINUM-SUPPORTED CATALYSTS FOR THE TOTAL OXIDATION OF NAPHTHALENE

4.1 Introduction

Pt-supported catalysts [1, 2, 3 – see chapter 1] and vanadium-modified platinum-alumina catalysts [4 - see chapter 3] are so-far the best catalysts researched for the complete abatement of naphthalene. In all the above studies, γ -alumina has been used as support material. The extensive use of γ -Al₂O₃ as metal support can be attributed to its high specific surface area, considerable thermal stability and low cost of production. Various research groups [5-9] have demonstrated that other metal oxides (TiO₂, ZrO₂ and SnO₂) were better metal catalyst supports than γ -Al₂O₃ in the oxidation of hydrocarbons. In this chapter, the use of Pt catalyst supports other than γ -Al₂O₃ for the complete oxidation of naphthalene is investigated.

0.5%Pt catalysts supported on a variety of metal oxides (γ -Al₂O₃, SiO₂, SnO₂, TiO₂, and CeO₂) were prepared by impregnation and characterised by BET, XRD, Raman spectroscopy, CO chemisorption and XPS (see chapter 2 for details of preparation and characterisation). The catalysts were tested in the fixed-bed laboratory micro reactor described in chapter 2. Catalysts were packed to a constant volume and a total flow rate of 50 ml min⁻¹ was maintained to give a GHSV of 45, 000 h⁻¹. The characterisation and catalytic activity data obtained are discussed in the following sections.

4.2 Characterisation data for Pt Catalysts Supported on various Metal Oxides

The BET surface area data for supported-Pt catalysts (table 4.1) show that each catalyst had a surface area similar to that of its support material. Hence the support material was crucial in determining the surface area of each Pt catalyst. For some catalysts (Al_2O_3 , TiO_2 , and CeO_2) the surface area decreased or remained unchanged with the impregnation of Pt on the support whereas for others (SiO_2 and SnO_2), there was an increase in surface area with impregnation of Pt. The decrease in surface area corresponds to the filling of micro pores in the support material. The porosity and size of support particles relative to the size of Pt particles probably determined the surface area of each catalyst.

Table 4.1 BET surface area for all supports and Pt-supported catalysts

Support or Catalyst	BET Surface Area / m^2g^{-1}
Al_2O_3	103
0.5%Pt/ Al_2O_3	102
TiO_2	54
0.5%Pt/ TiO_2	44
SiO_2	403
0.5%Pt/ SiO_2	442
SnO_2	5
0.5%Pt/ SnO_2	12
CeO_2	11
0.5%Pt/ CeO_2	11

Chapter 4: Influence of support on the performance of Pt-supported catalysts for the total oxidation of Np

The surface area of the Pt-supported catalysts decreased in the order: $\text{Pt/SiO}_2 > \text{Pt/Al}_2\text{O}_3 > \text{Pt/TiO}_2 > \text{Pt/SnO}_2 > \text{Pt/CeO}_2$. The 0.5% Pt/SiO_2 catalyst showed a higher surface area (about 4 – 40 times higher) than all other Pt-supported catalysts while the 0.5% Pt/CeO_2 catalyst showed the lowest surface area.

XRD patterns for all supported-Pt catalysts are shown in figures 4.1 (a-e). Table 4.2 gives the crystalline phases identified and the crystallite sizes of the support materials and corresponding supported-Pt catalysts.

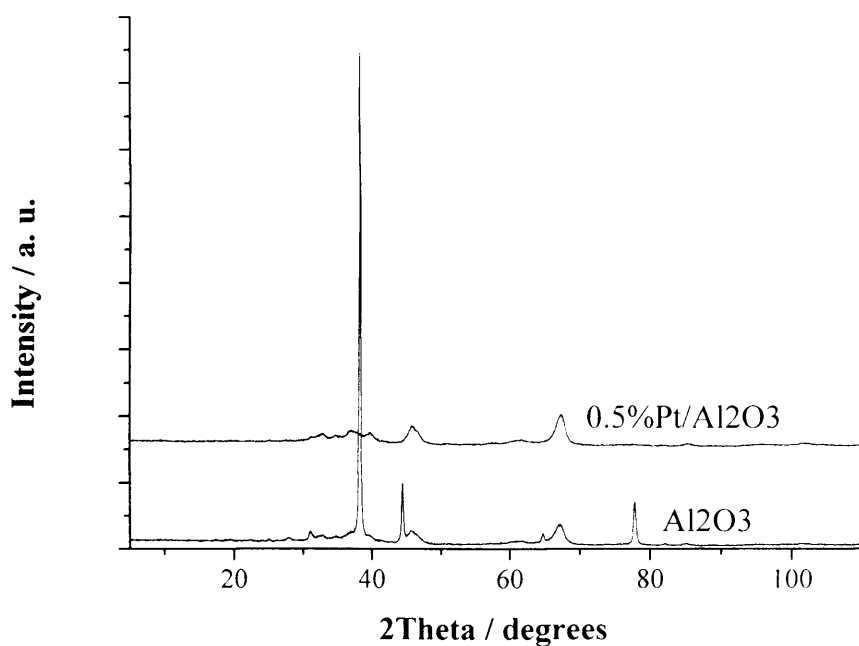


Fig. 4.1(a) XRD patterns for Al_2O_3 and 0.5% $\text{Pt/Al}_2\text{O}_3$

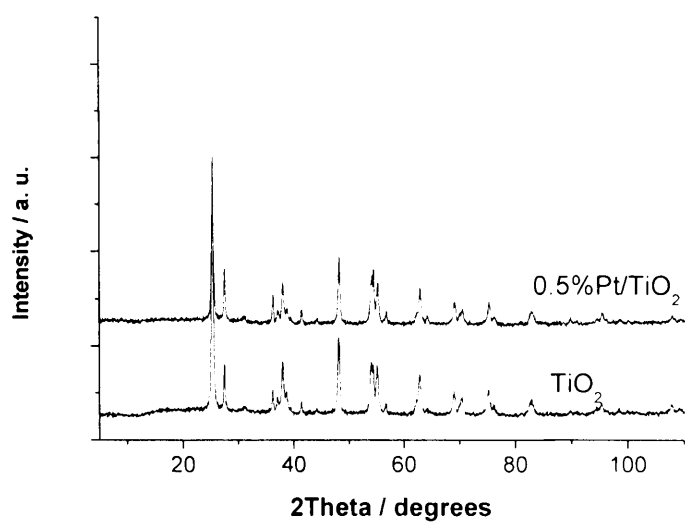


Fig. 4.1 (b) XRD patterns for TiO₂ and 0.5%Pt/TiO₂

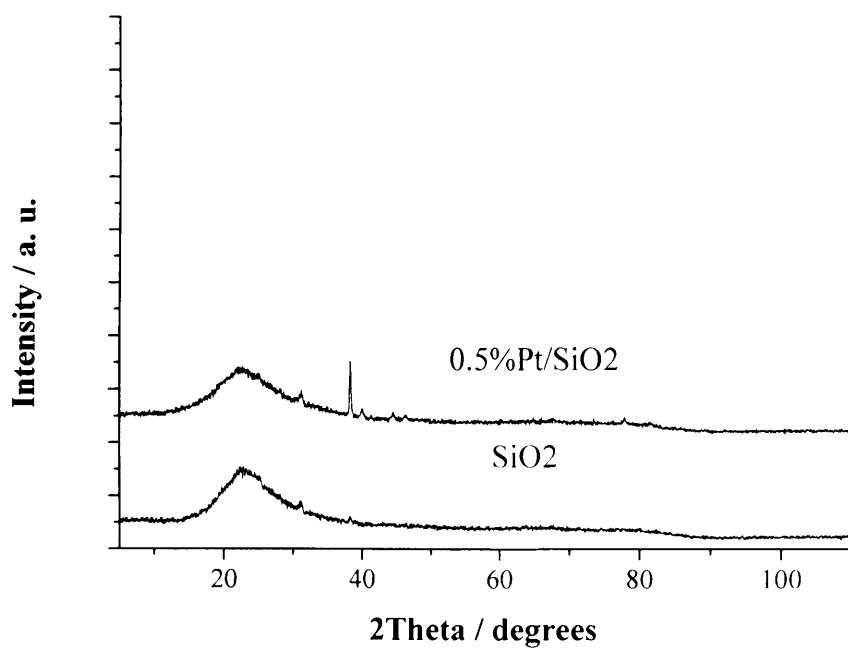


Fig. 4.1 (c) XRD patterns for SiO₂ and 0.5%Pt/SiO₂

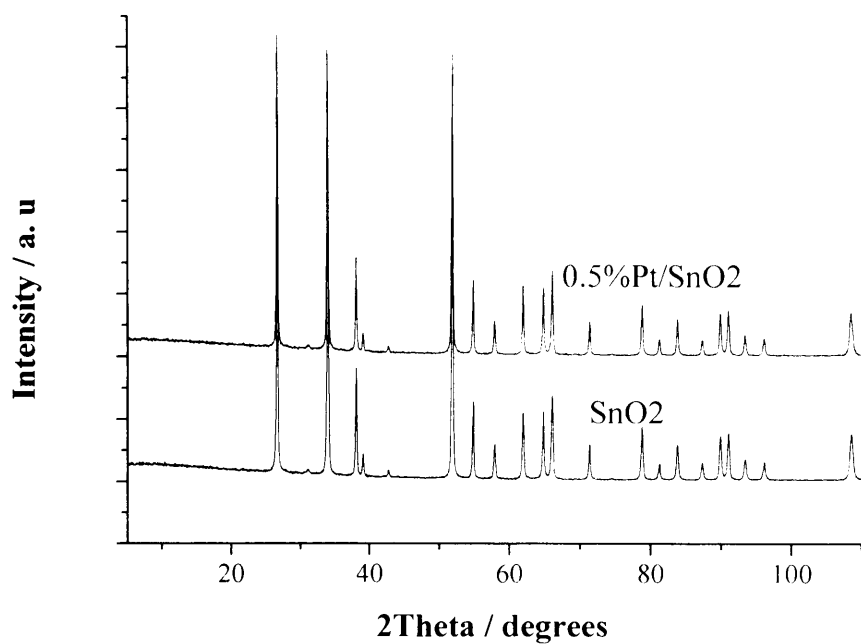


Fig. 4.1 (d) XRD patterns for SnO₂ and 0.5%Pt/SnO₂

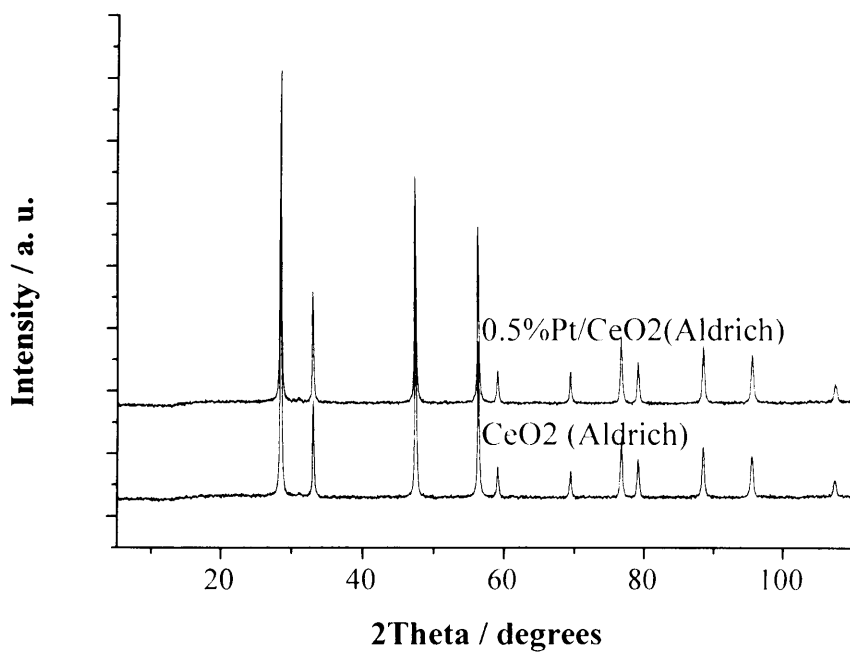


Fig. 4.1 (e) XRD patterns for CeO₂ and 0.5%Pt/CeO₂

Chapter 4: Influence of support on the performance of Pt-supported catalysts for the total oxidation of Np

Table 4.2 Identified crystal phase for all supports and Pt-supported catalysts

Support or Catalyst	Crystal Phase
Al_2O_3	γ - Al_2O_3 , defect cubic spinel
0.5%Pt/ Al_2O_3	γ Al_2O_3 , defect cubic spinel
TiO_2	TiO_2 (rutile and anatase) both tetragonal
0.5%Pt/ TiO_2	TiO_2 (rutile and anatase) both tetragonal
SiO_2	SiO_2
0.5%Pt/ SiO_2	SiO_2
SnO_2	SnO_2
0.5%Pt/ SnO_2	SnO_2
CeO_2	CeO_2 , cubic fluorite
0.5%Pt/ CeO_2	CeO_2 , cubic fluorite

The XRD patterns of all Pt-supported catalysts mainly showed the presence of the phase present in the support (figures 4.1 a-d and table 4.2). The absence of Pt species phase(s) can be attributed to the low Pt concentration or a high dispersion of the Pt species phase(s) on the surface of the support. While XRD patterns for Pt/ TiO_2 , Pt/ SnO_2 , and Pt/ CeO_2 (figures 4.1b, 4.1d, and 4.1e respectively) perfectly matched patterns of their respective supports, the patterns of Pt/ SiO_2 and Pt/ Al_2O_3 catalysts (figures 4.1c and 4.1a respectively), were slightly different from the patterns of their support materials. The Pt/ Al_2O_3 catalyst did not show the peak at 2θ value of 78° present in the pattern of the alumina support. The peak at 2θ value of ca. 45° in the pattern of the Pt/ Al_2O_3 catalyst

Chapter 4: Influence of support on the performance of Pt-supported catalysts for the total oxidation of Np

was equally not exact as that in the pattern of the alumina support. The Pt/SiO₂ catalyst showed a sharp XRD peak at $2\theta = 38^\circ$ which was not present in the pattern of its support. This peak probably corresponds to some sort of Pt species. XRD results thus show that the addition of Pt to TiO₂, SnO₂ and CeO₂ did not significantly modify the support whereas Pt impregnation to Al₂O₃ and SiO₂ modified the support.

Figure 4.2 (a-d) illustrates the Raman spectra recorded for Pt-supported catalysts. Raman spectra of SiO₂ and Pt/SiO₂ were not obtained due to strong fluorescence exhibited by silica. The Raman spectra obtained for the other four Pt-supported catalysts mainly confirmed the presence of the support material in accordance with XRD data. Raman bands observed in the spectra of Pt/Al₂O₃, Pt/TiO₂, Pt/SnO₂ and Pt/CeO₂ thus represented vibrations from bonds in Al₂O₃, TiO₂, SnO₂ and CeO₂ respectively. No Raman bands corresponding to Pt species were observed for the Pt/Al₂O₃, Pt/TiO₂, Pt/SnO₂ and Pt/CeO₂ catalysts and this was in agreement with XRD results. However, a shift (ca. 5 – 20 cm⁻¹ to the left) in the position of Raman bands was observed upon addition of Pt, indicating some interaction between Pt and the metal oxide support. This shift was larger for Pt/TiO₂ and Pt/CeO₂ (ca. 15-20 cm⁻¹) compared to Pt/Al₂O₃ and Pt/SnO₂ (ca. 5 cm⁻¹). The higher the shift in Raman frequencies of bands in the metal oxide, the stronger the interaction between the oxide and the support. Hence Pt interacted more strongly with CeO₂ and TiO₂ than with Al₂O₃ and SnO₂.

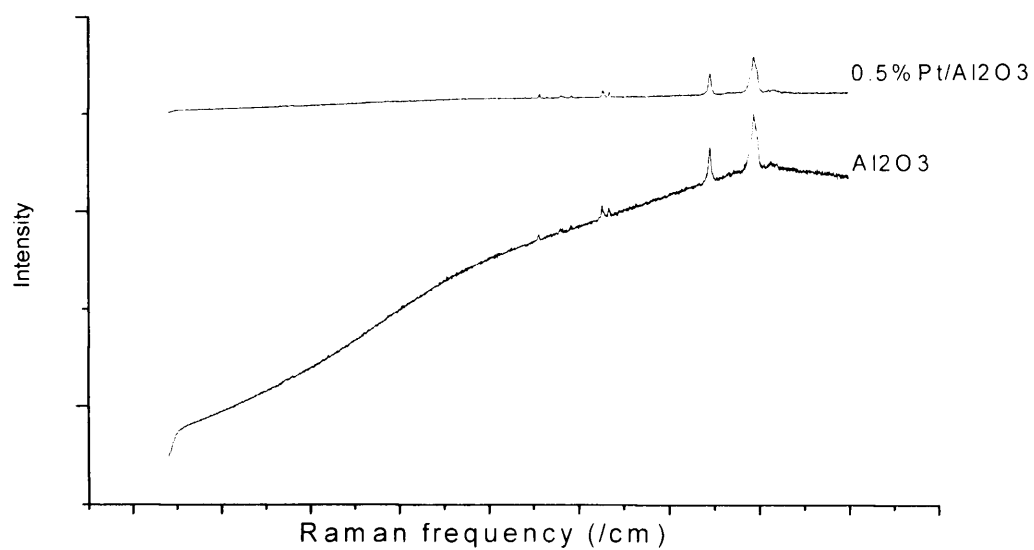


Fig 4.2 (a) Raman spectra of Al₂O₃ and 0.5%Pt/ Al₂O₃: Intensity (a.u.) and Raman frequency (cm⁻¹).

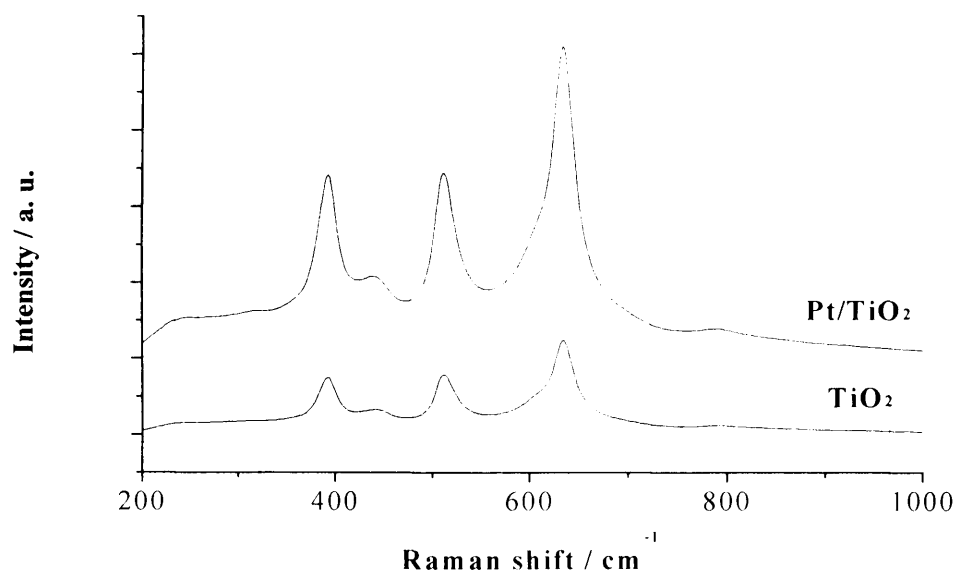


Fig 4.2 (b) Raman spectra of TiO₂ and 0.5%Pt/ TiO₂

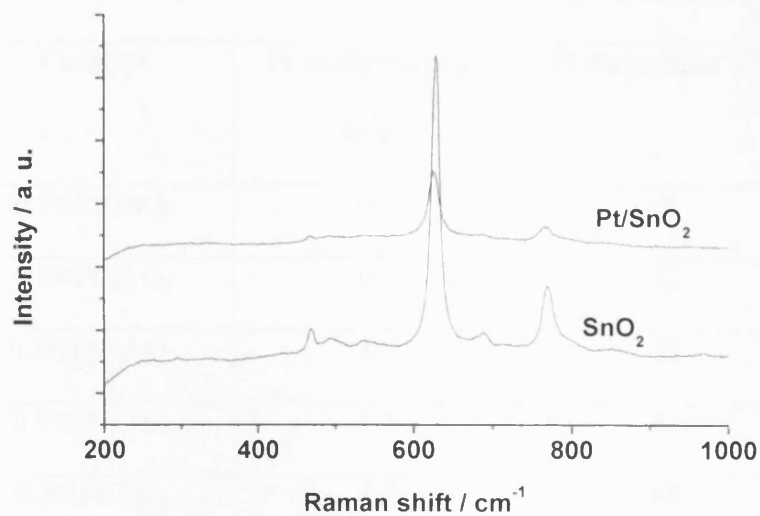


Fig 4.2 (c) Raman spectra of SnO₂ and 0.5%Pt/ SnO₂

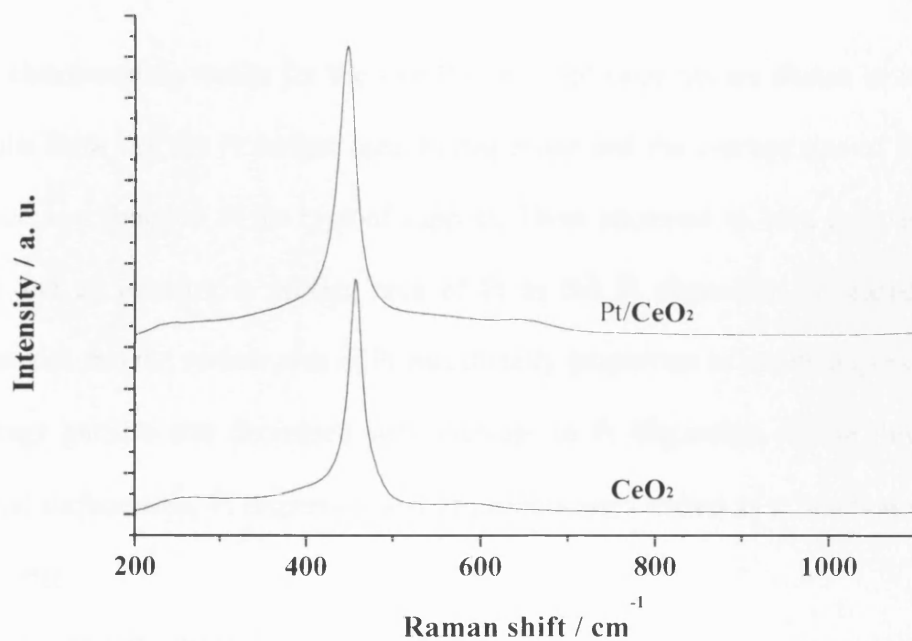


Fig 4.2 (d) Raman spectra of CeO₂ and 0.5%PtCeO₂

Chapter 4: Influence of support on the performance of Pt-supported catalysts for the total oxidation of Np

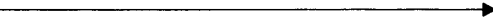
Table 4.3 Pt surface area, Pt dispersion, and Pt crystallite size of Pt-supported catalysts

Catalyst	Pt surface area ^a / m^2g^{-1}	Pt dispersion ^a / %	Average particle size of Pt ^a / Å
0.5%Pt/SnO ₂	0.1	3	189
0.5%Pt/Si O ₂	0.3	12	49
0.5%Pt/Al ₂ O ₃	1.3	52	10.9
0.5%Pt/CeO ₂	1.5	61	9.4
0.5%Pt/TiO ₂	1.7	68	8.3

^a By CO chemisorption analysis, 230 mg of catalyst, 40 °C.

CO chemisorption results for the five Pt-supported catalysts are shown in table 4.3. The results show that the Pt surface area, Pt dispersion and the average size of Pt particles all varied as a function of the type of support. There appeared to be a decrease in particle size and an increase in surface area of Pt as the Pt dispersion increased. Figure 4.3 illustrates that the surface area of Pt was directly proportion to the Pt dispersion while the average particle size decreased with increase in Pt dispersion. These three properties (metal surface area, Pt dispersion and Pt particle size) varied as a function of support in the order:

Pt/SnO₂, Pt/SiO₂, Pt/Al₂O₃, Pt/CeO₂, Pt/TiO₂

Increasing Pt surface area 

Increasing Pt dispersion

Decreasing Pt particle size

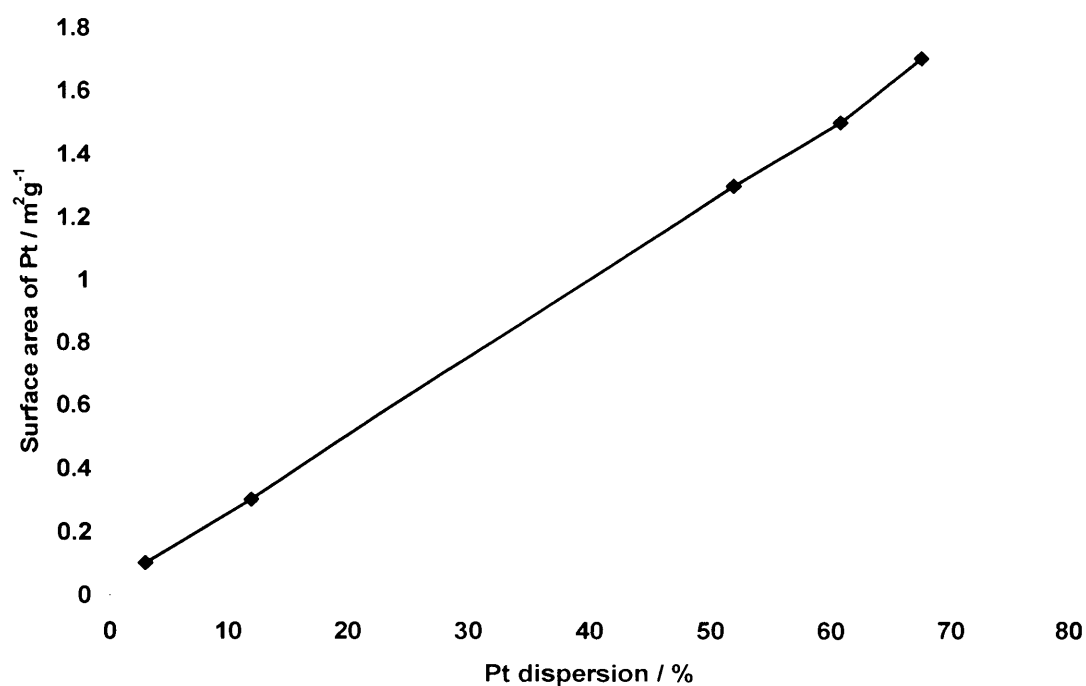


Fig 4.3 (a) Relationship between active metal (Pt) surface area and Pt dispersion

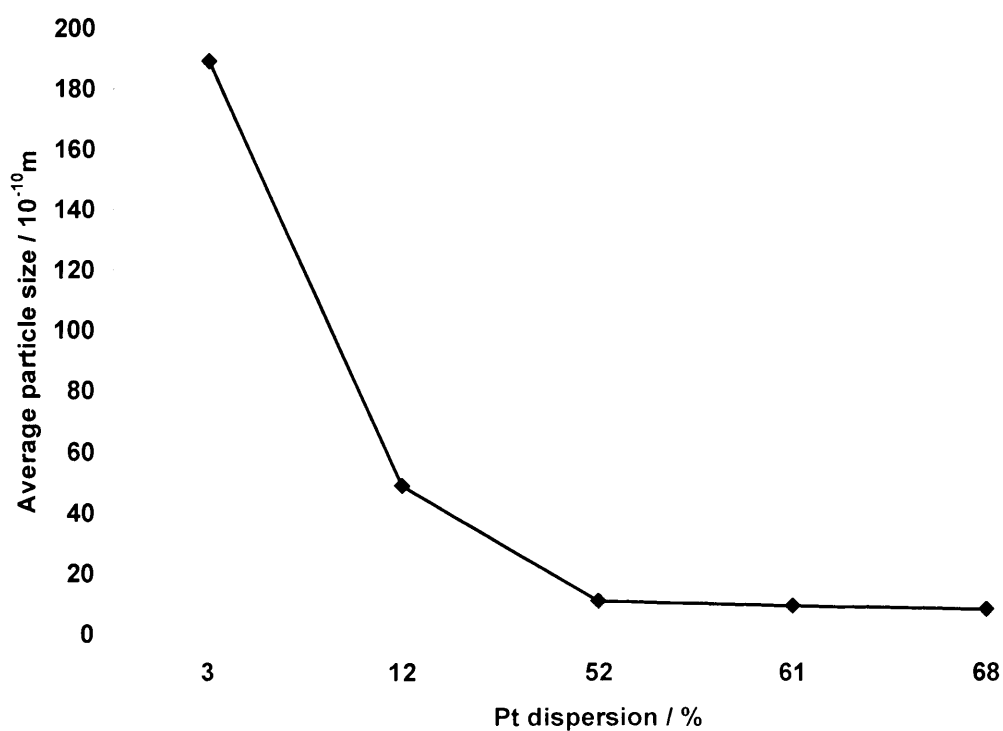


Fig 4.3 (b) Relationship between average particle size of Pt and Pt dispersion

4.3 Catalytic Activity Results for Pt Catalysts Supported on various Metal Oxides

Figure 4.4 shows the influence of support material on the performance of the five Pt-supported catalysts for Np oxidation.

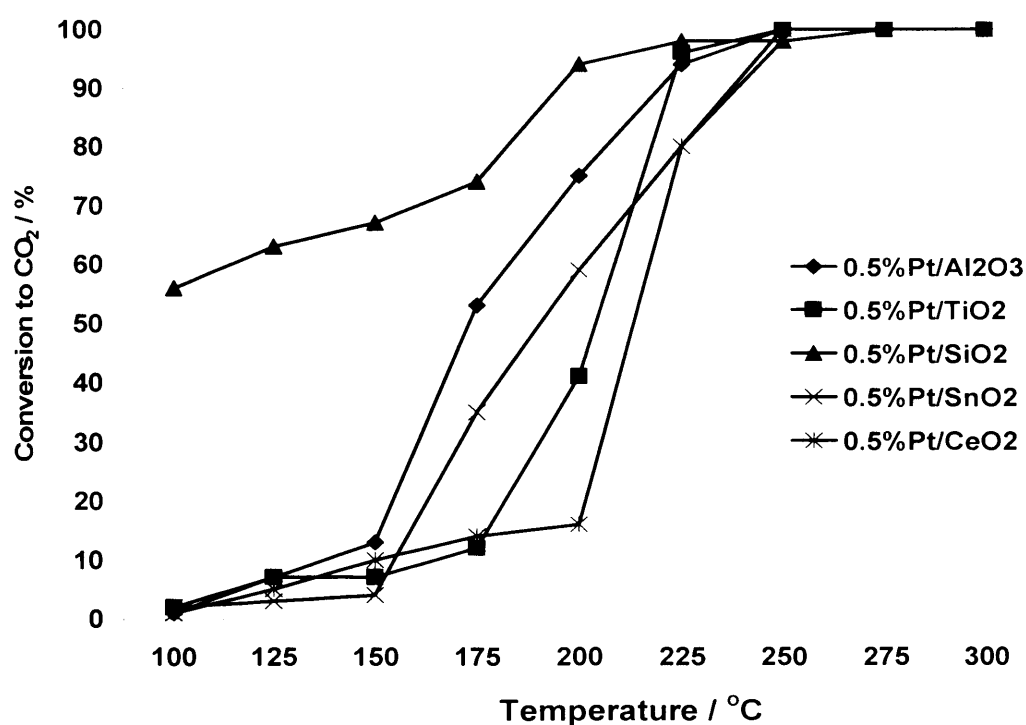


Fig. 4.4 Catalytic performance of Pt-supported catalysts in naphthalene total oxidation (100 vppm Np, GHSV = 45.000 h⁻¹).

It can be observed from the activity results (figure 4.4) that 0.5 %Pt/SiO₂ showed a considerably higher activity in Np oxidation than all other Pt-supported catalysts. This catalyst gave a CO₂ yield of over 50 % at 100 °C and over 90 % at 200 °C (100 vppm naphthalene, GHSV = 45,000 h⁻¹). The activity of all catalysts investigated in this work

Chapter 4: Influence of support on the performance of Pt-supported catalysts for the total oxidation of Np

decreased in the order: $\text{Pt/SiO}_2 > \text{Pt/Al}_2\text{O}_3 > \text{Pt/SnO}_2 > \text{Pt/TiO}_2 > \text{Pt/CeO}_2$. Notice that Pt-supported catalysts composed of redox supports (CeO_2 , SnO_2 and TiO_2) showed lower Np oxidation efficiency than Pt catalysts supported on non-redox supports (SiO_2 and Al_2O_3).

The catalytic performance of the best catalyst ($0.5\%\text{Pt/SiO}_2$) in this work was evaluated for naphthalene total oxidation in the temperature range of 100 – 300 °C in three consecutive cycles and as a function of time on stream for a period of 48 h (see figures 4.5a and 4.5b). The catalytic performance remained unchanged throughout the three cycles and the catalyst maintained its high (over 90 %) naphthalene conversion to CO_2 during the 48 h on stream at 225 °C. Since catalytic activity is expressed as yield to CO_2 and not Np conversion (figures 4.4 and 4.5), it can be concluded that the high activity of $0.5\%\text{Pt/SiO}_2$ at low temperatures (150 – 175 °C) is due to complete oxidation and not adsorption or partial oxidation. At lower temperatures (< 100 °C), Np tends to adsorb on the surface of the $0.5\%\text{Pt/SiO}_2$, yielding Np conversions higher than the CO_2 yield.

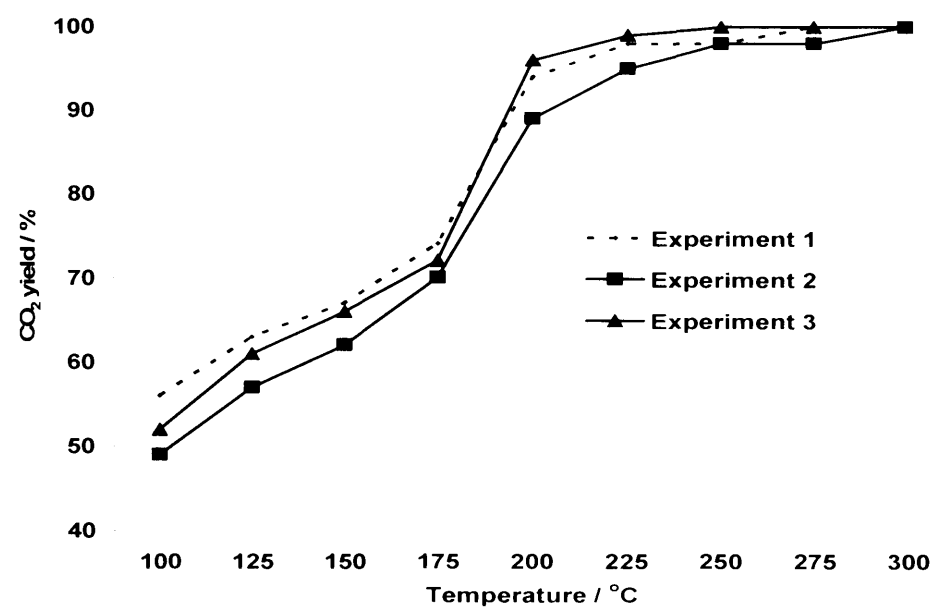


Fig. 4.5a Np oxidation activity of 0.5%Pt/SiO₂ obtained from three separate experiments

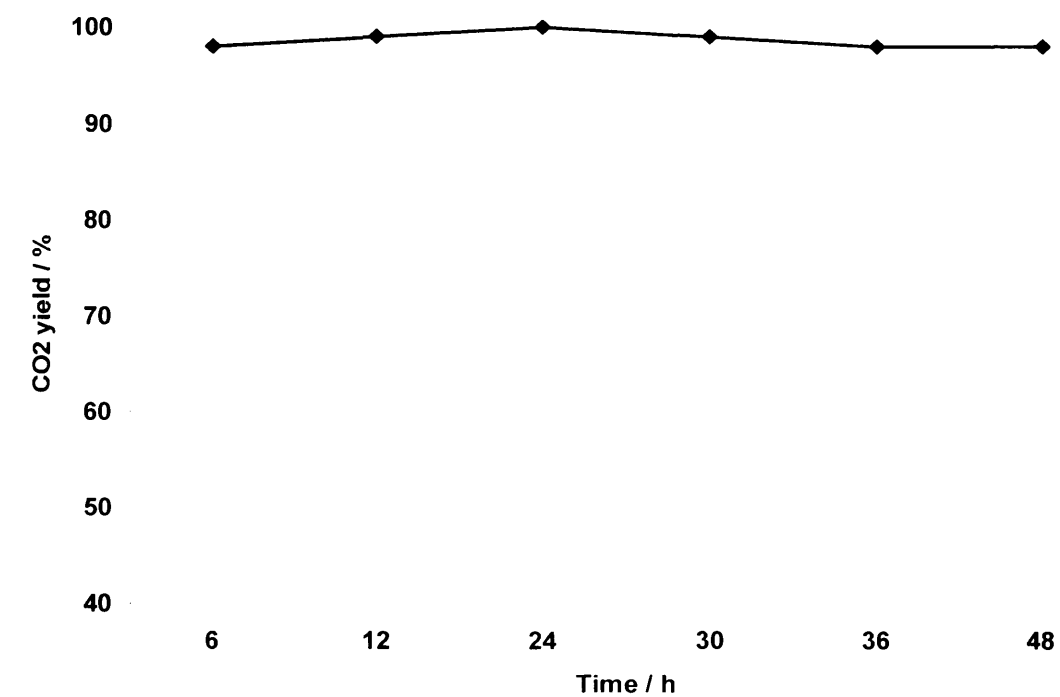


Fig. 4.5b Effect of reaction time on Np oxidation activity at 225 °C

Chapter 4: Influence of support on the performance of Pt-supported catalysts for the total oxidation of Np

Based on the differences observed in CO chemisorption data in this study and on the basis of the influence of support on catalytic activity of metal-supported catalysts reported in other studies [10 – 17], the variation observed between the performances of the five Pt-supported catalysts in Np oxidation can be related to three factors which all depend on the nature or type of the support. These include:

1. Pt dispersion (Pt particle size).
2. Interaction between metal (Pt) and the support.
3. Oxidation state of Pt.

The naphthalene oxidation activity of the Pt-supported catalysts decreased in an order almost analogous to the order established for Pt particle size, suggesting that the Pt particle size was crucial in determining the Np oxidation efficiency of the Pt-supported catalysts.

Np oxidation activity: $\text{Pt/SiO}_2 > \text{Pt/Al}_2\text{O}_3 > \text{Pt/SnO}_2 > \text{Pt/TiO}_2 > \text{Pt/CeO}_2$.

Pt particle size: $\text{Pt/SnO}_2 > \text{Pt/SiO}_2 > \text{Pt/Al}_2\text{O}_3 > \text{Pt/CeO}_2 > \text{Pt/TiO}_2$.

Larger Pt particles (lower Pt dispersion) appeared to favour naphthalene oxidation. The fact that 0.5%Pt/SnO₂ showed lower Np oxidation activity than Pt/SiO₂ and Pt/Al₂O₃ irrespective of the higher Pt particle size of this catalyst compared to the latter, suggests the influence of other factors. This also explains why 0.5%Pt/TiO₂ showed lower Np oxidation efficiency than 0.5%Pt/CeO₂ with higher Pt particle size. Figure 4.6 illustrates the change in Np oxidation activity at 175 °C (expressed as yield to CO₂) as a function of

Chapter 4: Influence of support on the performance of Pt-supported catalysts for the total oxidation of Np

Pt dispersion. The plot shows that the Np oxidation activity generally increased with a decrease in Pt dispersion. A decrease in Pt dispersion corresponds to an increase in Pt particle size (figure 4.3b). Hence, it can be concluded that larger Pt particles favoured naphthalene oxidation. This fact is further confirmed in figure 4.7.

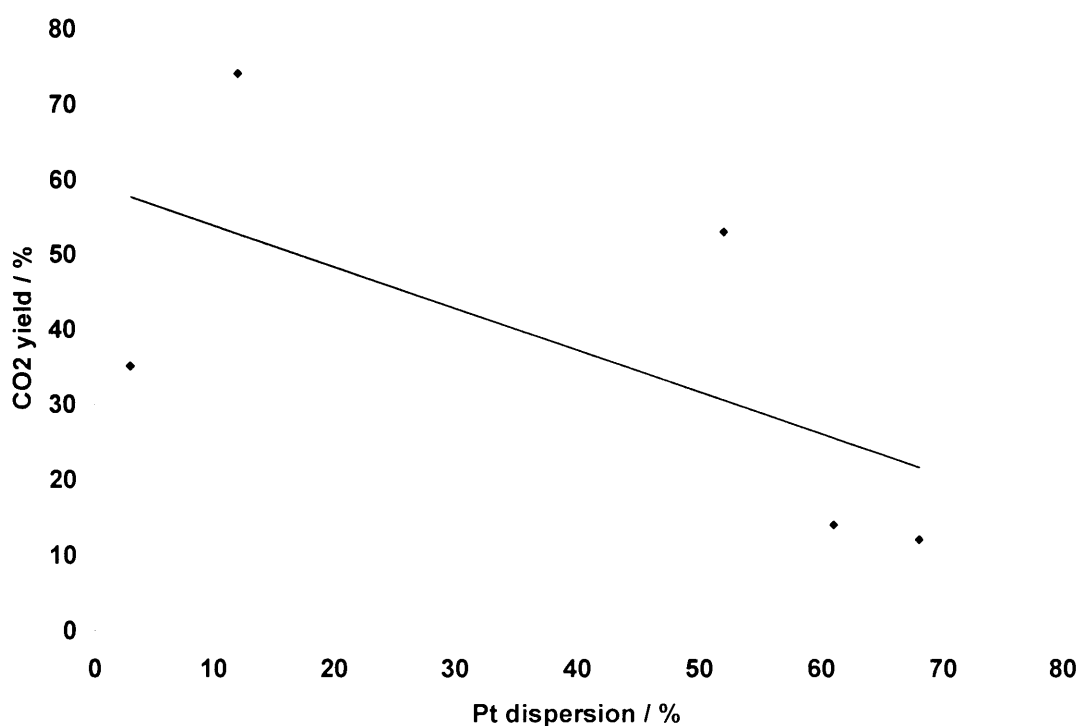


Fig 4.6 Effect of Pt dispersion on Np oxidation activity

Figure 4.7 shows that the turnover frequency (denoted by TOF, and defined as the amount of Np oxidised per Pt site per unit time) increased with increase in Pt particle size, thus confirming a strong dependence of Np oxidation on the size of Pt particles. However, the influence of other factors can not be undermined. The effect of other factors would explain why a catalyst with smaller Pt particles - higher Pt dispersion (12

Chapter 4: Influence of support on the performance of Pt-supported catalysts for the total oxidation of Np

%), gave a carbon dioxide yield (74 %) twice as much as a catalyst with relatively larger particles - lower Pt dispersion (3%), see figure 4.6.

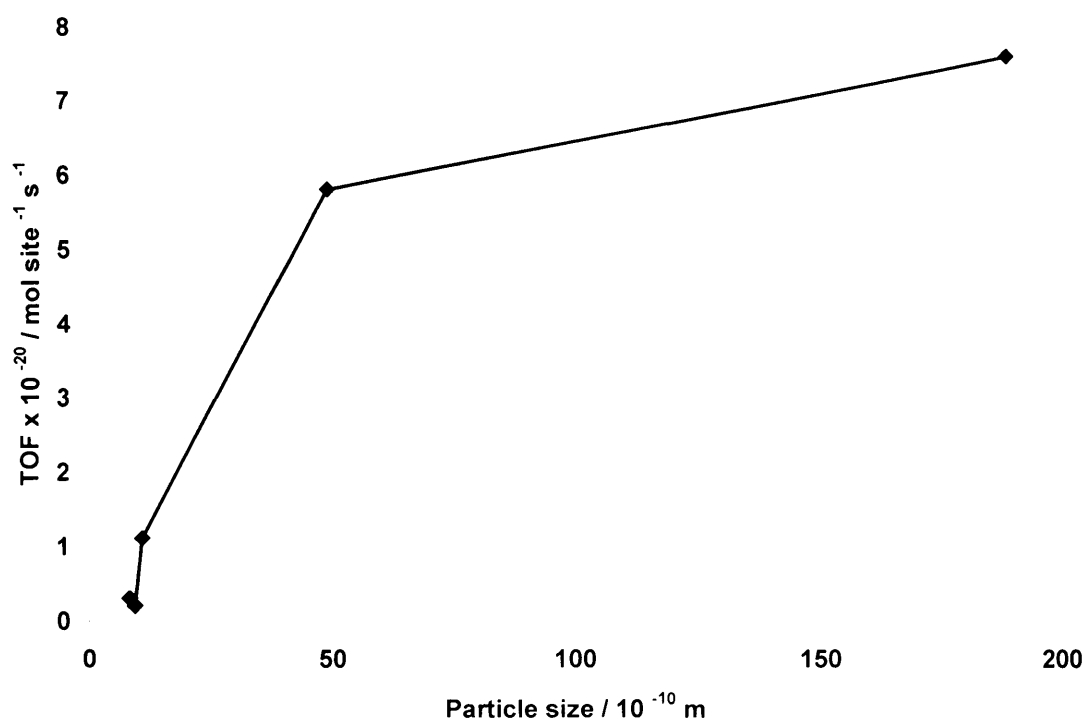


Fig. 4.7 Relationship between Np oxidation turnover frequency (TOF) and Pt particle size in Pt-supported catalysts

Strong metal-support interactions (SMSI) have been reported to account for the activity and selectivity of Ru-supported catalysts for a number of reactions involving CO and N₂ activation [10]. The nature of this metal support interaction was found to depend on the nature or type of support. Whilst CeO₂ is known to interact very strongly with Pt [11], SiO₂ has been found to only interact weakly with Pt [12]. Since SMSI is mainly associated with reducible supports [13-15], it can be concluded that whilst the CeO₂,

Chapter 4: Influence of support on the performance of Pt-supported catalysts for the total oxidation of Np

TiO₂ and SnO₂ supports in this study interacted strongly with the Pt metal, the SiO₂ and Al₂O₃ supports only interacted weakly with Pt. Based on the fact that the Pt/SiO₂ catalyst (with weak MSI) was the most active while Pt/CeO₂ (with SMSI) presented the lowest Np oxidation performance amongst all five catalysts investigated, it can be postulated that SMSI was detrimental to the performance of the Pt-supported catalysts in naphthalene oxidation. Hence, the strength of interaction between Pt and the support varied as a function of the nature of support and this resulted in differences in the Np oxidation performance of the Pt-supported catalysts reported in this study. Pt can interact with reducible supports by forming strong Pt-O-M bridges. For instance, it has been shown [11] that Pt interaction with CeO₂ results to the formation of Pt-O-Ce bond (i.e. MSI) which acts as an anchor and inhibits the sintering of Pt particles, thus favouring the dispersion of small Pt particles. In this same study [11], Pt was found to interact weakly with Al₂O₃, resulting to movement and sintering of Pt particles on the surface of the Al₂O₃ support. This is consistent with results obtained for Pt dispersion (Pt particle size) of Pt/CeO₂ compared to Pt/Al₂O₃ in this work (i.e. Larger Pt particles were obtained by using Al₂O₃ as oppose to CeO₂ support). Hence it can be concluded that MSI in the present work affected the size of Pt particles which was crucial for naphthalene oxidation. In addition to having an effect on the dispersion of Pt or size of Pt particles, SMSI could also affect the electronic nature of the support and/or Pt and the ease of oxygen mobility. Since the oxidation of Np over Pt-supported catalysts is known to occur by the Langmuir-Hinshelwood mechanism [1] or the Eley-Rideal mechanism [2], it is likely that SMSI was detrimental to the adsorption and/or diffusion of Np and/or O₂ on the surface of the catalyst.

In order to obtain information about the oxidation state of Pt, the Pt-supported catalysts were analysed using XPS. Figure 4.8 shows the Pt(4f) spectra obtained; also indicated on the figure are the expected binding energy values for Pt^0 , Pt^{2+} and Pt^{4+} species [16]. There was a wide variation in the intensity and position of component bands between the different catalysts (note that the $\text{Pt}/\text{Al}_2\text{O}_3$ spectrum was dominated by the $\text{Al}(2p)$ core-level peak), but only with Pt/SiO_2 was there any evidence for intensity at the binding energy corresponding to Pt^0 . This is highlighted in figure 4.9 where the Pt(4f) spectrum for Pt/CeO_2 has been subtracted from the spectrum for Pt/SiO_2 , in order to remove the Pt^{2+} component. The resulting spectrum consists of two doublets corresponding to Pt^0 and Pt^{4+} .

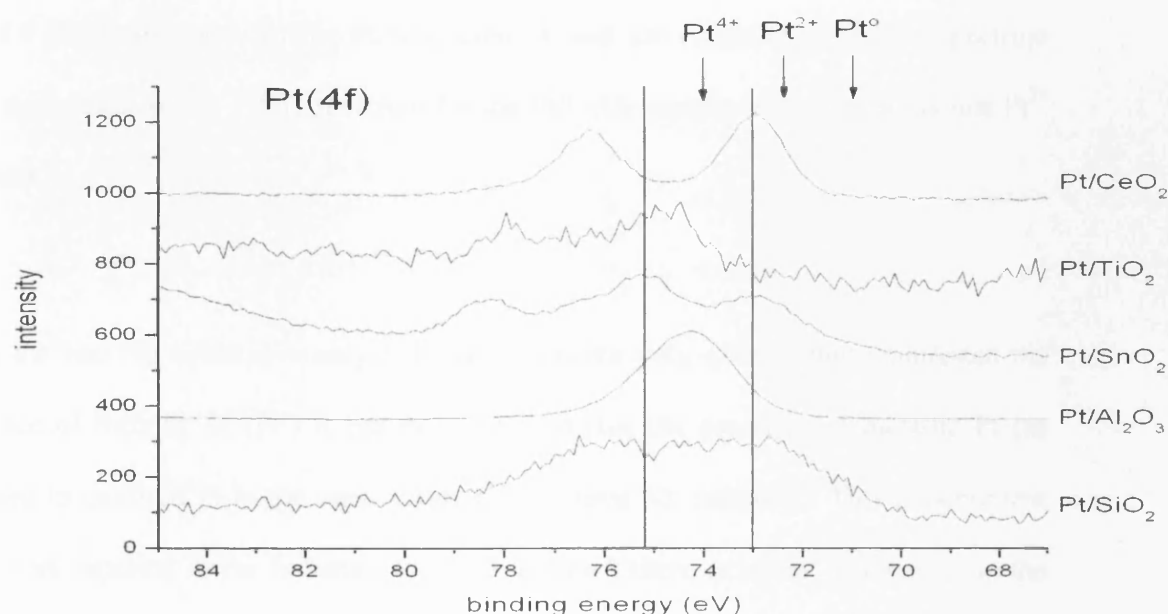


Fig. 4.8 Pt(4f) core-level photoelectron spectra for the different supported Pt catalysts, as indicated on the figure.

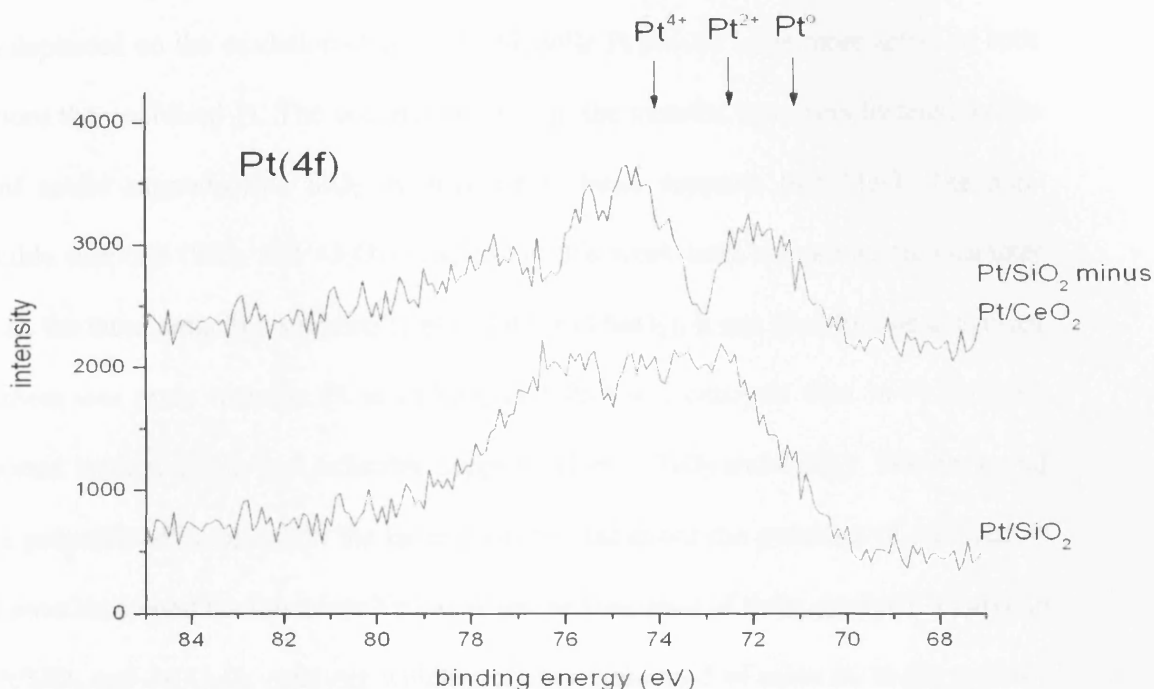


Fig. 4.9 Pt(4f) spectrum for the Pt/SiO₂ catalyst, and the resulting difference spectrum after subtraction of the Pt(4f) spectrum for the Pt/CeO₂ sample (which exhibits just Pt²⁺ species).

Since the best Np oxidation catalyst (Pt/SiO₂) was the only catalyst that manifested the presence of metallic Pt (Pt⁰) it can be concluded that the presence of metallic Pt (as opposed to oxidised Pt in the other catalysts) favoured Np oxidation. This is consistent with work reported in the literature [17, 18] in which there occurred differences in the oxidation state of Pt with the nature of support. Yazawa et al. [17] and Yoshida et al. [18] showed that the oxidation state of Pt in Pt-supported catalysts was strongly dependent on the nature of the support. Both groups of authors revealed that the activity of Pt-

Chapter 4: Influence of support on the performance of Pt-supported catalysts for the total oxidation of Np

supported catalysts (for propane combustion [17] and selective reduction of NO by H₂ [18]) depended on the oxidation state of Pt. Metallic Pt proved to be more active in both reactions than oxidised Pt. The occurrence of Pt in the metallic form was fostered by the use of acidic supports like SiO₂ as opposed to basic supports like MgO. The non-reducible supports (SiO₂ and Al₂O₃) reported in this work have a more acidic character than all the three reducible supports (CeO₂, TiO₂ and SnO₂). It can therefore be suggested that there was more metallic Pt in Pt/SiO₂ and Pt/Al₂O₃ catalysts than in Pt catalysts supported on less acidic and reducible supports (CeO₂, TiO₂ and SnO₂). The basic and redox properties of supports in the latter probably enhanced the presence of oxidised Pt and hence accounted for the lower Np oxidation performance of these catalysts relative to the Pt/SiO₂ and Pt/Al₂O₃ catalysts which probably composed of more Pt in the metallic state. The oxidised state of Pt in Pt/SnO₂, coupled with the SMSI probably accounted for the lower Np oxidation efficiency of this catalyst relative to Pt/SiO₂ and Pt/Al₂O₃ with lower Pt particle sizes (higher Pt dispersion) than the former. It can be assumed that the presence of metallic Pt fostered adsorption of reactants (Np and O₂) and/or their diffusion on the surface of the catalyst whereas oxidised Pt had a negative effect on adsorption and/or diffusion of reactants (Np and O₂) on the surface of the catalyst. This confirms the findings that Np oxidation over Pt-supported catalysts followed either the Langmuir-Hinshelwood mechanism [1] or the Eley-Rideal mechanism [2]. Since modification of the electronic nature (increasing defects) of the support or Pt via means of SMSI and the presence of oxidised Pt did not favour Np oxidation, it can be concluded that Np oxidation over the Pt-supported catalysts did not follow the redox process (Mars-Van Krevelen) reported in chapter 3 for Pd/V/Al₂O₃ catalysts.

4.4 Conclusions

Pt-supported catalysts prepared by impregnation of a variety of support materials (TiO_2 , SnO_2 , CeO_2 , Al_2O_3 and SiO_2) with equal loading of Pt (0.5 %) have been tested for the complete oxidation of naphthalene. The 0.5 %Pt/ SiO_2 catalyst showed considerably higher naphthalene oxidation efficiency than all other Pt-supported catalysts with equal Pt loading. This catalyst (0.5 % Pt/ SiO_2) gave a CO_2 yield of over 50 % at 100 °C and over 90 % at 200 °C. The differences in the performance of the Pt-supported catalysts have been related to differences in Pt dispersion (Pt particle size), SMSI (interaction between Pt metal and support) and oxidation state of Pt, which all depended on the nature of support employed. Large Pt particles (low Pt dispersion), weak interaction between Pt and support and the presence of Pt in the metallic state were found to favour the Np oxidation performance of the supported-Pt catalysts. The optimum combination of these properties was achieved in the use of SiO_2 as Pt support, hence making Pt/ SiO_2 the best naphthalene oxidation catalyst in this study.

Chapter 4: Influence of support on the performance of Pt-supported catalysts for the total oxidation of Np

References

1. X-W. Zhang, S-C. Shen, L. E. Yu, S.Kawi, K. Hidajat, and K. Y. Simon, Appl. Catal. A: Gen. 250 (2003) 341.
2. Je-L. Shie, C-Y. Chang, J-H. Chen, Wen-Tien Tsai, Yi-Hung Chen, C-S. Chiou and C-F. Chang, Appl. Catal., B: Environ. 56 (2005) 289.
3. J. Carno, M. Berg and S. Jaras., Fuel, 75 (1996) 959.
4. E. Ntainjua N., T. Garcia, and S. H. Taylor, Catal. Lett. 110 (2006) 125.
5. H. Bosch, and F. Janssen, Catal. Today, 2 (1988) 369.
6. R. Spinicci, and A. Tofanari, Appl. Catal. A, 227 (2002) 159.
7. C. A. Müller, M. Maciejewsky, R. A. Koepfel. and A. Baiker. Catal. Today, 47 (1999) 245.
8. K. Sekizawa, H. Widjaja, S. Maeda, Y. Ozawa, and K. Eguchi, Catal. Today, 59 (2000) 69.
9. M. S. Waiwright, and N. R. Foster, Catal. Rev., 19 (1979) 211.
10. A. Bossi, F. Garbassi, and G. Petrini, J. Chem. Soc., Faraday Trans. 1, 78 (1982) 1029.
11. Y. Nagai, T. Hirabayashi, K. Domae, N. Takagi, T. Minami, H. Shinjoh and S. Matsumoto, J. Catal. 242(2006) 103.
12. R. Burch, P. Fornasiero and B. W. L. Southward, Chem. Commun. (1998) 625.
13. S. J. Tauster, S.C. Fung, and R. L. Garten, J. Am. Chem. Soc. 100 (1978) 170.
14. S. J. Tauster, Acc. Chem. Res. 20 (11) (1987) 389.
15. G. L. Haller, and D. E. Resasco, Adv. Catal. 36 (1989) 173.

Chapter 4: Influence of support on the performance of Pt-supported catalysts for the total oxidation of Np

16. <http://www.lasurface.com/database/elementxps.php>
17. Y. Yazawa, N. Takagi, H. Yoshida, S. Komai, A. Satsuma, T. Tanaka, S. Yoshida and T. Hattori, Appl. Catal., A, 233 (2002) 103.
18. H. Yoshida, M. Hashimoto, J. Shibata, A. Satsuma and T. Hattori, Dep't of Appl. Chemistry, Graduate School of Engineering, Nagoya University, Photon Faraday Activity Report #20 Part B (2003).

CHAPTER 5: INFLUENCE OF PREPARATION CONDITIONS OF NANO- CRYSTALLINE CERIA CATALYSTS ON THE TOTAL OXIDATION OF NAPHTHALENE

5.1 Introduction

Ceria is a material known to have versatile properties as a catalyst [1] and is certainly the most significant member of the oxides of rare earth elements in industrial catalysis [2]. Ceria has potential for application in the removal of soot from diesel engine exhaust [3], catalytic waste oxidation for the removal of organics from waste waters [4], and as a component of combustion catalyst [5]. The ability of ceria to enhance the removal of CO, hydrocarbons (HCs) and NO_x makes it an inevitable component of high-performance three-way catalysts (TWC) in automotive exhaust treatment. The importance of CeO₂ in such TWC dwells mainly on its ability to act as an oxygen buffer, storing/releasing oxygen due to the Ce⁴⁺/Ce³⁺ redox couple [6-17]. In addition to acting as an oxygen reservoir in TWC, ceria gives stability to the alumina support and maintains a high surface area [18, 19]; it stabilizes the dispersed state of precious metals by preventing them from sintering [20, 21] and promotes CO oxidation [22-24] and water-gas shift reaction [25-27].

It is therefore clear that over the years, the excellent catalytic behaviour of ceria has attracted immense attention in industry. With the ever increasing quest for pollution control and environmental protection, various Physical Chemistry (Heterogeneous

Catalysis) and Chemical Engineering research laboratories [1-27] have concentrated much interest in developing ceria-based catalysts for VOC, CO and NO_x control.

Several synthetic methods have been used for the preparation of CeO₂ nanoparticles. These include hydrothermal [28, 29], redox reaction [30], sonochemical [31], pyrolysis [32], reverse micelles [33] and homogeneous precipitation methods [34-36]. The mild synthetic conditions and relatively simple procedure involved in homogeneous preparation gives it an advantage over the other synthetic techniques. T. Garcia et al. [37, 38] recently showed that a CeO₂ catalyst prepared by homogeneous precipitation with urea (CeO₂ (UR)) was more effective than all best Pt/Al₂O₃ and metal oxide catalysts reported for naphthalene oxidation. In this study, it is shown that naphthalene oxidation activity of a CeO₂ catalyst prepared in a similar manner as reported by T. Garcia et al. [37] can be optimized by varying preparation conditions (calcination temperature, calcination time, aging time and cerium salt to urea ratio). Ceria catalysts were synthesized (see chapter 2, section 2.2.2; table 2.2) and characterized by BET, XRD, TGA, Raman spectroscopy, SEM and TPR as earlier described in chapter 2. All catalysts were tested for naphthalene oxidation as described in chapter 2 (section 2.4). All conditions remained the same as earlier discussed.

In the following sections, the characterization and naphthalene oxidation activity results for nano-crystalline ceria catalysts prepared (under a variety of reaction conditions by homogeneous precipitation with urea) are discussed in-depth.

5.2 Effect of Calcination Temperature on Properties and Activity of CeO₂ (UR)

In this section, the influence of calcination temperature on the BET, XRD, Raman, SEM, TPR and naphthalene oxidation activity of CeO₂ (UR) is detailed.

5.2.1 Effect of Calcination Temperature on Surface Area of CeO₂ (UR)

The influence of the calcination temperature of CeO₂ (UR) has been studied on the oxidation of naphthalene. Thus the ceria precursor was treated at four different temperatures (300, 400, 500 and 600 °C). Table 5.1 shows the surface areas of CeO₂ catalysts calcined at different temperatures. The surface areas ranged between 85-120 m²g⁻¹. Catalysts calcined at higher temperatures presented higher surface areas (120 and 115 m²g⁻¹, for the samples calcined at 500 and 600 °C, respectively) than those calcined at lower temperatures (85 m²g⁻¹ for both catalysts calcined at 300 and 400 °C). This could be attributed to the presence of urea in catalysts calcined at 300 and 400 °C.

Table 5.1 Effect of calcination temperature on surface area of CeO₂ (UR) catalysts

Catalyst, Ce salt: urea ratio, aging time, calcination temperature / calcination time	Surface area ^a (m ² g ⁻¹)
CeO ₂ , 1:3, 24 h, 300 °C / 10 h	85
CeO ₂ , 1:3, 24 h, 400 °C / 10 h	85
CeO ₂ , 1:3, 24 h, 500 °C / 10 h	120
CeO ₂ , 1:3, 24 h, 600 °C/10 h	115

^aCalculated using the BET method.

TGA results (Figure 5.1) shows considerable weight loss between 250 – 450 °C. No loss in weight was evident above 450 °C. Hence CeO₂ (UR) catalysts calcined at 500 and 600 °C had no urea present in them and as such had higher surface areas than similar catalysts calcined at lower temperatures (300 and 400 °C). Calcination temperature is therefore crucial in determining the surface area of a CeO₂ (UR) catalyst. Two factors seem to determine the surface area: i) the increase of the calcination temperature, leading to a decrease in the catalyst crystal size and the surface area (sintering effect); ii) the degree of urea decomposition that drives to higher surface areas. Thus, it is necessary to search for a compromise between both factors in order to maximize the catalyst surface area. This fact is achieved at 500 and 600 °C.

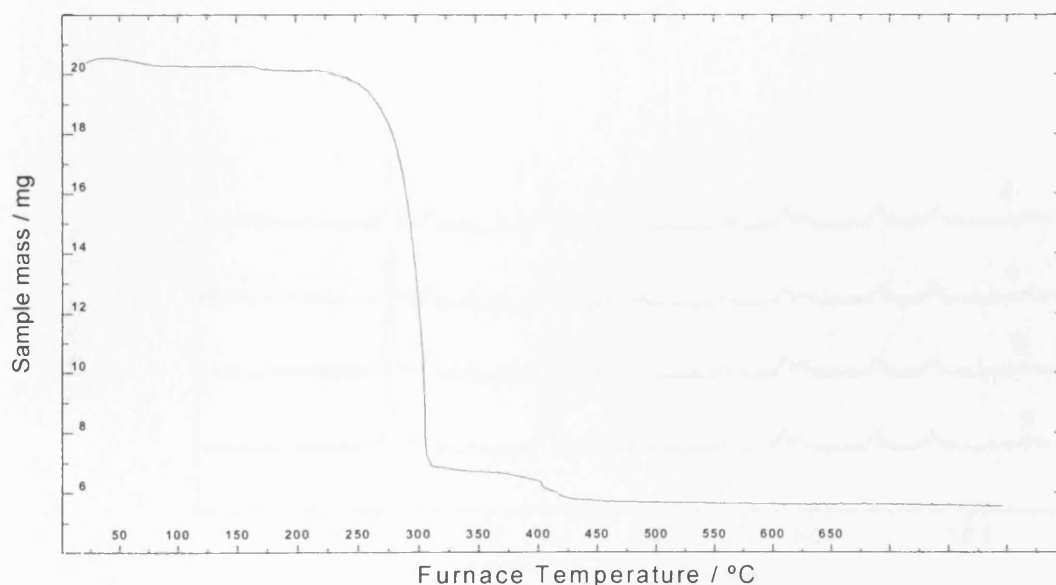


Fig. 5.1 TGA results for a CeO₂ (UR) catalyst precursor made from 1:3 cerium salt to urea ratio and aged for 24 h. Heating in air at a rate of 10⁰ min⁻¹.

5.2.2 Effect of Calcination Temperature on XRD Results of CeO₂ (UR)

Figure 5.2 shows the XRD patterns of the CeO₂ (UR) catalysts calcined at different temperatures. It can be observed that irrespective of calcination temperature, the XRD patterns of all catalysts are very similar showing diffraction peaks at $2\theta = 28.5, 33.1, 47.5, 56.3, 59.1, 69.5, 76.7, 79.1, 88.5, 95.4$ and 107.05° , which are characteristic of the cubic fluorite structured CeO₂. The figure confirms that variations in calcination temperature did not yield any other phases apart from cubic fluorite CeO₂. However, a thorough observation of the pattern of each catalyst revealed differences in the crystalline nature (evident in the differences in broadness of peaks and level of background noise in XRD patterns) of CeO₂.

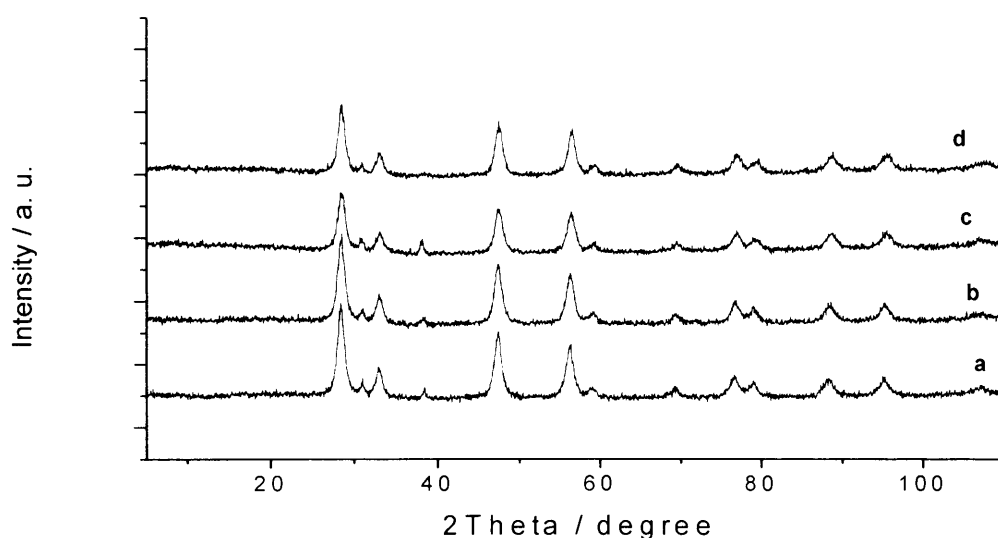


Fig.5.2 XRD patterns of CeO₂ (UR) catalysts calcined at different temperatures.

a: CeO₂, 1:3, 24 h, **300 °C**/10 h, b: CeO₂, 1:3, 24 h, **400 °C**/10 h, c: CeO₂, 1:3, 24 h, **500 °C**/10 h, d: CeO₂, 1:3, 24 h, **600 °C**/10 h.

It was equally observed (table 5.2) that variations in calcination temperature produced subtle differences in crystallite size. The lowest crystal size corresponds to the catalyst calcined at 500 °C (6.0 nm) whereas the other catalysts present crystallite sizes ranging between 6.4-7.5 nm.

Table 5.2 Effect of calcination temperature on crystal structure and crystallite size of CeO₂ (UR) catalysts

Catalyst, Ce salt: urea ratio, aging time, calcination temperature / calcination time	Crystallite size^a (nm)	Identified crystal phase^a
CeO ₂ , 1:3, 24 h, 300 °C / 10 h	7.5	Cubic fluorite
CeO ₂ , 1:3, 24 h, 400 °C / 10 h	7.2	Cubic fluorite
CeO ₂ , 1:3, 24 h, 500 °C / 10 h	6.0	Cubic fluorite
CeO ₂ , 1:3, 24 h, 600 °C /10 h	6.4	Cubic fluorite

^aBy XRD analysis.

5.2.3 Effect of Calcination Temperature on Raman Results of CeO₂ (UR)

Just like XRD patterns, Raman spectra for CeO₂ (UR) catalysts calcined at different temperatures (Figure 5.3) were alike regardless of the calcination temperature. All four CeO₂ (UR) catalysts showed a single Raman band centered at a Raman shift value of 460

cm^{-1} which is characteristic of CeO_2 vibrations (the triply degenerate TO mode). Other less intense Raman bands typical of CeO_2 can be appreciated at ca. 272 and 595 cm^{-1} (doubly degenerate TO mode and non-degenerate LO mode, respectively) [39].

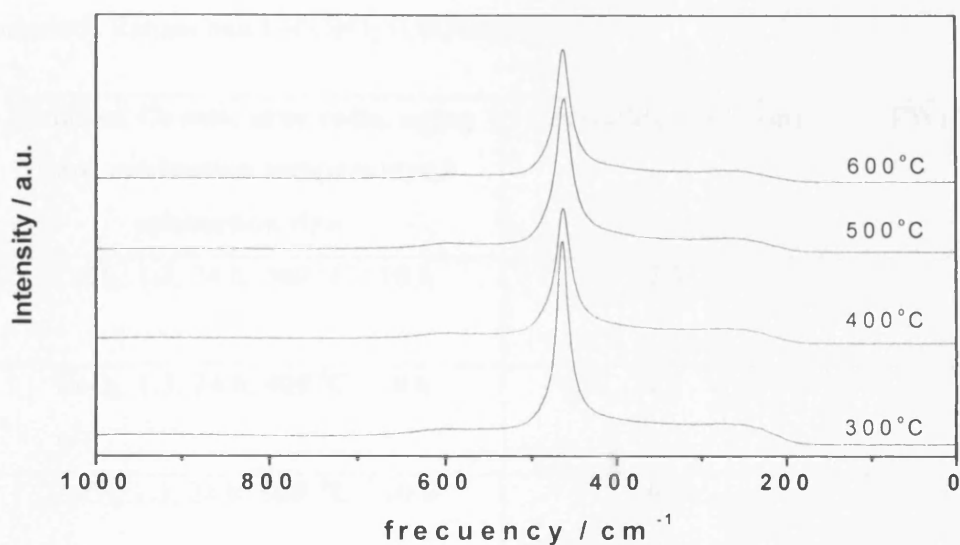


Fig. 5.3 Raman spectra of CeO_2 (UR) catalysts calcined at different temperatures.

Table 5.3 shows the full width at half maximum (FWHM) of this characteristic Raman band. Some authors [39, 40] have reported that the values of FWHM could be correlated with both the average crystal size of ceria and the defect concentration in the ceria structure. Thus an increase of the FWHM has been associated to a decrease of the crystallite size and/or a higher amount of oxygen vacancies in CeO_2 . From table 5.3, an inverse relationship can be seen between crystallite size and FWHM. It is therefore likely

that there exist fairly similar amount of oxygen defects regardless of the calcination temperature employed.

Table 5.3 Effect of calcination temperature on FWHM and crystallite size of characteristic Raman band of CeO₂ (UR) catalysts

Catalyst, Ce salt: urea ratio, aging time, calcination temperature / calcination time	Crystallite size ^a (nm)	FWHM ^b (cm ⁻¹)
CeO ₂ , 1:3, 24 h, 300 °C / 10 h	7.5	19.7
CeO ₂ , 1:3, 24 h, 400 °C / 10 h	7.2	20.0
CeO ₂ , 1:3, 24 h, 500 °C / 10 h	6.0	22.5
CeO ₂ , 1:3, 24 h, 600 °C/10 h	6.4	21,6

^aBy XRD analyses

^bFull width at half maximum of the CeO₂ line in the Raman spectra.

5.2.4 Effect of Calcination Temperature on SEM Results of CeO₂ (UR)

Figure 5.4 shows the variation in particle size and morphology of ceria with calcination temperature. From the micrographs, it is obvious that there occurred a change in particle size and morphology as the calcination temperature changed from 300-600 °C. Although it was difficult to measure the size of particles less than 40 μm, it is obvious that there

was a difference in particle size with calcination temperature. Particles of ceria calcined at low temperatures (300 and 400 °C) exist more like individual irregular particles whereas those of catalysts calcined at higher temperatures (500 and 600°C) tend to agglomerate, forming larger blocks of irregular particles.

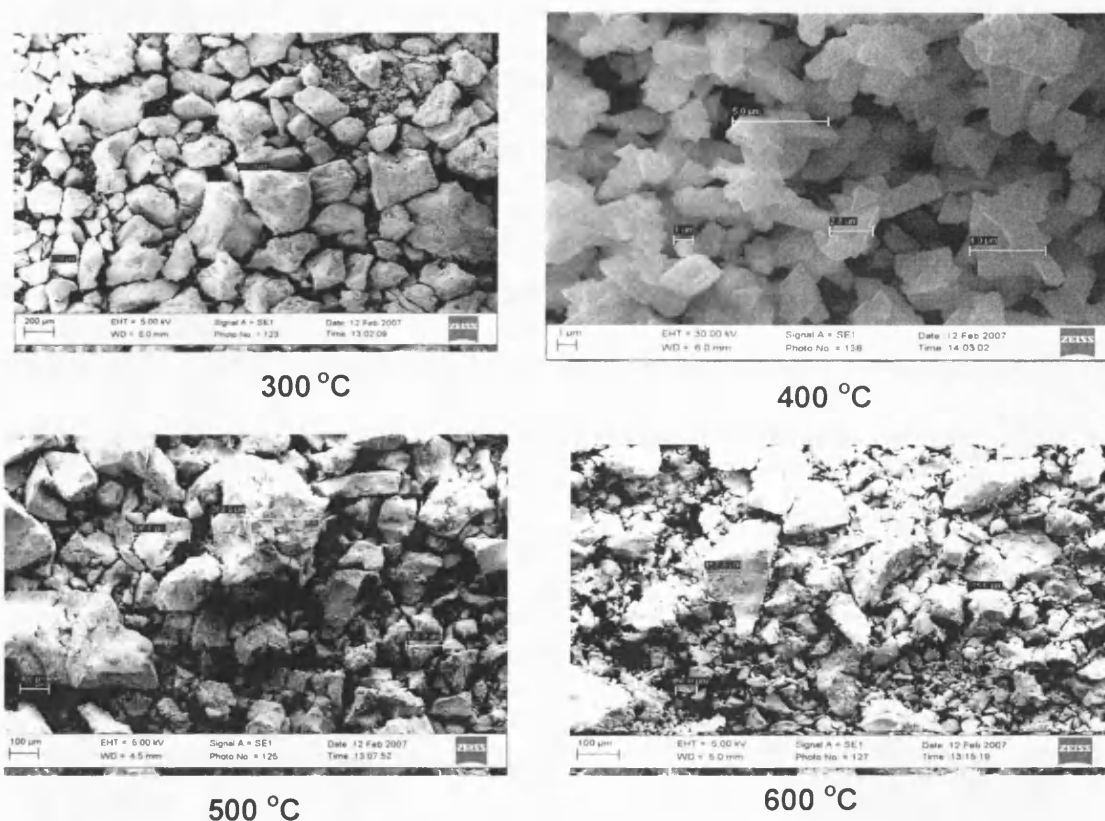


Fig. 5.4 Effect of calcination temperature on scanning electron micrograph of CeO₂ (UR)

5.2.5 Effect of Calcination Temperature on TPR Results of CeO₂ (UR)

TPR assays for the ceria catalysts studied in this work (e.g. fig. 5.5) mainly show two reduction bands between ambient temperature and 600 °C. A small low temperature

reduction peak centered at about 110 °C (LT peak) and a wide reduction band at higher temperature, from 300 to 600 °C (HT peak) with two maxima centered at ca. 400 and 550 °C, respectively. The low reduction band is related to highly reducible surface ceria species, whereas high temperature reduction peaks can be attributed to surface reduction of capping oxygen [17, 40]. It must be noted that the reduction in the bulk of CeO₂ does not take place in the interval of temperature studied, since it only occurs above 750 °C [40, 41]. As discussed later, the hydrogen consumption for the low and high temperature TPR peaks was found to fluctuate with preparation condition. The fact that these values fluctuate with preparation conditions suggests differences in surface structure of the ceria catalyst with preparation condition. In any case, these hydrogen consumptions are ca. 1.5% of the hydrogen consumption that would take place for the total reduction of CeO₂.

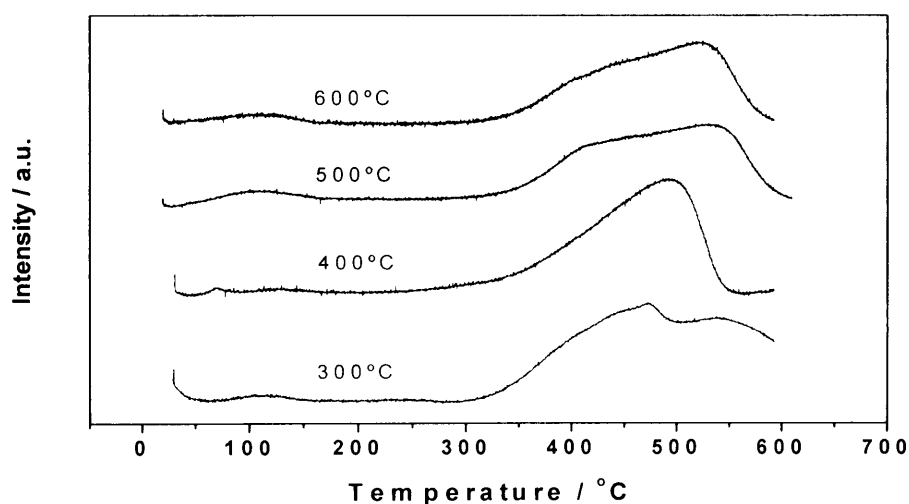


Fig. 5.5 Hydrogen temperature programmed reduction profiles for CeO₂ (UR) catalysts showing effect of calcination temperature (110 mg of sample, 20 mL min⁻¹ H₂, 5 °C min⁻¹).

Figure 5.5 illustrate the effect of calcination temperature on the TPR profile of CeO₂ (UR) catalysts. All four catalysts calcined at different temperatures (300-600 °C) showed the high temperature reduction peak covering the range 300-600 °C. Table 5.4 shows that hydrogen consumption for the HT peak ranged between 216-280 μmol/g. This variation in hydrogen consumption can be related to the formation of slightly different surface structures of CeO₂, although in all cases the hydrogen consumed in the TPR experiment only means a 1-2% of the hydrogen consumed if CeO₂ were completely reduced to Ce (0). It can also be observed in figure 5.5 that catalysts calcined at 500 and 600 °C also showed LT peak, which is higher in the case of the catalyst prepared at 600 °C

Table 5.4 Effect of calcination temperature on hydrogen consumption by CeO₂ (UR) catalysts during TPR

Catalyst, Ce salt: urea ratio, aging time, calcination temperature / calcination time	H ₂ consumption (μmoleg ⁻¹) at LT ^a	H ₂ consumption (μmoleg ⁻¹) at HT ^a	Total H ₂ consumption (μmoleg ⁻¹) ^a
CeO ₂ , 1:3, 24 h, 300 °C / 10 h	0	280	280
CeO ₂ , 1:3, 24 h, 400 °C / 10 h	0	216	216
CeO ₂ , 1:3, 24 h, 500 °C / 10 h	9	248	257
CeO ₂ , 1:3, 24 h, 600 °C/10 h	22	205	227

^aBy TPR analysis, 110 mg of sample, 20 mL min⁻¹ H₂, 5 °C min⁻¹.

5.2.6 Effect of Calcination Temperature on Activity of CeO₂ (UR) for the Total Oxidation of Naphthalene

Figure 5.6 shows the effect of the calcination temperature on the catalytic activity (expressed as yield to CO₂) achieved for naphthalene oxidation. The reason for using the CO₂ yield is that naphthalene is a polyaromatic molecule, which can easily be adsorbed onto the surface of high surface area materials, which may lead to over estimation of the catalytic oxidation activity as discussed earlier in chapter 2. Moreover, it should be taken into account that the use of total naphthalene conversion may also lead to erroneous conclusions due to the formation of by-products [see chapter 2]. Therefore, the yield to CO₂ and not the total conversion of naphthalene is used to establish the catalytic activity.

All four catalysts calcined at different temperatures were tested in two separate experiments and in both cases, similar activity results were obtained (see figure 5.6a and 5.6b). The catalyst calcined at 500 °C was the most active. This could be attributed to the high surface area/low crystallite size of this catalyst relative to the other catalysts. Notice that ceria catalysts calcined at 500 and 600 °C had considerably higher activities than the catalysts calcined at lower temperatures. TGA results suggested that catalysts calcined at 300 and 400 °C probably still contained urea, which resulted in lower surface areas and hence lower naphthalene oxidation activities.

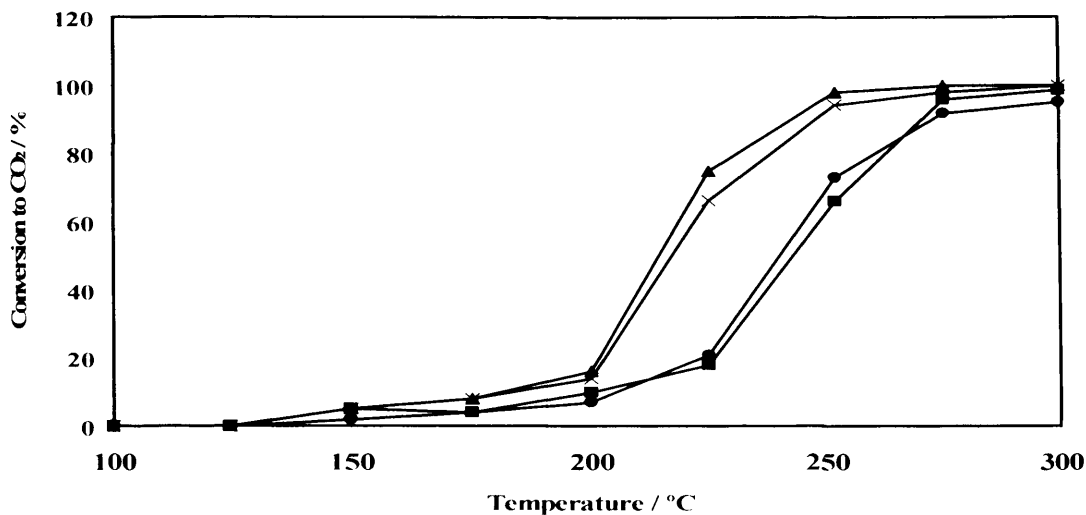


Fig. 5.6 (a) Plot showing the effect of calcination temperature on the activity of CeO₂ (UR) catalyst for naphthalene oxidation (Experiment 1). All 4 catalysts were prepared from 1:3 cerium salt to urea mixture, aged for 24 h and calcined at different temperatures for 10 h. ● 300 °C; ■ 400 °C; ▲ 500 °C; and X 600 °C.

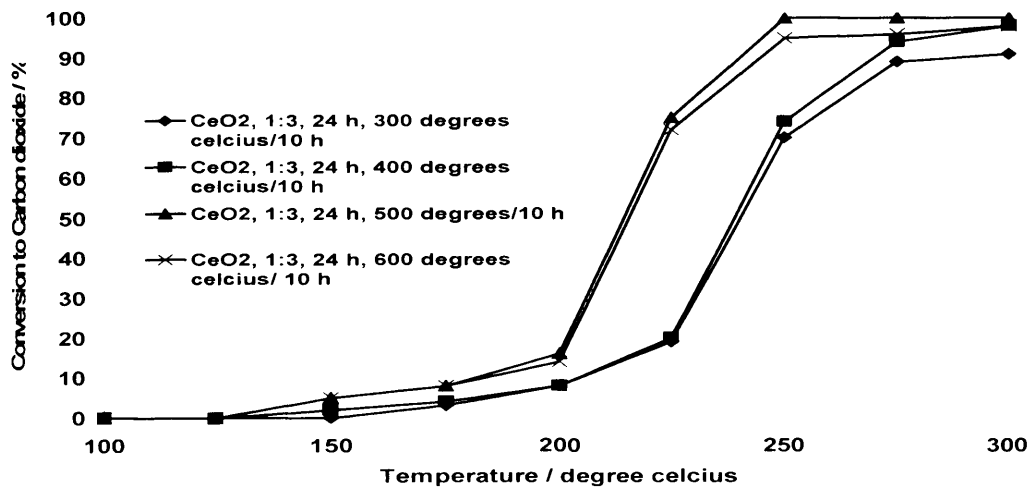


Fig. 5.6 (b) Plot showing the effect of calcination temperature on the activity of CeO₂ (UR) catalyst for naphthalene oxidation (Experiment 2).

The higher activity demonstrated by catalysts calcined at higher temperatures (500-600 °C) might also be related to the presence of more intense low temperature TPR bands that correspond to more easily reducible surface species. The difference observed between the morphology of catalysts calcined at high temperatures and those calcined at low temperatures could also account for the difference in catalytic activity.

Figure 5.7 shows that catalysts calcined at 300-600 °C did not show any considerable deactivation after prolonged treatment in the reaction flow at 300 °C whereas the catalyst precursor (before calcination) suffered considerable deactivation after 12 h in the reactor at 300 °C. The deactivation of the latter might be related to the influence of a high amount of un-decomposed urea present in the catalyst.

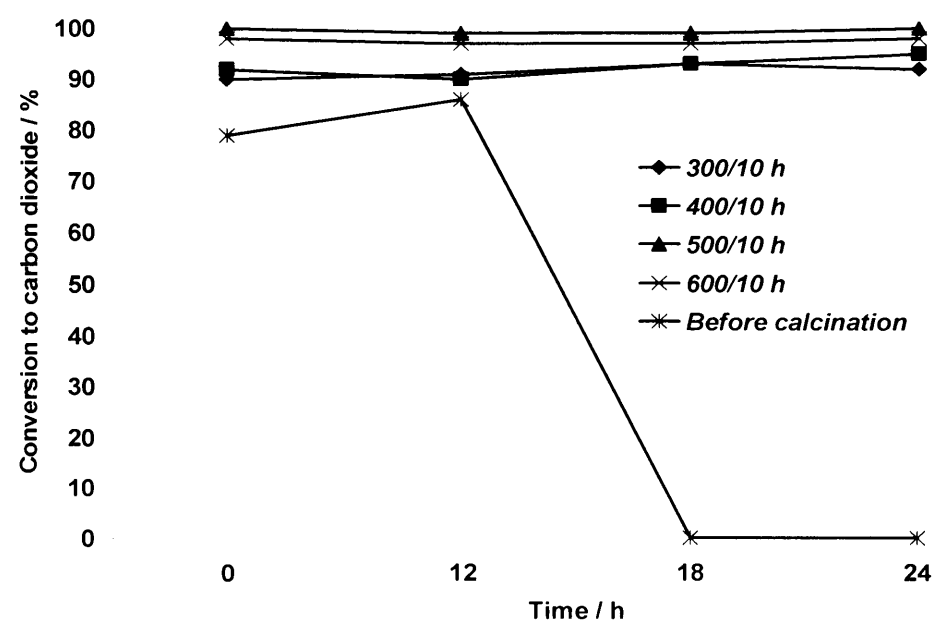


Fig. 5.7 Thermal treatment of CeO₂ (UR) in reactor at 300 °C for 24 h.

Table 5.5 shows the effect of calcination temperature on the rate of naphthalene oxidation per unit surface area of ceria catalyst at constant temperature (210 °C). It can be observed that the catalysts calcined at different temperatures (300-600 °C) showed rather different specific naphthalene oxidation rates. This fact suggests that surface area is not the only factor governing the activity of catalysts calcined at different temperatures.

Table 5.5 Effect of calcination temperature on naphthalene oxidation per unit surface area of ceria catalyst at 210 °C

Catalyst, Ce salt: urea ratio, aging time, calcination temperature / calcination time	r_{Np}^a [mol m ⁻² ·sec ⁻¹]
CeO ₂ , 1:3, 24 h, 300 °C / 10 h	1.2
CeO ₂ , 1:3, 24 h, 400 °C / 10 h	1.2
CeO ₂ , 1:3, 24 h, 500 °C / 10 h	2.0
CeO ₂ , 1:3, 24 h, 600 °C/10 h	2.0

^aNaphthalene oxidation per unit surface area of ceria catalyst at 210 °C

5.3 Effect of Calcination Time on Properties and Activity of CeO₂ (UR)

Since 500 °C has been shown as the preferred calcination temperature, the influence of the calcination time on the properties and Np oxidation activity of CeO₂ (UR) calcined at 500 °C has been studied. Characterization and catalytic activity results for these catalysts are elaborated in this section.

5.3.1 Effect of Calcination Time on the Surface Area of CeO₂ (UR)

BET results (table 5.6) showed that CeO₂ (UR) catalyst calcined for 3 h presented a very low surface area (33 m²g⁻¹). Conversely, catalysts calcined for 6 and 10 h showed higher and similar surface area (120-125 m²g⁻¹), with catalyst calcined for 6 h having the highest surface area (125 m²g⁻¹) amongst the three catalysts. The lower surface area of the catalyst calcined for 3 h can be related to the lack of time to completely remove the urea, thus preventing the formation of small crystal size ceria structures.

Table 5.6 Effect of calcination time on BET surface area of CeO₂ (UR) catalysts

Catalyst, Ce salt: urea ratio, aging time, calcination temperature / calcination time	Surface area^a (m²g⁻¹)
CeO ₂ , 1:3, 24 h, 500 °C / 10 h	120
CeO ₂ , 1:3, 24 h, 500 °C / 6 h	125
CeO ₂ , 1:3, 24 h, 500 °C / 3 h	33

^aCalculated using the BET method.

5.3.2 Effect of Calcination Time on XRD Results of CeO₂ (UR)

Just like the calcination temperature did not show any significant effect on the XRD patterns of the CeO₂ (UR) catalysts, the modification of the calcination time also did not

yield any major differences in the crystalline phases detected (Figure 5.8). In this way, XRD patterns only showed peaks representative of the cubic fluorite ceria.

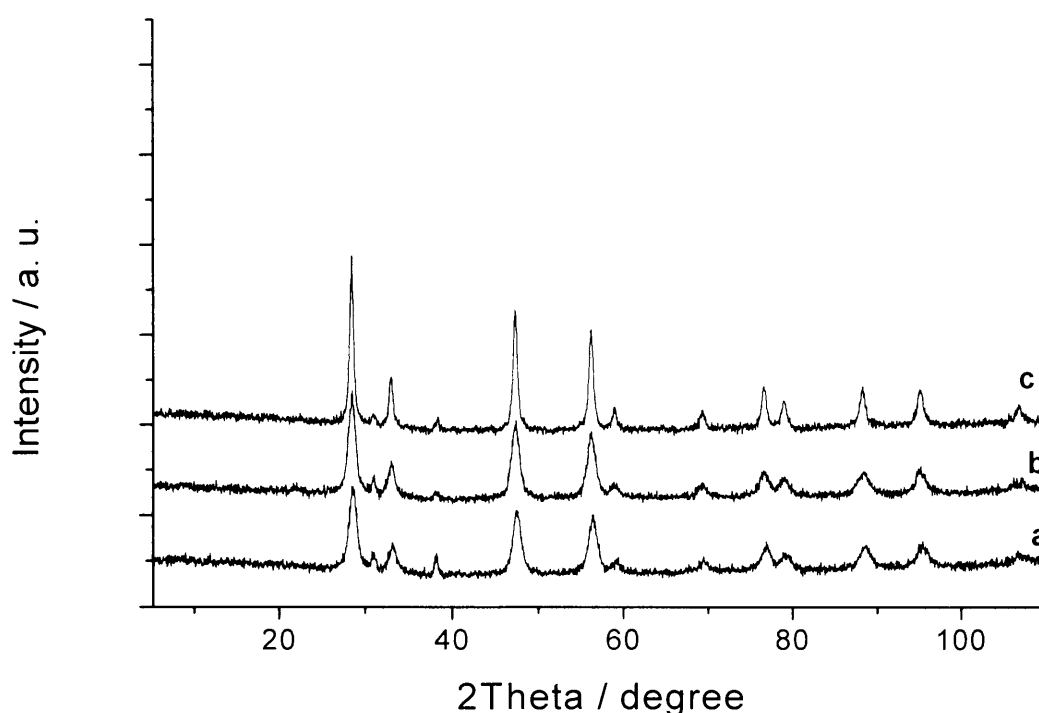


Fig. 5.8 XRD patterns of CeO₂ (UR) catalysts calcined at 500 °C for: (a) **10 h**, (b) **6 h** and (c) **3 h**. All three catalysts were prepared from 1:3 Ce salt/urea mixture and aged for 24 h.

Table 5.7 shows that CeO₂ crystallite sizes are in the range 6.0-19.2 nm. CeO₂ catalyst calcined for 3 h, with the lowest surface area (33 m²g⁻¹), had the highest crystallite size (19.2 nm) whereas CeO₂ catalysts calcined for 6 and 10 h with significantly higher and similar surface areas (125 and 120 m²g⁻¹ respectively) had considerably lower crystallite sizes (7.5 and 6.0 nm respectively). It is clear therefore that by changing the calcination time used for synthesis of the reference catalyst (10 h), it was possible to tune the

crystallite size of the CeO₂ (UR) catalyst. XRD data reveal a dependence of crystallite size of CeO₂ (UR) on the calcination time.

Table 5.7 Effect of calcination time on crystal size and phase of CeO₂ (UR) catalysts

Catalyst, Ce salt: urea ratio, aging time, calcination temperature / calcination time	Crystallite size^a (nm)	Identified crystal phase^a
CeO ₂ , 1:3, 24 h, 500 °C / 10 h	6.0	Cubic fluorite
CeO ₂ , 1:3, 24 h, 500 °C / 6 h	7.5	Cubic fluorite
CeO ₂ , 1:3, 24 h, 500 °C / 3 h	19.2	Cubic fluorite

^aBy XRD analysis.

5.3.3 Effect of Calcination Time on Raman Results of CeO₂ (UR)

Raman spectra for CeO₂ (UR) catalysts (figure 5.9) show that the calcination time did not produce significant changes in the Raman bands. All three catalysts mainly showed the characteristic Raman band for CeO₂ vibrations. Table 5.8 however indicates a change in the FWHM of this Raman band with calcination time. Whilst catalysts calcined for 6 and 10 h have Raman bands with similar FWHM (22.5 and 23.5 cm⁻¹), the CeO₂ (UR) catalyst calcined for 3 h with the highest crystallite size (19.2 nm) showed a slightly narrower Raman band (FWHM = 20 cm⁻¹). As it has previously been mentioned, these

values can be correlated with both the average crystal size of ceria and/or defect creation in the ceria structure.

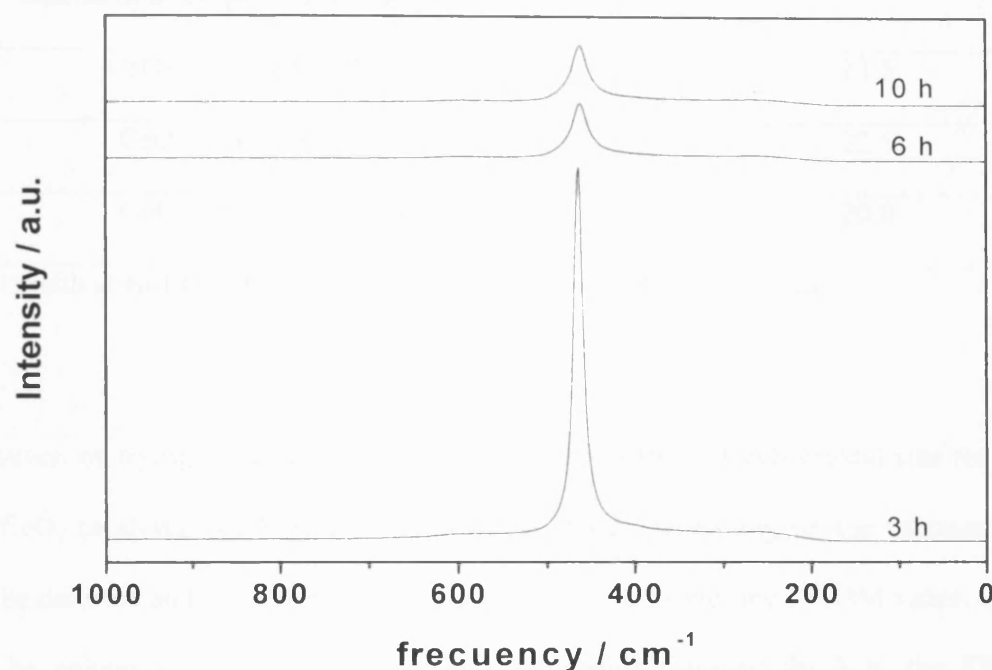


Fig. 5.9 Raman spectra of CeO_2 (UR) catalysts calcined at 500 °C for 10, 6 and 3 h.

By comparing the FWHM values of the three ceria catalysts, it cannot be conclusively propose that differences in the amount of oxygen vacancies occurred, since XRD data showed the expected trend in the crystallite size for these catalysts.

Table 5.8 Effect of calcination time on FWHM of characteristic Raman band of CeO₂ (UR) catalysts

Catalyst, Ce salt: urea ratio, aging time, calcination temperature / calcination time	FWHM ^a (cm ⁻¹)
CeO ₂ , 1:3, 24 h, 500 °C / 10 h	23.5
CeO ₂ , 1:3, 24 h, 500 °C / 6 h	22.5
CeO ₂ , 1:3, 24 h, 500 °C / 3 h	20.0

^aFull width at half maximum of the CeO₂ band in the Raman spectra.

However, on trying to correlate the FWHM values with the CeO₂ crystal size for most of the CeO₂ catalysts, see Figure 5.10, different trends depending on the calcination time can be detected and the lower the calcination time, the higher the FWHM value. In fact, it can be pointed out that in the case of the catalyst calcined for 3 h, the FWHM is remarkably higher than expected if the average crystal size is the only affecting factor and therefore, the concentration of oxygen vacancies in the ceria surface of the sample calcined for 3h seems to be much higher than in the other catalysts. It apparently looks that the higher the calcination time the lower the amount of oxygen vacancies in the ceria structure.

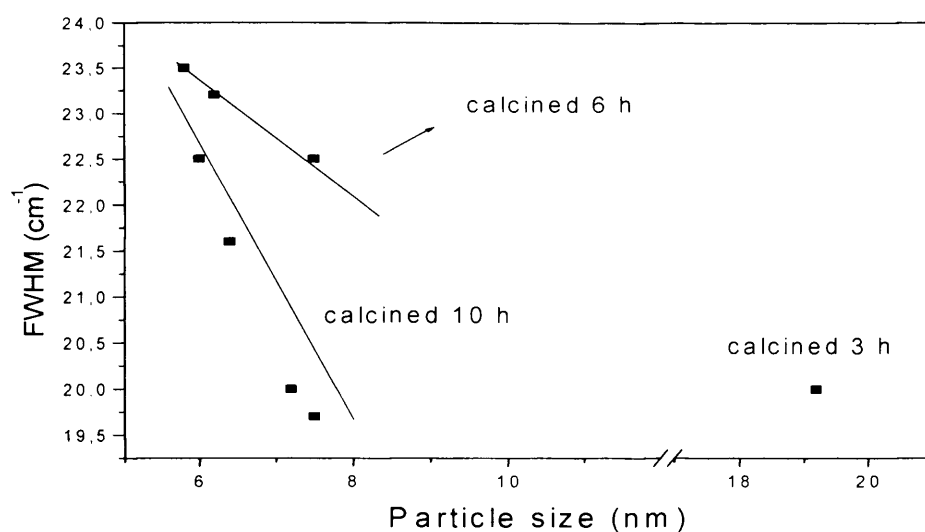


Fig. 5.10 Relationship between FWHM and crystallite size of CeO₂ (UR) catalysts

5.3.4 Effect of Calcination Time on SEM Results of CeO₂ (UR)

Figure 5.11 shows the SEM images for catalysts calcined at 500 °C for 10, 3 and 6 h. The figures reveal a change in particle size and morphology with calcination time. Catalysts calcined for 10 and 6 h demonstrated a mark similarity in morphology (dense irregular particles of varying sizes <40µm to approximately 400µm). The morphology of these two catalysts varied greatly from that of catalyst calcined for 3 h (porous irregular particles most of which ranged between 40 to approximately 200µm). This difference in morphology exhibited by the latter is consistent with its very low surface area and large crystallite size (from XRD analysis) relative to catalysts calcined for 10 and 6 h. Notice

that particles of these catalysts tend to agglomerate, forming larger lumps of irregular particles.

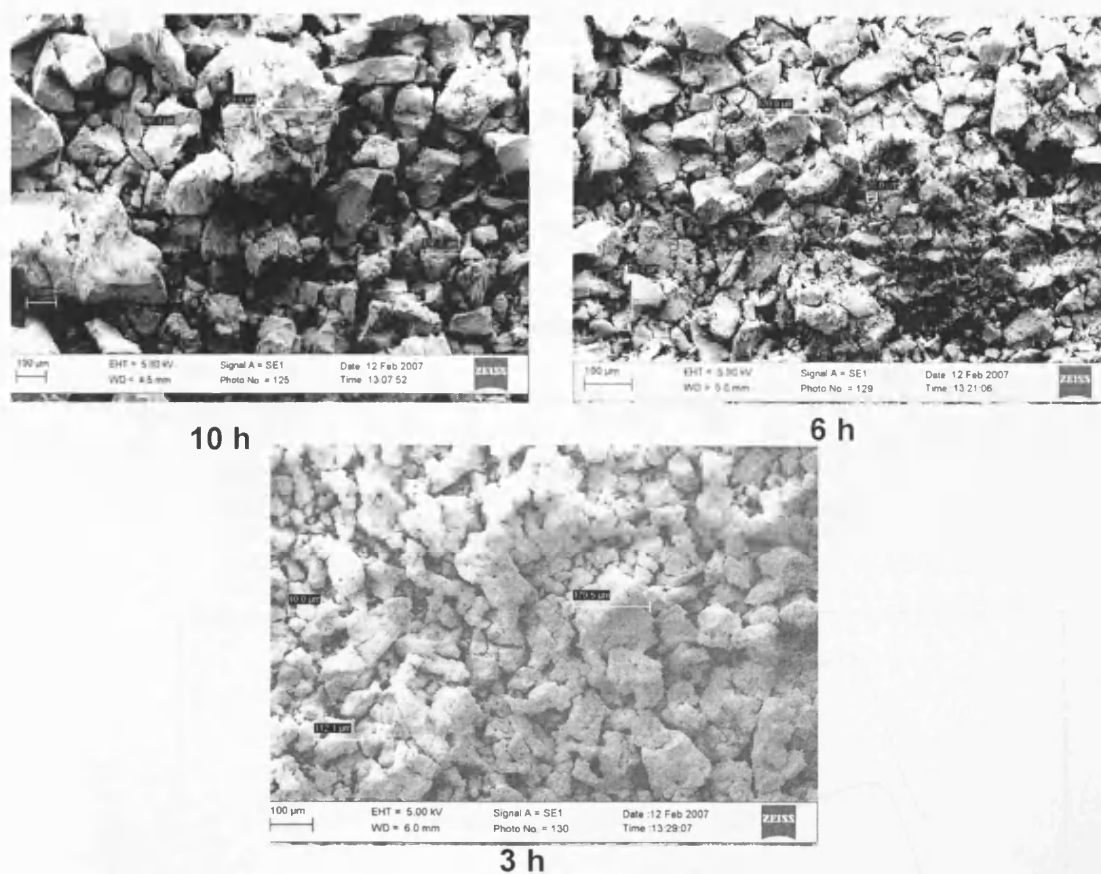


Fig. 5.11 Scanning electron micrographs of CeO_2 (UR) catalysts calcined at 500 °C for 10, 6 and 3 h. All three catalysts were prepared from 1:3 Ce salt/urea ratio and aged for 24 h.

5.3.5 Effect of Calcination Time on TPR Results of CeO₂ (UR)

TPR profiles of catalysts calcined at 500 °C for 10 h, 6 h and 3 h are shown in figure 5.12. Similar TPR profiles were observed for these catalysts, although the intensity of the reduction bands is lower in the catalysts heat treated for 3 h. A relationship between H₂ consumption and the surface area can be observed (table 5.9). Catalysts with higher surface areas showed higher hydrogen consumption. This suggests again that the ceria species reduced until 600 °C are surface species. Notice that the catalyst calcined for 3 h did not show the LT TPR peak present in the catalyst calcined for 6 and 10 h.

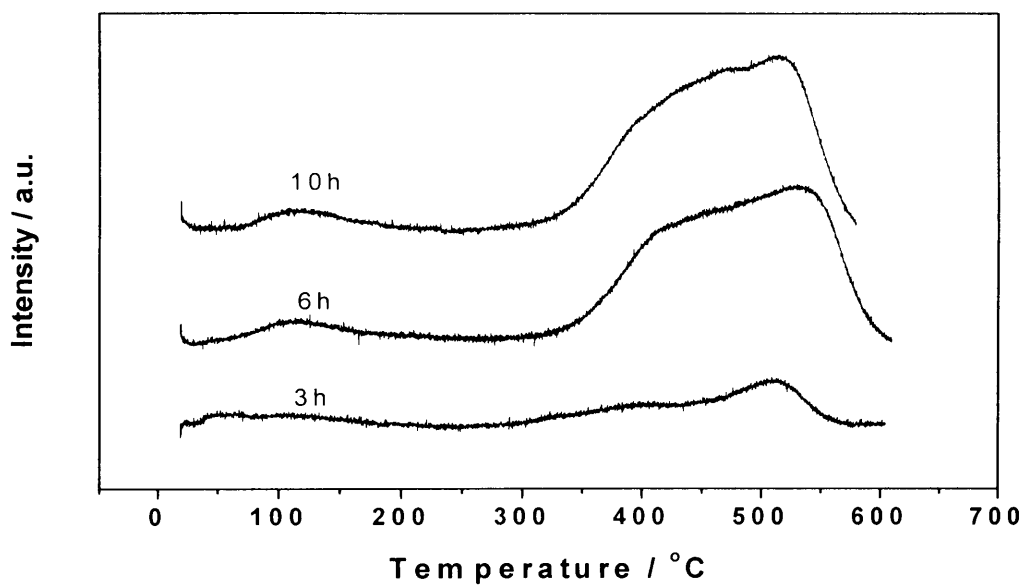


Fig. 5.12 Hydrogen temperature programmed reduction profiles for CeO₂ (UR) catalysts showing effect of calcination time. Conditions: 110 mg of sample, 20 mL min⁻¹ H₂, heating rate of 5 °C min⁻¹.

Table 5.9 Effect of calcination time on surface area and H₂ consumption (TPR) of CeO₂ (UR) catalysts

Catalyst, Ce salt: urea ratio, aging time, calcination temperature / calcination time	Surface area ^a (m ² g ⁻¹)	H ₂ consumption (μmoleg ⁻¹)at LT ^b	H ₂ consumption (μmoleg ⁻¹) at HT ^b	Total H ₂ consumption (μmoleg ⁻¹) ^b
CeO ₂ , 1:3, 24 h, 500 °C / 10 h	120	9	248	257
CeO ₂ , 1:3, 24 h, 500 °C / 6 h	125	18	212	230
CeO ₂ , 1:3, 24 h, 500 °C / 3 h	33	0	62	62

^aCalculated using the BET method.

^bBy TPR analysis, 110 mg of sample, 20 mL min⁻¹ H₂, 5 °C min⁻¹.

5.3.6 Effect of Calcination Time on Activity of CeO₂ (UR) for the Total Oxidation of Naphthalene

Figure 5.13 shows the variation of the catalytic activity (expressed as yield to CO₂) in naphthalene oxidation with calcination time. The highest activity was obtained for the catalyst heat treated for 6 h. The order of activity was as follows: 6h > 10h> 3h. Therefore, it would be needless to calcine CeO₂ (UR) catalyst for 10 h, since a shorter calcination time (6 h) resulted in a more active catalyst. CeO₂ (UR) calcined for 3 h was the least active, probably due to the lower surface area, although it might also be related

to its unique porous morphology and the absence of the low temperature (50-160 °C) peak in its TPR profile.

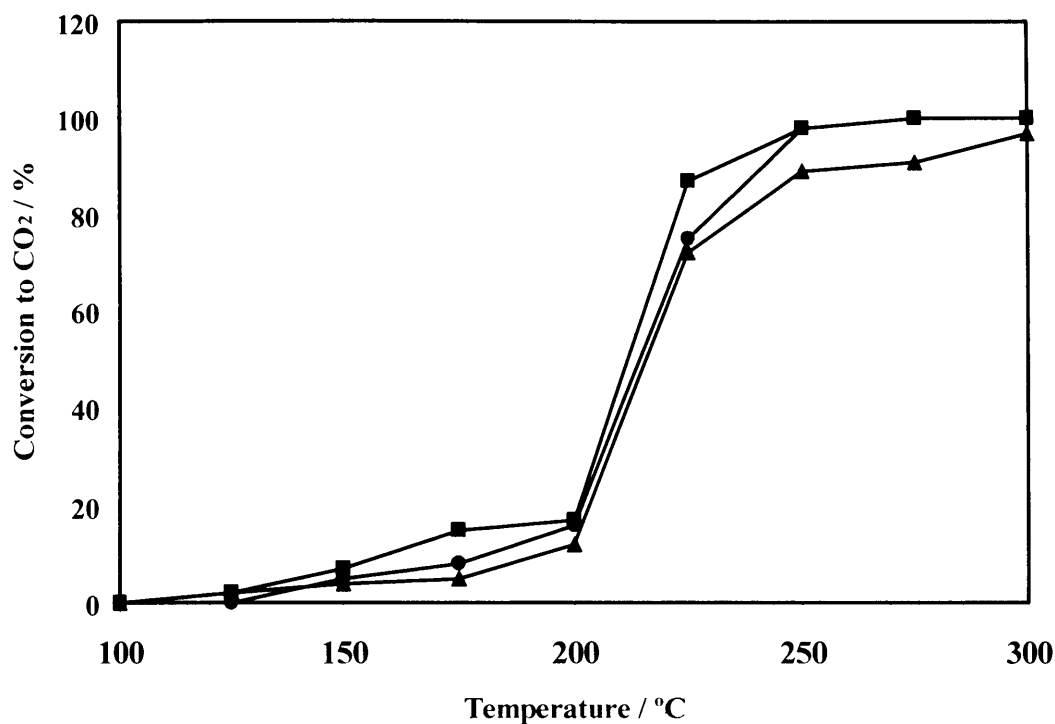


Fig 5.13 Effect of calcination time on the activity of CeO₂ (UR) catalyst for naphthalene oxidation. All 3 catalysts were prepared from 1:3 cerium salt to urea mixture, aged for 24 h and calcined at 500 °C for different times (10, 6, and 3 h). Calcination time: ▲ 3 h; ■ 6 h; ● 10 h.

LT TPR peak observed in CeO₂ (UR) catalysts synthesized in this work have been assigned to the reduction of highly reducible surface species. Whilst this LT peak could be observed in the TPR profiles of CeO₂ (UR) catalysts calcined for 6 and 10 h, TPR profile of the catalyst calcined for 3 h did not show this peak; this explains the lower

activity of the latter relative to catalysts calcined for 6 and 10 h. The highly reducible surface species present in these two catalysts facilitate the oxidation of naphthalene.

Table 5.10 shows the effect of calcination time on the rate of naphthalene oxidation per unit surface area at 175 °C. The catalyst calcined for 3 h (with the lowest surface area) gave a rate of naphthalene oxidation per unit surface area of ca. 3 times higher than catalysts calcined for 6 and 10 h. According to these data, the surface area plays an important role in the catalytic activity since the higher the surface area the higher the catalytic activity. However, the specific activity is remarkably higher in the catalyst heat treated for 3 h, so other factors apart from the specific area, should be taken into account. As explained earlier, it can be tentatively proposed that the concentration of oxygen defects could be another important factor to explain the activity of the ceria catalyst, as the sample calcined for 3 h, which showed the highest concentration of oxygen defects (see figure 5.10), was the catalyst with the highest specific activity. This might also be related to its unique porous morphology discussed earlier.

Table 5.10 Effect of calcination time on Np oxidation rate over CeO₂ (UR) catalysts

Catalyst, Ce salt: urea ratio, aging time, calcination temperature / calcination time	r_{Np}^a [mol m ⁻² ·sec ⁻¹]
CeO ₂ , 1:3, 24 h, 500 °C / 10 h	2.0
CeO ₂ , 1:3, 24 h, 500 °C / 6 h	2.3
CeO ₂ , 1:3, 24 h, 500 °C / 3 h	7.0

^aNaphthalene oxidation per unit surface area of ceria catalyst at 210 °C

5.4 Effect of Aging Time on Properties and Activity of CeO₂ (UR)

The influence of the aging time on CeO₂ (UR) was studied for catalysts calcined at 500 °C for 6 h. Characterization and Np oxidation activity data of catalysts aged for 3, 12 and 24 h are reported in this section.

5.4.1 Effect of Aging Time on BET Surface Area of CeO₂ (UR)

Table 5.11 shows that no remarkable differences in BET areas were appreciated, although CeO₂ (UR) catalyst aged for 3 and 12 h presented slightly lower surface areas (113 and 112 m²g⁻¹ respectively) than the catalyst aged for 24 h (125 m²g⁻¹).

Table 5.11 Effect of aging time on BET surface area of CeO₂ (UR) catalysts

Catalyst, Ce salt: urea ratio, aging time, calcination temperature / calcination time	Surface area ^a (m ² g ⁻¹)
CeO ₂ , 1:3, 24 h , 500 °C / 6 h	125
CeO ₂ , 1:3, 12 h , 500 °C / 6 h	112
CeO ₂ , 1:3, 3 h , 500 °C/6 h	113

5.4.2 Effect of Aging Time on XRD Results of CeO₂ (UR)

XRD patterns of ceria catalysts aged for three different durations (24, 12 and 3 h) were all alike (figure 5.14) representing the presence of cubic fluorite ceria.

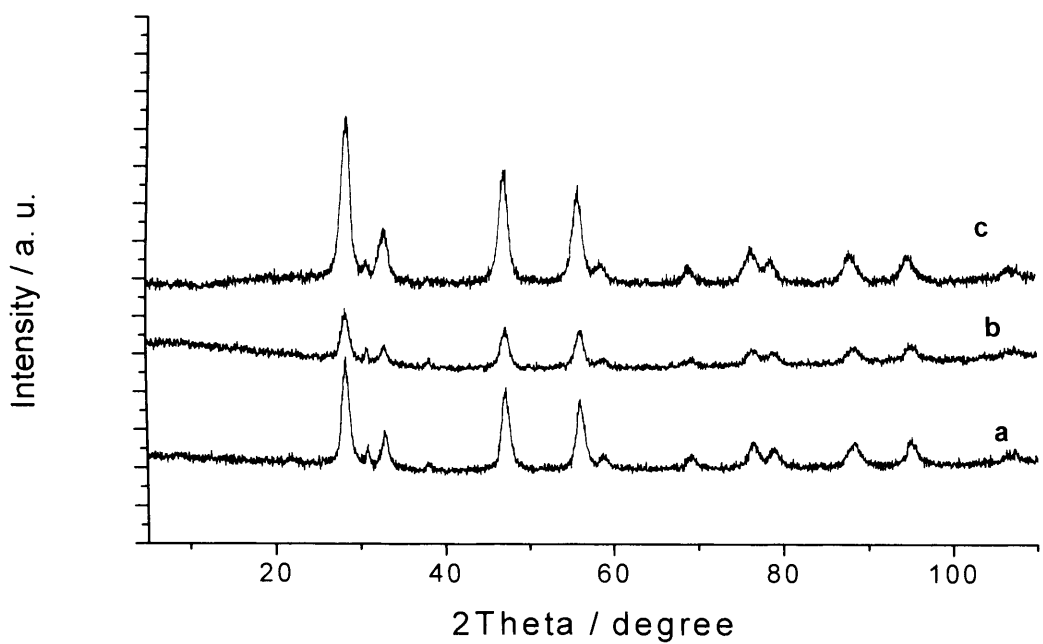


Fig. 5.14 XRD patterns of CeO₂ (UR) catalysts aged for 24, 12 and 3 h.

a: CeO₂, 1:3, **24 h**, 500 °C/6 h, b: CeO₂, 1:3, **12 h**, 500 °C/6 h, c: CeO₂, 1:3, **3 h**, 500 °C/6 h.

Table 5.12 shows that the crystallite sizes of these 3 catalysts increased with the aging time (7.5, 6.2 and 5.8 nm for aging times of 24, 12 and 3 h, respectively). Surprisingly, an inverse relationship is observed between surface areas and crystallite sizes.

Table 5.12 Effect of aging time on surface area and crystallite size of CeO₂ (UR)
catalysts

Catalyst, Ce salt: urea ratio, aging time, calcination temperature / calcination time	Surface area ^a (m ² g ⁻¹)	Crystallite size ^b (nm)
CeO ₂ , 1:3, 24 h , 500 °C / 6 h	125	7.5
CeO ₂ , 1:3, 12 h , 500 °C / 6 h	112	6.2
CeO ₂ , 1:3, 3 h , 500 °C/6 h	113	5.8

^aCalculated using the BET method.

^bBy XRD analysis.

5.4.3 Effect of Aging Time on Raman Results of CeO₂ (UR)

Just like Raman spectra of other ceria catalysts discussed earlier in sections 5.2 and 5.3, Raman spectra recorded for catalysts aged for different times (figure 5.15) were alike showing a single band representative of CeO₂ vibrations. Table 5.13 shows that this characteristic Raman band was only slightly broader for the catalyst aged for 3 h and 12 h (FWHM = 23.5 and 23.2cm⁻¹) than catalyst aged for 24 h (FWHM = 22.5). These values show that the aging time mainly affects the CeO₂ crystalline size rather than the concentration of oxygen defects.

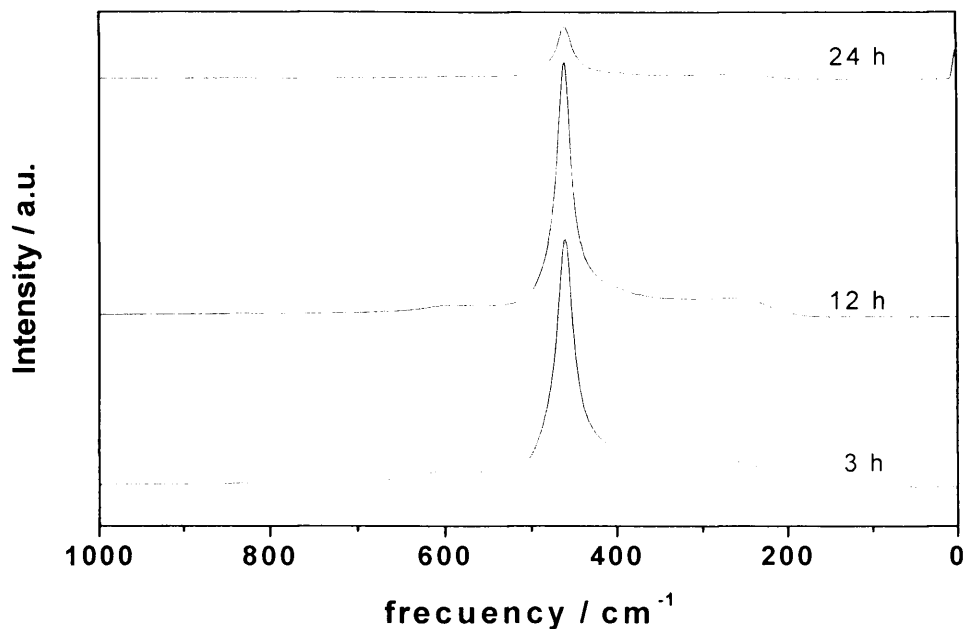


Fig. 5.15 Raman spectra of CeO_2 (UR) catalysts aged for 24, 12 and 3 h.

Table 5.13 Effect of aging time on crystallite size and FWHM for Raman band of CeO_2 (U) catalysts

Catalyst, Ce salt: urea ratio, aging time, calcination temperature / calcination time	Crystallite size ^a (nm)	FWHM ^b (cm^{-1})
CeO_2 , 1:3, 24 h, 500 °C / 6 h	7.5	22.5
CeO_2 , 1:3, 12 h, 500 °C / 6 h	6.2	23.2
CeO_2 , 1:3, 3 h, 500 °C/6 h	5.8	23.5

^bBy XRD analysis

^bFull width at half maximum of the CeO_2 band in the Raman spectra.

5.4.4 Effect of Aging Time on SEM Results of CeO₂ (UR)

The change in particle size and morphology of the ceria catalyst with aging time is illustrated in figure 5.16. The figures show a variation in morphology with aging time. Particles of catalysts aged for shorter time (3-12 h) showed higher porosity than the catalyst aged for 24 h. The three catalysts under consideration showed particle sizes in the range of approximately 40-400 μm . Particles < 40 μm were visible although these could not be measured accurately.

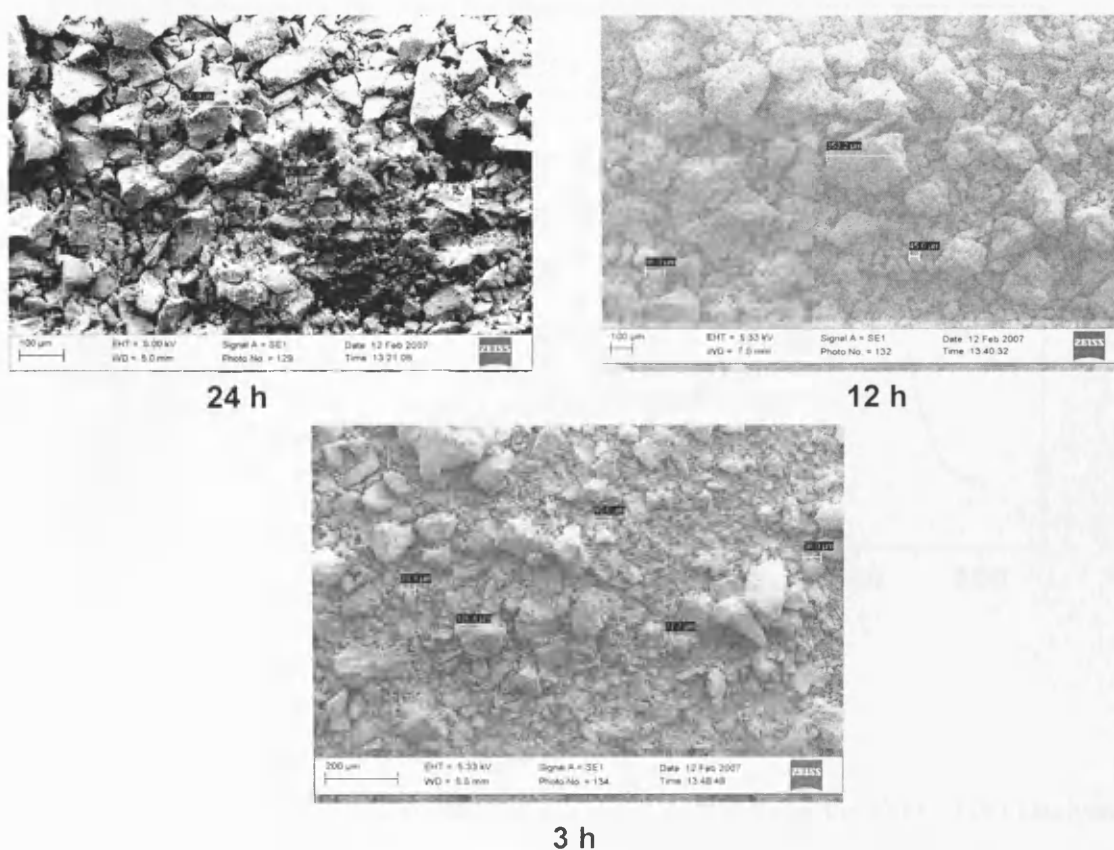


Fig. 5.16 Scanning electron micrographs of CeO₂ (UR) catalysts aged for 24 h, 12 h and 3 h.

5.4.5 Effect of Aging Time on TPR Results of CeO₂ (UR)

TPR profiles of ceria catalyst aged for different times are shown in Figure 5.17. It can be observed that the three catalysts have similar profiles, where both LT and HT peaks can be distinguished. Only a slight change in the position of peak maxima and range covered was observed, when the aging time was varied.

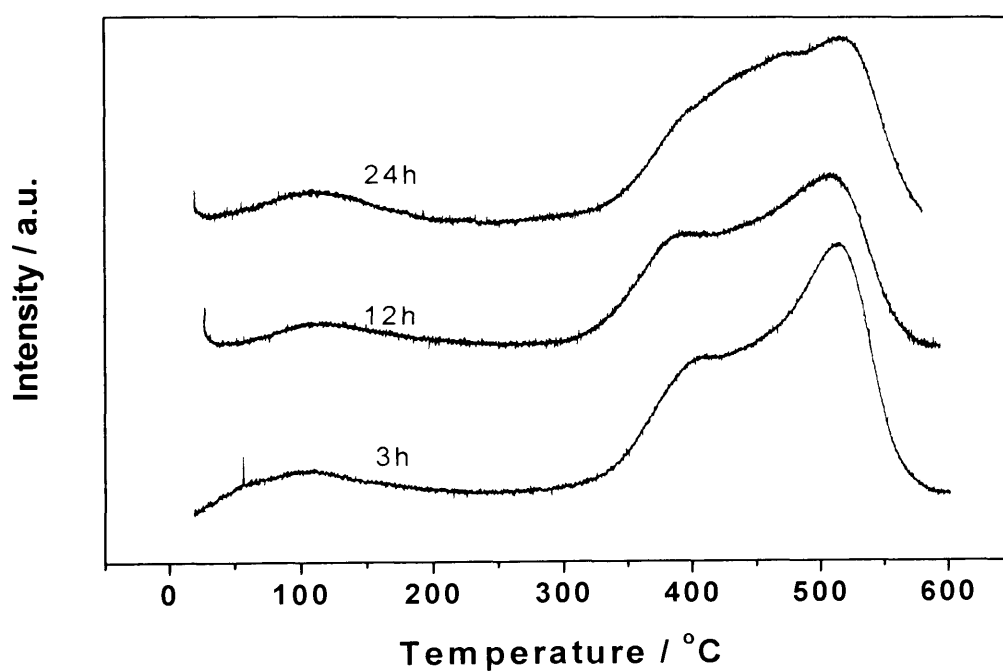


Fig. 5.17 Hydrogen temperature programmed reduction profiles for CeO₂ (UR) catalysts showing effect of aging time. TPR conditions: 110 mg of sample, 20 mL min⁻¹ H₂, heating rate of 5 °C min⁻¹.

Table 5.14 shows that all three catalysts gave slightly different values of total hydrogen consumption (222-250 μmoleg^{-1}). This variation in hydrogen consumption can be attributed to the formation of subtle different surface structures as the aging time was varied.

Table 5.14 Effect of aging time on TPR hydrogen consumption of CeO_2 (UR) catalysts

Catalyst, Ce salt: urea ratio, aging time, calcination temperature / calcination time	H₂ consumption (μmoleg^{-1}) at LT^a	H₂ consumption (μmoleg^{-1}) at HT^a	Total H₂ consumption (μmoleg^{-1})^a
CeO_2 , 1:3, 24 h , 500 °C / 6 h	18	212	230
CeO_2 , 1:3, 12 h , 500 °C / 6 h	19	203	222
CeO_2 , 1:3, 3 h , 500 °C/6 h	20	230	250

^aBy TPR analysis, 110 mg of sample, 20 mL min⁻¹ H₂, 5 °C min⁻¹.

5.4.6 Effect of Aging Time on the Activity of CeO_2 (UR) Catalyst for the Total Oxidation of Naphthalene

Figure 5.18 shows the evolution of the catalytic activity for naphthalene oxidation (expressed as yield to CO_2) with reaction temperature for CeO_2 catalysts aged for different durations. The optimum aging time for catalyst preparation was found to be 12 h. The catalyst aged for 12 h had an activity slightly higher than that aged for 3h. These catalysts were dramatically more active than the ceria catalyst aged for 24 h, in spite of

the smaller specific surface area of the formers. Therefore, it is obvious that catalysts were being over-aged using a 24 h aging time, as the catalytic activity of CeO₂ catalyst was remarkably higher with a 3 h aging time.

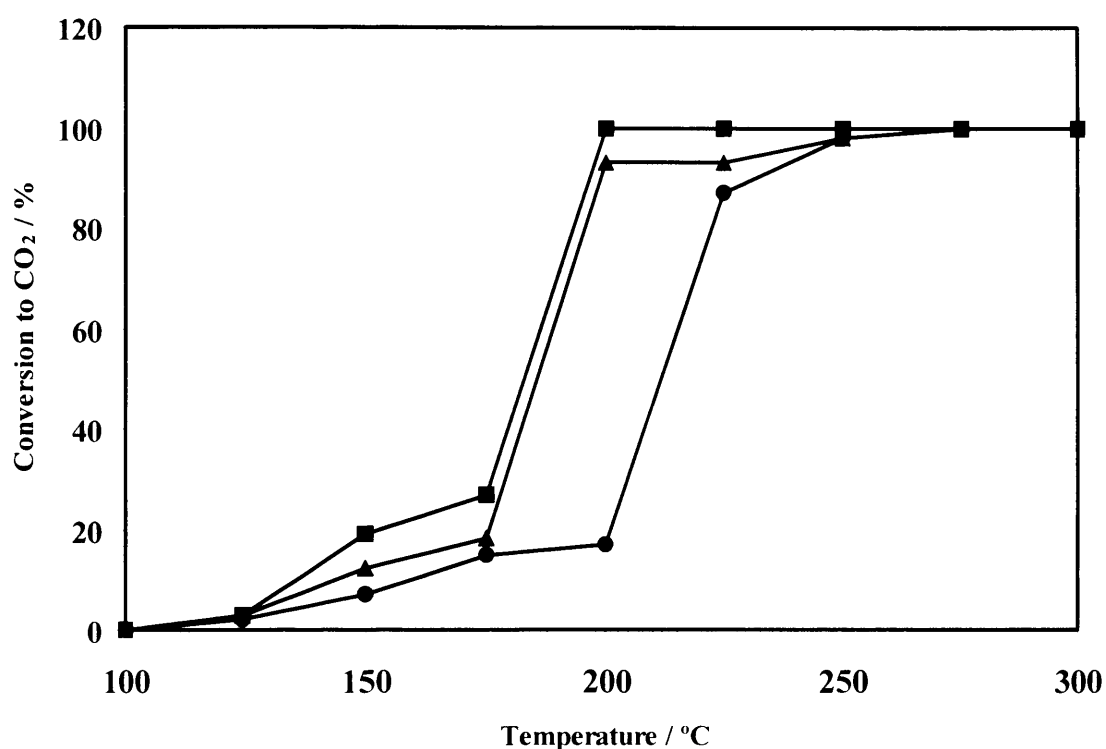


Fig. 5.18 Plot showing the effect of aging time on the activity of CeO₂ (UR) catalyst for naphthalene oxidation. All 3 catalysts were prepared from 1:3 cerium salt to urea mixture, aged for different durations (24, 12 and 3 h) and calcined at 500 °C for 6 h. Aging time: ▲ 3 h; ■ 12 h; ● 24 h

Table 5.15 shows the effect of aging time on the rate of naphthalene oxidation per unit surface area at 210 °C.

Table 5.15 Effect of aging time on surface area, crystallite size and naphthalene oxidation rate of CeO₂ (UR) catalysts

Catalyst, Ce salt: urea ratio, aging time, calcination temperature / calcination time	Surface area ^a (m ² g ⁻¹)	Crystallite size ^b (nm)	r _{Np} ^c [mol m ⁻² ·sec ⁻¹]
CeO ₂ , 1:3, 24 h , 500 °C / 6 h	125	7.5	2.3
CeO ₂ , 1:3, 12 h , 500 °C / 6 h	112	4.1	4.2
CeO ₂ , 1:3, 3 h , 500 °C/6 h	113	5.9	4.2

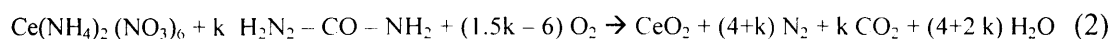
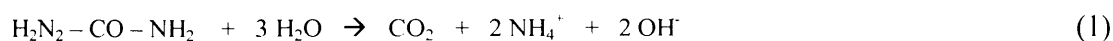
^aCalculated using the BET method.

^bBy XRD analysis.

^cNaphthalene oxidation per unit surface area of ceria catalyst at 210 °C

No straightforward explanations can be made according to results presented in table 5.15.

However, it can be tentatively proposed that two important reactions can be involved during the aging of the cerium salt with urea. Firstly, the unreacted urea is decomposing yielding OH⁻, NH₄⁺ and CO₂, according to reaction (1). During this step, both the pH of the solution and the particle size of the precipitate were gradually increasing as the reaction proceeded [42].



Secondly, the combustion of the cerium salt with the remaining urea takes place according to equation (2). During this second step, it has previously been reported that the combustion of cerium ammonium nitrate salt in the presence of urea favors the agglomeration of CeO₂ particles [43]. Thus during the preparation method, it can be

assumed that the second reaction would be predominant at low aging times, as an excess of urea was used ($\text{Ce-salt/urea} = 1/3$ molar ratio), and the hydrolysis of urea would be prevalent at high aging times. These facts could explain the unexpected relationship between surface areas and CeO_2 particle size. Whilst long aging times are favoring larger crystallite sizes with a low level of agglomeration, short aging times are driving to smaller crystal particles with a higher degree of agglomeration. This is clearly shown in the SEM images of these catalysts (figure 5.16). Catalysts aged for shorter times (3 and 12 h) showed higher degree of porosity (probably due to aggregation of small particles) than the catalyst aged for a longer time (24 h); less porous, dense, and irregular particles (lower agglomeration of large particles). Therefore, it can be concluded that the high catalytic activity achieved by the samples aged for 3 and 12 h can be due to their lower particle size and/or to the concentration of oxygen defects, rather than to a higher specific surface area.

5.5 Effect of Ce Salt/Urea Ratio on Properties and Activity of CeO_2 (UR)

It has been established in sections 5.2, 5.3 and 5.4 that a calcination temperature of 500 °C, calcination time of 6 h and an aging time of 24 h are appropriate in achieving highly active Np oxidation CeO_2 (UR) catalyst. In this section, the influence of Ce salt/urea ratio on the properties and activity of a CeO_2 (UR) prepared using the above mentioned conditions is evaluated.

5.5.1 Effect of Ce Salt/Urea Ratio on BET Surface Area of CeO₂ (UR)

BET results (table 5.16) show that these catalysts had surface areas in the range 92-128 m²g⁻¹. Catalysts with cerium salt to urea ratios of 2:1, 1:1 and 1:2 had fairly similar surface areas (92-94 m²g⁻¹) while 1:3 and 1:4 ratios yielded catalysts with higher surface areas (125 and 128 m²g⁻¹ respectively).

Table 5.16 Effect of cerium salt to urea ratio on BET surface area of CeO₂ (UR) catalysts

Catalyst, Ce salt: urea ratio, aging time, calcination temperature / calcination time	Surface area ^a (m ² g ⁻¹)
CeO ₂ , 2:1, 24 h, 500 °C / 6 h	94
CeO ₂ , 1:1, 24 h, 500 °C / 6 h	94
CeO ₂ , 1:2, 24 h, 500 °C / 6 h	92
CeO ₂ , 1:3, 24 h, 500 °C / 6 h	125
CeO ₂ , 1:4, 12 h, 500 °C/6 h	128

^aCalculated using the BET method.

5.5.2 Effect of Ce Salt/Urea Ratio on XRD Results of CeO₂ (UR)

Similar to all other catalysts investigated in this chapter, XRD patterns of CeO₂ (UR) prepared from varying cerium salt to urea ratios (figure 5.19) showed peaks at 2θ values characteristic of cubic fluorite ceria.

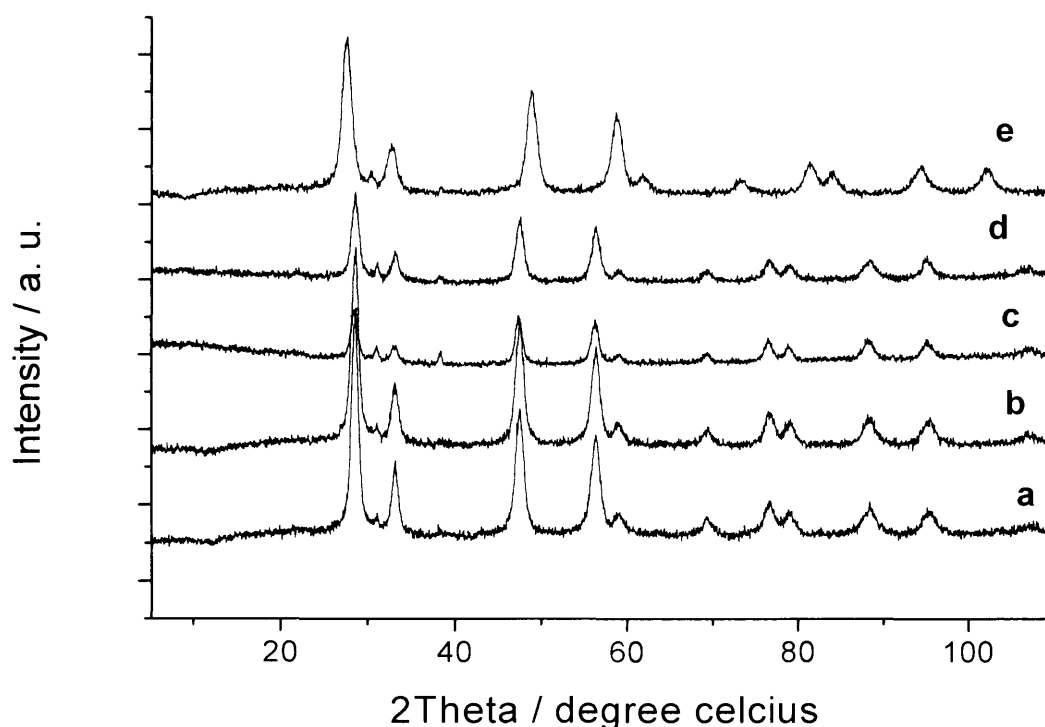


Fig. 5.19 XRD patterns of CeO_2 (UR) catalysts prepared from different cerium salt to urea ratios. a: CeO_2 , 2:1, 24 h, 500 °C/6 h, b: CeO_2 , 1:1, 24 h, 500 °C/6 h, c: CeO_2 , 1:2, 24 h, 500 °C/6 h, d: CeO_2 , 1:3, 24 h, 500 °C/6 h, e: CeO_2 , 1:4, 24 h, 500 °C/6 h.

Detailed examination of the background noise and broadness of peaks in the individual patterns suggested subtle differences in the crystalline nature of these catalysts. CeO_2 (UR) catalysts derived from cerium salt to urea ratios of 2:1, 1:1, and 1:4 showed similarity in their crystalline nature and were slightly more crystalline than catalysts prepared from 1:2 and 1:3 ratios of cerium salt and urea. The crystallite sizes of these catalysts (table 5.17) only varied slightly (6.6-7.6 nm). While catalysts with a ratio of 1:2 cerium salt/urea had the highest crystallite size (7.6 nm), CeO_2 (U) catalyst prepared from 1:4 Ce salt/urea yielded the lowest crystallite size (6.6 nm).

Table 5.17 Effect of cerium salt to urea ratio on crystal size and phase of CeO₂ (UR) catalysts

Catalyst, Ce salt: urea ratio, aging time, calcination temperature / calcination time	Crystallite size^a (nm)	Identified crystal phase^a
CeO ₂ , 2:1 , 24 h, 500 °C / 6 h	7.3	Cubic fluorite
CeO ₂ , 1:1 , 24 h, 500 °C / 6 h	7.2	Cubic fluorite
CeO ₂ , 1:2 , 24 h, 500 °C / 6 h	7.6	Cubic fluorite
CeO ₂ , 1:3 , 24 h, 500 °C / 6 h	7.4	Cubic fluorite
CeO ₂ , 1:4 , 12 h, 500 °C/6 h	6.6	Cubic fluorite

^aBy XRD analysis.

5.5.3 Effect of Ce Salt/Urea Ratio on Raman Results of CeO₂ (UR)

Raman spectra recorded for the five catalysts with varying Ce salt/urea ratio (figure 5.20) were all alike, showing the single characteristic Raman band for CeO₂ vibrations.

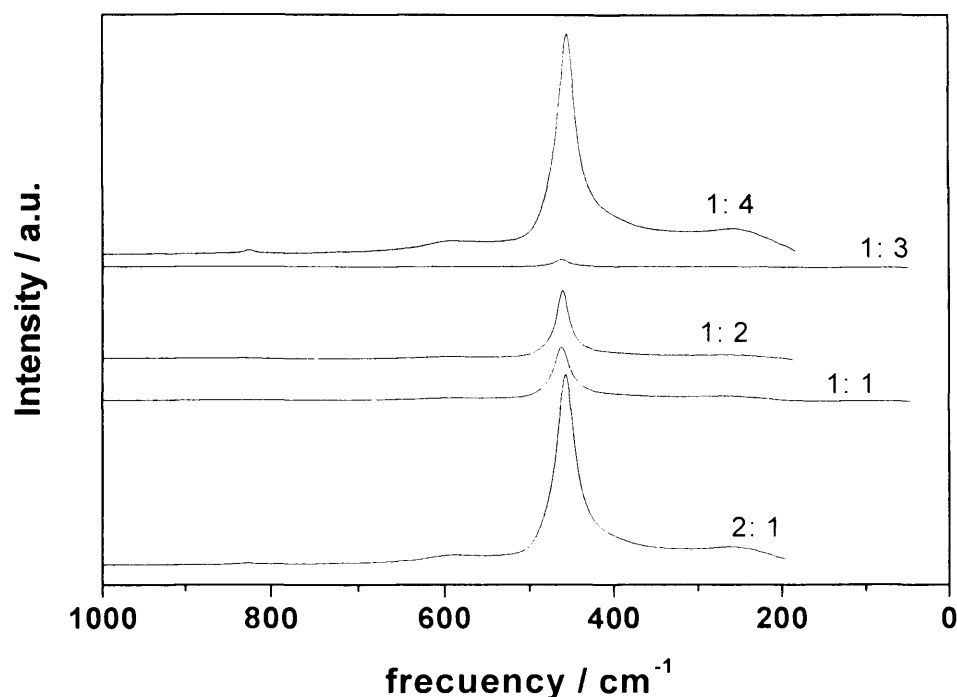


Fig. 5.20 Raman spectra of CeO₂ (UR) catalysts prepared from different cerium salt to urea ratios.

Table 5.18 shows a great variation in the FWHM of the characteristic Raman band with the change in cerium salt/urea ratio. Since the crystallite size only varied slightly with the change in this ratio, it can be assumed that an increase in FWHM corresponds to an increase in the concentration of oxygen defects. Ceria catalysts prepared from cerium salt/urea ratios of 2:1 and 1:4 showed considerably higher FWHM values (28.6 and 28 cm⁻¹ respectively) than the other three catalysts. The FWHM of the five catalysts prepared from varying Ce salt/urea ratios decrease in the order: 2:1 > 1:4 > 1:1 > 1:3 >

1:2. A comparison between the FWHM values and crystallite sizes of the five catalysts suggests that the concentration of oxygen defect decreased in the order: 1:4 \geq 2:1 > 1:1 > 1:3 > 1:2.

Table 5.18 Effect of cerium salt to urea ratio on crystal size and FWHM of Raman band of CeO₂ (UR) catalysts

Catalyst, Ce salt: urea ratio, aging time, calcination temperature / calcination time	FWHM ^a (cm ⁻¹)	Crystallite size ^b [nm]
CeO ₂ , 2:1, 24 h, 500 °C / 6 h	28.6	7.3
CeO ₂ , 1:1, 24 h, 500 °C / 6 h	23.8	7.2
CeO ₂ , 1:2, 24 h, 500 °C / 6 h	19.6	7.6
CeO ₂ , 1:3, 24 h, 500 °C / 6 h	23.0	7.4
CeO ₂ , 1:4, 12 h, 500 °C/6 h	28	6.6

^aFull width at half maximum of the CeO₂ line in the Raman spectra.

^bBy XRD analysis.

5.5.4 Effect of Ce Salt/Urea Ratio on SEM Results of CeO₂ (UR)

The SEM images of catalysts prepared from varying Ce salt/urea ratio (figure 5.21) revealed a dependence of morphology and particle size of ceria on the Ce salt/urea ratio. The figure shows a great variation in the morphology of these catalysts with Ce salt/urea ratio. Catalysts with 2:1 and 1:1 ratios of Ce salt/urea showed some similarity in morphology (composed of circular particles; all of which had fairly similar sizes for the

same catalyst). However, particles in the catalyst with 2:1 ratio appeared to be smaller and showed higher degree of agglomeration than those in catalyst with 1:1 Ce salt/urea content. Particles in the latter existed as small circular particles with a very low degree of agglomeration. Catalysts with 1:2 and 1:3 Ce salt/urea content showed large irregular shaped particles which acted as centres of aggregation for smaller particles. The catalyst with Ce salt/urea content of 1:4 showed a rather unique morphology; comprised of fairly uniform-sized tiny particles with some larger particles dispersed in it. The small size of the particles in the catalyst with 1:4 ratio relative to the other four catalyst agrees with the lowest crystallite size of the former as calculated by XRD analysis.

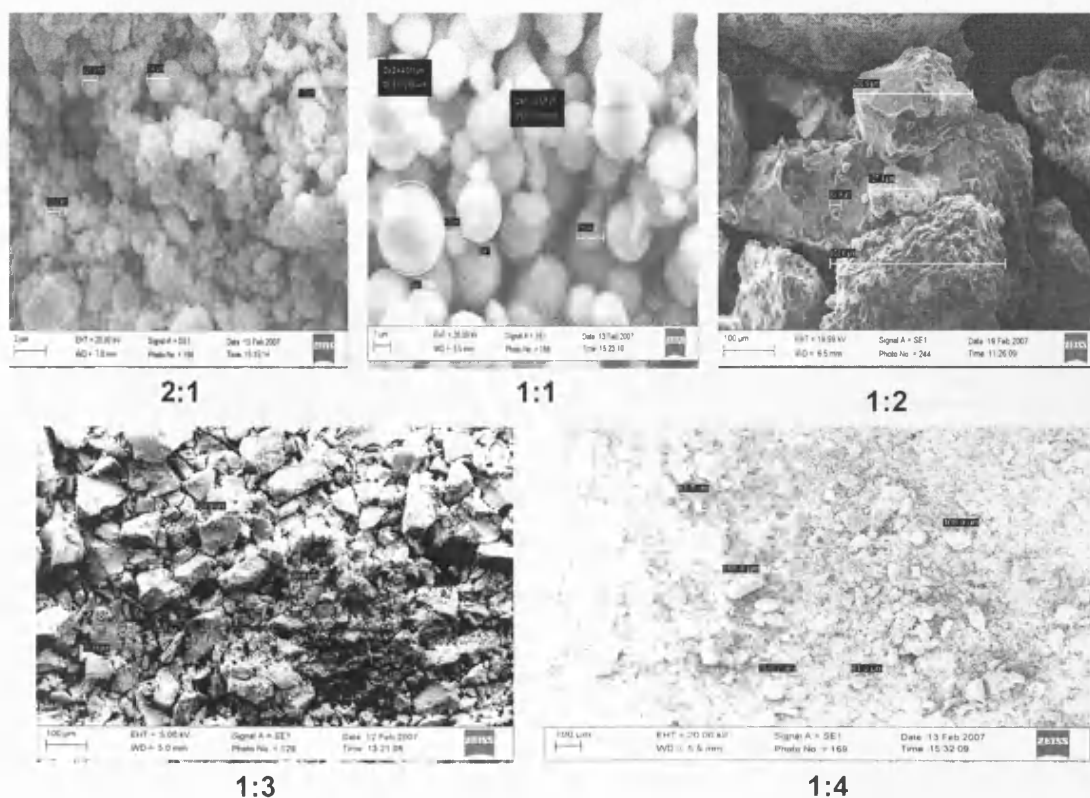


Fig. 5.21 Scanning electron micrographs of CeO₂ (UR) catalysts prepared from varying Ce salt/urea ratios.

5.5.5 Effect of Ce Salt/Urea Ratio on TPR Results of CeO₂ (UR)

Catalysts prepared from different cerium salt to urea ratios showed both the low and high temperature TPR peaks (figure 5.22).

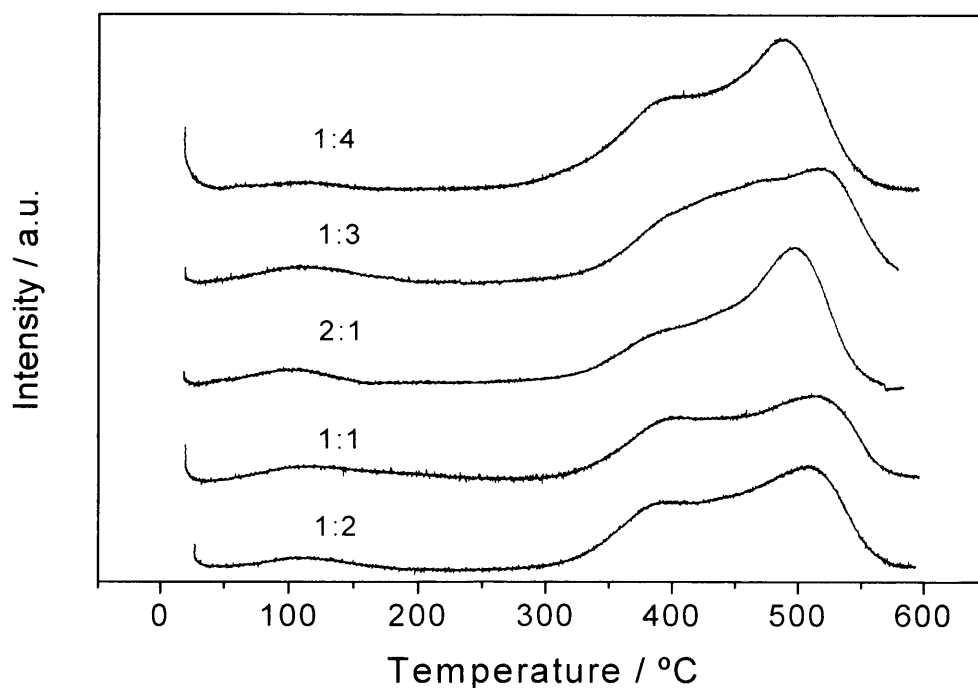


Fig. 5.22 Hydrogen temperature programmed reduction profiles for CeO₂ (UR) catalysts showing effect of cerium salt to urea ratio. TPR conditions: 110 mg of sample, 20 mL min⁻¹ H₂, 5 °C min⁻¹.

It was observed (table 5.19) that the total hydrogen consumption for these catalysts varied between 186-239 $\mu\text{mole g}^{-1}$. This variation was reflected in the variation of hydrogen

consumption both at LT ($4\text{--}29\ \mu\text{moleg}^{-1}$) and HT ($169\text{--}235\ \mu\text{moleg}^{-1}$). The total hydrogen consumption increased as the Ce salt/urea ratio was changed from 2:1 to 1:4. The variation in hydrogen consumption with cerium salt to urea ratio probably represents the formation of slightly different surface structures of ceria as the Ce salt/urea content is varied. This is consistent with differences observed in the SEM images of these catalysts.

Table 5.19 Effect of cerium salt to urea ratio on hydrogen consumption (TPR) of CeO_2 (UR) catalysts

Catalyst, Ce salt: urea ratio, aging time, calcination temperature / calcination time	H_2 consumption (μmoleg^{-1}) at LT ^a	H_2 consumption (μmoleg^{-1}) at HT ^a	Total H_2 consumption (μmoleg^{-1}) ^a
CeO_2 , 2:1, 24 h, 500 °C / 6 h	10	176	186
CeO_2 , 1:1, 24 h, 500 °C 6 h	29	169	198
CeO_2 , 1:2, 24 h, 500 °C / 6 h	15	189	204
CeO_2 , 1:3, 24 h, 500 °C / 6 h	18	212	230
CeO_2 , 1:4, 12 h, 500 °C/6 h	4	235	239

^aBy TPR analysis, 110 mg of sample, $20\ \text{mL min}^{-1}\ \text{H}_2$, $5\ ^\circ\text{C min}^{-1}$.

5.5.6 Effect of Cerium Salt to Urea Ratio on Activity of CeO₂ (UR) Catalyst for the Total Oxidation of Naphthalene

Figure 5.23 shows the effect of the ratio of starting materials (cerium salt and urea) on the activity of CeO₂ (UR) catalyst in naphthalene oxidation. The activity of CeO₂ (UR) prepared from a cerium salt to urea ratio of 1:4 was slightly higher than those from 1:1 and 2:1. The CeO₂, 1:4 catalyst equally showed an activity considerably higher than CeO₂, 1:2 and 1:3. 1:4, 1:1 and 2:1 ratios of cerium salt to urea resulted in more efficient naphthalene oxidation catalysts than the 1:3 ratio employed for the synthesis of the reference catalyst.

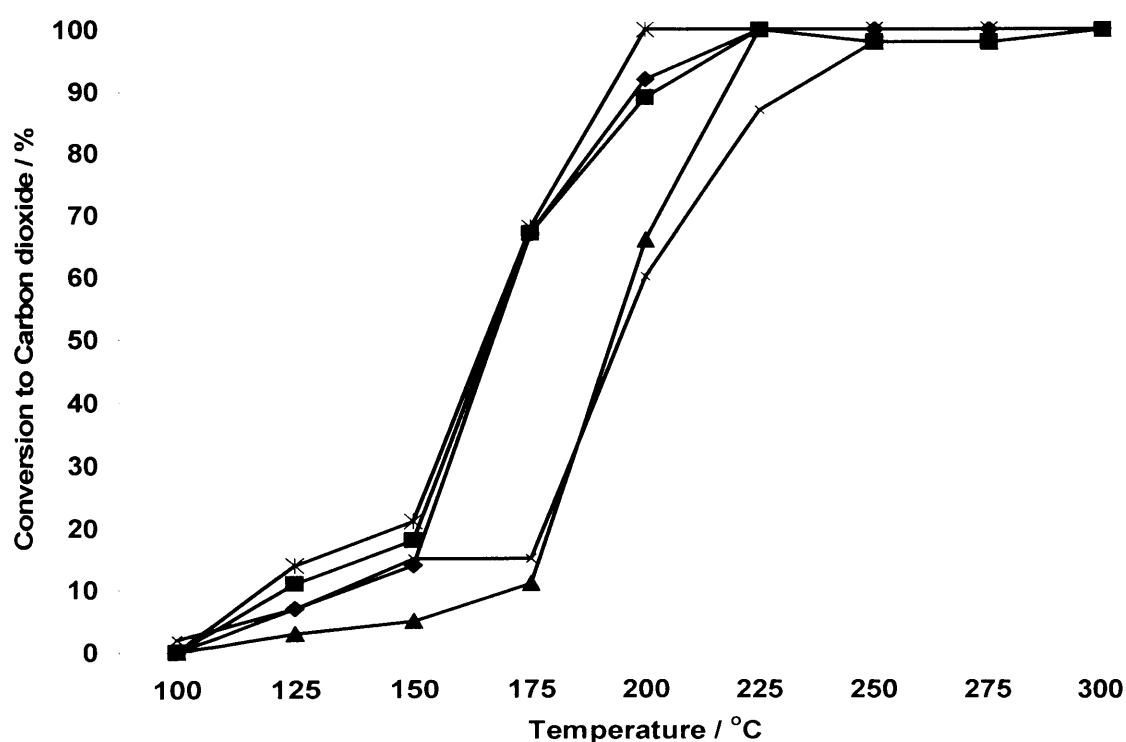


Fig. 5.23 Effect of Ce salt/urea ratio on the Np oxidation activity of CeO₂ (UR) catalyst

CeO₂ (UR), 1:4, 24 h, 500 °C / 6 h had the highest surface area (128 m²g⁻¹) , lowest crystallite size (6.6 nm) and about the highest concentration of oxygen defect amongst catalysts with varying cerium salt to urea ratios and this probably accounted for the higher activity. No clear correlations could be made between naphthalene oxidation activity and BET surface area, crystallite size or hydrogen consumption during TPR. However, it was observed that Naphthalene oxidation activity increased with an increase in FWHM (figure 5.24). Ceria catalysts with higher values of FWHM and hence higher oxygen defect concentrations (prepared from cerium salt/urea ratios of 2:1, 1:4 and 1:1) showed considerably higher naphthalene oxidation activities than catalysts with lower FWHM values or lower oxygen defect concentrations (prepared from 1:2 and 1:3 Ce salt/urea ratios) over the temperature range investigated. It is therefore obvious that the concentration of oxygen defect was a major factor determining the activity of ceria catalysts prepared from varying cerium salt to urea ratios. The differences in catalytic activity can also be linked to differences in morphology as SEM images of the five catalysts showed a mark variation in the morphology with cerium salt/urea ratio. This was consistent with the variation in surface structure as suggested by differences in hydrogen consumption during TPR. The variation in morphology and oxygen defect concentration with Ce salt/urea ratio therefore appear to be the major factors accounting for the differences observed in Np oxidation activity. High surface area of CeO₂ also seems to favor the oxidation of naphthalene.

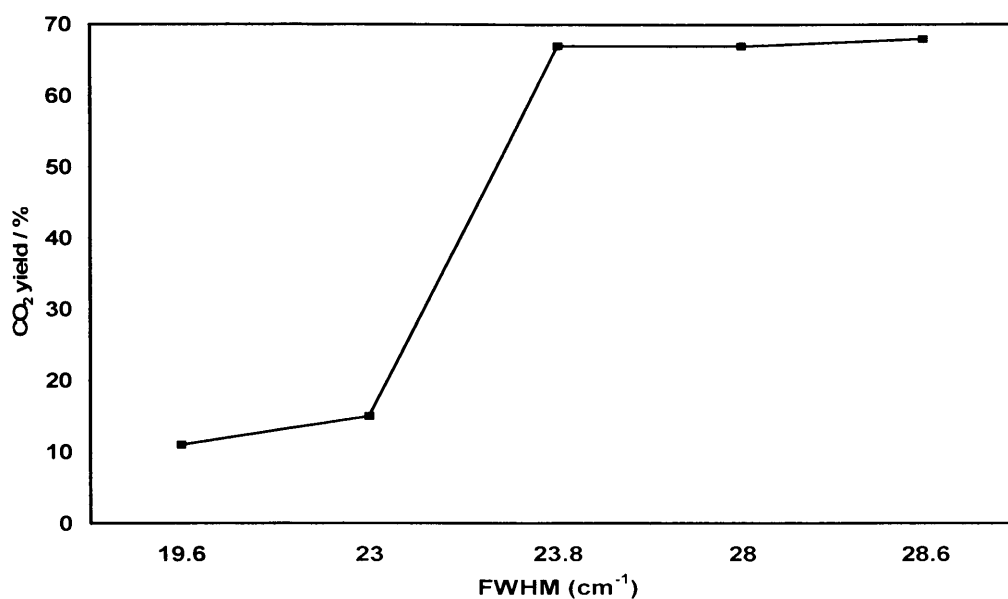


Fig. 5.24 Relationship between FWHM and naphthalene oxidation activity (yield to CO₂) at 175 °C

Figure 5.25 shows the effect of cerium salt to urea ratio on the rate of naphthalene oxidation per unit surface area of catalyst at 175 °C. The figure reveals that the naphthalene oxidation rate per unit surface area of catalyst decreased in the order: 2:1 > 1:1 > 1:4 > 1:2 > 1:3. CeO₂ (UR) catalysts with cerium salt to urea ratios of 2:1, 1:1, and 1:4 showed considerably higher naphthalene oxidation rates per unit surface area than catalysts with 1:2 and 1:3 ratios.

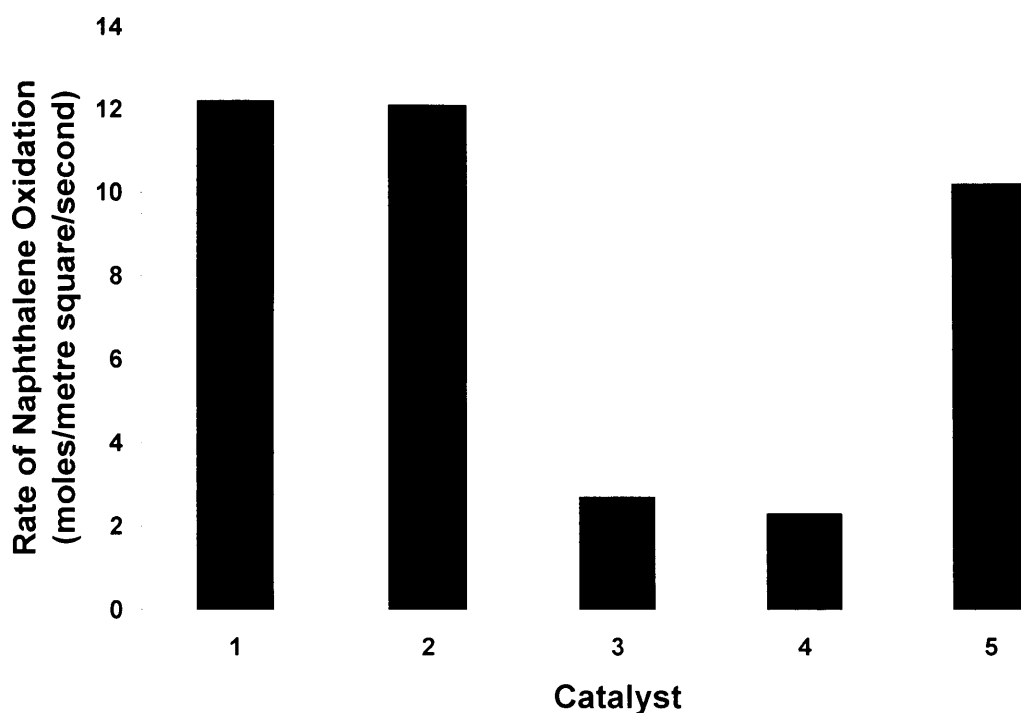


Fig. 5.25 Effect of cerium salt to urea ratio on the rate of naphthalene oxidation per unit surface area of ceria catalyst at constant temperature (175 °C). 1: CeO₂, 2:1, 24 h, 500 °C/6 h, 2: CeO₂, 1:1, 24 h, 500 °C/6 h, 3: CeO₂, 1:2, 24 h, 500 °C/6 h, 4: CeO₂, 1:3, 24 h, 500 °C/6 h, 5: CeO₂, 1:4, 24 h, 500 °C / 6 h. Values of rate are x 10⁻¹¹.

The concentration of oxygen defects for the five catalysts increased in an order (1:4 ≥ 2:1 > 1:1 > 1:2 > 1:3) that reflects the order discussed for the rate of naphthalene oxidation. It is therefore obvious that changes in the concentration of oxygen defects with the cerium salt to urea ratio resulted in differences in the naphthalene oxidation rate. Catalysts with high oxygen defect concentrations (higher FWHM of Raman band) gave higher naphthalene oxidation rates compared to catalysts with low oxygen defect concentrations (see figure 5.26). Ceria catalysts with 2:1 and 1:1 cerium salt to urea ratios demonstrated

a mark disparity in naphthalene oxidation rate per unit surface area irrespective of their similarity in surface area ($94 \text{ m}^2\text{g}^{-1}$). This suggests that surface area was not the only important parameter determining the rate of naphthalene oxidation for this set of catalysts. Hence oxygen defect concentration and morphology of the ceria catalyst prepared from varying cerium salt to urea ratio were crucial in determining the rate of naphthalene oxidation.

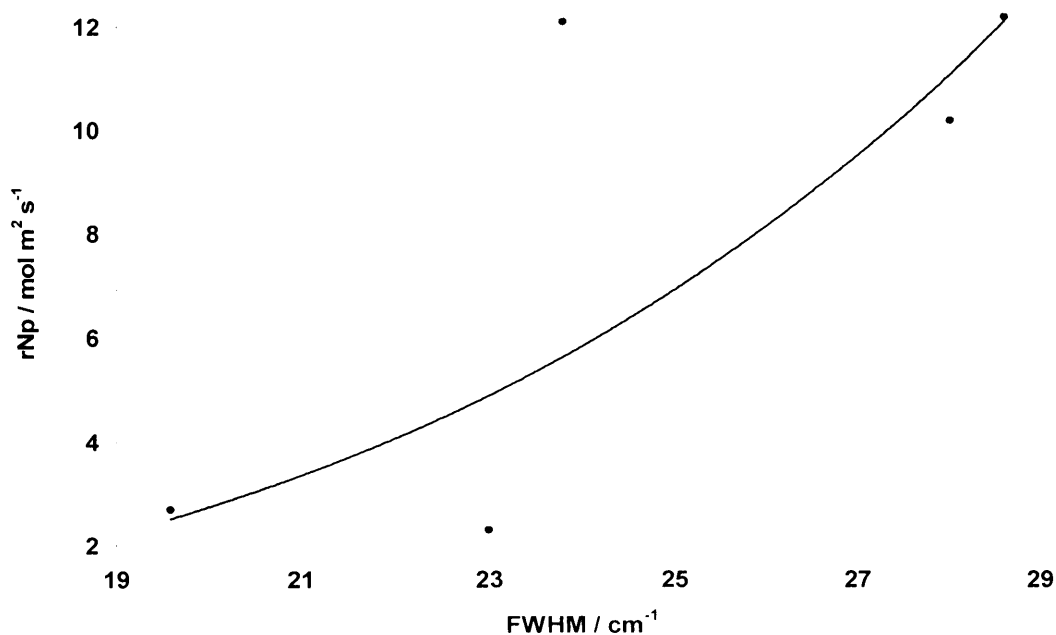


Fig. 5.26 Relationship between FWHM of Raman band of CeO₂ (UR) catalysts and Np oxidation rate at 175 °C

5.6 Effect of GHSV on the activity of CeO₂ (UR) catalysts for Naphthalene Oxidation

The activity results reported herein suggest that the optimum preparation conditions for CeO₂ (UR) catalyst for the total oxidation of naphthalene include: a cerium salt to urea ratio of 1:4, 2:1 or 1:1, aging time of 12 h, calcination temperature of 500 °C and a calcination time of 6 h. The use of some of these optimum preparation conditions (ratio of 1:4, aging time of 12 h, calcination temperature/time of 500 °C/6 h) yielded a CeO₂ (UR) catalyst with a relatively high surface area (126 m²g⁻¹) and small crystallite size (5.4 nm). Figure 5.27 shows that the activity of a CeO₂ (UR) catalyst prepared using these optimum preparation conditions decreased with increase in GHSV at constant temperature. The catalyst gave a 100 % naphthalene conversion and a carbon dioxide yield of over 90 % at 175 °C (GHSV = 25,000 h⁻¹).

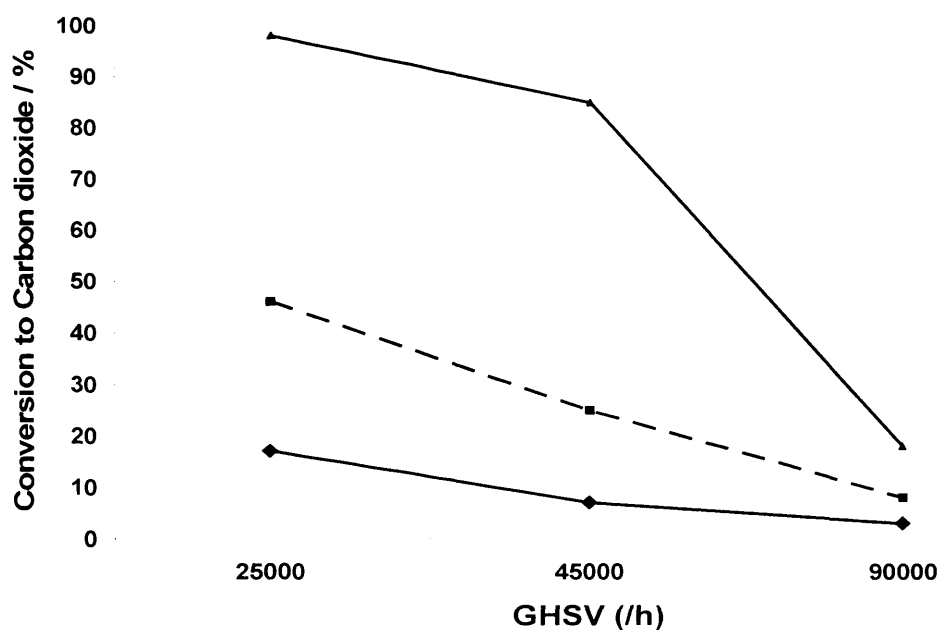


Fig. 5.27 Plot showing the effect of GHSV on the activity of CeO_2 (UR) prepared using optimum preparation conditions.

◆ 125 °C, -■- 150 °C, -▲- 175 °C.

5.7 Summary of the activity of CeO_2 (UR) catalysts for Naphthalene Oxidation

In this chapter a detailed study of catalysts based on CeO_2 prepared using urea has been carried out for the oxidation of naphthalene. A similar preparation method has been described to be very efficient in naphthalene oxidation at moderate temperatures and with a high adsorption capacity at low temperatures. Thus, by employing urea during the synthesis procedure, higher reaction rates have been reported compared to conventionally prepared CeO_2 catalysts [37, 38].

It has been demonstrated in this chapter that preparation conditions are of significant importance to obtain highly active catalysts. Depending on the conditions employed the catalytic activity can vary by a factor until 3. However, it would be desirable to know the parameters that determine this catalytic performance.

Figure 5.28a plots the CO₂ yield obtained at 225 °C with different CeO₂ (UR) catalysts prepared in this work versus their surface area. High surface areas seem to be positive to achieve high conversions although the relationship is not as direct as mentioned. In fact, a catalyst with a surface area of 33 m²g⁻¹ gave a conversion similar to other catalysts with higher surface areas (ca. 120 m²g⁻¹).

Figure 5.28b represents the variation of catalytic activity with crystallite size. The relationship again is not a straightforward one. It is worth noting that the catalyst with the largest crystal size yielded the highest naphthalene oxidation rate, showing the influence of other factors. Figure 5.28c shows a plot of the catalytic activity versus the full width at half maximum of the Raman band at 464 cm⁻¹.

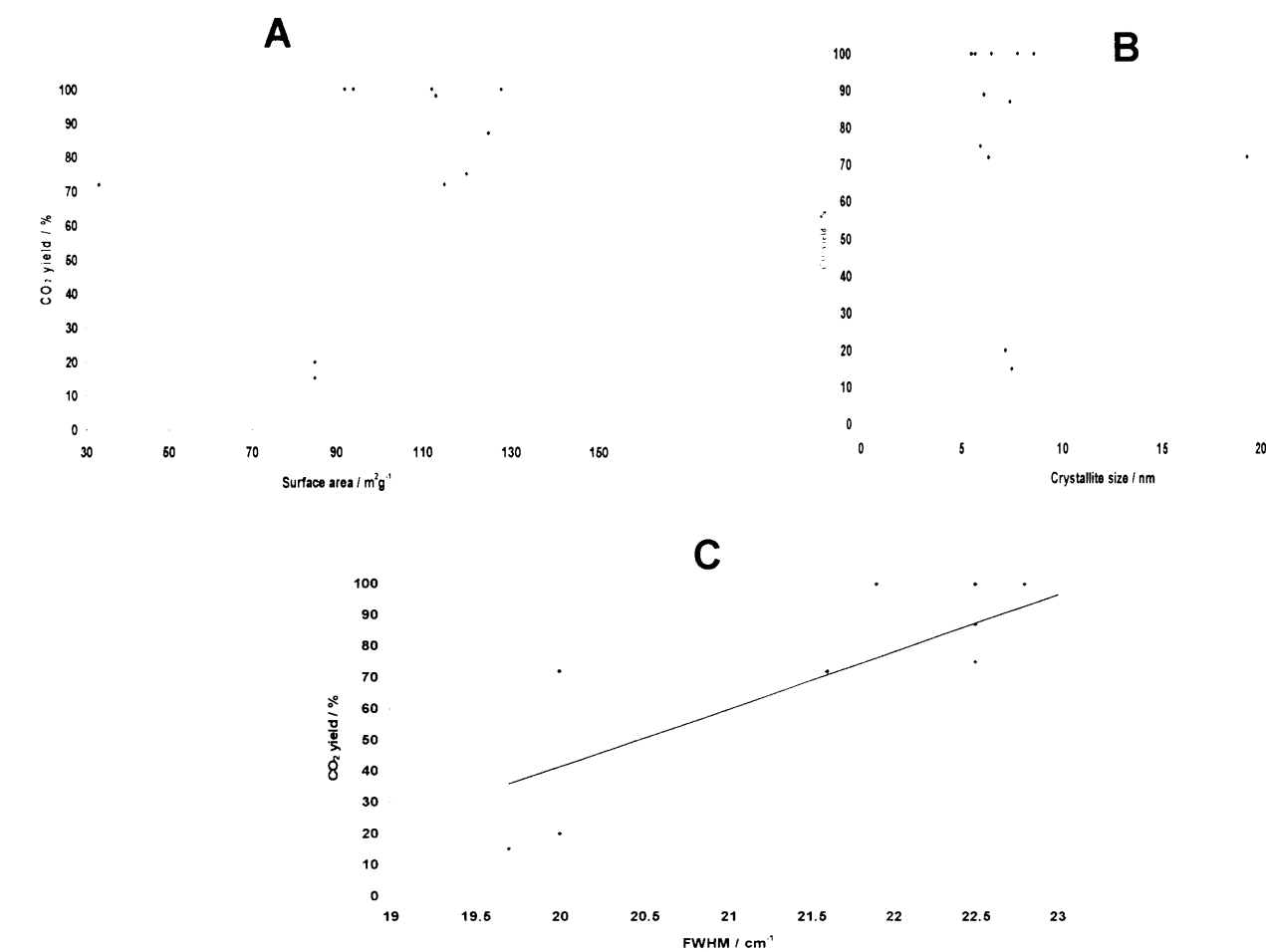


Fig. 5.28 Influence of a) surface area, b) crystal size of CeO₂ and c) FWHM of Raman band on the catalytic activity. Note: Catalytic activity at a reaction temperature = 225°C. Reaction conditions as described in chapter 2. Catalytic activity expressed as yield to CO₂.

A more reasonable relationship is observed in this case as the higher the FWHM the higher the catalytic activity. The FWHM has been associated to the presence of oxygen defects and/or the crystal size of ceria. Since no clear correlation was evident between

crystallite size and Np oxidation activity, it can be concluded that the FWHM was more related to the oxygen defect concentration than to the crystallite size of ceria. Note however that the crystallite size and oxygen defect concentration were both very crucial in determining the activity of the ceria catalyst for naphthalene oxidation.

5.8 Conclusions

It has been shown that the activity of a CeO₂ catalyst prepared by homogeneous precipitation with urea in naphthalene total oxidation can be optimized by varying the preparation conditions (calcination temperature, calcination time, aging time and cerium salt to urea ratio). A variation in these conditions resulted to differences in surface area, crystallite size, oxygen defect concentration (FWHM of characteristic Raman band), morphology and reducibility of the CeO₂ (UR) catalyst. A combination of high surface area, small crystallite size and high oxygen defect concentration was found to favor the activity of the CeO₂ catalyst in naphthalene oxidation. Optimum preparation conditions in this study included: a cerium salt to urea ratio of 1:4, 2:1 or 1:1, aging time of 12 h, calcination temperature of 500 °C and a calcination time of 6 h. CeO₂ catalyst prepared from these optimum preparation conditions yielded 100 % naphthalene conversion and over 90 % CO₂ yield at 200 °C (GHSV = 45,000 h⁻¹).

References

1. H.-I. Chen, and H.-Y. Chang, Solid State Commun. 133 (2005) 593.
2. A. Trovarelli, C. de Leitenburg, M. Boaro, and G. Dolcetti, Catal. Today 50 (1999) 353.
3. J. Lahaye, S. Boehm, P. H. Chambrion, and P. Ehrburger, Combustion and Flame, 104 (1996) 199.
4. Y. I. Matatov-Meytal, and M. Sheintuch, Ind. Eng. Chem. Res. 37 (1998) 309.
5. W. Liu, and M. Flytzani-Stephanopoulos, J. Catal. 153 (1995) 317.
6. K. Otsuka, M. Hatano, and A. Morikawa, J. Catal. 79 (1983) 493.
7. M. Shelef, and G. W. Graham, Catal. Rev.-Sci. Eng. 36 (1994) 433.
8. A. Trovarelli, Catal. Rev.-Sci. Eng. 38 (1996) 439.
9. H. S. Gandhi, and M. Shelef, Stud. Surf. Sci. Catal. 30 (1987) 199.
10. R. W. McCabe, and J. M. Kisenyi, Chem. Ind. 15 (1995) 605.
11. G. B. Fisher, J. R. Theis, M. V. Casarella, and S. T. Mahan, SAE paper 931034 (1993).
12. K. K. Herz, and J. A. Sell, J. Catal. 94 (1985) 199.
13. J. G. Nunan, H. J. Robota, M. J. Cohn, and S.A. Bradley, J. Catal. 133 (1992) 309.
14. E. C. Su, C. N. Montreuil, and W. W. Rothschild, Appl. Catal. 17 (1985) 75.
15. S. Kasimi, J. Barbier Jr., R. Taha, and D. Duprez, Catal. Lett. 22. (1993) 343.
16. G. S. Zafiris, and R. J. Gorte, J. Catal. 143 (1993) 86.
17. H. C. Yao, and Y. F. Yu , J. Catal. 86 (1984) 254.
18. J. Sarlis, and D. Berk, Ind. Eng. Chem. Res. 27 (1988) 1951.

19. D. J. Mulligan, and D. Berk, *Ind. Eng. Chem. Res.* 28 (1989) 926.
20. T. S. Wiltowski, K. Sangster, and W. S. O' Brien, *J. Chem. Tech. Biotech.* 7 (1996) 204.
21. E. M. Nekrich, A. N Kontsevaya, and G. F. Ganzha, *J. Appl. Chem. U. S. S. R.* 51 (1978) 517.
22. D. J. Mulligan, and D. Berk, *Ind. Eng. Chem. Res.* 31 (1992) 119.
23. J. Sarlis, and D. Berk, *Chem. Eng. Commun.* 140 (1996) 73.
24. J. J. Yu, Q. Yu, Y. Jin, and S. G. Chang, *Ind. Eng. Chem. Res.* 36 (1997) 2128.
25. V.A. Zazhigalov, S. V. Gerei, and M. Rubanik, *Kinet. Katal.* 4 (1975) 967.
26. T. Chivers, J. B. Hyne, and C. Lau, *Int. J. Hydrogen Energy* 5 (1980) 499.
27. S. C. Moffat, and A. A. Adesina, *Catal. Lett.* 37 (1996) 167.
28. N. C. Wu, E. W. Shi, Y. Q. Zheng, and W. J. Li, *J. Am. Ceram. Soc.* 85 (2002) 2462.
29. M. Hirano, and E. Kato, *J. Mater. Sci. Lett.* 15 (1996) 1249.
30. C. H. Wang, and S. S. Lin, *Appl. Catal. A: Gen.* 268 (2004) 227.
31. L. Yin, Y. Wang, G. Pang, Y. Koltypin and A. Gedanken, *J. Colloid Interf. Sci.* 246 (2002) 78.
32. H. Xu, L. Gao, H. Gu, J. Guo, and D. Yan, *J. Am. Ceram. Soc.* 85 (2002) 139.
33. T. Masui, K. Fujiwara, K. I. Machida, G. Y. Adachi, T. Sakata, and H. Mori, *Chem. Mater.* 9 (1997) 2197.
34. W. Liu and M. Flytzani-Stephanopoulos, *J. Catal.* 53 (1995) 304.
35. X. D. Zhou, W. Huebner and H. U. Anderson, *Appl. Phys. Lett.* 80 (2002) 3814.

36. M. Yamashita, K. Kameyama, S. Yabe, S. Yoshida, Y. Fujishiro, T. Kawai, and T. Sato, *J. Mater. Sci.* 37 (2002) 683.
37. T. Garcia, B. Solsona, and S. H. Taylor, *Catal. Lett.*, 105 (2005) 183.
38. T. Garcia, B. Solsona, and S. H. Taylor, *Appl. Catal. B:Environ.* 66 (2006) 92.
39. W.H. Weber, K.C. Hass, and J.R. McBride 48 (1993) 178.
40. D. Andreeva, R. Nedyalkova, L. Ilieva and M. V. Abrashev, *Appl. Catal. B: Environ.* 52 (2004) 157.
41. M. F. L. Johnson, and J. Mooi, *J. Catal.* 103 (1987) 502.
42. C. C. Hwang, T. H. Huang, J. S. Tsai, C. S. Lin, C. H. Peng *Mater. Sci. and Eng.: B* 132 (2006) 229.

CHAPTER 6: CERIA AND Pt-LOADED CERIA CATALYSTS FOR TOTAL OXIDATION OF NAPHTHALENE

6.1 Introduction

In chapter 5, it has been shown that preparation conditions can be varied to improve the activity of a ceria catalyst prepared by homogeneous precipitation with urea [CeO_2 (UR)] for naphthalene oxidation. In this chapter, ceria catalysts, prepared using other methods, are compared with the best CeO_2 (UR) catalyst for total naphthalene oxidation. T. Garcia et al. [1] showed that CeO_2 (UR) was a better naphthalene oxidation catalyst than CeO_2 prepared by precipitation with the carbonate [CeO_2 (CR)] and CeO_2 prepared by a redox reaction with H_2O_2 [CeO_2 (H_2O_2)]. In this chapter characteristics and naphthalene oxidation catalytic data for CeO_2 (UR), CeO_2 (CR) prepared in a slightly different way as reported by T. Garcia et al. and CeO_2 prepared using supercritical carbon dioxide (scCeO_2) are compared. The CeO_2 (UR) catalyst was prepared using the optimum preparation conditions derived in chapter 5. The catalyst was made from Ce salt/urea ratio of 1:4, aged for 12 h and calcined at 500 °C for 6 h. This CeO_2 (UR) catalyst was equally compared for naphthalene complete oxidation with a Pt-loaded CeO_2 (UR) catalyst prepared in a similar manner as the CeO_2 (UR) catalyst.

6.2 Influence of Preparation Method of Crystalline Ceria Catalysts for the Total Oxidation of Naphthalene

In this section, properties and naphthalene oxidation activity of ceria catalysts prepared by four different methods (homogeneous precipitation with urea [CeO_2 (UR)], precipitation with the carbonate [CeO_2 (CR)], using supercritical carbon dioxide [scCeO_2] and a commercially available ceria catalyst [CeO_2 (Aldrich)]) are evaluated. CeO_2 (UR), CeO_2 (CR) and scCeO_2 , were prepared as detailed in chapter 2. The method used for the preparation of the commercial ceria catalyst, CeO_2 (Aldrich), is unknown. Characteristics and naphthalene oxidation activity for these catalysts are reported in the following sections.

6.2.1 Influence of Preparation Method on Characteristics of Crystalline Ceria Catalysts

Ceria catalysts derived from the four methods mentioned above were characterized by BET, XRD, Raman spectroscopy, SEM and H_2 -TPR.

Table 6.1 shows the BET surface areas of the four ceria catalysts. The surface areas varied greatly ($11\text{--}126\text{ m}^2\text{g}^{-1}$) with preparation method. Whilst CeO_2 (UR) had a surface area ($126\text{ m}^2\text{g}^{-1}$) considerably higher than the other three catalysts, the commercial catalyst showed the lowest surface area ($11\text{ m}^2\text{g}^{-1}$) amongst the four catalysts. Surface area decreased in the order: CeO_2 (UR) > CeO_2 (CR) > scCeO_2 > CeO_2 (Aldrich). Hence

the method of ceria preparation played a very important role in determining the surface area of the catalyst.

The use of different starting materials and preparation conditions could be used to explain the differences in surface area observed. For instance, calcination temperature and time has been known to determine the surface area of CeO_2 [2]. It is therefore likely that the calcination conditions contributed significantly to the variation in surface area with preparation method. While the CeO_2 (UR) catalyst was calcined at 500 °C for 6 h, scCeO_2 and CeO_2 (CR) were calcined at 400 °C for 2 h and 500 °C for 10 h respectively. Notice that CeO_2 (UR) and CeO_2 (CR) calcined at a higher temperature (500 °C) and for a longer time (6-10 h) than scCeO_2 (400 °C for 2 h) both had higher surface areas (126 and 105 m^2g^{-1} respectively) than the scCeO_2 catalyst (surface area = 31 m^2g^{-1}). High calcination temperature and longer calcination time probably led to the complete removal of any un-decomposed starting materials (e.g. urea or carbonate) or undesired derivative of the starting materials from the ceria pores. Although the calcination temperature for the commercial CeO_2 (Aldrich) catalyst is unknown, it can be inferred based on the above argument that this catalyst (with the lowest surface area) was either calcined at a lower or higher temperature/duration than the other ceria catalysts. Very high calcination temperatures can result in the collapse of the porous structure and sintering.

Table 6.1 Effect of preparation method on BET surface area of Ceria catalysts

Catalyst	BET Surface Area ^a / m ² g ⁻¹
CeO ₂ (UR)	126
CeO ₂ (CR)	105
scCeO ₂	31
CeO ₂ (Aldrich)	11

^a By BET method

The XRD patterns for the four ceria catalysts are shown in figure 6.1. The figure suggests that all four preparation methods led to the formation of the same cubic fluorite ceria phase.

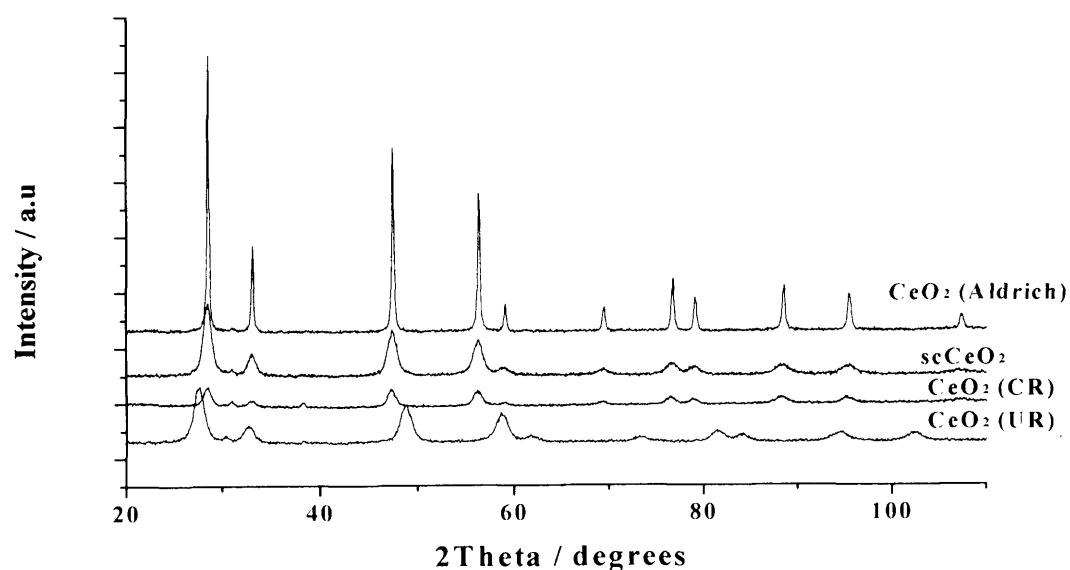


Fig. 6.1 XRD patterns of ceria catalysts prepared using four different preparation methods.

It is obvious from the broadness of the peaks observed in the XRD patterns that the commercial CeO₂ (Aldrich) catalyst was considerably more crystalline than the other three CeO₂ catalysts. This is reflected in its remarkably higher crystallite size (determined using the Scherer method) relative to the other ceria catalysts (see table 6.2). It has been reported that high crystallinity of ceria can be induced by a high calcination temperature of the ceria precursor [2, 3, 4]. However, a short calcination time favors incomplete removal of less crystalline (more amorphous) components (e.g carbonate) derived from the starting materials and this result in lower crystallite size of ceria [2]. It can therefore be concluded that the preparation of the commercial ceria catalyst which had the highest crystallite size and lowest surface area, involved higher calcination temperature and/or longer calcination time than the other three ceria catalysts (UR, CR, sc) synthesized in this study.

Table 6.2 shows the variation in crystallite size of ceria with preparation method. There occurred an inverse relationship between surface area and crystallite size. CeO₂ (UR) with the highest surface area (126 m²g⁻¹) had the lowest crystallite size (5.4 nm) while the commercial CeO₂ (Aldrich) catalyst which showed the lowest surface area (11 m²g⁻¹) had the largest crystallite size (> 100 nm). This inverse relationship observed between crystallite size and surface area is probably due to differences in calcination conditions (temperature and time). Both factors probably affected the surface area and crystalline size of ceria in a similar manner as discussed earlier. Note however that the relationship between calcination conditions and properties (crystallite size and surface area) of the four ceria catalysts is not very direct, suggesting the influence of other factors. It is

therefore likely that the differences in the nature of starting materials and reaction conditions used to yield the ceria precursor were equally very important contributing factors. The nature of the precursor determines the ease with which ceria is derived and hence the effect of calcination conditions on properties of ceria. Some precursors might require severe or mild heat-treatment than others to achieve similar properties of ceria.

Table 6.2 Effect of preparation method on crystallite size and surface area of ceria catalysts

Catalyst	Calcination temperature (°C)	Calcination time (h)	BET Surface Area ^a / m ² g ⁻¹	Crystallite size ^b / nm
CeO ₂ (UR)	500	6	126	5.4
CeO ₂ (CR)	500	10	105	6.1
scCeO ₂	400	2	31	6.3
CeO ₂ (Aldrich)	unknown	Unknown	11	> 100

^a By BET method

^b By XRD analysis

Fig 6.2 shows that the Raman spectra for all four CeO₂ catalysts were alike irrespective of the preparation method. The main Raman band observed at ca. 460 cm⁻¹ corresponds to CeO₂ vibration. Table 6.3 shows that the FWHM of this characteristic Raman band varied with preparation method.

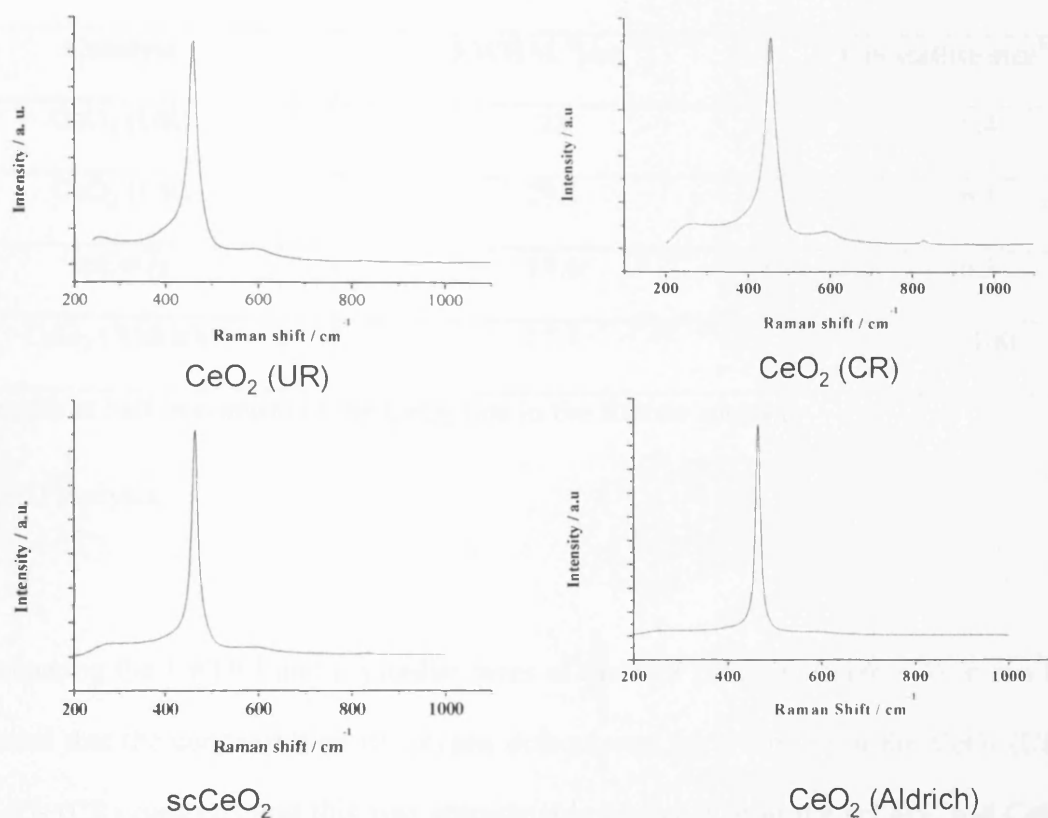


Fig 6.2 Raman spectra of Ceria catalysts prepared using three different methods (UR, CR, sc and commercial Aldrich)

The FWHM of the main Raman band for the four ceria catalysts decreased in the order: CeO_2 (CR) > CeO_2 (UR) > scCeO_2 > CeO_2 (Aldrich). CeO_2 (UR) and CeO_2 (CR) showed fairly similar values of FWHM which were considerably higher than the FWHM for scCeO_2 and CeO_2 (Aldrich). As discussed earlier in chapter 5, an increase in FWHM can be related to a decrease in crystallite size or an increase in the concentration of oxygen defects.

Table 6.3 FWHM and crystallite size of ceria catalysts prepared from varying methods

Catalyst	FWHM ^a [cm ⁻¹]	Crystallite size ^b / nm
CeO ₂ (UR)	28	5.4
CeO ₂ (CR)	29.5	6.1
scCeO ₂	19.6	6.3
CeO ₂ (Aldrich)	17.1	> 100

^aFull width at half maximum of the CeO₂ line in the Raman spectra.

^bBy XRD analysis.

By comparing the FWHM and crystallite sizes of the four catalysts (table 6.3), it can be concluded that the concentration of oxygen defects was fairly similar in the CeO₂ (UR) and CeO₂ (CR) catalysts and this was considerably higher than in the scCeO₂ and CeO₂ (Aldrich) catalysts. The CeO₂ (Aldrich) catalyst with a marginally higher crystallite size appears to have the lowest concentration of oxygen defect. It has been reported that incompletely calcined ceria particles have highly activated surfaces due to oxygen vacancies [3, 5, 6]. This suggest that in addition to influencing the surface area and crystallite size, the differences in calcination conditions also affect the amount of oxygen vacancies in ceria catalyststs prepared from varied methods. Ceria prepared by UR, CR and sc showed higher FWHM and considerably lower crystallite sizes than the commercial ceria (Aldrich) catalyst, suggesting higher concentration of oxygen defect in the former. This again, implied that there was more incompletely calcined ceria particles in CeO₂ (UR), CeO₂ (CR) and scCeO₂ than in the commercial CeO₂ (Aldrich) catalyst.

Hence, higher calcination temperature and/or time were employed in the synthesis of the latter than the former.

Figure 6.3 shows that different preparation methods resulted in ceria catalysts with differences in particle size and morphology. Hence the preparation method is crucial in determining the particle size and morphology of a ceria catalyst.

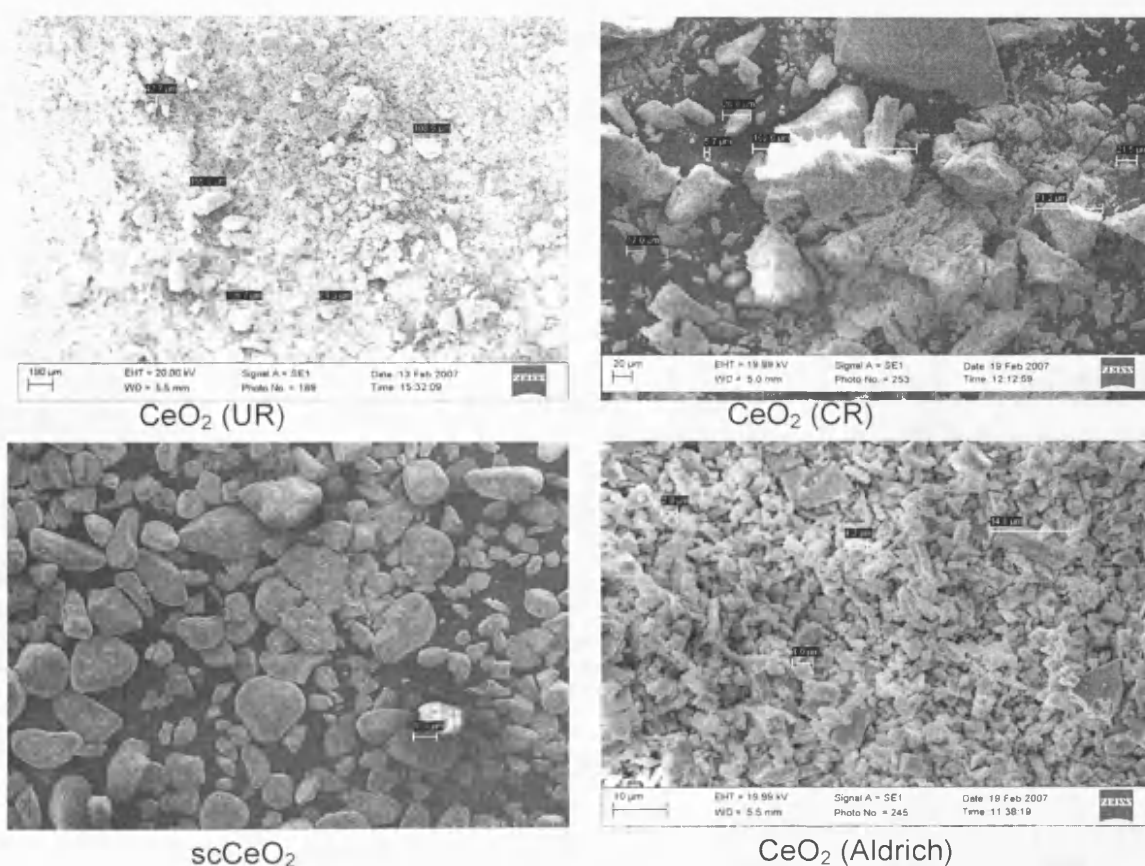


Fig. 6.3 Scanning electron micrographs for ceria catalysts showing effect of preparation method on morphology. Black regions represent carbon from the circular disc used to mount the sample on the sample holder.

TPR assays of ceria catalysts prepared using the four different preparation methods are shown in figure 6.4. While CeO_2 (UR), CeO_2 (CR) and scCeO_2 showed both the LT and HT peaks in the regions 75-150 °C and 250-600 °C respectively, the commercial CeO_2 (Aldrich) catalyst only showed a very small HT peak in the range 300-600 °C. As discussed earlier in chapter 5, the LT peak has been attributed to highly reducible surface ceria species, whereas the HT peak has been related to surface reduction of capping oxygen. The reduction of scCeO_2 at HT was completed at a lower temperature (250-500 °C) than the other CeO_2 catalysts. scCeO_2 and CeO_2 (Aldrich) showed considerably less intense HT TPR peaks than CeO_2 (UR) and CeO_2 (CR).

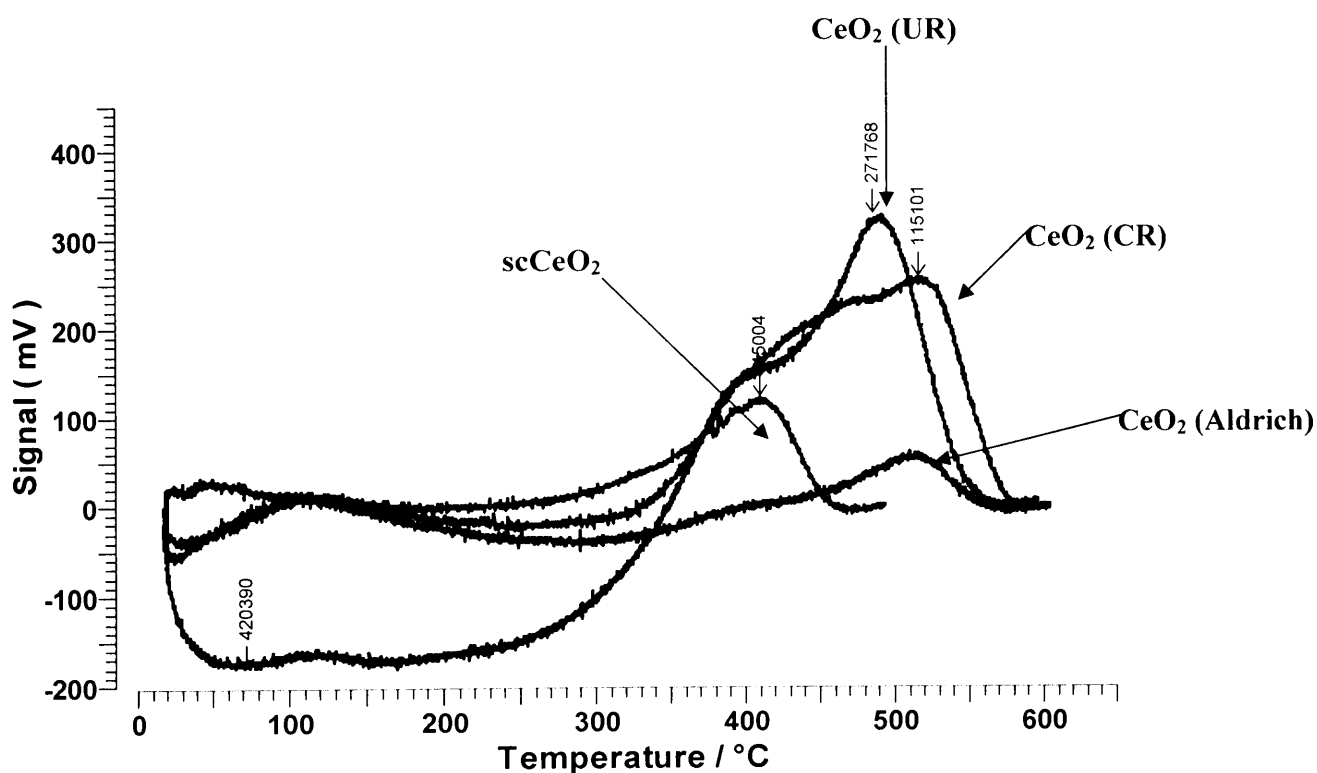


Fig. 6.4 Effect of preparation method on hydrogen TPR profile of ceria catalyst (110 mg of sample, 20 mL min⁻¹ H₂, 5 °C min⁻¹)

Table 6.4 shows the variation in hydrogen consumption at LT and HT with preparation method. The total hydrogen consumption decreased in the order: CeO_2 (UR) > CeO_2 (CR) > scCeO_2 > CeO_2 (Aldrich). The total hydrogen consumption was proportional to the surface area of the ceria catalyst (see table 6.4). CeO_2 (UR) and CeO_2 (CR) with marginally higher surface areas than the scCeO_2 and CeO_2 (Aldrich) showed considerably higher hydrogen consumption than the latter. This confirmed earlier suggestion that the LT and HT TPR peaks observed were mainly due to reduction of surface species. It can therefore be concluded that CeO_2 (UR) and CeO_2 (CR) with higher surface areas presented more surface capping oxygen, which consumed more hydrogen during the TPR experiment, than the other two ceria catalysts. This observation is consistent with TPR data reported in the literature [7, 8] in which high surface area CeO_2 and Au/ CeO_2 catalysts showed higher hydrogen consumption than low surface area CeO_2 and Au/ CeO_2 catalysts.

Table 6.4 Effect of preparation method on hydrogen consumption by CeO₂ catalysts during TPR

Catalyst	H ₂ consumption (μmoleg ⁻¹) at LT ^a	H ₂ consumption (μmoleg ⁻¹) at HT ^a	Total H ₂ consumption (μmoleg ⁻¹) ^a	BET Surface Area ^b / m ² g ⁻¹	Total H ₂ consumption per m ²
CeO ₂ (UR)	4	235	239	126	1.90
CeO ₂ (CR)	3	199	202	105	1.92
scCeO ₂	9	64	73	31	2.35
CeO ₂ (Aldrich)	0	57	57	11	5.18

^aBy TPR analysis, 110 mg of sample, 20 mL min⁻¹ H₂, 5 °C min⁻¹.^bBy the BET method.

If surface area is the only factor determining the total amount of hydrogen consumed, the total hydrogen consumption per m² (table 6.4) should be the same for all four catalysts but this is not the case here. There exist an inverse relationship between surface area and total hydrogen consumption per m², in the sense that, lower surface area ceria catalysts (sc and Aldrich) showed higher total hydrogen consumption per m² than higher surface area ceria prepared via UR and CR. This suggests that apart from forming ceria catalysts with significant differences in surface area, the four preparation methods resulted in the formation of different surface structures. This is clearly evident in SEM images shown in figure 6.3.

6.2.2 Influence of Preparation Method on the Naphthalene Oxidation Activity of Ceria Catalysts

Figure 6.5 illustrates the evolution of naphthalene oxidation activity of ceria with preparation method.

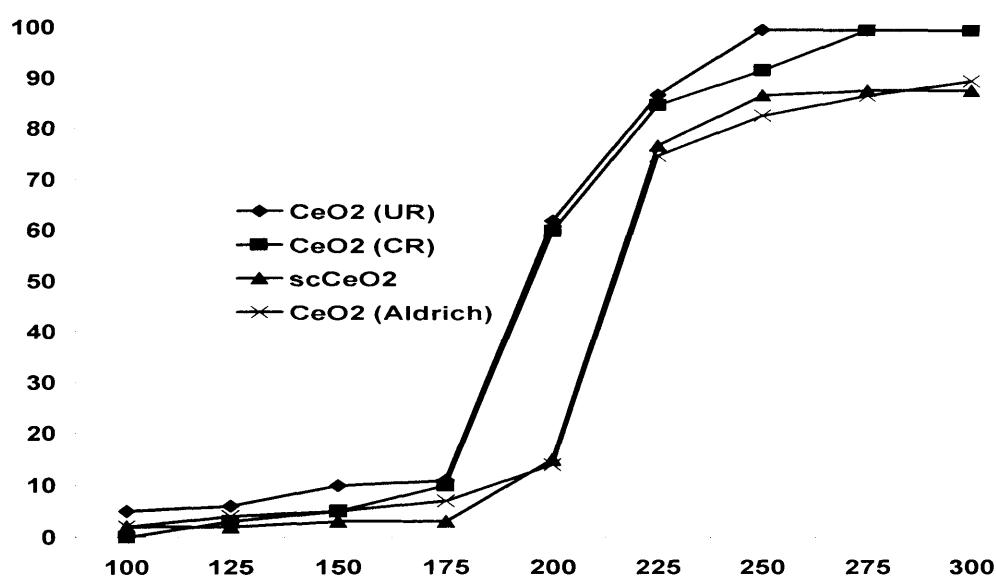


Fig. 6.5 Effect of preparation method on the activity of ceria catalyst for the total oxidation of naphthalene, 100 vppm Np, GHSV = 45000 h⁻¹.

Ceria catalysts prepared using UR and CR showed similar activities in naphthalene oxidation. The activities of these two catalysts were considerably higher than the activity of scCeO₂ and the commercially available CeO₂ (Aldrich) catalysts. The higher activity of CeO₂ (UR) and CeO₂ (CR) can be related to higher surface areas, smaller crystallite sizes and higher oxygen defect concentrations relative to the other two catalysts. BET results showed that CeO₂ (UR) and CeO₂ (CR) had higher surface areas (126 and 105

m^2g^{-1} respectively) than scCeO_2 and CeO_2 (Aldrich) which had surface areas of 31 and 11 m^2g^{-1} respectively. XRD analysis also showed that the latter had higher crystallite sizes (6.3 and > 100 nm for the sc ceria and commercially available ceria catalysts respectively) than ceria prepared by UR and CR. Raman results showed that the concentration of oxygen defects was also significantly higher in ceria catalysts prepared via UR and CR than the commercial catalyst and catalyst prepared using supercritical carbon dioxide. High surface area, small crystallite size and high concentration of oxygen defects therefore favored the activity of the ceria catalysts in naphthalene oxidation. The above properties of ceria were determined by the nature of starting material, reaction conditions for preparation of the ceria precursor and the calcination conditions. The optimum characteristics of ceria for Np oxidation were achieved in catalysts prepared via UR and CR. TPR data suggested that high surface area CeO_2 (UR) and CeO_2 (CR) had more reactive surface species like capping oxygen than the lower surface area scCeO_2 and CeO_2 (Aldrich). The higher amount of these reactive surface species in the former is reflected in their higher Np oxidation activity and rate (see table 6.5).

Table 6.5 shows the relationship between the specific activity (rate of Np oxidation) at 175 °C with the surface area, crystallite size and FWHM of Raman band. It can be observed that the rate of naphthalene oxidation was directly proportional to the surface area and FWHM and inversely proportional to the crystalline size of ceria.

Table 6.5 Effect of surface area, crystallite size and FWHM of Raman band on NP oxidation rate

Catalyst	$r_{\text{Np}} \times 10^{-10}$ (moles $\text{s}^{-1}\text{m}^{-2}$)	Surface area (g m^{-2})	Crystallite size (nm)	FWHM (cm^{-1})
CeO ₂ (UR)	6.2	126	5.4	28
CeO ₂ (CR)	6.1	105	6.1	29.5
scCeO ₂	5.8	31	6.3	19.6
CeO ₂ (Aldrich)	2.8	11	> 100	17.8

 r_{Np} - Np oxidation rate

The variation in the specific activity of ceria with surface area suggests the relevance of other factors in determining the Np oxidation activity of the ceria catalysts. Notice that the specific activity was fairly similar for catalysts prepared using UR and CR, suggesting that surface area was the main reason for the differences observed in the Np oxidation activity of these two catalysts. This is quite reasonable since these two catalysts showed fairly similar crystallite sizes (6.1-6.2 nm) and concentration of oxygen defect (FWHM = 28-29.5 cm^{-1}). The effect of differences observed in the morphology of these catalysts can however not be undermined. The inverse relationship observed between crystallite size and Np oxidation rate suggest that small crystallite size of ceria favored the Np oxidation activity of the ceria catalyst. On the other hand, the fact that Np oxidation rate was directly proportional to the FWHM (associated with concentration of oxygen defect) reveals that a high concentration of oxygen defect is needed to achieve high naphthalene oxidation activity for a ceria catalyst. Although surface area, crystallite

size and concentration of oxygen defect were quantifiable parameters found to relate to the naphthalene oxidation activity, it should be noted that the differences observed in the morphology of these ceria catalysts with preparation method could also contribute immensely in influencing the naphthalene oxidation activity of the ceria catalysts. This would explain why scCeO_2 showed a Np oxidation rate almost as high as the UR and CR ceria catalysts irrespective of the fact that this catalyst had a relatively very low surface area, fairly similar crystallite size and lower concentration of oxygen defects than the UR and CR ceria catalysts.

The naphthalene oxidation activity of the CeO_2 (CR) catalyst reported in this work was considerably higher than that of a similar catalyst reported in the literature [1]. T. Garcia et al. showed that the activity of a ceria catalyst prepared via the UR was considerably higher than the activity of a ceria catalyst prepared using the CR. Contrary to the above findings; naphthalene oxidation activity results reported in this study showed that the activity of the ceria catalyst was similar irrespective of whether the UR or CR was employed. The CR ceria catalyst investigated in this study was prepared using similar conditions (except for calcination temperature and calcination time) as the CR ceria catalyst reported in the literature. The calcination temperature/time for the ceria catalyst prepared by precipitation with the carbonate (CR) in this work was higher ($500\text{ }^\circ\text{C}/10\text{ h}$) than calcination temperature/calcination time used for the preparation of the catalyst reported by T. Garcia et al. ($400\text{ }^\circ\text{C}/3\text{ h}$). Higher calcination temperature/time employed in this work resulted in a ceria (CR) catalyst with a significantly higher surface area ($105\text{ m}^2\text{g}^{-1}$), higher reactive surface species like capping oxygen, than the ceria (CR) catalyst

reported in the literature (surface area = $87 \text{ m}^2\text{g}^{-1}$) and hence higher naphthalene oxidation activity of the former. It is likely therefore that the high calcination temperature and longer calcination time employed in this work led to complete removal of carbonate from ceria pores. Lower calcination temperature/time employed by T. Garcia et al. probably resulted in a ceria catalyst which contained some amount of carbonate in the ceria pores and thus had a lower surface area. The morphology of the CR ceria in this work differed considerably with the morphology of the ceria (CR) catalyst reported by T. Garcia et al. and as such confirms the dependence of morphology of ceria on calcination conditions as seen earlier in chapter 5. This difference in morphology also probably contributed to the difference in the Np oxidation activity observed between the CR ceria catalyst in this work and that reported in the literature [1].

6.3 Influence of Pt-doping of Nano-crystalline Ceria Catalysts in the Total Oxidation of Naphthalene

In chapter 5 it was established that optimum preparation conditions for the preparation of ceria catalyst by homogeneous precipitation with urea [CeO_2 (UR)] included a cerium salt to urea ratio of 2:1, 1:1, or 1:4, ageing time of 12 h and a calcination temperature and time of 500 °C and 6 h. In the first part of this chapter (section 6.2), it has been shown that a CeO_2 (UR) catalyst prepared from a combination of some of these conditions (1:4 Ce salt/urea ratio, aged for 12 h and calcined at 500 °C for 6 h) was a better naphthalene oxidation catalyst than ceria prepared using supercritical carbon dioxide as well as a commercial ceria catalyst. In chapter 2 the preparation of Pt/ CeO_2 (UR) catalysts composed of 1:4 cerium salt to urea ratio was reported. Optimum ageing and calcination conditions for the preparation of CeO_2 (UR) were used to prepare two Pt/ CeO_2 (UR) catalysts with varying Pt loadings. The composition of the Pt-ceria catalysts were in the ratio of 0.2 g Pt salt: 20 g cerium salt: 80 g urea [denoted Pt/ CeO_2 (UR), 0.2:20:80] and 1.0 g Pt salt: 20 g Cerium salt: 80 g urea [denoted Pt/ CeO_2 (UR), 1:20:80]. In this section (6.3) the effect of adding Pt during the preparation of CeO_2 (UR) catalyst for the total oxidation of naphthalene is evaluated by comparing characterization and naphthalene oxidation activity data of the CeO_2 (UR) catalyst (prepared from 1:4 Ce salt/urea ratio, aged for 12 h and calcined at 500 °C for 6 h) with data obtained for the two Pt/ CeO_2 (UR) catalysts mentioned above. The results obtained are presented in the following sections.

6.3.1 Surface and Structural Studies of CeO₂ (UR) and Pt/ CeO₂ (UR) Catalysts

Table 6.6 shows the BET surface areas obtained for CeO₂ (UR) and the two Pt/CeO₂ (UR) catalysts. The results show that the addition of Pt resulted to a decrease in the surface area of the ceria catalyst. The Pt-free CeO₂ (UR) catalyst showed a higher surface area than both Pt/CeO₂ (UR) catalysts. During the preparation of the Pt/CeO₂ (UR) by precipitation, Pt can interact with CeO₂ in two ways: It can be incorporated in the bulk of ceria or dispersed on the surface. SEM images (figure 6.6) reveal that this interaction between Pt and ceria favors the agglomeration of particles. While the Pt-free ceria catalysts was composed of very tiny dust-like particles with some larger particles dispersed in them, the Pt/ceria catalyst showed relatively larger particles which seemed to emanate from the agglomeration of smaller particles. This thus explains the decrease in surface area with the addition of Pt.

Table 6.6 Effect of Pt addition on the surface area of CeO₂ (UR) catalyst

Catalyst	BET Surface Area ^a / m ² g ⁻¹
CeO ₂ (UR)	126
Pt/CeO ₂ (UR), 0.2:20:80	96
Pt/CeO ₂ (UR), 1:20:80	95

^a By BET method

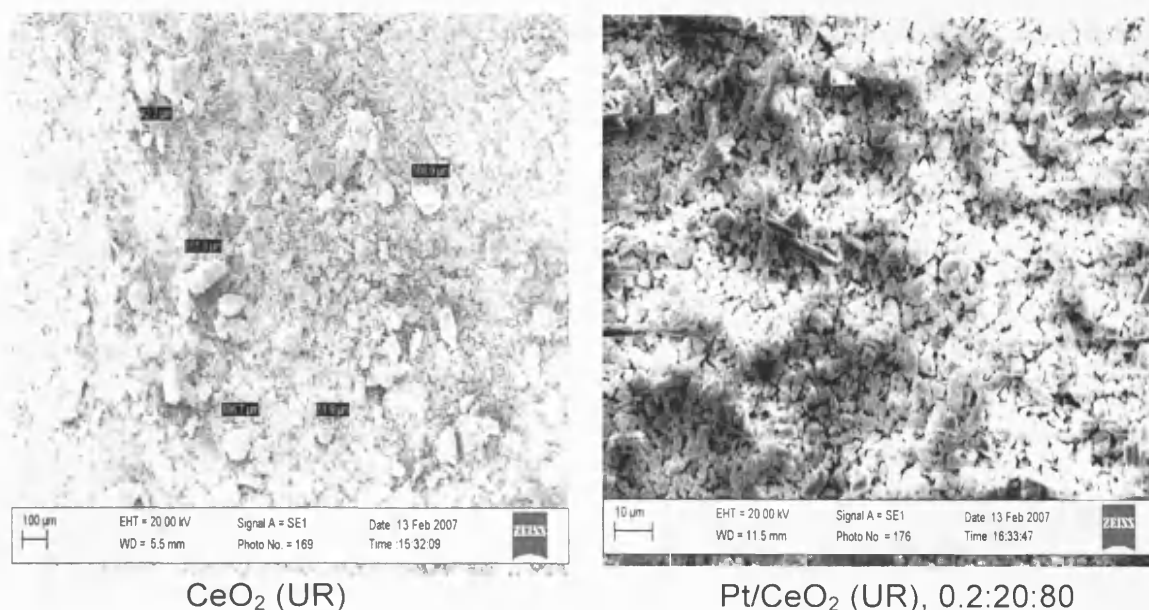


Fig. 6.6 SEM micrographs for CeO₂ (UR) and Pt/ CeO₂ (UR)

CO chemisorption results confirmed that there was Pt dispersed on the surface of CeO₂ in Pt/CeO₂ catalysts. The catalyst with a lower Pt content (Pt/CeO₂, 0.2:20:80) yielded a higher Pt dispersion (42 %) than the catalyst with a higher metal content (Pt/CeO₂, 1:20:80, Pt dispersion = 25 %). The Pt surface area increased while the Pt particle size decreased as the Pt dispersion increased.

The effect of Pt addition on the microstructure of ceria was evaluated by XRD analysis. XRD patterns of CeO₂ (UR) and the two Pt/CeO₂ (UR) catalysts are illustrated in figure 6.7. CeO₂ (UR) and both Pt/CeO₂ (UR) catalysts all showed major XRD peaks characteristic of cubic fluorite ceria. In addition to the peaks representative of the ceria phase, both Pt/CeO₂ (UR) catalysts showed two very sharp peaks at ca. 38 and 65 ° which were both absent in the pattern of the Pt-free ceria catalyst. Both peaks have been assigned to the presence of some Pt species (crystalline Pt or mixed Pt-CeO₂ phase),

hence confirming the dispersion of crystallites of Pt on the ceria surface in accordance with CO chemisorption results. It is obvious from the peak sizes and the level of background noise that the addition of Pt during precipitation led to Pt/CeO₂ (UR) catalysts that were quite less crystalline than the CeO₂ (UR) catalyst.

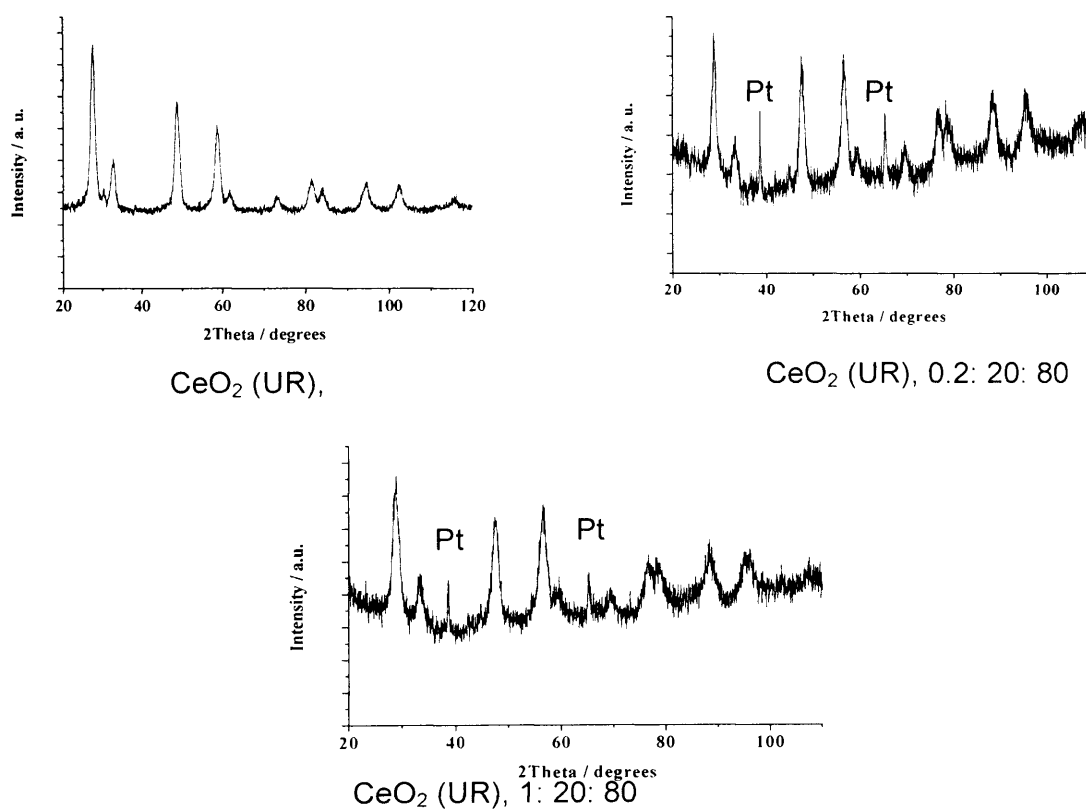


Fig. 6.7 XRD patterns of CeO₂ (UR) and Pt/CeO₂ (UR) catalysts

The crystallite sizes of CeO₂ (UR) and Pt/CeO₂ (UR) catalysts calculated by XRD analysis using the Scherrer equation (table 6.7), revealed a considerable decrease in crystallite size with the addition of Pt. The Pt-free CeO₂ (UR) catalyst showed a considerably higher crystallite size (5.4 nm) than the Pt/CeO₂ (UR) catalysts (crystallite

sizes of 2.6 and 3.3 nm for catalyst with low and high Pt loading respectively). Based on BET and SEM results, it is likely that these very small crystallites in Pt-containing ceria tend to cluster together, forming larger particles which lead to a decrease in surface area. There is no or relatively low degree of aggregation of larger crystallites in the Pt-free ceria catalyst.

Table 6.7 Effect of Pt addition on the crystallite size of CeO₂ (UR) catalyst

Catalyst	Crystallite size ^a / nm
CeO ₂ (UR)	5.4
Pt/CeO ₂ (UR), 0.2:20:80	2.6
Pt/CeO ₂ (UR), 1:20:80	3.3

^a By XRD analysis

6.3.2 Raman Results for CeO₂ (UR) and Pt/CeO₂ (UR) Catalysts

Raman spectra recorded for CeO₂ (UR) and Pt/CeO₂ (UR) catalysts are shown in figure 6.8. All three catalysts showed the main Raman band at 460 cm⁻¹ characteristic of CeO₂ vibrations (triply degenerate TO mode). Other less intense Raman bands typical of CeO₂ were observed at ca. 272 and 595 cm⁻¹ (doubly degenerate TO mode and non-degenerate LO mode, respectively). The Pt/CeO₂ (UR) catalysts showed an additional Raman band at ca. 690 cm⁻¹ and this was most intense for the catalyst with a higher Pt content. The assignment of this band is not clear but it is likely that it relates to vibration of some Pt species in accordance with CO chemisorption and XRD results. The interaction of Pt with

ceria is known to form Pt-O-Ce bond [9] which could be responsible for the above mentioned Raman band in the Pt/CeO₂ (UR) catalysts.

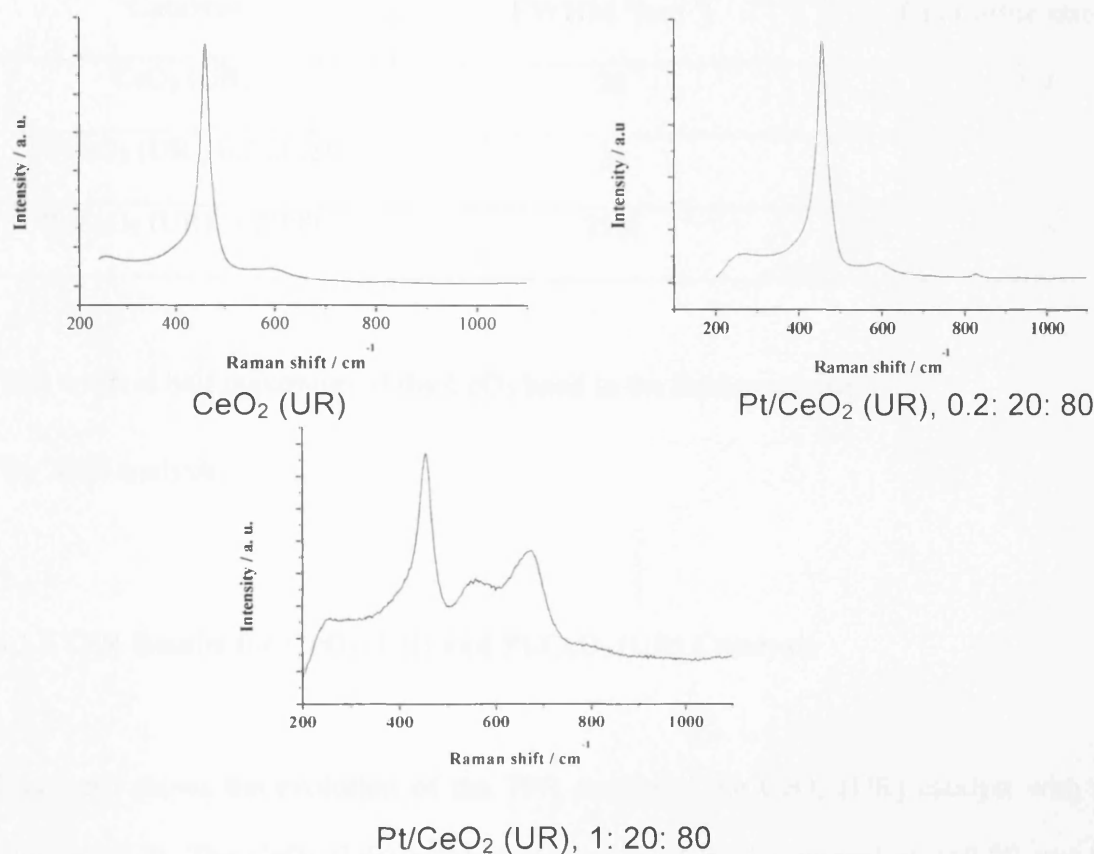


Fig.6.8 Raman spectra for CeO₂ (UR) and Pt/CeO₂ (UR) catalysts

Table 6.8 shows that the FWHM of the main Raman band varied only slightly with the addition of Pt to the CeO₂ (UR) catalyst. Since the crystallite size decreased considerably with increase in FWHM it can be concluded that the change in FWHM observed upon addition of Pt is more related to the decrease in crystallite size than to the oxygen defect concentration. However if the concentration of oxygen defect changes, it can be inferred based on the FWHM values that the Pt/CeO₂ (UR) catalysts would be more defective than the CeO₂ (UR) catalyst.

Table 6.8 Effect of Pt addition on the FWHM of Raman band and crystallite size of CeO₂

(UR) catalyst

Catalyst	FWHM ^a [cm ⁻¹]	Crystallite size ^b / nm
CeO ₂ (UR)	28	5.4
Pt/CeO ₂ (UR), 0.2:20:80	31	2.6
Pt/CeO ₂ (UR), 1:20:80	29.5	3.3

^aFull width at half maximum of the CeO₂ band in the Raman spectra.^bBy XRD analysis.

6.3.3 TPR Results for CeO₂ (UR) and Pt/CeO₂ (UR) Catalysts

Figure 6.9 shows the evolution of the TPR profile of the CeO₂ (UR) catalyst with the addition of Pt. The CeO₂ (UR) catalyst showed a LT peak centered at 110 °C and HT peaks at 390 and 470 °C while the Pt/CeO₂ (UR) catalyst with lower Pt content (0.2:20:80) only showed a single intense peak centered at 290 °C.

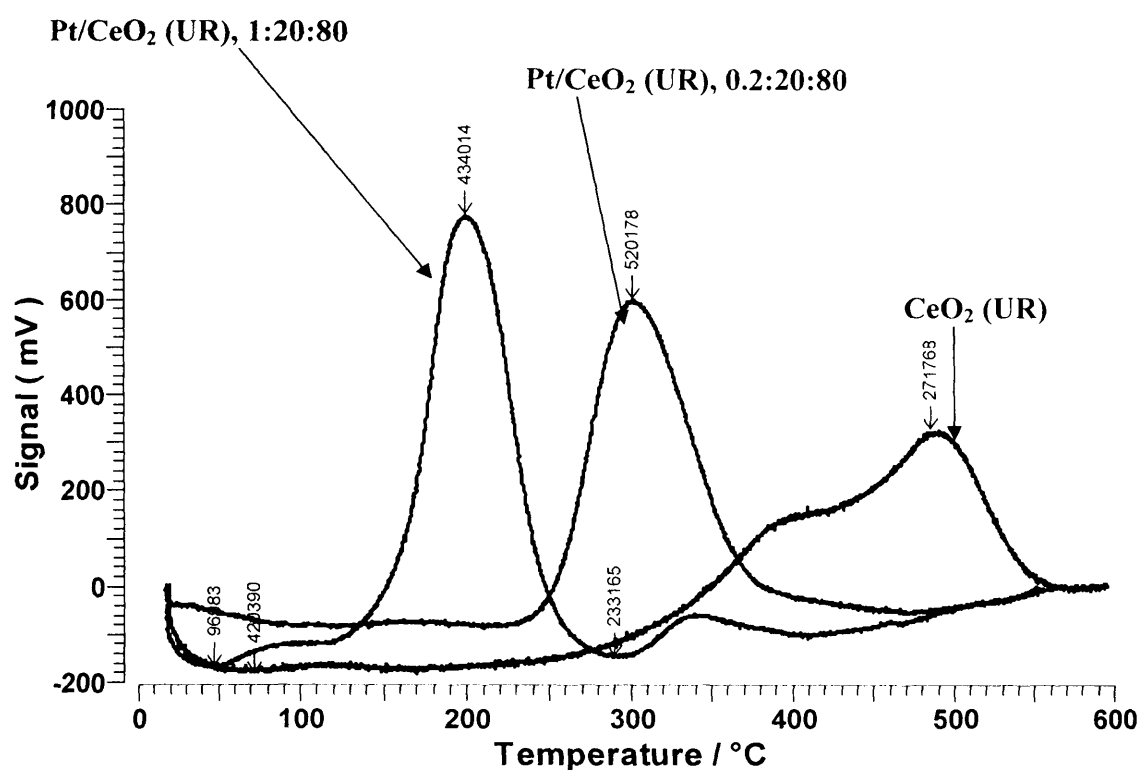


Fig. 6.9 Hydrogen TPR profiles for CeO_2 (UR) and Pt/CeO_2 (UR) catalysts

The Pt/CeO_2 (UR) catalyst with higher Pt content (1:20:80) showed an intense peak at lower temperature (190 °C) and a considerably less intense peak that coincided with the intense peak for the other Pt/CeO_2 (UR) catalyst (at 290 °C). The TPR results therefore show that the addition of Pt to the CeO_2 (UR) catalyst resulted to a decrease in the reduction temperature of the most intense TPR peak. This suggests that the Pt/CeO_2 (UR) catalysts were more susceptible to reduction by hydrogen than the CeO_2 (UR) catalyst. This can be attributed to the effect of hydrogen spillover (surface diffusion of activated hydrogen) on the Pt particles dispersed on the surface of ceria. Hydrogen and small molecules like methanol are known to dissociatively adsorb on Pt easily [10-13]. This dissociative adsorption results in the formation of very reactive atomic hydrogen species which can easily reduce ceria. In the Pt-free CeO_2 (UR) catalyst the hydrogen spill over

effect does not occur, leading to reduction of the CeO_2 (UR) catalyst to be completed at higher temperatures than the Pt/CeO_2 (UR) catalysts. Pt/CeO_2 (UR), 0.2:20:80 and 1:20:80 yielded higher hydrogen consumption per m^2 (2.7 and 2.3 $\mu\text{mole m}^{-2}$ respectively) than the CeO_2 (UR) catalyst (1.9 $\mu\text{mole m}^{-2}$). Thus, confirming that the Pt-doped ceria had more surface oxygen species than the ceria catalyst. This equally suggests that the addition of Pt resulted to the formation of slightly different surface structures of ceria.

6.3.4 Effect of Pt-doping on the Activity of a Nanocrystalline CeO_2 (UR) catalyst for the Complete Oxidation of Naphthalene

Figure 6.10 shows the effect of doping the CeO_2 (UR) catalyst with Pt on the activity of the ceria catalyst in naphthalene oxidation. The CeO_2 (UR) catalyst showed higher activity in naphthalene oxidation than both Pt/CeO_2 (UR) catalysts. Hence, the addition of Pt to the CeO_2 (UR) catalyst led to a decrease in activity.

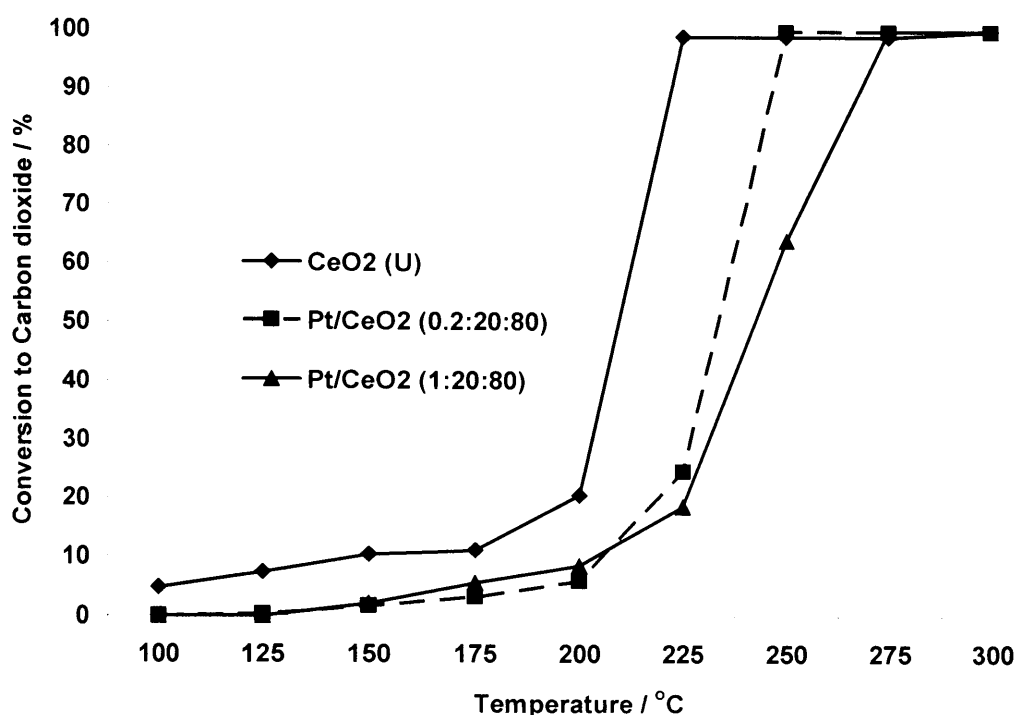


Fig 6.10 Naphthalene oxidation activity of CeO₂ (UR) and Pt/CeO₂ (UR) catalysts showing the influence of Pt addition, 100 vppm Np, GHSV = 45000 h⁻¹.

In chapter 5 and the first part of chapter 6 (section 6.2), it was shown that high surface area and small crystallite size of ceria favored the activity of ceria catalysts in naphthalene decomposition. Although Pt/CeO₂ (UR) catalysts had lower surface areas (95-96 m²g⁻¹) and considerably lower crystallite sizes (2.6-3.3 nm) than the CeO₂ (UR) catalyst (with surface area of 126 m²g⁻¹ and crystallite size of 5.4 nm) the latter proved to be a more effective naphthalene oxidation catalyst than both Pt/CeO₂ (UR) catalysts. Hence it can be assumed that the interaction between Pt and CeO₂ was more crucial in determining the activity of each Pt/CeO₂ (UR) catalyst than the surface area and crystallite size of the catalyst. TPR results suggested that the Pt/CeO₂ (UR) catalysts were

more easily reduced by hydrogen than the CeO_2 (UR) catalyst. Np oxidation activity data did not reflect the TPR data. The effect of hydrogen spillover facilitates the reduction of Pt/ CeO_2 (UR) catalysts by hydrogen. Naphthalene is a large polycyclic aromatic molecule and is not likely to adsorb on to the surface of Pt in a similar manner as hydrogen. Unlike the effect of Pt in this work, Au has been found to promote the activity of ceria catalysts for the oxidation of VOCs [2]. The enhanced activity of the Au/ceria catalyst was attributed to the ability of gold particles to weaken the Ce—O bond, thus resulting in the increase in the mobility or reactivity of lattice oxygen which is involved in the oxidation of VOCs via the Mars-Van Krevelen mechanism. Contrary to the effect of Au on ceria, Imamura et al. [13] have shown that Pt interacts very strongly with CeO_2 making it possible for the formation of Pt-O-Ce bond (which in this study could be accounted for by the presence of dispersed Pt as indicated by CO chemisorption results and the presence of additional Pt species XRD peaks at 35° and 65° and an additional Raman band at 690 cm^{-1} in the XRD patterns and Raman spectra of the Pt/ CeO_2 (UR) catalysts) and the penetration of Pt in to the bulk of CeO_2 . It is therefore possible that this strong interaction between Pt and CeO_2 leads to the formation some species that limit the ease at which naphthalene is reduce in the redox cycle. It has been reported [2] that the oxidation of VOCs over CeO_2 and Au/ CeO_2 catalysts occurs via the Mars Van-Krevelen Mechanism in which oxygen from the lattice is used. Naphthalene oxidation over the CeO_2 (UR) catalyst therefore followed the Mars-Van Krevelen mechanism. The interaction between Pt and CeO_2 limits the ease with which the lattice oxygen is consumed in the redox cycle. This makes the CeO_2 (UR) catalyst more active in naphthalene oxidation than the Pt/ CeO_2 (UR) catalysts. The above explanation has also

been used [14] to account for a decrease in activity of a ceria catalyst for the oxidation of ethanol on addition of noble metals like Pt. The addition of Pt suppressed the oxidation of ethanol to acetate at ambient temperature since there were fewer surface oxygen atoms available for the oxidation.

Np oxidation over the Pt-doped ceria catalyst in this study probably followed a mechanism different from the Mars-Van Krevelen mechanism or a combination of this mechanism and other(s). As discussed earlier in Chapter 3, Np oxidation over Pt-supported catalysts proceed via the Eley-Rideal mechanism, Langmuir-Hinshellwood scheme or a combination of both. It can be postulated that Np oxidation over the Pt/ceria catalysts followed a more complex scheme which could involve a combination of the Mars-Van Krevelen mechanism and one or both of the other mechanisms mentioned above. This resulted in the lower Np oxidation activity exhibited by the Pt-doped ceria catalysts relative to the pure ceria catalyst which oxidized naphthalene effectively in a less complex scheme (Mars-Van Krevelen cycle).

6.4 Conclusions

Ceria catalysts were prepared using three different methods and tested for the complete oxidation of naphthalene. The results obtained for the synthesized ceria catalysts were compared with those derived using a commercial ceria catalyst. The preparation method affected the crystallite size, surface area, oxygen defect concentration and morphology of the ceria catalysts and this resulted in differences in naphthalene oxidation activity. High

surface area, small crystallite size and high oxygen defect concentration were found to be favorable for the oxidation of naphthalene. The best ceria catalysts in this study were ceria prepared by homogeneous precipitation with urea [CeO_2 (UR)] and ceria prepared by precipitation with the carbonate [CeO_2 (CR)]. The commercial ceria catalyst [CeO_2 (Aldrich)] and ceria prepared using supercritical carbon dioxide (scCeO_2) showed considerably lower activities. Pt-ceria catalysts prepared by homogeneous precipitation with urea were also evaluated for the complete oxidation of naphthalene. It was observed that the addition of Pt to the CeO_2 (UR) catalyst was detrimental to the efficiency of the catalyst in naphthalene oxidation. This has been related to a strong interaction between Pt and CeO_2 which tends to hinder the ease at which lattice oxygen is used up for naphthalene oxidation in the Mars-Van Krevelen redox cycle.

References

1. T. Garcia, B. Solsona, and S. H. Taylor, *Catal. Lett.*, 105 (2005) 183.
2. S.-K. Kim, U. Paik and J.-G. Park, *Journal of Ceramic Processing Research*, 7 (2006) 5357.
3. F. Sadi, D. Duprez, F. Gerard, and A. Miloudi, *J. Catal.* 213 (2003) 226.
4. Y. Wang, T. Mori, J.-G. Li, T. Ikegami and Y. Yajima, *J. Mater. Res.* 18 (2003) 1239.
5. S.-K. Kim, P. W. Yoon, U. Paik, T. Katoh and J. G. Park, *Jpn. J. Appl. Phys.* 43 (2004) 7427.
6. C. H. Lu, and H. C. Wang, *Mat. Sci. and Eng. B*90 (2002) 138.
7. V. Perrichon, A. Laachir, G. Bergeret, R. Frety and L. Tournayan, *J. Chem. Soc., Faraday Trans.* 90 (1994) 773.
8. S. Scire, S. Minico, C. Crisafulli, C. Satriano and A. Pistone, *Appl. Catal. B: Environ.* 40 (2003) 43.
9. J. Wang, and R. I. Masel, *Surf. Sci.* 243 (1991)199.
10. A. K. Bhattacharya, M. A. Chesters, M. E. Pemble, and N. Sheppard, *Surf. Sci.*206 (1988) L845.
11. G. E. Gdowski, J. A. Fair, and R. J. Madix, *Surf. Sci.*127 (1983) 541.
12. I. Toyoshima, and G. A. Somorjai, *Catal. Rev.-Sci. Eng.* 19 (1979) 105.
13. S. Imamura, T. Higashihara, Y. Saito, H. Aritani, H. Kanai, Y. Matsumura, and N. Tsuda, *Catal. Today* 50 (1999) 369.
14. H. Idris, *Platinum Metals Review*, 48, (2004) 105.

CHAPTER 7: CONCLUSIONS AND RECOMMENDATIONS

Volatile organic compounds such as polycyclic aromatic hydrocarbons (PAHs) emitted into the atmosphere pose enormous health and environmental threats. Fuel combustion and industrial processes account for a great deal of PAH and VOC emissions. In this thesis, various catalyst formulations based on oxides and two precious metals (Pd and Pt) have been investigated for the complete oxidation of naphthalene which is a model PAH. This was done in a bid to develop catalysts potentially applicable for the effective destruction of PAH and possibly other VOCs from fuel-combusting devices and end-of-pipe in industries. To date, there is very limited work in the literature patterning to the catalytic oxidation of PAHs.

The influence of the addition of varying loadings of vanadium modifier to Pd/Al₂O₃ and Pt/Al₂O₃ catalysts known to be effective for Np oxidation was investigated. Low loadings of V (0.5 % for Pt catalysts and 0.5-3% for Pd catalysts) promoted the activity of both catalysts for Np oxidation whilst higher loadings (6-12% for Pd/V and 1-12% for Pt/V catalysts) were detrimental to the activity of these catalysts. The enhanced activity for catalysts with low V loadings has been related to the redox chemistry of a low concentration of some kind of V species and the modification of the metal (Pd or Pt) dispersion while high concentrations of crystalline V₂O₅ species accounted for the drop in the activity of the catalysts with higher V loadings (6 and 12% for Pd catalysts and 1-12% for Pt catalysts). While the Mars Van Krevelen redox mechanism is suggested as the mechanism for Np oxidation over Pd/V/Al₂O₃ catalysts, the oxidation over Pt/V/Al₂O₃

catalyst is thought to follow the Eley- Rideal mechanism, the Langmuir Hinshel-wood kinetics or a combination of both.

Since a strong promotional effect has been observed for the use of V as modifier for both Pd and Pt-supported alumina catalysts, it is likely that the use of other modifiers such as Nb, W and possibly other metal oxides (e.g CeO₂, ZrO₂) might also promote the activity of these metal-supported alumina catalysts for naphthalene oxidation. It is recommended that other modifiers be used as there is a possibility of generating better Pd/X/Al₂O₃ and Pt/X/Al₂O₃ catalysts, where X is a modifier, to deal with the emission of PAHs and VOCs from fuel combusting devices and end-of-pipe in industry.

From the study reported above and in the literature (see chapter 1) it was deduced that Pt-based alumina catalysts showed superior naphthalene oxidation efficiencies over Pd-based alumina catalysts. As such, various supports (SiO₂, TiO₂, Al₂O₃, CeO₂, and SnO₂) were investigated for their effectiveness as support materials for Pt catalysts for Np oxidation. In this study, SiO₂ proved to be the best Pt catalyst support for naphthalene oxidation. For Pt-supported catalysts with equal metal loading, the Pt dispersion varied with the nature of the support used. The differences observed between the Np oxidation activity of these Pt catalysts was related to the differences in the metal dispersion and this depended mainly on the type of support used. Large Pt particles (low Pt dispersion) promoted the activity of the Pt-supported catalysts for Np oxidation. It was postulated that SMSI and metallic state of Pt which are characteristic of the use of reducible and acidic supports respectively, influenced the Np oxidation efficiency of the Pt-supported

catalysts. Weak MSI and zero oxidation state of Pt achieved via the use of non-reducible and acidic supports (alumina and silica) were thought to favor the Np oxidation performance of these Pt catalysts. The optimum Pt dispersion, MSI, and oxidation state of Pt for Np oxidation was achieved by using SiO_2 as support material for the Pt-supported catalyst.

CeO_2 is a material known to have been extensively used as an additive in TWC for exhaust treatment due to its excellent redox properties and ability to act as an oxygen reservoir. Preparation methods and conditions for crystalline CeO_2 catalysts were studied for the complete oxidation of naphthalene. A variation in the preparation method affected the surface area, crystallite size, morphology and reducibility of the ceria catalyst and hence the Np oxidation activity. High surface area and small crystallite size of CeO_2 favored the activity of the catalyst for Np oxidation. The best preparation methods in this study were found to be homogeneous precipitation with urea (UR) and precipitation with the carbonate (CR). A variation in the preparation conditions (calcination temperature/time, aging time and Ce salt/urea ratio) of the CeO_2 (UR) catalyst resulted in variations in the surface area, crystallite size, particle size, morphology, oxygen defect concentration and surface reducibility of the CeO_2 (UR) catalyst. The variation in the above properties of this CeO_2 catalyst led to the differences in the Np Oxidation activity of the CeO_2 (UR) catalysts. High surface area, small crystallite size and high oxygen defect concentration of the CeO_2 (UR) catalyst were also found to favor the naphthalene oxidation activity of this CeO_2 (UR) catalyst. Optimum preparation conditions for Np oxidation included: Ce salt/urea ratios of 2:1, 1:1, and 1:4, calcination temperature of 500

and 600 °C, calcination time of 6 h and an aging time of 12 h. Although homogeneous precipitation with urea produced the most active naphthalene oxidation ceria catalysts, precipitation of ceria using carbonate (CR) and CeO₂ preparation involving the use of supercritical CO₂ (sc) also gave reasonably high naphthalene oxidation efficiencies. It can be proposed that the crystallite size, surface area, morphology and oxygen defect concentration of ceria (which were crucial for the efficiency of the ceria catalysts for Np oxidation) could also be tuned to achieve higher naphthalene oxidation rates by optimizing the CR and sc methods of preparing CeO₂. It would thus be worth carrying out a detailed study to investigate the effect of the variation in preparation conditions of CeO₂ (CR) and scCeO₂ catalysts for naphthalene oxidation. Preparation parameters to be considered for the CR include: reaction temperature, calcination temperature/time, aging time, and pH of the Ce nitrate + carbonate mixture. For the sc method, possible variable parameters include: the temperature of the system, pressure, flow rates and calcination conditions (temperature and time).

The influence of doping the CeO₂ (UR) catalyst with Pt was also studied. The addition of Pt during the precipitation of the CeO₂ catalyst with urea resulted in the drop in the activity of CeO₂ (UR) catalyst. The decrease in the activity with Pt doping has been related to a strong interaction between Pt and CeO₂ which leads to the formation of Pt-O-Ce species that interferes with the ease of oxygen uptake from the CeO₂ lattice during the Mars-Van Krevelen (M-V K) mechanism. Whereas Np oxidation over pure ceria followed the Mars-Van Krevelen mechanism, it is postulated that the oxidation of Np over the Pt/CeO₂ catalysts involved a combination of the M-V K and other mechanisms.

Since SMSI is suggested as the main reason for deactivation of ceria on doping with Pt, it would be worth studying the influence of other dopants (e.g. Au, Co, Ni, Cu, Fe). It can be assumed that if any of these metal dopants or others interacts with ceria such that the Ce-O bond is weakened, then, oxygen abstraction during the M-V K cycle will be relatively easier and this might enhance the efficiency of ceria in Np oxidation.

Catalysts synthesized in this work yielded complete naphthalene oxidation at appreciably lower temperatures (175-225 °C) than temperatures reported for the best catalysts researched for Np oxidation (see chapter 1). CeO₂ (UR) and 0.5%Pt/SiO₂ were the best catalysts in this study, yielding complete Np conversion and 100 % CO₂ yield at 175-225 °C (100 vppm Np, and GHSV = 45000 h⁻¹). The 0.5%Pt/SiO₂ catalyst showed a LOT lower than all catalysts in this study and in the literature (chapter 1).

To the best of my knowledge, the following catalysts [0.5%Pt/0.5%V/Al₂O₃, CeO₂ (UR), CeO₂ (CR) and 0.5%Pt/SiO₂] reported in this thesis are currently the best catalysts that have been researched for the complete oxidation of naphthalene, a model PAH. However, it is not certain whether similar or better oxidation efficiencies can be achieved if these catalysts are used for the oxidation of other VOCs and higher PAHs like phenanthrene, pyrene and xylene. Detail reaction sequence(s) and mechanism(s) of Np oxidation over these catalysts are still to be understood. It is recommended that the oxidation of other VOCs and higher PAHs (e.g. Phenanthrene and pyrene) be studied using 0.5%Pt/0.5%V/Al₂O₃, CeO₂ (UR) prepared using optimum preparation conditions, CeO₂ (CR) and 0.5%Pt/SiO₂. It will also be of great importance to carry out detailed

mechanistic studies (e.g. by infra-red spectroscopy, use of tap reactor) of PAH oxidation over these catalysts. Pt/V/Al₂O₃, CeO₂ (UR), CeO₂ (CR) and 0.5%Pt/SiO₂ catalysts prepared in this study are worthy of further research and application in catalytic systems for PAH emission control from fuel-combusting devices and treatment of PAH and VOCs from industrial emissions. Note however that the method of fabrication, forming or molding of these catalysts will also be critical for their effectiveness in such applications.

PUBLICATIONS

Part of the work reported in this thesis has been published in the following catalysis journals:

1. Naphthalene Oxidation over Vanadium-modified Pt Catalysts Supported on γ -Al₂O₃, Edwin Ntainjua Ndifor, Tomas Garcia and Stuart H. Taylor, Catal. Lett. 110 (2006) 125.
2. Influence of Preparation Conditions of Nano-crystalline Ceria Catalysts on the Total Oxidation of naphthalene a model Polycyclic Aromatic Hydrocarbon, Edwin Ntainjua Ndifor, Tomas Garcia, Benjamin Solsona and Stuart H. Taylor, Appl. Catal. B: Environ. (2007) Accepted on 29 May 2007.

3. The influence of cerium to urea preparation ratio of nanocrystalline ceria catalysts for the total oxidation of naphthalene, Edwin Ntainjua Ndifor, Tomas Garcia, Benjamin Solsona and Stuart H. Taylor, Catal. Today (2007) Submitted – June 2007.
4. The Role of Support on the Performance of Platinum-based Catalysts for the Total Oxidation of Polycyclic Aromatic Hydrocarbons, Edwin Ntainjua Ndifor, Albert F. Carley and Stuart H. Taylor, Catal. Today (2007) Submitted – June 2007.

